Università degli Studi di Torino
Scuola di Dottorato

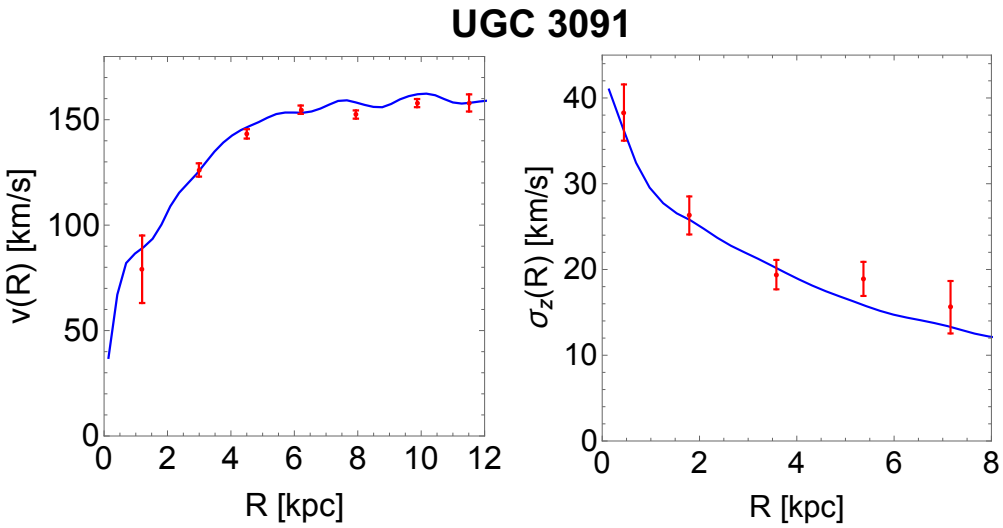

Dynamics of disk and elliptical galaxies in refracted gravity

Valentina Cesare

Università degli Studi di Torino
Scuola di Dottorato

Dottorato in Fisica ed Astrofisica

Dynamics of disk and elliptical galaxies in refracted gravity

Valentina Cesare

Tutor: Prof. Antonaldo Diaferio

Abstract

I investigate the dynamics of galaxies in refracted gravity (RG), a novel classical theory of modified gravity inspired to electrodynamics in matter, which does not resort to dark matter (DM). The presence of DM is mimicked by a gravitational permittivity, a monotonic increasing function of the local mass density which depends on three, in principle, universal parameters. RG properly describes the rotation curves and the vertical velocity dispersion profiles of 30 disk galaxies from the DiskMass Survey (DMS), with mass-to-light ratios consistent with stellar population synthesis (SPS) models, disk scale heights in agreement with edge-on galaxies observations, and RG free parameters from different galaxies consistent with each other, suggesting their universality. RG produces a radial acceleration relation of DMS galaxies with the correct asymptotic limits but with residuals correlating with some galaxy properties and with a too large intrinsic scatter, at odds with observations. Further investigation is required to assess if this issue indicates a failure of RG or depends on the galaxy sample. RG also models the velocity dispersions of stars and of blue and red globular clusters of the elliptical E0 galaxies NGC 1407, NGC 4486, and NGC 5846 belonging to the SLUGGS survey with mass-to-light ratios in agreement with SPS predictions, anisotropy parameters consistent with the literature, and the three RG parameters in agreement with each other. Two out of three RG parameters are also consistent with those estimated from the DMS galaxies. Given these encouraging results, RG is a theory that certainly deserves further investigation.

Contents

Chapter 1

Thesis plan

The target of this thesis work consists in testing, on galaxy scales, Refracted Gravity (RG), a novel theory of modified gravity inspired to electrodynamics in matter which does not resort to dark matter (DM).

This thesis is organised as follows. Chapter 2 introduces the general context of our work. In Sect. 2.1, we give an overview of the mass discrepancy problem in the Universe, observed from cosmological to galaxy scales, and of how the most investigated cosmological model, ΛCDM, accounts for it. According to ΛCDM, only ∼5% of the mass-energy budget of the Universe is made of ordinary and baryonic matter and the remaining ∼95% is made of two dark components, dark energy (DE, ∼70%) and DM (∼25%), implying a mass discrepancy of 80–90%.

Section 2.1.1 details the most important pieces of evidence of the mass discrepancy problem on large scales, and of the nonbaryonic and cold nature of DM. In Sect. 2.1.2, we describe the most striking piece of evidence of the mass discrepancy problem on galaxy scale: the flatness of rotation curves in disk galaxies. We also show three very tight relations between the properties of baryonic and dark matter in galaxies, that neatly quantify the mass discrepancy in these systems: the baryonic Tully–Fisher relation (BTFR), the mass discrepancy–acceleration relation (MDAR), and the radial acceleration relation (RAR). Moreover, we describe the mass discrepancy problem in dwarf galaxies, which are DM-dominated even in their innermost regions, in globular clusters (GCs), apparently DM-free, and in elliptical galaxies.

In Sect. 2.2, we present the major challenges encountered by the ΛCDM paradigm in describing the phenomenology in the Universe. The ΛCDM model faces some issues on large scale, like the *cosmological constant* and the *coincidence* problems and some tensions between cosmological parameters measured from the late-time and the early-time Universe. However, the important challenges presented by the ΛCDM model appear at the scale of galaxies. Among them, we describe the smallness of the scatter of the DM-baryons relations and the lack of correlations between their residuals and the galaxy properties. In Sect. 2.2.1 we illustrate some possible solutions to these problems on large scales, provided by dynamical DE and modified gravity models. In Sect. 2.2.2, we present, instead, the most investigated solutions on galaxy scale remaining within the context of the CDM paradigm, considering alternative DM models, and modifying the law of gravity with respect to Newtonian one. One of the most investigated theories of modified gravity on galaxy scale is MOdified Newtonian Dynamics (MOND).

In our work, we present RG, another theory of modified gravity which aims to describe the phenomenology observed on galaxy scale without resorting to DM. Chapter 3 summarises the main features of RG. In Section 3.1, we present the basic equations that formulate this theory. Specifically, the RG field equations yield a Poisson equation modified with respect to the Newtonian one by the presence of a gravitational permittivity, an arbitrary monotonic function of the local mass density that contains three free universal parameters. Section 3.1 also illustrates the first successes achieved by the theory

in modelling the rotation curves and the BTFR of disk galaxies and the temperature profiles of galaxy clusters. Sections 3.2 and 3.3 describe the main applications of RG on galaxy and cluster scales: the theory might explain the different dynamical properties in flattened and spherical systems, like elliptical galaxies with different ellipticities or dwarf galaxies and GCs, and the BTFR extended to galaxy groups and clusters. We conclude this chapter by highlighting the analogies and the differences between RG and MOND theories (Sect. 3.4) and by presenting the ongoing project of a covariant formulation of RG (Sect. 3.5).

In Chapters 4 and 5, which is the original work of this thesis, we test RG on galaxy scale, by investigating the dynamics of disk and elliptical galaxies. In Chapter 4 we model the rotation curves, the vertical velocity dispersions profiles, and the RAR of 30 close to flace-on disk galaxies belonging to the DiskMass Survey (DMS). In Sect. 4.1, we model the rotation curves of the DMS galaxies alone, whereas in Sect. 4.2 we model both their rotation curves and vertical velocity dispersion profiles, at the same time. Modelling the dynamics of each galaxy in RG requires five free parameters: two parameters for the galaxy, namely, its mass-to-light ratio and its disk-scale height, and three RG free parameters. Introducing the vertical velocity dispersion profiles in the modelling requires disk-scale heights smaller than the values observed from edge-on galaxies of about a factor of 2. However, this result is not due to an issue of the theory but to an observational bias, as described in Sect. 4.2.1.

RG reproduces these kinematic profiles with mass-to-light ratios consistent with stellar population synthesis models, disk-scale heights in agreement with the observations from edge-on galaxies, and the three RG parameters from different galaxies consistent with each other, suggesting their universality. In Sect. 4.3, we demonstrate that the DMS sample could, in principle, be modelled by a single set of these three RG free parameters. The parallel code we wrote to model all the DMS galaxies at the same time, named *astroMP*, is described in Appendix C.2, whereas Appendix D summarises the diagnostics we employ to assess the convergence of the Monte Carlo Markov Chains run from this code. The model of the galaxy mass distribution and the Poisson solver we wrote to obtain the RG gravitational potential are, instead, illustrated in Appendixes A and B, and Appendix E shows the RG models obtained from our different analyses superimposed to the observational data from the DMS galaxies. Besides the astroMP code, Appendix C describes the semi-automatic metodology we define to parallelise both this code and a 2D Laplace solver, detailed in Sect C.3.

In Sect. 4.4, we show that RG can also model the RAR of the DMS galaxies, albeit with some drawbacks. Indeed, RG reproduces a RAR with a too large intrinsic scatter and with residuals correlating with some galaxy properties, apparently in contrast with observations. This issue requires further investigation to assess if it is due to the chosen galaxy sample or to a problem of RG.

In Chapter 5, we model, at the same time, the root-mean-square velocity dispersions of the stars, the blue GCs, and the red GCs of three elliptical E0 galaxies belonging to the SLUGGS survey. Sections 5.1 and 5.2 illustrate the derivation of the photometric and spectroscopic data we exploit to perform this analysis and Appendix F describes the derivation of the errors on the kinematic profiles of the two GCs populations. In Sect. 5.3, we detail the mass modelling, derived from spherical Jeans equations, that we adopt to model the data of the three kinematic tracers. Modelling the dynamics of each E0 elliptical galaxy in RG requires seven free parameters: four parameters for the galaxy, namely, the stellar mass-to-light ratio and the anisotropy parameters of each kinematic tracer, and three RG free parameters. In Sect. 5.4, we report our results, showing that RG can properly model these kinematic profiles with sensible mass and anisotropy parameters and with RG free parameters from different galaxies in agreeement with each other. Yet, the RG parameters present some tensions with the unique set derived from the DMS sample. This result requires further investigation to assess if it is due to a nonuniversality

of the RG parameters or to a too approximate modelling.

Chapter 6 concludes this thesis, remarking the most important points of our analyses and presenting the future projects concerning RG. Given these encouraging results on galaxy scale, we can state that RG can compete with other theories of gravity to describe the phenomenology of these systems and it deserves further investigation on larger scales.

Chapter 2

Introduction[1]

General relativity (GR) and its Newtonian weak field limit cannot account for ∼95% of the components of the Universe. This probably represents the most outstanding open issue in modern cosmology. The most investigated cosmological model is ΛCDM [2] which explains this missing 95% with two dark components. One component is an exotic fluid with negative pressure called *dark energy* (DE), which causes the accelerated expansion of the Universe and represents ∼70% of its mass-energy budget. It can be associated to a cosmological constant term, Λ, appearing on the right-hand side of the Einstein equations [3]. The second dark component is a nonbaryonic and invisible form of matter, the *dark matter* (DM), which represents ∼25% of the mass-energy budget of the Universe and interacts with baryonic matter only gravitationally. To account for the observed scenario of the formation of the cosmic structure, DM has also to be "cold", that is nonrelativistic at the time of decoupling from radiation [4]. The name "ΛCDM" derives from these two dark components, since "Λ" is the cosmological constant and "CDM" stands for "cold dark matter". The remaining ∼5% is made of ordinary, or "baryonic", visible matter, implying that ∼85% of the mass is dark [5, 6, 7].

2.1 The mass discrepancy problem

This mass discrepancy is evident at every scale in the Universe, from cosmological to galaxy ones. If we assume that GR is correct, we observe this mass discrepancy from the flatness of the rotation curves of disk galaxies [8, 9], the dynamics of galaxy clusters [10], the gravitational lensing [11, 12, 13], the dynamics and the large-scale distribution of cosmic structures [14, 15], and the cosmic microwave background (CMB) radiation [2]. The mass-to-light ratios of galaxy clusters, the radial peculiar velocity field, the evolution of the exponential tail of the mass function of virialised structures, and the large-scale distribution of galaxies all provide a consistent value for the density contrast, $\Omega = \rho/\rho_{\rm crit}$, of DM equal to 0.3 (e.g. [16, 17]). $\rho_{\rm crit} = \frac{3H_0^2}{8\pi G}$ is the critical density of the Universe, namely, the average density that the Universe needs to stop its expansion [18], and H_0 is the Hubble parameter at the present epoch. A critical Universe has a flat curvature [18].

In Sect. 2.1.1 and in Sect. 2.1.2 I detail the mass discrepancy problem on large and galaxy scales, respectively.

2.1.1 Large scales

In galaxy clusters, the mass discrepancy is evident from the virial theorem, the temperature of the hot intracluster gas, and the gravitational lensing effect. In 1933 Fritz Zwicky calculated, with the virial theorem, the dynamical mass of the Coma cluster (see Fig. 2.1) which resulted ∼100 times larger than the sum of the masses of the single galaxies present

[1] Part of the content in this chapter is published in [1].

in the cluster. Specifically, he measured a line-of-sight velocity dispersion of $\sim$1000 km s^{-1} for 8 galaxies in Coma, about 13 times larger than the one expected in a system of N massive galaxies in dynamical equilibrium ($\sim$80 km s^{-1}) [10]. In fact, he underestimated by a factor of $\sim$10 the baryonic mass of the cluster because he did not know about the presence of the hot X-ray emitting gas, but, even if this further component is included, the mass discrepancy subsists and it is quantified between 5 and 10 [19, 20, 21]. The equation of hydrostatic equilibrium of the hot gas and the gravitational lensing effect provide values for the dynamical mass consistent with the virial theorem [22].

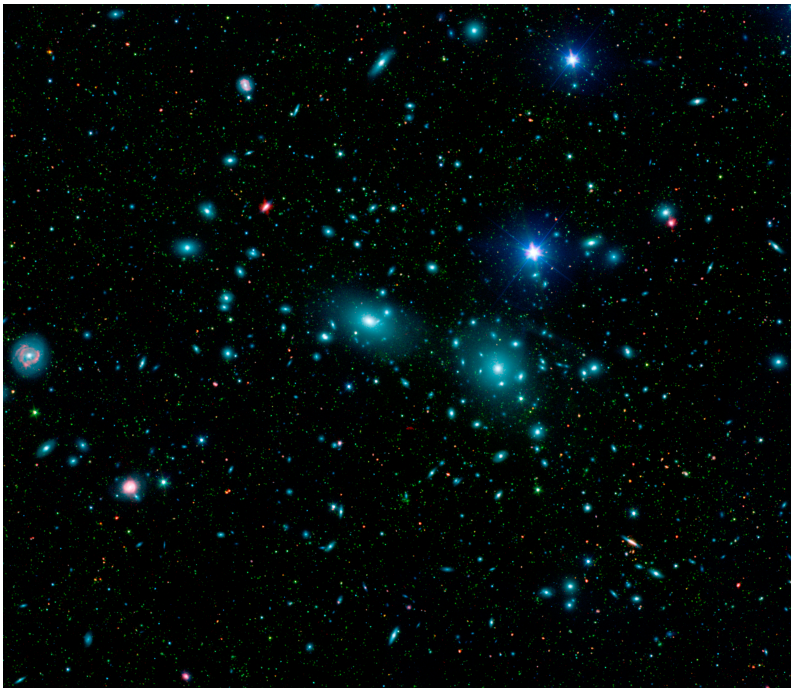

Figure 2.1: The Coma cluster, of which Fritz Zwicky calculated the dynamical mass in 1933 [10]. Image Credit: NASA/JPL-Caltech/L. Jenkins (GSFC).

The strongest evidence in favour of the DM hypothesis from the gravitational lensing effect is provided by the Bullet Cluster (see Fig. 2.2, left panel), composed by two colliding galaxy clusters [11, 12, 13]. Each cluster is composed by hot gas, the dominant baryonic component, and galaxies. Being a collisional fluid, the gas electromagnetically interacts during the collision, and, consequently, it slows down and concentrates in the most central region. Instead, the galaxies are a noncollisional fluid, and, for this reason, they pass through the inner part, distributing on the left and on the right of the gas. Since the gas is the dominant mass component we would expect a stronger lensing effect in correspondence of the area where it is concentrated but, instead, we observe a stronger signal where the galaxies settle. According to GR, this can be explained by the presence of massive DM halos embedding the galaxy regions. Actually, another colliding galaxy cluster, Abell 520 (see Fig. 2.2, right panel), might challenge this conclusion since the strongest lensing signal is observed in the cluster core, where the X-ray gas emission is maximum but galaxies are almost not present [23]. This result is very hard to interpret in the most quoted collisionless CDM paradigm and it is in contrast with the observations from the Bullet Cluster. Yet, this evidence might not represent a challenge for CDM model, since this apparent DM-dominated core might be explained by assuming that Abell 520 is forming at the crossing of three filaments in the large-scale structure [24].

This missing mass cannot be made of baryonic matter too faint to be detected, like brown dwarfs, planets, white dwarfs, neutron stars, or black holes, called also MAssive Compact Halo Objects (MACHOs). All these systems can only represent a small fraction of DM, set to 8% by microlensing measurements in the Milky Way [25, 26]. The largest

Figure 2.2: *Left panel*: the Bullet cluster. Image Credit: X-ray: NASA/CXC/CfA/M.Markevitch et al. (pink); Optical: NASA/STScI; Magellan/U.Arizona/D.Clowe et al.; Lensing Map: NASA/STScI; ESO WFI; Magellan/U.Arizona/D.Clowe et al. (blue). *Right panel*: the Abell 520 cluster. Image Credit: NASA, ESA, CFHT, CXO, M.J. Jee (University of California, Davis), and A. Mahdavi (San Francisco State University). The optical light from stars is shown in orange (CFHT), the X-ray signal from the hot gas is shown in green (CXO), and the gravitational lensing map produced by DM is shown in blue (Hubble Wide Field Planetary Camera 2).

fraction of DM has necessarily to be nonbaryonic, following several pieces of evidence. The first one is due to the abundances of the light elements, ^{4}He, D, ^{3}He, and ^{7}Li, produced during the Big Bang nucleosynthesis (BBN) [27]. These abundances are function of the number of photons per baryon, η, that depends, in turn, on the density contrast of baryons, $\Omega_{\rm b}$. By measuring these abundances, $\Omega_{\rm b}$ is constrained in the range of $[0.01, 0.04]$, a factor of $\sim$10 smaller than $\Omega_{\rm DM} = 0.3$. This indicates that DM cannot be baryonic and that baryons represent only a minimal fraction of the Universe content.

The second piece of evidence is provided by the density perturbation anomaly of the CMB [28, 7]. At the epoch of the formation of the CMB, 380000 years after the Big Bang, corresponding to redshift $z \sim 1000$, radiation and baryons were still coupled and the temperature and baryonic density perturbations coincided. They were equal to $\delta = 10^{-5}$ on an angular scale of 7 degrees, corresponding to $\sim$100 Mpc. In an Einstein-deSitter Universe, namely a flat universe with zero cosmological constant [29], the density perturbation evolves with redshift according to:

$$\delta(z) = \frac{\delta_0}{1+z}, \tag{2.1}$$

where δ_0 is the density perturbation today. Setting $\delta = 10^{-5}$ and $z = 1000$ in the above equation, we obtain $\delta_0 = 10^{-2}$. Yet, today we measure a baryonic density perturbation $\delta_0 \sim 1$ on the same scale, two orders of magnitude larger than the expected value. This can be explained by the presence of an additional component, dominant in the Universe, that decouples from radiation before the CMB epoch. In this way, its density perturbations can start evolving before $t = 380000$ years and its density perturbation does not have to be equal to the radiation density perturbation at that time. This component has to be nonbaryonic because, otherwise, it would have decoupled from radiation at $z = 1000$. At $t = 380000$ years, baryonic matter decouples from radiation and it is obliged to follow the deep potential wells generated by the already collapsed stuctures of the dominant fluid that permeates the Universe. From that moment on, the density perturbation of the baryonic matter evolves with the same law of the dominant component and this would explain why we detect a density perturbation different from expectations at the present epoch. The growth of density perturbations in a DM-dominated Universe is shown in Fig. 2.4.

Besides being nonbaryonic, DM should be cold, that is nonrelativistic at the epoch of decoupling from radiation, to account for the observed formation scenario of cosmic structure. As said before, during the expansion of the Universe the evolution of baryonic perturbations is regulated first by radiation and then by DM, before and after the

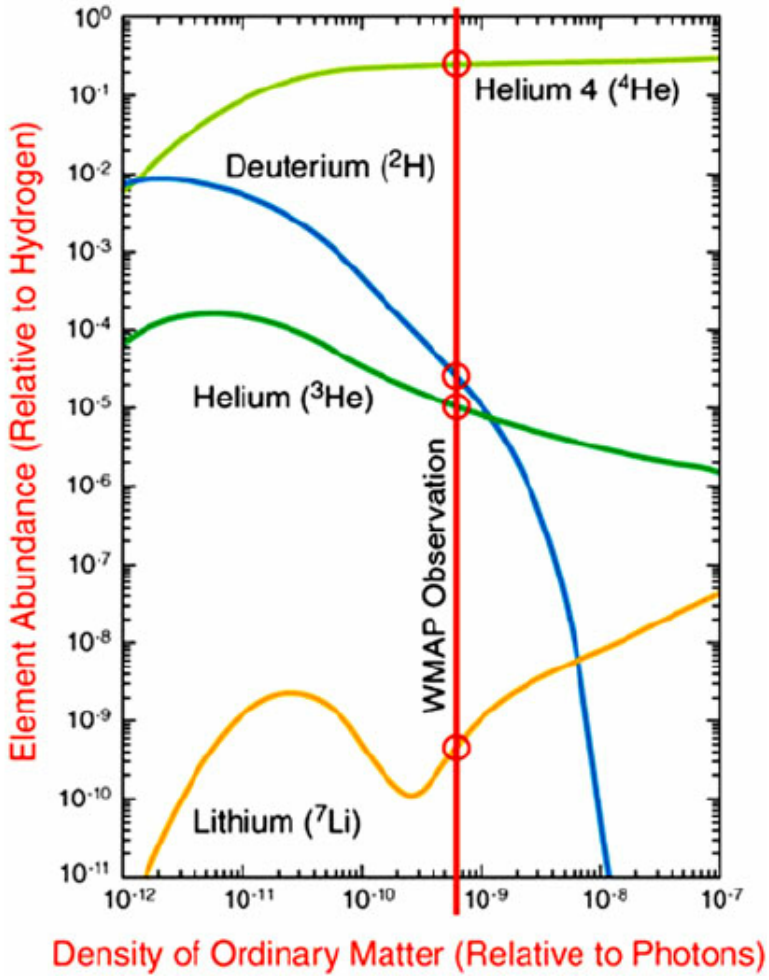

Figure 2.3: BBN light element abundances relative to hydrogen as a function of η^{-1}, the number of baryons per photon in the Universe. The red vertical line corresponds to the measued value of η^{-1}. The figure is from [27].

epoch of recombination, respectively. During the radiation-dominated epoch, DM fluctuations are damped by random thermal motions below a characteristic free-streaming scale, $\lambda_{\rm fs}$, inversely proportional to the mass of the DM particle, m_χ: $\lambda_{\rm fs} \propto m_\chi^{-1}$ [30]. The free-streaming length approximately coincides with the comoving distance that the DM particle crosses in a time equal to the age of the Universe. Three possible scenarios for DM particles are hot dark matter (HDM, relativistic at the epoch of decoupling), warm dark matter (WDM, relativistic at the epoch of decoupling), and cold dark matter (CDM, nonrelativistic at the epoch of decoupling), which might have a typical mass of $m_\chi \sim 30$ eV, $m_\chi \sim 2$ keV, and $m_\chi \sim 100$ GeV, respectively [30]. These masses might correspond to a neutrino [30], as measured by [31], a sterile neutrino [32] and a WIMP, or neutralino [32], respectively. These three particles have a free-streaming length correspondent to a characteristic mass of large galaxy clusters ($\sim 10^{16}\ M_\odot$), dark halos of dwarf galaxies ($\sim 10^{6} - 10^{7}\ M_\odot$), and the Earth ($\sim 10^{-8} - 10^{-2}\ M_\odot$) [30]. This implies three different formation scenarios: in the HDM case, large structures form first through gravitational instability and then they fragment to form small structures (top-down scenario); in the other two cases small structures form first through gravitational instability and then they hierarchically merge to form large structures (bottom-up scenario), where DM halos much smaller than galaxies can only result in CDM case [30]. Figure 2.5 illustrates the late-time (epoch of recombination) linear power spectrum for a Universe gravitationally dominated by HDM (green line), WDM (red line), and CDM (black line) with the previously mentioned masses for the DM particle: we can clearly see that in the HDM and WDM cases a cut-off in the power spectrum is present and that for HDM it corresponds

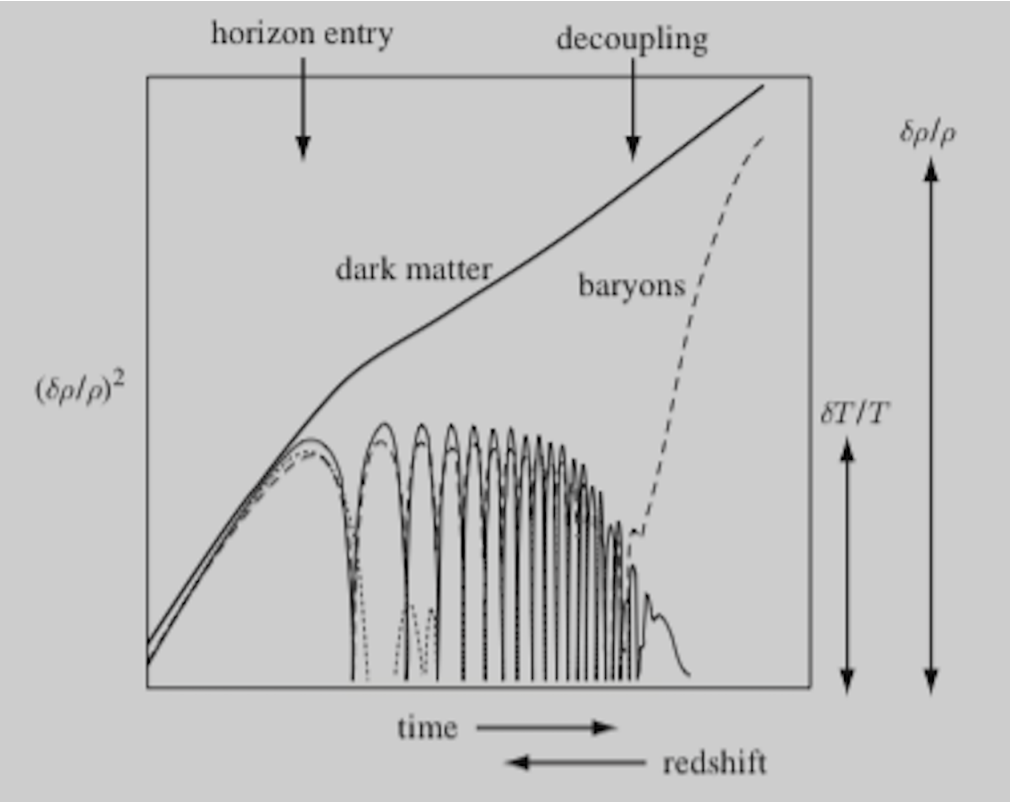

Figure 2.4: Growth of density perturbations in a DM-dominated Universe. Solid curve: density perturbation of the DM component. Dashed curve: density perturbation of the baryonic component. Oscillating solid curve: photons perturbation. The figure is from [28].

to larger scales (smaller wave numbers k) [30]. Observations seem to rule out a top-down formation scenario and to favour a bottom-up one produced by CDM, since galaxies are observed forming at higher redshift z with respect to galaxy clusters [30, 33, 34].

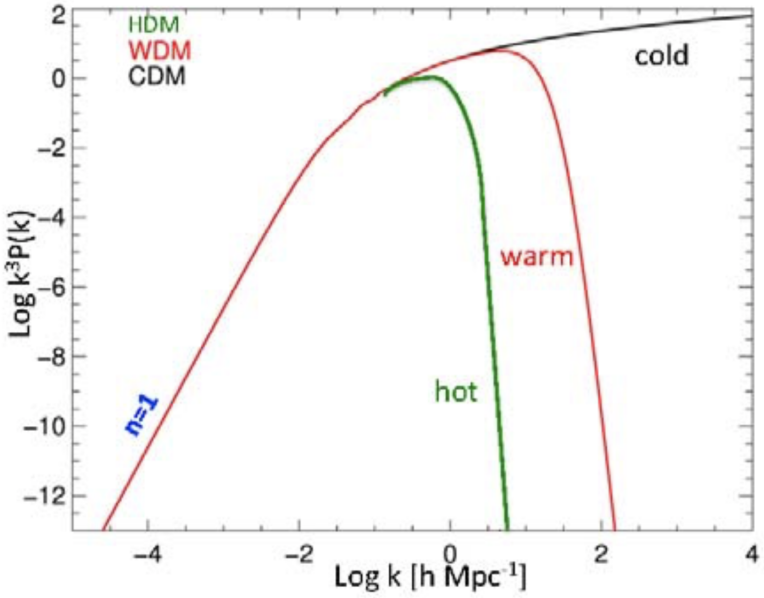

Figure 2.5: Late-time (epoch of recombination) linear power spectra for density perturbations generated from inflation in a HDM (green line), WDM (red line), and CDM (black line) scenario with a DM particle mass equal to $m_\chi \sim 30$ eV, $m_\chi \sim 2$ keV, and $m_\chi \sim 100$ GeV, respectively. The figure is from [30].

Moreover, the distribution of the large-scale structure (see Fig. 2.6), measured by the

galaxy correlation function, cannot be reproduced without a dominant nonbaryonic and cold form of matter, if we assume the theory of gravitational instability for structure formation (e.g. [35]).

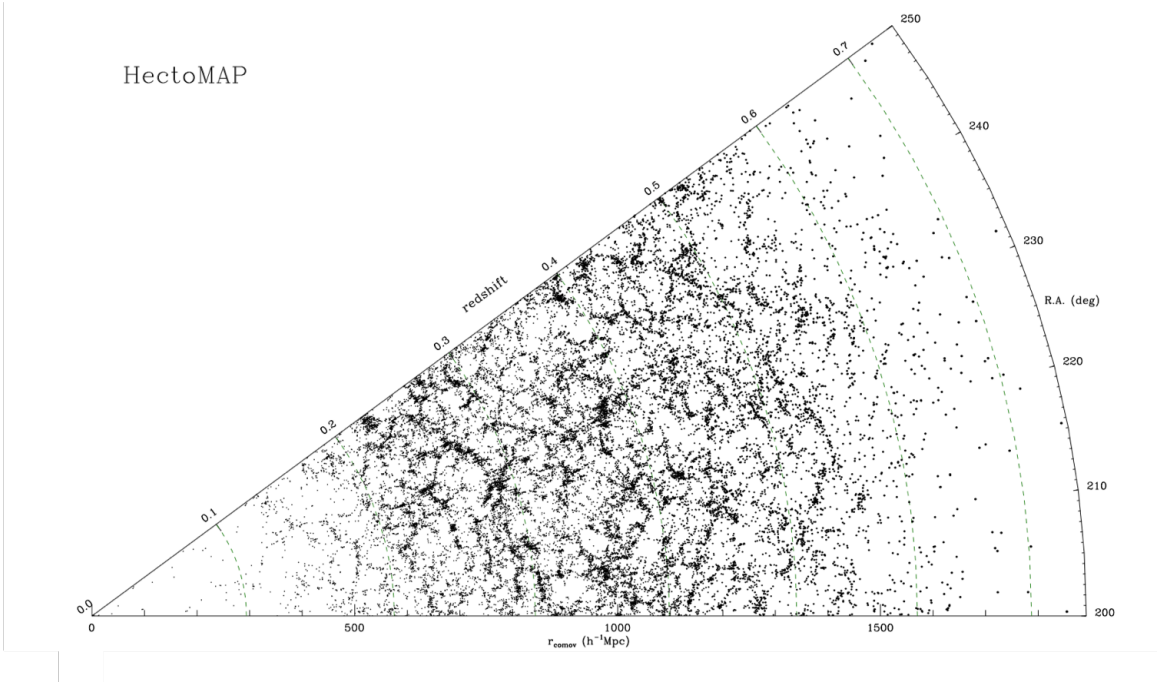

Figure 2.6: Large-scale structure in the HectoMAP redshift survey. The figure is adapted from [36].

2.1.2 Galaxy scale

Since in my Ph.D. analysis I investigated the dynamics of galaxies, I detail now the mass discrepancy problem on galaxy scale. The most striking evidence of this issue is the flatness of rotation curves of disk galaxies. The rotation curve of a galaxy is obtained by equalling the contributions of the centripetal and the gravitational forces on its mid-plane:

$$v(R, z = 0) = \sqrt{R \frac{\partial \phi(R, z)}{\partial R}}, \tag{2.2}$$

where ϕ is the gravitational potential generated by the galaxy mass distribution, R is the distance from the galaxy centre, and z is oriented along the galaxy symmetry axis. If we assume spherical symmetry we obtain:

$$v(r) = \sqrt{\frac{GM(< r)}{r}}, \tag{2.3}$$

where $G = 6.67 \times 10^{-11}$ N m^2 kg^{-2} is the Newtonian gravitational constant, $r = \sqrt{R^2 + z^2}$ is the spherical radius, and $M(< r)$ is the galaxy mass enclosed within a certain r.

The baryonic mass in galaxies, made of stars, gas, and dust, is mainly concentrated in their inner regions and, if it were the only component, the galaxy mass would remain constant beyond a certain distance from the centre and $v(r)$ would be proportional to $r^{-1/2}$ (Keplerian fall). Instead, we observe that the neutral hydrogen (HI), which extends up to much larger distances than stars, move as fast as the inner matter, that is the rotation curve is flat. This evidence was first observed in the Ph.D. thesis of Albert Bosma, in 1978 [37]. He measured, from the 21-cm emission line of HI, the rotation curves of the spiral galaxies NGC 5055, NGC 2841, and NGC 7331 up to 30-40 kpc from the centre, observing that their trends were nearly flat in their external regions [37] (see

Fig. 2.7). This phenomenology can be explained by a pressure-supported spheroidal DM halo, embedding the entire galaxy, as suggested by theoretical studies of the stability of disk against the development of a bar [5]. In this way, the mass would continue growing linearly proportional to the radius, accounting for a flat rotation curve, if the DM density profile decreases $\propto r^{-2}$ in the outer regions of the galaxy. In fact, the flatness of the rotation curve is the result of a fine-tuning between the contributions of the stellar disk and of the DM halo, known as the *disk-halo conspiracy* [38, 39] (see Fig. 2.8). DM-only simulations of ΛCDM predict a Navarro-Frenk-White density profile for the dark halo, which shows a central cusp with $\rho(r) \propto r^{-1}$ [40, 41].

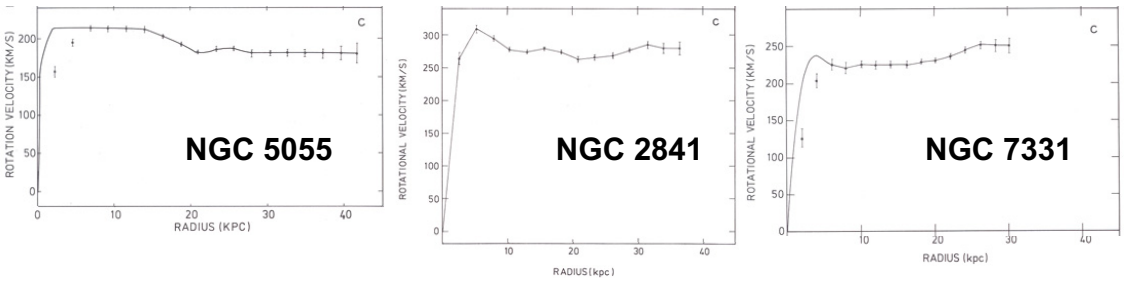

Figure 2.7: Rotation curves of NGC 5055, NGC 2841, and NGC 7331 as a function of the distance from the galaxy centre. Grey dots with error bars are the measurements. Grey solid lines are the models. The figure is adapted from [37].

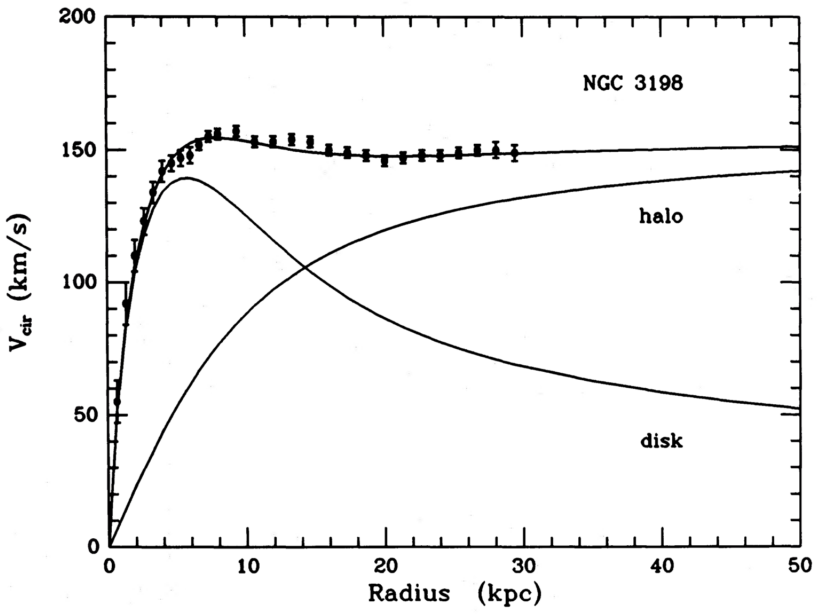

Figure 2.8: Rotation curve of NGC 3198 as a function of the distance from the galaxy centre. Black dots with error bars are the measurements. The black solid line is the model, where the flat trend of the rotation curve is obtained by the fine-tuning of the contributions of the stellar disk and the DM halo (*disk-halo conspiracy*). The contributions to the total rotation curve of the stellar disk and of the DM halo are highlighted in the figure. The figure is from [38].

This mass discrepancy can be neatly quantified by some very tight phenomenological relations between the properties of baryonic and dark matter: the baryonic Tully–Fisher relation (BTFR) [42], the mass discrepancy–acceleration relation (MDAR) [43], and the radial acceleration relation (RAR) [44].

The BTFR (see Fig. 2.9) correlates the total baryonic mass ($M_{\rm bar}$) and the asymptotic flat part of rotation curves ($V_{\rm f}$) of galaxies, spanning 6 orders of magnitude of galaxy mass. The BTFR follows this power law:

$$M_{\rm bar} = AV_{\rm f}^{b}, \tag{2.4}$$

where A and b are free parameters. Fitting the data from 47 gas-rich galaxies with

different techniques, McGaugh [45] found normalisations always in agreement between each other and slopes always consistent with 4. By setting the slope to 4, McGaugh found a normalisation equal to $A = (47 \pm 6)\ M_\odot\ \mathrm{km}^{-4}\ \mathrm{s}^4$, comparable to the quantity $(Ga_0)^{-1}$, where $a_0 = 1.2 \times 10^{-10}\ \mathrm{m\ s}^{-2}$ is an acceleration scale. For mass-to-light ratios in the 3.6 μm band $\Upsilon_{[3.6]} \gtrsim 0.5\ M_\odot/L_\odot$, the BTFR shows a minimum intrinsic scatter of $\sim$0.10 dex [46]. The residuals of the observed BTFR from Eq. (2.4) show no correlations with some galaxy properties like the radius or the surface brightness [47].

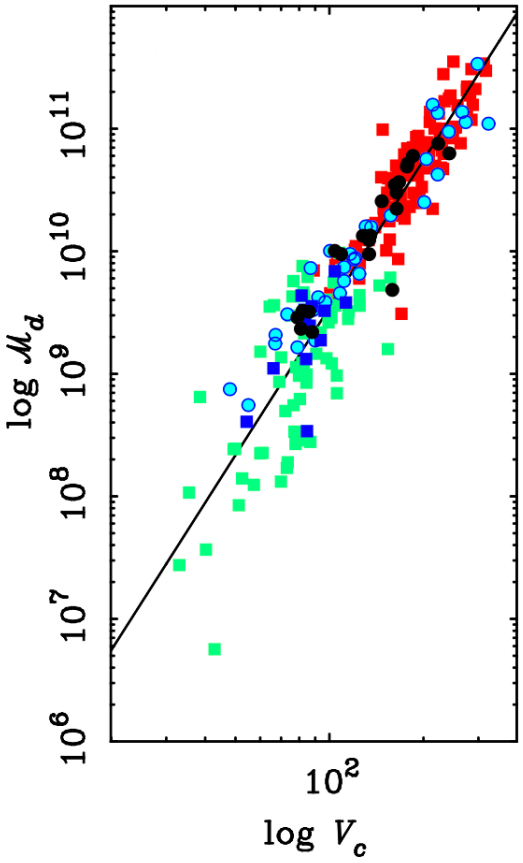

Figure 2.9: The baryonic Tully–Fisher relation (BTFR). The dots and squares are the measurements from [48] (red), [49] (black), [50, 51] (green), [52] (light blue), and [53] (dark blue). The black solid line is an unweighted linear fit to the data. The figure is from [42].

The MDAR (see Fig. 2.10) anti-correlates, at each radius R from the galaxy centre, the Newtonian acceleration due to the mass density of baryons, g_{bar}, and the squared ratio between the total and the baryons-induced galaxy velocities, $(V/V_{\mathrm{bar}})^2$, that, assuming spherical symmetry, coincides with the mass discrepancy, M/M_{bar} [43]. The mass discrepancy remains $\sim$1 for accelerations $a \gtrsim a_0$ and it starts to increase as the acceleration goes below a_0, where a_0 is found from the normalisation of the BTFR. The intrinsic scatter in both the MDAR and the BTFR is minimised by the same mass-to-light ratio, in agreement with stellar population synthesis models (SPS) [43].

At last, the RAR (see Fig. 2.11) correlates the observed centripetal acceleration, $g_{\mathrm{obs}}(R) = V(R)^2/R$, derived from the measured rotation curve $V(R)$, with the Newtonian acceleration from the baryonic matter distribution alone, namely, g_{bar} [44]. McGaugh and collaborators [44] fitted the RAR data of 153 edge-on disk galaxies from the SPARC sample [55] with this simple relation:

$$g_{\mathrm{obs}}(R) = \frac{g_{\mathrm{bar}}(R)}{1 - \exp\left(-\sqrt{\frac{g_{\mathrm{bar}}(R)}{g_\dagger}}\right)}, \tag{2.5}$$

where $g_\dagger = (1.20 \pm 0.02 \pm 0.24) \times 10^{-10}\ \mathrm{m\ s}^{-2}$ is the only free parameter and is consistent

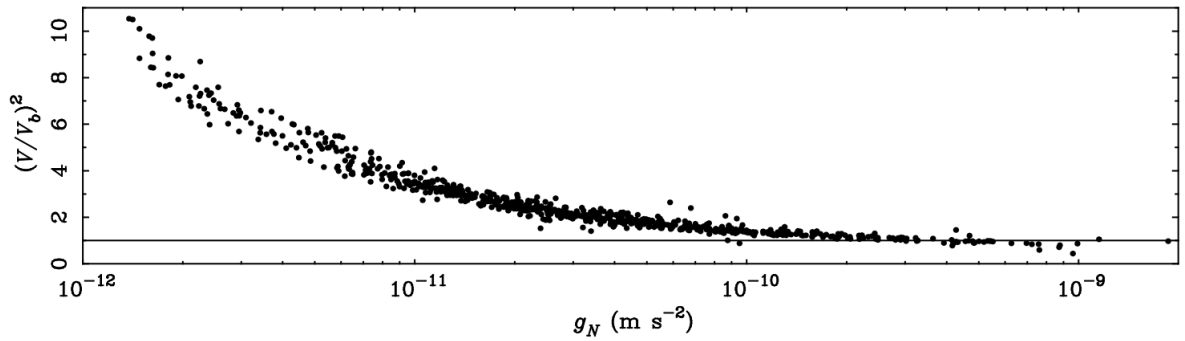

Figure 2.10: The mass discrepancy–acceleration relation (MDAR). The black dots are several hundreds of individual points measured from the rotation curves of ∼100 spiral galaxies. The figure is from [54].

within 1σ with the acceleration scale $a_0 = 1.2 \times 10^{-10}$ m s^{-2}. To build the RAR of SPARC galaxies, McGaugh and collaborators set the mass-to-light ratios of the disk and the bulge components to 0.5 and 0.7 $M_\odot/L_\odot$, respectively, which are reasonable values in the 3.6 μm band, and they found an observed scatter of 0.13 dex. This scatter is consistent with the scatter of 0.12 dex due to the observational uncertainties on the measured rotation curves, the distances, and the inclinations of galaxies, and to the different mass-to-light ratios of each galaxy, leaving little room for intrinsic scatter. Indeed, fitting the mass-to-light ratios from the measured rotation curves of individual galaxies and marginalising over the distances and inclinations errors, the intrinsic scatter results equal to 0.057 dex [56].

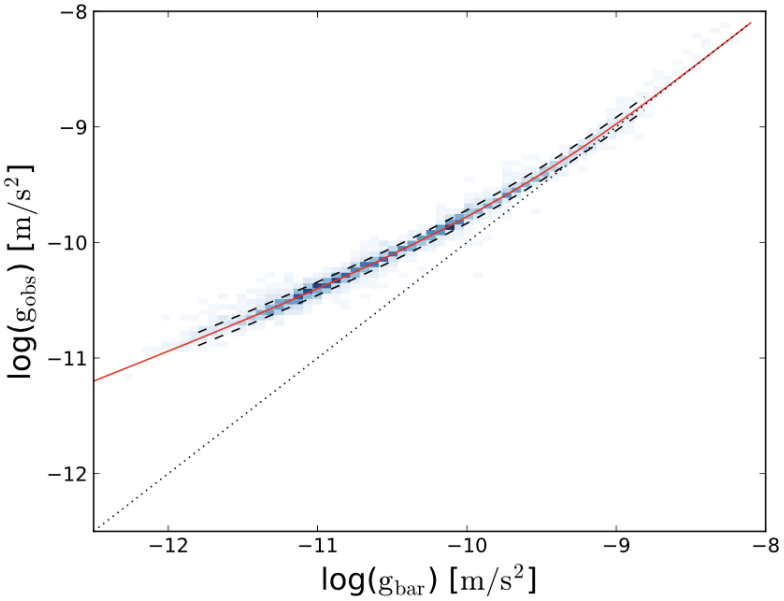

Figure 2.11: The radial acceleration relation (RAR). The blue color-scale rectangles represent 2694 individual points measured from the rotation curves of 153 galaxies in the SPARC sample. The red solid line is the fit to the data with Eq. (2.5) and the black dotted line shows the line of equality, for comparison. The figure is from [56].

These three relations hold from the most massive, high-surface-brightness (HSB) spiral galaxies with a $M_{\rm bar} \sim 10^{12}$ $M_\odot$ to the dwarf and low surface brighteness (LSB) galaxies with a $M_{\rm bar} \sim 10^6$ $M_\odot$ [42, 43, 44], even if the observed scatter of the RAR seems to increase from 0.13 to 0.24 dex for small $g_{\rm bar}$ when dwarf and LSB galaxies with slowly-rising rotation curves are included in the sample [57] (see Fig. 2.12). However, caution must be taken when dealing with these galaxies with complex dynamics.

The dynamics of dwarf galaxies provides one of the best pieces of evidence of the mass discrepancy problem on galaxy scale. Dwarf spheroidal and LSB galaxies are among the

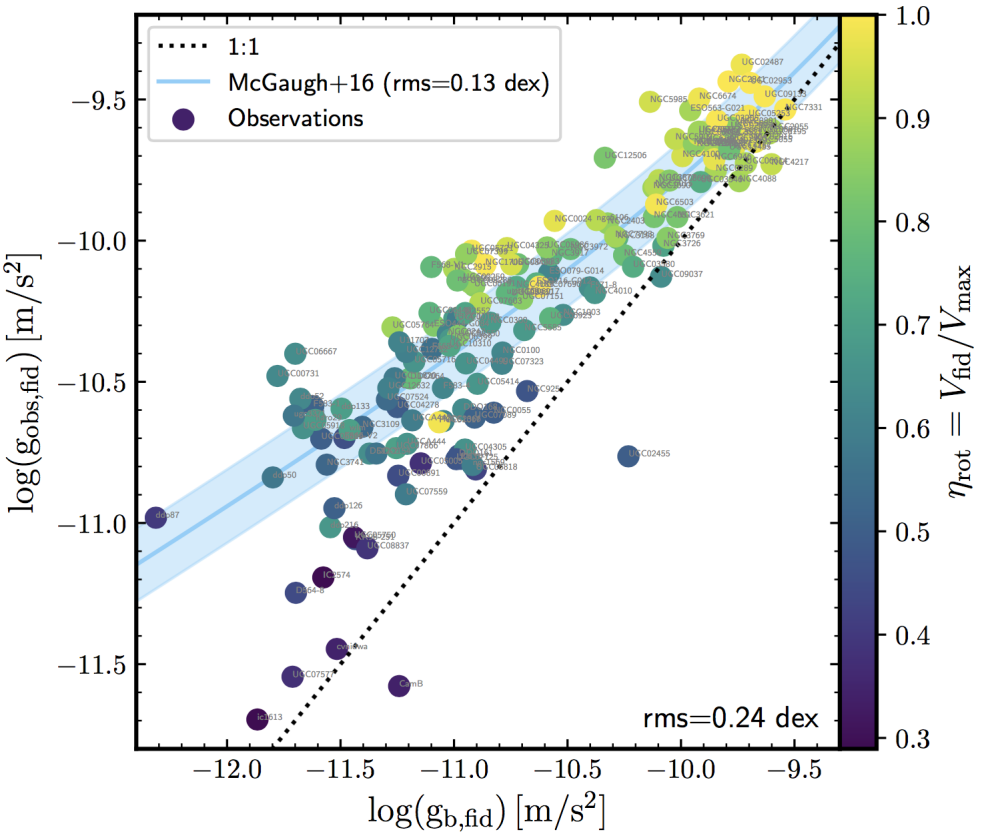

Figure 2.12: The radial acceleration relation (RAR) for both cuspy and cored galaxies. Color-coded dots show the measurements, the light blue solid line and shaded area represent the RAR and its observed scatter found by [44], and the black dotted line shows the line of equality, for comparison. Cored galaxies with slowly-rising rotation curves, coloured with darker points, locate with a larger scatter around the RAR and they typically fall outside this relation. The only way to reconcile them with the RAR is to assume that the most internal rotation velocities of these galaxies has substantial errors [57]. The figure is from [57].

darkest galaxies in the Universe. The velocity dispersion observed in their inner regions is $\sim$10 km s^{-1}, about a factor of 10 larger than the expectations for a self-gravitating system of the same luminosity and scale radius at equilibrium [58]. Whereas, for HSB galaxies, the stellar disk maximally contributes to the central regions of their rotation curves (*maximum disk hypothesis*), in dwarf and LSB galaxies the DM seems to dominate even in the innermost radii, where the rotation curve rises more slowly than in HSB galaxies [59, 60].

Despite having baryonic masses similar to those of dwarf galaxies, globular clusters (GCs) seem not to require at all a DM component to account for their dynamics. Indeed, the internal dynamics of GCs belonging to the outer halo of the Milky Way, where the acceleration is below a_0, is well reproduced by Newtonian gravity without including a DM halo [61, 62, 63, 64, 65, 66, 67]. Yet, this issue is still open [68] since some theories of formation and evolution of GCs predict the existence of DM in these systems and its observational evidence is under discussion [69, 70]. The determination of either the presence or the absence of DM in GCs is further complicated by their often inaccurate data, usually due to low-resolution spectroscopy and to errors on GCs distances larger than 10% of their values (e.g. [64]).

A more difficult task is to assess the amount of mass discrepancy in early type galaxies (ETG), which include ellipticals and lenticulars. The majority of the surveys of ETG probe the kinematics of stars which extends up to $\sim$1 effective radius, R_e, from the galaxy centre, where the effective radius encloses half of the total luminosity of the galaxy. Among these surveys we can mention ATLAS^{3D} [71], SAMI [72], CALIFA [73], and MaNGA [74],

which all employ an integral field spectroscopy observational technique. The effective radius encloses less than 10% of the galaxy total mass (e.g. [75, 76]) and within that distance the Newtonian expectations are generally in agreement with the data, even without needing a DM halo (e.g. [77]). However, this does not necessarily mean that ETG are DM-free systems but that one effective radius might not be representative of the dynamics of ETG. Deep long-slit observations and other pioneering methods (e.g. [78, 75, 79]) probed the kinematics of ETG until $\sim$3 $R_{\rm e}$ and the detection of kinematic tracers, like GCs and planetary nebulae, until 8–13 $R_{\rm e}$. As an example, the SLUGGS [76] and the ePN.S [80] surveys exploit this last technique, respectively considering GCs and planetary nebulae. To simultaneously account for the dynamics of stars and of these external tracers, DM seems to be required (e.g. [81]), which indicates that a mass discrepancy in ETG is also present. A work by Alexander Deur suggests a possible correlation between the ellipticities and the total mass-to-light ratios of elliptical galaxies, stating that the flatter a system the stronger its mass discrepancy [82, 83]. Yet, further investigation is required since the majority of the data used by Deur extends up to $\sim$1 $R_{\rm e}$.

2.2 Problems of the CDM model

Despite being successful in describing the majority of the phenomenology in the Universe, the ΛCDM model faces some important challenges. Two of the most puzzling challenges on cosmological scales are the *cosmological constant* (e.g. [84, 85, 86]) and the *coincidence* (e.g. [84, 87]) problems. Both questions pose very severe fine-tuning mechanisms. The former consists in a very serious tension between the expectations from quantum field theory (QFT) and the observations of the cosmological constant, if we interpret it as the zero-point of the energy density of the vacuum. Indeed, QFT predicts a value of $\Lambda_{\rm QFT} = (10^{19}{\rm GeV})^4$ whereas the observed value is of $\Lambda_{\rm obs} = (10^{-12}{\rm GeV})^4$, resulting in a difference of about 124 orders of magnitude [86]. If expressed in units of the Planck mass, $M_{\rm Planck}$, the observed value of the cosmological constant is equal to $\Lambda_{\rm obs} = (10^{-30} M_{\rm Planck})^4$. To reconcile the vacuum energy density from QFT with the observed value, we should add to it a correction term, presumably from the fundamental theory above the Planck energy scale, opposite in sign but incredibly close in modulus such that the discrepancy is canceled with a 10^{-124} precision [86].

The coincidence problem is due to the fact that the energy density of the cosmological constant, $\Omega_\Lambda \approx 0.7$, and the energy density of DM, $\Omega_\Lambda \approx 0.3$, are of the same order of magnitude at the present epoch, which would require very special initial conditions in the primordial Universe (e.g. [84, 87]).

Moreover, some tensions involving cosmological parameters are present. One of these is the *Hubble tension*, where the Hubble parameter, H_0, from local measurements of type Ia Supernovae appears 3.6σ larger than the Hubble parameter from the early Universe, derived from the modelling of the CMB power spectrum measured with the Planck satellite (e.g. [2, 88]) (see Fig. 2.13, top panel). Another tension occurs between the matter density contrast at the present time, $\Omega_{\rm m,0}$, and the amplitude of the density fluctuation power spectrum, σ_8, measured from low redshift galaxy surveys (e.g. KIDS, CFHTLS, and DES) exploiting weak lensing and from the CMB [89]. In particular, all low redshift large scale structure probes provide results consistent with each other and privilege $\Omega_{\rm m,0}$ and σ_8 parameters smaller than the ones obtained from the CMB (Fig. 2.13, bottom left panel). Moreover, these two cosmological parameters also present a tension, at 2.4σ, between the measurements from the Sunyaev Zel'dovich signal in 200 galaxy clusters and from the CMB, both taken with the Planck satellite in 2013 [89] (see Fig. 2.13, bottom right panel). However, considering the more recent measurements taken with Planck in 2016, as in particular an updated value of the optical depth of reionisation $\tau = 0.055 \pm 0.009$, this tension is reduced to 1.5σ [90, 89, 91] (Fig. 2.13, bottom right panel).

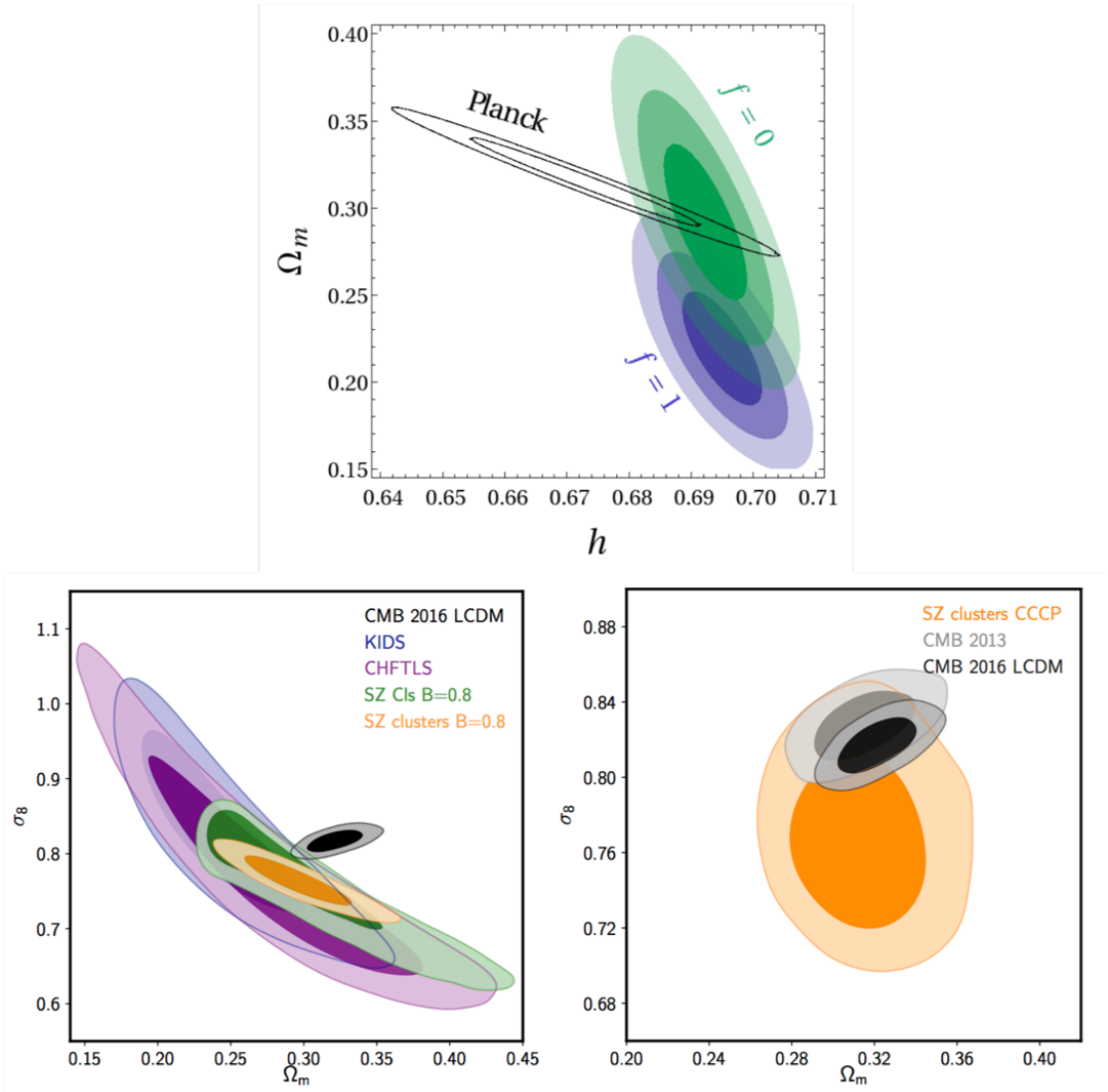

Figure 2.13: *Top panel:* The H_0 and $\Omega_{m,0}$ tensions. The panel compares the constraints in the (H_0,$\Omega_{m,0}$) plane obtained with the Planck satellite (black contours) and with the Hubble diagram constructed from the SNLS 3 catalogue (blue and green filled contours). The blue and green filled contours show constraints from the Hubble diagram in two different cosmologies, specifically in a spatially flat universe with a Friedmann-Lemaître geometry and in a spatially flat universe described with a "Swiss-cheese" model, where matter is completely clumped, respectively. Whereas the two different models basically unaffect H_0, the "Swiss-cheese" model reduces the tension on $\Omega_{m,0}$ with Planck with respect to the Friedmann-Lemaître model. The Hubble parameter, H_0, is expressed as $h = H_0/100$. *Bottom panels:* the $\Omega_{m,0}$ and σ_8 tensions. The bottom left panel illustrates the tension between these two cosmological parameters measured from different low redshift large scale structure probes (blue, purple, green, and orange filled contours) and from the CMB (black filled contours). Low redshift probes drive $\Omega_{m,0}$ and σ_8 toward smaller values than in the CMB. The bottom right panel compares the Sunyaev Zel'dovich cluster constraints from Planck (orange filled contours) and the CMB constraints from Planck in 2013 (grey filled contours) and 2016 (black filled contours), for the same two cosmological parameters. The tension between the Sunyaev Zel'dovich clusters and the CMB is alleviated in the 2016 data with respect to the 2013 data thanks to the new value of the optical depth of reionisation. The figures are from [88] (top panel) and from [89] (bottom panels).

Yet, the most severe challenges of the CDM model appear at the scale of galaxies. The small scatter of the BTFR, the MDAR, and the RAR, usually consistent with the observational errors, and the apparent lack of correlations between their residuals and the galaxy properties do not occur naturally in the CDM model, where structures form hierarchically through a stochastic merging process. According to these relations, the kinematics of galaxies seems to be tightly regulated by their baryonic components, despite baryons represent only ∼10% of the matter in galaxies. This could only be explained by a very precise fine-tuning between the dark and baryonic matter components of galaxies [92, 93]. Specifically, semi-analytic models of galaxy formation in ΛCDM and DM-only cosmological simulations predict a BTFR with a minimum scatter larger than observed [94, 95], and with a slope $b = 3$, discrepant at the 8σ level from the observed value $b = 3.98 \pm 0.12$ [42].

The RAR poses an even more serious issue with respect to the BTFR due to its local, rather than global, nature. Its intrinsic scatter of 0.057 dex is smaller than the scatter $\gtrsim$0.09 dex predicted by the EAGLE simulation [56]. Yet, the problem of the RAR requires further investigation since, for small baryonic accelerations, its scatter might appear larger for dwarf galaxies [57] (see Sect. 2.1.2 and Fig. 2.12) and, for some galaxy samples different from SPARC, some correlations between its residuals and galaxy properties might exist [96, 97].

Another fact hard to explain in ΛCDM is the emergence of the same acceleration scale, $a_0 = 1.2 \times 10^{-10}$ m s^{-2}, from all the mentioned relations. In natural units, a_0 can also be written as $a_0 \sim H_0$.[2] Intriguingly, a_0 can also be expressed in the same units as $a_0 \sim \sqrt{\Lambda}$. This arises another striking coincidence, which shows that both the DM and DE sectors are regulated by the same acceleration scale [54].

Besides DM-baryons relations, other small scale problems of ΛCDM are present. Some of the most relevant are (1) the *cusp/core problem*, that is the discrepancy between the centrally cuspy profiles for the DM halo density predicted by collisionless DM-only simulations and the centrally cored profiles required to account for the dynamics of dwarf and LSB galaxies; (2) the *missing satellites problem*, where the total amount of substructures around Milky Way-like galaxy haloes emerging from cosmological simulations seems to be a factor of ∼10–20 larger than observed; (3) the *too-big-to-fail-problem*, where dissipationless ΛCDM simulations of Milky Way-like galaxy haloes predict that the majority of the most massive subhalos of the Milky Way should form luminous dwarf spheroidal satellites with densities, or equivalently circular velocities, larger than observed values; and (4) the *planes of satellite galaxies problem*, where CDM simulations can hardly account for the flattened distribution of the orbits and the kinematic correlations shown by the satellite galaxies of the Milky Way, M31, and Centaurus A (e.g. [98, 1]).

2.2.1 Possible solutions on large scales

The cosmological constant and the coincidence problems represent two aspects of the same issue: the smallness of the cosmological constant [104]. One possible explanation of this evidence is given by the anthropic principle: the cosmological constant is so small because otherwise the formation of large-scale structures and of life would not have been possible. The upper bound of the cosmological constant-to-DM density contrast ratio to allow the formation of large-scale structures is $\Omega_\Lambda/\Omega_{\rm DM} \sim 10 - 100$ [105, 85, 104] and the measured value is $\Omega_\Lambda/\Omega_{\rm DM} \sim 2-3$, well within this boundary. This idea is accepted within the context of string theories, which claim the possibility of multiple realisations of the Universe, each with a different value for the cosmological constant [106, 107, 108, 109, 110, 104], although there are still many open questions about this possible explanation [104].

Two other well-explored possible solutions are dynamical DE and modified gravity models. Both classes of models invoke the introduction of a scalar field, φ, which produces the effect of cosmic acceleration and is minimally or nonminimally coupled to gravity and baryonic matter, for dynamical DE and modified gravity theories, respectively [111]. I detail below the two categories of models.

Every fluid in the Universe is characterised by its equation of state w, given by the ratio between its pressure and density, P/ρ. For the cosmological constant, w is set to -1. Dynamical DE models assume that the equation of state of DE is not constant but it varies across cosmic time. Specifically, DE is associated with a cosmological scalar field, φ, minimally coupled to gravity, which slowly-rolling[3] varies during time toward a flat potential, such that its equation of state stays close to $w_\varphi = -1$ along its entire evolution [112, 104]. The potential energy of this field causes the accelerated expansion of the Universe [104]. These models provide the simplest generalisation of ΛCDM and are

[2] More specifically, $a_0 \approx cH_0/2\pi$. In natural units ($c = G = \hbar = 1$), we have that $a_0 \sim H_0$.

[3] A slow-rolling field φ must have a kinetic energy much smaller than the potential energy: $\dot{\varphi} \ll V(\varphi)$.

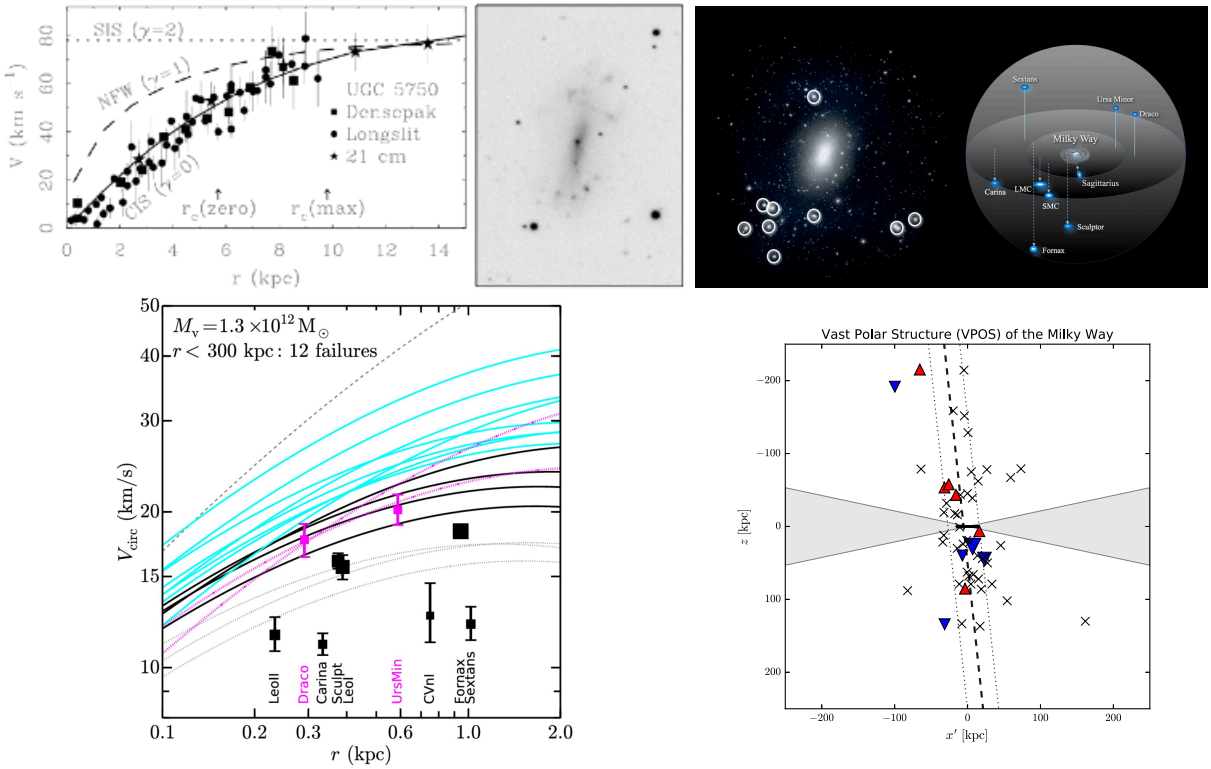

Figure 2.14: *Top left panel*: the *cusp/core problem*. The panel illustrates the rotation curve of the LSB galaxy UGC 5750, whose 2D image is shown next to the plot. This slowly-rising rotation curve can be properly fitted with a cored isothermal sphere profile for the DM halo density (solid line) but neither with a singular isothermal profile (dotted line) nor with a NFW profile (dashed line), at odds with DM-only simulations that predict cuspy NFW profiles for the DM halo density. This is an example of the cusp-core problem. *Top right panel*: the *missing satellites problem*. On the left we can see the projected distribution of DM subhalos within a radius of 600 kpc from a 10^{12} DM halo predicted in ΛCDM from the ELVIS simulation. The most massive subhalos are highlighted with white circles. On the right we can see the spatial distribution of the closest nine of the 11 most luminous (classical) satellites of the Milky Way, where the diameter of the most external sphere is equal to 300 kpc. The number of small subhalos predicted by ΛCDM simulations largely exceeds the number of known satellite galaxies of the Milky Way, arising the missing satellites problem. *Bottom left panel*: the *too-big-to-fail-problem*. The panel shows that the circular velocity profiles of DM subhalos predicted by the ELVIS simulation within 300 kpc from a Milky Way-like galaxy of virial mass $M_{\rm vir} = 1.3 \times 10^{12}\ M_\odot$ exceed the measured velocity dispersions of the dwarf spheroidal satellites of the Milky Way, illustrating the too-big-to-fail-problem. Specifically, the cyan solid lines represent the "strong massive failures", i.e. subhalos that are too dense to host *any* of the observed Milky Way dwarf spheroidals and the black solid lines represent the "massive failures", i.e. additional subhaloes that cannot be explained by the dense galaxies in the observational sample. The dotted lines show the subhalos that are consistent with at least one of the remaining seven dwarfs in the sample and the grey dashed line indicates the unique subhalo expected to host a Magellanic Cloud. The measured velocity dispersions of the dwarf spheroidal satellites of the Milky Way, illustrated as filled squares with sizes proportional to the logarithm of their stellar mass, derive from [99]. *Bottom right panel*: the *planes of satellite galaxies problem*. The panel represents the edge-on view of the vast polar structure (VPOS) around the Milky Way and the disk (solid black line at the center), one of the most striking pieces of evidence of the planes of satellite galaxies problem. The VPOS shows that the satellite galaxies, the distant GCs and the stellar streams of the Milky Way all lie almost on the polar great circle. The orientation and the width of the best-fit satellite plane are indicated by the dashed and dotted lines, respectively. The colored triangles, red upward (blue downward) for receding from (approaching towards) an observer at rest with respect to the host galaxy, indicate coherent kinematics of the co-orbiting satellites. The satellites with no proper motion measurements are plotted as crosses. The grey area corresponds to the region ±12 from the Milky Way disk which is obscured by galactic foreground. The figures are from [100] (top left panel), [101] (top right panel), [102] (bottom left panel), and [103] (bottom right panel).

generally called *quintessence* theories (e.g. [113, 114, 115, 116]).

This slowly-rolling scalar field can produce cosmic acceleration in two ways, which result in two different classes of quintessence models [117]. In the former type, the field does not change at early times, frozen by the Hubble friction, and recently it starts to roll down its potential, having $w_\varphi \sim -1$ up to almost the present epoch. In the latter type, the scalar field varies at early times, slowly converging to $w_\varphi \sim -1$ toward the present day, and then it freezes [117, 118, 119, 120, 121, 122, 123, 104]. Another possibility is to let w_φ become smaller than -1, producing the so called *phantom dark energy* (e.g. [124, 125, 126, 127]). This model properly describes the data from the SNIa, the CMB anisotropy, and the mass power spectrum [124], deserving further investigation.

Another class of dynamical DE models is provided by the K-essence theories, which, with respect to quintessence, have noncanonical kinetic energy terms (e.g. [128, 129, 130, 131]). Extensions of quintessence have been developed to embed these models in a more general and fundamental theory [104], like supersimmetry (e.g. [132, 133, 134, 135, 136]) and string theory (e.g. [137, 138, 139, 140, 141]).

The other possibility to solve the cosmological constant and the coincidence problems is to modify Einstein equations of GR, by adding one or more degrees of freedom with respect to the metric. The addition of degrees of freedom to the theory of gravity can be achieved by introducing one or more scalar fields nonminimally coupled to gravity [142], which can mimic the phenomenology produced by DE. These particular modified theories of gravity are called *scalar-tensor theories* and they should be built with particular carefulness to prevent the theory developing instabilities, like the Ostrogradsky's ones [143, 144].

The most general scalar-tensor theory with second-order equations of motion is Horndeski gravity [145], which is equivalent to the generalised Galileons theory [146]. Given the constraints resulting from the detection of the gravitational wave GW170817 and its electromagnetic counterpart GRB170817A from Ligo-Virgo collaboration [147], the most general Horndeski lagrangian is equal to (e.g. [148, 149, 150]):

$$\mathcal{L}_{\rm H} = \mathcal{G}_4(\varphi)R + \mathcal{G}_2(\varphi, X) - \mathcal{G}_3(\varphi, X)\Box\varphi, \tag{2.6}$$

where $\mathcal{G}_4$, $\mathcal{G}_2$, and $\mathcal{G}_3$ are functions of the scalar field φ, R is the Ricci scalar, $X = \nabla_\mu\varphi\nabla^\mu\varphi$ is the kinetic term, and $\Box$ is the Dalambertian operator.

Among the particular cases of Horndeski theory we can remember Brans-Dicke gravity [151]. $f(R)$ gravity [152, 153, 154, 155, 156] is instead equivalent to a scalar-tensor theory with an appropriate potential. This theory is obtained by replacing the standard Einstein-Hilbert action equal to the Ricci scalar R with a linear function of R and, besides the effects produced by DE, it can also reproduce the phenomenology of DM (e.g. [156]) (see Sect. 2.2.2 for a more in-depth discussion about the unified dark sector).

The scalar field, φ, introduced in both dynamical DE and modified gravity models has to have some peculiar features. To neutralise the cosmological constant to a precision of $\sim H_0^2 M_{\rm Planck}^2 \sim (\text{meV})^4$, φ must have an upper bound for its mass of the order of the Hubble constant[4] [104]:

$$m_\varphi \lesssim H_0. \tag{2.7}$$

Moreover, this scalar field has to couple to Standard Model fields and, thus, it mediates a force between these fields, with an interaction length of $\sim m_\varphi^{-1}$ which is of the order of the Hubble radius, given Eq. (2.7) [104]. This means that, besides the four classical forces (electromagnetic, strong, weak, and gravitational), a fifth force is present and we should observe its effect from the cosmological to the solar system scales. This might represent an issue, since gravitational tests of GR are well satisfied at solar system scales [157, 158, 159, 160, 161]. To overcome this problem, a screening mechanism is necessary, where deviations from GR are suppressed in high-density environments, such as in the solar system [104]. Some of the most popular screening mechanisms are the *Chameleon* [162, 112, 163, 164], the *Symmetron* [165, 166, 167, 168], the kinetic, and the *Vainshtein* [169, 111] mechanisms.

In the Chameleon mechanism, the mass of the scalar field depends on the density: in high-density environments, such as the Earth or the solar system, the mass of the field is sufficienty large to "screen" the effect of the fifth force, whereas in low-density environments, such as at cosmological scales, the mass of the field is $\sim H_0$ and the effects of the fifth force are evident [112]. This mechanism is exploited in $f(R)$ theory (e.g. [152, 153]). In the Symmetron mechanism, the coupling between the scalar field and the matter is weakened in high-density or high-Newtonian-potential regions [165, 166]. This mechanism is also employed to account for inflation [170]. The kinetic screening

[4]Equation (2.7) is written in natural units (see Sect. 2.2).

involves modified Lagrangians with exotic kinetic terms that include only the first derivatives of the scalar field [104]. Among the models that exploit this mechanism we can mention K-inflation [171, 172] and, again, K-essence (e.g. [128, 129, 130, 131]). In the Vainshtein mechanism, which is classified as a kinetic screening [104], some nonlinear derivative interactions make the kinetic term of the scalar field become effectively large in proximity of high-density regions, screening the effect of the fifth force [111]. Both Galileon-like theories [173] and nonlinear massive gravity (e.g. [174, 175, 176]) are based on this screening mechanism [111].

2.2.2 Possible solutions on galaxy scale

The possible solutions for the problems of ΛCDM paradigm emerging on the scale of galaxies can be categorised in three groups: (1) remaining within the CDM paradigm, (2) going beyond CDM paradigm, and (3) going beyond Newtonian dynamics, that is modifying the law of gravity [1].

The ΛCDM model provides only partial or not so natural solutions for the observed problems on galaxy scale. The normalisation and the slope of the BTFR can be reproduced in ΛCDM if baryons are included in the simulations (hydrodynamical simulations) (e.g. [177, 178]), but its small scatter can only be accounted for by an extremely accurate balance between star formation efficiency and stellar feedback mechanisms [45, 46]. Concerning the MDAR, Di Cintio and Lelli built a semi-empirical model that properly describes its shape and scatter, but that cannot simultaneously account for the small scatter of the BTFR, which results equal to 0.17 dex at odds with the observed value of ∼0.10 dex [95].

Possible solutions invoked by the CDM paradigm to solve the cusp/core problem can involve processes of the baryonic matter, like supernova feedback and dynamical friction that have been neglected in simulations [1]. For example, winds generated either by supernovae [179, 180] or by stars [181, 182] can convert the cuspy DM density profiles into cored ones in dwarf galaxies and the dynamical friction between gas clumps of masses of $10^5 - 10^6\ M_\odot$ transfers angular momentum from the gas to the DM particles which, at this point, go from the inner to the outer regions of the galaxies, turning the central cusp of the DM halo density into a core [183, 184]. The problem of this last solution is that usually gas clumps in dwarf galaxies are less massive than $10^5 - 10^6\ M_\odot$ and, thus, the mechanism is not sufficient to solve the cusp/core problem [185].

The missing satellites problem can be addressed within the CDM paradigm with the abundance matching argument, according to which the cumulative distribution of an observed property of baryonic matter and of a predicted property of DM in galaxies are linked together [98]. If the observed property is the mean star formation rate, we observe that the missing satellites problem in the Galaxy can be solved for sub-halos with a DM mass larger than $\sim 10^9\ M_\odot$ [186]. Indeed, the cumulative mass function of the satellite galaxies concentrated within 280 kpc from the Milky Way centre is consistent with the results from ΛCDM simulations that due the depletion of the satellites with a halo mass $\gtrsim 10^9\ M_\odot$ to the presence of the Milky Way stellar disk. For satellites with halo masses $\lesssim 10^9\ M_\odot$, the missing satellites problem might be solved thanks to the reionisation UV feedback [98] but this issue requires further investigation.

If the mass of the Milky Way were overestimated by a factor of ∼2, the number of massive dark sub-halos not correspondent to observed dwarf satellites would be of the order of 3, and it might be, thus, attributed to statistical fluctuations, solving in this way the too-big-to-fail problem [187]. Yet, the issue would remain open, both because there is no evidence for an overestimate of the Milky Way mass and because this problem appears also in other galaxies other than the Milky Way, such as M31 [1]. One way to solve this problem would be to account for baryonic physics in simulations [188, 189, 190], even if the results depend on the mass resolution of baryonic particles [1].

Concerning the planes of satellite galaxies problem, so far no viable solution has been found within the CDM model since the proposed solutions are either not able to describe the observed phenomenology or their assumptions are not built on solid basis [1]. As an example, some mechanisms can reproduce the planar structures observed in M31 and Centaurus A [191] but not in the Milky Way [192, 103].

We now illustrate some possible solutions beyond the CDM paradigm. Specifically, we will consider the WDM (already mentioned in Sect. 2.1.1), the self-interacting dark matter (SIDM), the quantum cromodynamics (QCD) axions, and the fuzzy dark matter (FDM) models.

As already stated at the end of Sect. 2.1.1, each type of DM particle is characterised by its free-streaming length, $\lambda_{\rm fs}$, or equivalently by its free-streaming wavenumber, $k_{\rm fs}$, below which DM fluctuations are suppressed by random thermal motions. $\lambda_{\rm fs}$ corresponds to a typical halo mass below which structures cannot form via gravitational instability. $\lambda_{\rm fs}$ is inversely proportional to the mass of the DM particle and depends also on the mean velocity and on the temperature of the DM particle at the decoupling from radiation [1]. Besides $k_{\rm fs}$, the DM particle is also defined by its decaying rate Γ and Fig. 2.15 illustrates the different DM particle candidates in the $\Gamma - k_{\rm fs}$ plane [1].

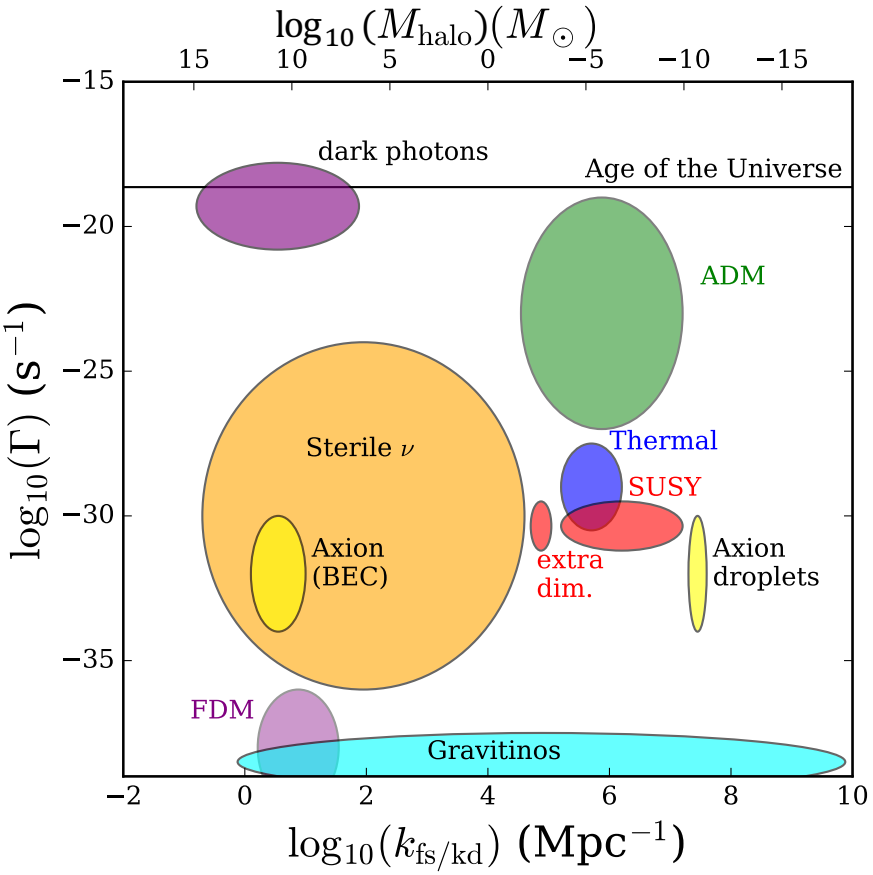

Figure 2.15: Allowed parameter space for the currently most quoted DM models. The bottom axis shows the wavenumber set either by free-streaming, $k_{\rm fs}$, or by kinetic decoupling, $k_{\rm kd}$, the top axis shows its corresponding typical halo mass below which structures cannot form through gravitational instability, and the vertical axis shows the DM particle decaying rate, Γ. The acronyms ADM and BEC mean "asymmetric dark matter" and "Bose-Einstein condensate", respectively. The figure is adapted from [32].

Differently from CDM particles, WDM particles are relativistic at the epoch of their decoupling from radiation and, consequently, present a cut-off in their power spectrum [193] (see Fig. 2.5). The lower bound for the mass of WDM particles is $m_X = 4.65$ keV [194] and its most quoted candidate is the sterile neutrino, whose mass ranges from 0.4 to 10^5 keV [32]. This results in a $k_{\rm fs} \sim 0.5(m_X/{\rm keV})$ Mpc^{-1} which corresponds to a charac-

teristic mass in the range of $M_{\rm fs} \sim [10^{-6} - 10^{11}]\ M_\odot$ [32]. Given the larger free-streaming length with respect to CDM particles (see Sect. 2.1.1), WDM particles suppress the formation of structures below a mass scale larger than in CDM model. This provides a solution for the missing satellites problem, since in WDM model the subhalo mass function is consistent with the observed number of satellites [193, 195, 196]. WDM can also provide a solution for the cusp/core and the too-big-to-fail problems. The gravitational collapse in WDM paradigm forms less centrally concentrated cuspy profiles for the DM halo density with respect to the CDM case [193] and the fact that WDM particles have a relic thermal velocity distribution may provide a cusp-to-core transition in the inner part of DM halo density profiles [197]. Concerning the too-big-to-fail problem, a WDM particle with a mass of $1.5 - 2$ keV or of $\sim$1 keV might solve it for satellite [198, 199] and field dwarf galaxies [200], respectively. This is possible because in WDM the subhalos around Milky Way-sized halos are less and less dense than in CDM [198, 199]. Yet, some issues are present also with this model since the cores produced in WDM are too small to account for LSB galaxies [201, 202], and WDM particle masses between 1 and 2 keV, necessary to solve the too-big-to-fail problem, are below the lower bound for the mass of this particle from the high-resolution HIRES/MIKE spectrographs [194].

SIDM particles act like collisionless CDM particles in small density regions, where the collisional rate becomes negligible, and they are parametrised as a function of the cross section-to-mass ratio, σ/m, that is a function of the relative speed between the DM particles, $v_{\rm rel}$ [203, 1]. SIDM paradigm can solve the cusp/core problem with $\sigma/m \gtrsim 0.5\ {\rm cm}^2\ {\rm g}^{-1}$ for halos of $M \sim 10^{11}\ M_\odot$ (galaxy scale) [204, 205] and with $\sigma/m \sim 0.1\ {\rm cm}^2\ {\rm g}^{-1}$ for halos of $M \sim 10^{14}\ M_\odot$ (cluster scale) [204, 206, 207, 203], implying a velocity-dependent cross section [1]. SIDM model can also alleviate the too-big-to-fail problem, both for satellite and field dwarf galaxies. Specifically, whereas velocity-independent SIDM models present some issues to solve this problem [208, 209], velocity-dependent SIDM models can completely account for it [210, 209, 211], although they still remain largely unconstrained [1]. Moreover, if dissipative or inelastic scattering between SIDM particles is taken into account, SIDM models can also mitigate the problem of the planes of satellite galaxies [212, 213]. Instead, SIDM models can hardly solve the missing satellites problem [214, 215, 210, 208], unless we do not include nonminimal interactions between SIDM particles [203].

QCD axions are another candidate to be taken into consideration. They provide an interesting subject of study since they can both account for the Strong CP problem in the Standard Model of particle physics [216, 217, 218, 219] and they are a possible DM candidate [220, 221, 222]. Ultra-light axion-like particles (ULALPs) with a mass of $\sim 10^{-22}$ eV might solve both the cusp/core problem, resulting in DM density profiles with a $\sim$1 kpc extended core, and the missing satellites problem. Yet, QCD axions cannot simply solve the cusp/core problem by extrapolating the ULALPs scenario since the size of the DM core they produce is of the order of 1 km, that is extremely small [223]. Further investigation is required to assess whether QCD axions are able or not to solve the galaxy-scale problems of ΛCDM.

The last DM candidate we mention is FDM, an ultra-light boson with a mass between 10^{-23} and 10^{-20} eV [224, 225]. They are real scalar fields with a mass minimally coupled to the metric [226], they have a mass equal to 0 until the Universe stays above a critical temperature, and they acquire a mass afterwards, through oscillations around the minimum of a potential generated in a nonperturbative way [227]. They have a de-Broglie wavelength, $\lambda_{\rm dB}$, of the order of kpc and the resulting large-scale structure is identical to the one generated by the CDM model for scales larger than $\lambda_{\rm dB}$ [228]. Instead, for smaller scales the two models behave in different ways, and, for masses larger than the Jeans mass, the minimum halo mass that can be formed in a FDM scenario is $M_{\rm halo} \sim 10^7\ M_\odot$, if the mass of the FDM particle is $m_X \sim 10^{-22}$ eV [226]. N-body simulations of FDM, based on simultaneously solving the Schrödinger and the Poisson equations, show the formations

of cores, usually called solitons, in the central regions of DM halos, generated by the ground-state solution of the Schrödinger-Poisson equations [228, 229]. These solitons can account for the widely-cored profiles required in dwarf galaxies and they might address the cusp/core problem [223, 230, 231, 232, 233, 234]. Moreover, FDM paradigm can even explain the too-high velocity dispersion of the stars settling in the central region of the Galaxy bulge [235] and might provide a solution for the missing satellites problem, since the number of halos with $M \lesssim 10^{10}\ M_{\odot}$ results suppressed in N-body simulations [236]. Yet, the assumption of FDM as a viable DM canditate is still under debate and many pieces of evidence, like the contribution of baryons or the constraints on FDM mass, have yet to be explored [1].

At last, the challenges observed on galaxy scale could be due to a modification of the law of gravity. In contrast to the much larger number of theories of modified gravity formulated to explain the phenomenology produced by DE on cosmological scales (see Sect. 2.2.1), a smaller number of theories of modified gravity conceived to explain the effect of DM on small scales is present. Yet, these theories were historically born previously, already in the 1980s [237, 238, 9, 239], and some ideas already emerged at earlier times [240]. The most investigated alternative theory of gravity that focuses on galactic scale and does not resort to DM is the MOdified Newtonian Dynamics (MOND) [241, 237].

MOND was first introduced by Milgrom in 1983 [241] and it is a general paradigm that assumes spacetime scale-invariance at accelerations $a \ll a_0$ [242]. Newtonian gravity is recovered for accelerations much larger than a_0, whereas we observe a departure from it for accelerations much smaller than this value:

$$a = \begin{cases} g_{\mathrm{N}}, & a \gg a_0 \\ \sqrt{g_{\mathrm{N}} a_0}, & a \ll a_0, \end{cases} \tag{2.8}$$

where g_{N} is the Newtonian acceleration. The MOND paradigm may be achieved by modifying either gravity or inertia, where both options are discussed in [241]. In the nonrelativistic modified gravity version, fully addressed by Bekenstein and Milgrom in 1984 [237], MOND gravitational potential obeys to the following Poisson equation:

$$\nabla \cdot \left[\mu \left(\frac{|\nabla \phi|}{a_0} \right) \nabla \phi \right] = 4\pi G \rho, \tag{2.9}$$

where μ is an interpolating function, monotonic in its argument, with these two asymptotic limits:

$$\mu \left(\frac{|\nabla \phi|}{a_0} \right) = \begin{cases} 1, & a \gg a_0 \\ \frac{|\nabla \phi|}{a_0}, & a \ll a_0. \end{cases} \tag{2.10}$$

For $a \gg a_0$ the Newtonian Poisson equation is recovered:

$$\nabla^2 \phi = 4\pi G \rho, \tag{2.11}$$

whereas for $a \ll a_0$ the gravitational field is boosted with respect to the Newtonian one and it is proportional to R^{-1}, deviating from the Newtonian inverse square law. Successively, other modified gravity versions of MOND, like QUMOND [243], were formulated. Instead, the modified inertia version of MOND, poorly developed, was fully addressed by Milgrom in 1994 [244].

MOND did not only describe but actually predicted most of the phenomenology observed on galaxy scale [245]. Some of the most important predictions are (1) the BTFR, the MDAR, and the RAR with zero-intrinsic scatter, and (2) the difference between the rotation curve shapes of high and low surface brightness galaxies, providing a natural solution for the cusp/core problem [245]. It should be specified that the intrinsic scatter of the RAR is predicted to be zero only for the modified inertia version of MOND and for circular orbits [244]. For the modified gravity versions of MOND, the RAR is recovered

with a very small intrinsic scatter, consistent with the observations, unless the systems are spherical, in which case we obtain again a null intrinsic scatter [237, 246, 247].

Despite its numerous successes on galaxy scale, MOND fails to describe the phenomenology on larger scales. For example it can only reduce, but not eliminate at all, the mass discrepancy in clusters of galaxies [248, 249, 250]. Moreover, it seems that MOND cannot be extended in a covariant sense. Some attempts of relativistic extensions of MOND failed to reproduce the features of gravitational lenses, provided superluminal velocities or were not consistent with the post-Newtonian tests of general relativity [237, 251, 252]. In 2004 Bekenstein built the Tensor-Vector-Scalar (TeVeS) gravity [253], a relativistic MOND inspired theory, which solved some of these issues but failed to describe cosmological observations like the CMB or the matter power spectra. Yet, further investigation about the building of a relativistic version of MOND is still ongoing and some recent results might look promising [254, 255]. In particular, Hernandez and collaborators [254] show that a fully covariant equivalence between a_0 and the scalar quantity

$$\mathcal{K}_{\rm B} = K\frac{r^4}{M} = \frac{28Ga_0}{c^4}, \tag{2.12}$$

where K is the Kretschmann curvature scalar for a Schwarzschild metric, M is the total mass of the baryonic component in a galactic system, G is the universal gravitational constant and c is the speed of light, can be constructed at galaxy level and that this same identification naturally yields a Universe with late time accelerated expansion in accordance with ΛCDM predictions.

Another challenge for MOND is provided by the internal dynamics of GCs residing in the most external regions of the Milky Way. Since the background acceleration is much smaller than a_0 and the external field effect is negligible, we expect that their stellar velocity dispersion profiles obey the MOND theory. Instead, Newtonian gravity without the inclusion of a dark component can better describe these measurements than MOND, whose predicted velocity dispersions can exceed their Newtonian counterparts by a factor of ∼3 [61, 62, 63, 64, 65, 66, 67]. Three of the most striking examples are the GCs NGC 2419, Palomar 14, and Palomar 4 [62, 63, 65, 66, 67]. However, the disagreement between MOND predictions and observations might not be necessarily due to an issue of the theory but, instead, either to inaccurate data (see Sect. 2.1.2) or to approximate modelling. In most cases, the adopted models were spherically symmetric, nonrotating and orbitally isotropic. Whereas the first two assumptions can be justified by observations, orbital anisotropies in GCs are predicted by N-body simulations [256] and the adoption of strong radial anisotropies can reconcile MOND predictions and observations. A more clear answer to this question can only be provided by high-precision data, where the effect of a strong radial anisotropy and the adopted theory of gravity can be properly disentangled [64].

Another theory of modified gravity acting on galaxy scale is Scalar-Vector-Tensor gravity, also known as MOdified Gravity (MOG) [257]. In MOG the modification of the theory of gravity is already present in the action, where three contributions from a scalar, a tensor, and a massive vector fields are added to the classical Einstein-Hilbert action. The total action is, thus, given by:

$$\mathcal{S}_{\rm MOG} = \mathcal{S}_{\rm EH} + \mathcal{S}_{\varphi} + \mathcal{S}_S + \mathcal{S}_M, \tag{2.13}$$

where $\mathcal{S}_{\rm EH}$ is the Einstein-Hilbert action, $\mathcal{S}_{\varphi}$ and $\mathcal{S}_S$ are the actions correspondent to the massive vector and the scalar fields, respectively, and $\mathcal{S}_M$ is the matter action.

Rather than depending on an acceleration scale, the modification of gravity in MOG depends on a length scale. In particular, in the weak field limit of the modified Einstein equations, the resulting gravitational potential is modified with respect to Newtonian case by a Yukawa-like correction term. This correction produces different effects on small and large scales: below a certain length scale a repulsive gravitational force that suppresses

gravity at galactic, sub-galactic or even smaller scales is present and stabilises the system, and above the same length scale this repulsive force becomes weaker and Newtonian gravity is recovered with an effective larger gravitational constant [258]. The resulting potential is [258]:

$$\phi_{\rm eff}(\vec{x}) = -G_{\rm N} \int \frac{\rho(\vec{x'})}{\left|\vec{x} - \vec{x'}\right|} \left[1 + \alpha - \alpha \times \exp\left(-\mu \left|\vec{x} - \vec{x'}\right|\right)\right] \, {\rm d}^3\vec{x'}, \tag{2.14}$$

where ρ is the mass density of the self-gravitating system, μ, given by the inverse of the length scale, is function of the mass of the system, $\alpha = (G_\infty - G_{\rm N})/G_{\rm N}$, G_∞ is the modified gravitational constant at infinite distance from the system, and $G_{\rm N}$ is the Newtonian gravitational constant. MOG is successful at extragalactic and cosmological scales, properly reproducing gravitational lensing effects [259, 260], the X-ray and Sunyaev-Zel'dovich emissions from clusters of galaxies [261, 259, 262, 263, 264], and the accelerated expansion of the Universe [265, 266], mimiking the effect of DE.

However, the successes of MOG on galaxy scale are more controversial. Despite some successes found at earlier times, more recent results seem to disfavour the theory. At first, it was believed that MOG could solve the cusp/core problem. Indeed, the potential (2.14) can properly reproduce the rotation curves of both the HSB and the LSB galaxies in the THINGS sample with a unique combination of μ and α parameters, equal to $\mu = 0.042 \pm 0.004$ kpc^{-1} and $\alpha = 8.89 \pm 0.34$ [258], and it can also describe the rotation curves of less massive galaxies belonging to LITTLE THINGS catalogue, with μ and α parameters different at most at 10% level [267]. Moreover, MOG might also reproduce the RAR of SPARC galaxies [268] and the velocity dispersion of the ultra-diffuse galaxy NGC 1052-DF2 [269, 270]. Yet, some inconsistencies with these results recently emerged. A previous study where the rotation curve of the Milky Way was properly fit by MOG [271] is at odds with a more recent one, where the data for $R < 20$ kpc are badly described [272]. Moreover, MOG recovers the velocity dispersion profiles of the dwarf spheroidal satellites of the Galaxy with mass-to-light ratios inconsistent with stellar population synthesis models and with μ and α parameters in disagreement between the different satellites [273], and it reproduces the velocity dispersion profile of the satellite Antlia II with an unreasonable tangential stellar anisotropy parameter [274, 275]. These results challenge the ability of MOG of solving the cusp/core problem. Furthermore, MOG recently presented also an inconsistency on large scale, since a tension between the normalisation of the power spectrum, σ_8, predicted by MOG and measured by Planck is present. Further studies are certainly needed to better investigate whether all these incongruities represent a real problem for MOG.

Another class of models that is worth mentioning are those which attribute the effects both of DM and of DE to a single cause that can be, for example, the presence of a scalar field. The idea of a unified dark sector is theoretically justified and it is shared by different models. Martin Kunz claimes that gravity can only probe the total energy momentum tensor, implying a degeneracy between the dark components [276], and tries to constrain this unique dark fluid in a model-independent way [277]. Moreover, the acceleration scale coincidence [54], that is the fact that both DM and DE are regulated by the same acceleration scale a_0 (see Sect. 2.1.2), might further suggest a unification of the dark sector. This idea is commonly known as Unified Dark Matter, Unified Dark Energy, or quartessence [278, 279, 280] and includes different theories like the generalised Chaplygin gas [281, 282, 283], the K-essence [284, 285], the fast transition models [286, 287], and other models that assume the presence of condensates [288, 289, 290]. Other possibilities are given by $f(R)$ theories (e.g. [156]), mimetic gravity [291], and by models where the cosmic acceleration emerges from interactions between DM and baryons [292].

One of the first models invoking a unique description of the DE and DM phenomenologies is Conformal gravity [293, 294]. This theory introduces a further local conformal

invariance principle with respect to GR. Specifically, this additional symmetry makes the action remain invariant under local conformal Weyl transformations of the metric [295]:

$$g_{\mu\nu}(x) \rightarrowtail \phi(x) g_{\mu\nu}(x), \tag{2.15}$$

where x are the spacetime coordinates, $g_{\mu\nu}(x)$ is the metric tensor, and $\phi(x)$ is an arbitrary function, regular and positively defined, of x [295]. Recent works involving this alternative theory of gravity include [296, 297, 298, 295]. In [295] some issues in reproducing the rotation curves of galaxies and gravitational lensing effects are presented, which requires further investigation.

One of the most recent models implying a unified dark sector is the *unified superfluid dark sector* [278], where a unique DM superfluid made of axion-like particles dominates the Universe. In this superfluid, two energy states with an energy gap smaller than H_0 coexist and can interact between each other. These interactions at the microscopic level change the macroscopic bahaviour of the fluid, producing an accelerated expansion of the Universe that mimics DE. This model can reproduce both the cosmological effect that in ΛCDM is due to DE, and the phenomenology at the scale of galaxies of MOND without facing some issues, like superluminal sound speeds or the need of a UV completion, encountered by some of the previously mentioned models [278].

An even more recent and innovative model is the *fuzzy dark fluid* [299], where a single scalar field can mimic, at the same time, the behaviours of DM, DE, and inflation by assuming a nonminimal coupling to the gravitational field, a Mexican hat-shape potential, and a spontaneous symmetry breaking before the inflationary period. Also mimetic gravity [291] provides a unified geometrical description for the behaviours usually attributed to these three different phenomena.

In the work of this Ph.D. thesis, we present another theory of modified gravity, originally proposed by Matsakos and Diaferio in 2016 [300]. This theory is called Refracted Gravity (RG) and it was formulated in a nonrelativistic way, aimed at reproducing the phenomenology of DM on galactic scale without resorting to it, as MOND. Actually, RG is based on a completely different idea from MOND but it is expected to share most of its successes without encountering its failures. Recently, a relativistic version of this theory has been developed [301] and it seems to simultaneously account for both the effects of DE and DM, resorting to a single scalar field, entering in this way in the class of theories based on the unified dark sector. In the following sections, we present the formulation and the properties of RG and the tests we performed on galaxy scale, by describing the dynamics of nearby disk and elliptical galaxies.

Chapter 3

Refracted Gravity

3.1 Formulation of RG theory

RG is a classical theory of gravity inspired to electrodynamics in matter which does not imply the presence of DM [300]. An electric field within a dielectric medium with no free charges is described by the following Laplace equation:

$$\nabla \cdot (\epsilon \vec{E}) = 0, \tag{3.1}$$

where $\epsilon \geq 1$ is the electric permittivity. Following Eq. (3.1), an electric field line crossing a surface that separates two different dielectric media with permittivities ϵ_1 and ϵ_2 is refracted according to:

$$\frac{\tan \alpha_1}{\tan \alpha_2} = \frac{E_{2,\perp}}{E_{1,\perp}} = \frac{\epsilon_1}{\epsilon_2}, \tag{3.2}$$

where α_1 and α_2 are the refraction angles and "$\perp$" indicates the component of the field perpendicular to the separating surface. In this refraction process, the component of the field parallel to the interface does not vary whereas the perpendicular component decreases. This means that, when the electric field crosses a dielectric medium with a nonuniform permittivity, both its direction and its intensity change.

To explore a similar framework for gravity, RG field equations yield this modified Poisson equation:

$$\nabla \cdot [\epsilon(\rho) \nabla \phi] = 4\pi G \rho, \tag{3.3}$$

where ϕ is the gravitational potential, and $\epsilon(\rho)$ is the gravitational permittivity, an arbitrary monotonic increasing function of the local mass density ρ with the following asymptotic limits:

$$\epsilon(\rho) = \begin{cases} 1, & \rho \gg \rho_{\rm c} \\ \epsilon_0, & \rho \ll \rho_{\rm c}. \end{cases} \tag{3.4}$$

In the above equation, $0 < \epsilon_0 \leq 1$ and $\rho_{\rm c}$ are the gravitational permittivity in vacuum and the critical density, respectively, and are two of the three free parameters of the theory. When the local density is much larger than $\rho_{\rm c}$, Eq. (3.3) reduces to the Newtonian Poisson equation (2.11), whereas, when the local density is much smaller than $\rho_{\rm c}$, the RG gravitational field is boosted with respect to the Newtonian case. Summarising, ϵ_0 regulates the magnitude of this boost and $\rho_{\rm c}$ sets where the transition between the two regimes occurs.

In principle, the gravitational permittivity could depend on other scalar quantities besides the mass density ρ, like the total mechanical and thermodynamical energy or the entropy. Yet, since these quantities are also function of the density, we might expect that assuming a more complex dependence of the permittivity ϵ would return a phenomenology consistent to the one resulting by adopting a permittivity dependent only on ρ.

One possible expression for the gravitational permittivity, adopted in [300], is the following:

$$\epsilon(\rho) = \epsilon_0 + (1-\epsilon_0)\frac{1}{2}\left\{\tanh\left[\ln\left(\frac{\rho}{\rho_c}\right)^Q\right] + 1\right\}. \tag{3.5}$$

Besides ϵ_0 and ρ_c, this expression contains a third free parameter, Q, which regulates the steepness of the transition between the asymptotic limits of Eq. (3.4). In particular, the larger its value, the steeper the transition. Figure 3.1 shows the trend of the gravitational permittivity (3.5) for $Q = 1/2$, $Q = 3/4$, and $Q = 2$ with ϵ_0 set to 0.25. We expect that ϵ_0, Q, and ρ_c are universal free parameters. Equation (3.5) provides only a possible expression for the gravitational permittivity: any other equation that increases monotonically with ρ and has the asymptotic limits of Eq. (3.4) is certainly viable.

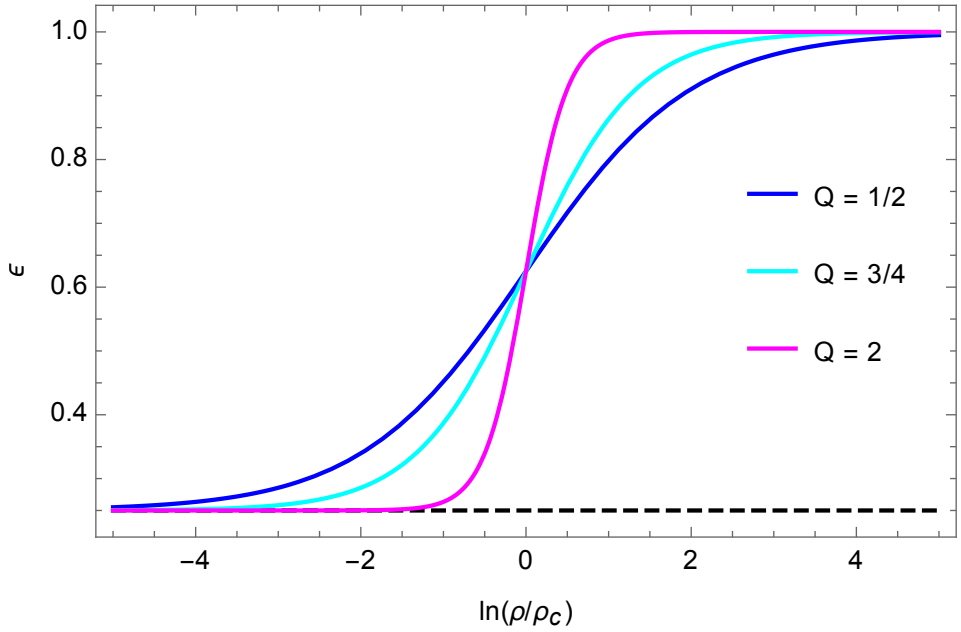

Figure 3.1: Gravitational permittivity for different values of Q. The black dashed line shows $\epsilon_0 = 0.25$. The figure is from [97].

For spherically symmetric systems, the integration of Eq. (3.3) provides this expression for the gravitational field:

$$\frac{\partial\phi}{\partial r} = \frac{G}{\epsilon(\rho)}\frac{M(<r)}{r^2}, \tag{3.6}$$

where $M(<r)$ is the mass of the system within the spherical radius r. In this configuration, RG field has the same direction and r-dependence as the Newtonian case, proportional to r^{-2}, in the most external regions, but, it is enhanced by $1/\epsilon(\rho)$[1]

For not-spherically symmetric systems, the expansion of the first member of Eq. (3.3),

$$\frac{\partial\epsilon}{\partial\rho}\nabla\rho\cdot\nabla\phi + \epsilon(\rho)\nabla^2\phi = 4\pi G\rho, \tag{3.7}$$

shows that ϕ depends both on the density field ρ, according to the second term in the left-hand side of the equation, as for spherical systems, and on its variation, according to the first term in the left-hand side of the equation.

[1]Equation (3.6) shows that the gravitational field is $\propto r^{-2}$ in the vacuum, where both $M(r)$ and $\epsilon(\rho)$ are constant. This behaviour of the RG gravitational field does not necessarily contradict the observed velocity dispersion profiles of elliptical galaxies [302, 303, 304] and of GCs [305, 306, 303, 307], or the external $\rho \propto r^{-3}$ mass density profiles of spherical stellar systems [308] that suggest a gravitational field falling off as r^{-1}. No astrophysical system is completely isolated and exactly satisfies the conditions $M(r) = \text{const}$ and $\epsilon(\rho) = \text{const}$ in its outer regions. Therefore, in principle, the permittivity $\epsilon(\rho)$ can determine an r^{-1} behaviour of the gravitational field in each of these systems depending on the actual density field of its environment.

The term "$\frac{\partial\epsilon}{\partial\rho}\nabla\rho\cdot\nabla\phi$" is responsible for the refraction of the field lines and, thus, the analogy with the behaviour of the electric field in matter is evident for nonspherical systems, where this term is different from zero. In the external regions of flattened systems, the acceleration boost that in Newtonian gravity is due to DM, in RG is explained by the focussing of the field lines toward the mid-plane of the object. This means that RG predicts that the flatter a system the larger its mass discrepancy when interpreted in Newtonian gravity. Figure 3.2 illustrates the analogies and the differences between Newtonian (top) and refracted (bottom) gravities for flat (left) and spherical (right) systems.

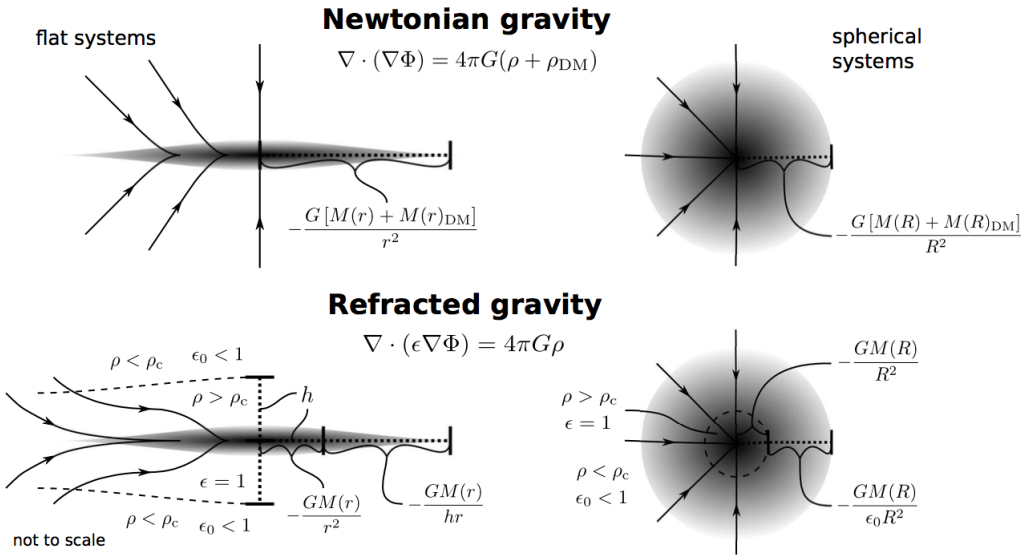

Figure 3.2: Analogies and differences between the gravitational field in Newtonian (top) and refracted (bottom) gravities for flat (left) and spherical (right) systems. The figure is from [300].

In flat systems this redirection process implies the asymptotic behaviour $\partial\phi/\partial R \sim \sqrt{a_0\times|\partial\phi_{\rm N}/\partial R|}\propto R^{-1}$ for the radial component of the gravitational field, in low-density environments at large distances R from the galaxy centre. In the above expression, $\phi_{\rm N}$ is the Newtonian potential and a_0 is the MOND acceleration scale, set by the observed normalisation of the BTFR. This asymptotic limit coincides with the low-acceleration limit in MOND, which suggests that the successes of MOND on the scale of galaxies might be shared by RG. Instead, for the vertical component of the gravitational field, $\partial\phi/\partial z$, the asymptotic behaviour is $\partial\phi/\partial z\sim 0$, which means that the field lines are refracted parallel to the galaxy equatorial plane.

The proportionality of RG field to r^{-2} in the external low-density regions of spherical bodies and to R^{-1} in the external low-density regions of flattened systems guarantees the preservation of the Gauss theorem in both cases [300].

Matsakos and Diaferio reported the first encouraging results of RG theory: they showed that RG can model the BTFR, the rotation curves of two disk galaxies, the HSB NGC 6946 and the LSB NGC 1560, and the intracluster gas temperature profile from the hydrostatic equilibrium equation and the ideal-gas equation of state of two galaxy clusters, A1991 and A1795. For this reason RG certainly deserves further investigation. These results are shown in Fig. 3.3.

3.2 Applications of RG on galaxy scale

RG seems to describe the phenomenology on galaxy scale. RG describes the flatness of rotation curves in disk galaxies thanks to the focussing of the field lines in the external

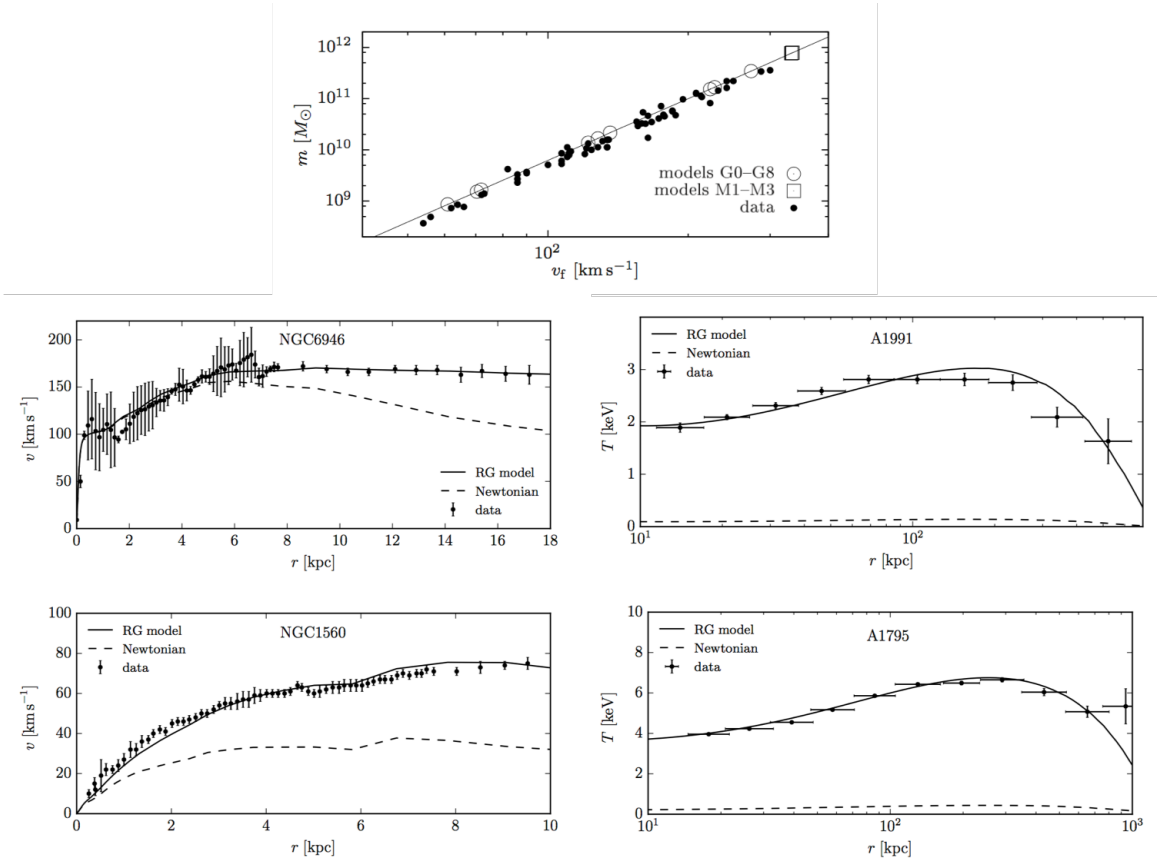

Figure 3.3: First encouraging results obtained by Matsakos and Diaferio with RG: the BTFR (top panel), the fit to the rotation curves of the HSB and LSB galaxies NGC 6946 and NGC 1560 (bottom left panels), and the fit to the temperature profile of the intracluster hot X-ray emitting gas of two galaxy clusters, A1991 and A1795 (bottom right panels). The figure is adapted from [300].

regions of these systems. As MOND, RG can also describe the difference between the dynamical features of high and low surface brightness galaxies. If interpreted in Newtonian gravity, LSB galaxies are more DM-dominated than HSB galaxies and they show large mass discrepancies even in their innermost regions, whereas the dynamics of HSB galaxies can be recovered with the "maximum disk hypothesis". If we assume that light traces mass, RG explains the difference between these two classes of galaxies because, when the mass density of HSB galaxies is still above the critical value, the mass density of LSB galaxies is already below it and, thus, RG gravitational field is already boosted with respect to the Newtonian case. This could provide a natural solution for the cusp/core problem.

Moreover, the prediction of RG that the flatter a system the larger its mass discrepancy can explain some observed phenomenology. This is in agreement with the preliminary analysis of Alexander Deur [82, 83], which shows the existence of a monotonically increasing relation between the ellipticities and the total mass-to-light ratios of elliptical galaxies. This prediction of RG might also account for the difference in the dynamics of dwarf galaxies and GCs. The two systems have similar baryonic masses, but very different dynamical features, the former showing large mass discrepancies even in their most internal regions, and the latter being DM-free, when interpreted in Newtonian gravity. According to RG, this difference can be due to their diverse shape, since dwarf galaxies are flattened systems and GCs show a spherical morphology.

3.3 Applications of RG on cluster scale

As already stated, RG properly models the intracluster hot gas temperature radial profiles of two galaxy clusters, A1991 and A1795, having different gas temperatures [309] (see the bottom right panels of Fig. 3.3). Matsakos and Diaferio modeled the two profiles from the ideal-gas equation of state and the hydrostatic equilibrium equation derived from the RG gravitational field obtained, in turn, from Eq. (3.3) assuming a spherical density model. The two temperature predictions resulted in agreement with the data taken from the *Chandra* satellite [309]. An interesting application of RG would be to extend this study to a larger sample of galaxy clusters, to assess whether RG always provides a good modelling. Furthermore, a less simplified model could be formulated, for example by including the mass profiles of the single galaxies by exploiting the results from N-body simulations, to verify if the modelling could be even further improved. We have to keep in mind that modelling the temperature profiles of galaxy clusters is complicated by a series of uncertainties due to the equation of state, the entropy profiles, the inflows, the outfows, and the turbulent motions of the hot X-ray emitting gas causing local deviations from the hydrostatic equilibrium status (e.g. [310]). They should be certaintly taken into account when interpreting the results obtained with RG.

Another aspect of RG on cluster scale which could be explored is how the gravitational interaction between galaxies in galaxy groups and clusters would behave. These interactions are not trivial to treat in RG, since the field lines in each galaxy suffer from redirection in low-density regions. Yet, we could simplify this configuration and we could assume that the gravitational field at large distances from the centre in each galaxy descreases $\propto R^{-1}$ and that the only difference with respect to Newtonian gravity is that it is enhanced by ϵ_0^{-1}. This would imply the following expression for the BTFR extended to galaxy groups and clusters:

$$\sigma_V^4 = GAf\frac{km}{\epsilon_0}, \tag{3.8}$$

where σ_V is the velocity dispersion of the galaxies in the cluster, k is the number of galaxies, m is the mass of each galaxy, A is the normalisation of the BTFR, and $f < 1$ is a geometric factor that accounts for the fact that, since the geometry of the RG field in disk galaxies is anisotropic, only a fraction of the k galaxies belonging to the clusters will cross the plane of a certain disk galaxy where the force is $\propto R^{-1}$. The comparison of this predicted extended BTFR with the observed one for galaxy groups and clusters would provide another test for RG and a method to constrain both ρ_c and ϵ_0. Particularly, it would be able to set a lower bound for ρ_c.

3.4 Comparison between RG and MOND theories

RG and MOND Poisson equations (Eqs. (3.3) and (2.9), respectively) have the same structure but are only formally similar. Indeed, whereas the MOND interpolating function, μ, depends on the gravitational field or acceleration, $\nabla\phi$, which is a vector quantity, the gravitational permittivity, ϵ, depends on its source, ρ, which is a scalar quantity. Moreover, wherever the acceleration is much below a_0, the field dependence in MOND departs from the Newtonian case, being proportional to r^{-1}. This is true for RG and the critical density, ρ_c, only in the external regions of flat systems, like disk galaxies, whereas is no more true in the external regions of spherical systems, where the field is magnified but its trend remains Newtonian and proportional to r^{-2}. This guarantees, in RG, the preservation of the Gauss theorem both for flattened and for spherical systems, whereas, in MOND, Gauss theorem is preserved only for flattened systems. Spherical systems, like globular or galaxy clusters, are, thus, the best places to test the differences between these two theories of modified gravity. In particular, RG might naturally explain

the dynamics of GCs that MOND cannot properly describe (see Sect. 3.2). Having three more parameters than MOND, where one of them is ϵ_0 that regulates the magnitude of the acceleration boost, RG might fully account for the mass discrepancy observed in galaxy clusters that MOND cannot explain, as suggested by the first tests performed by Matsakos and Diaferio [300].

Despite the potential improvements that RG could offer with respect to MOND in describing some phenomenology on galaxy and cluster scales, it should be pointed out that several pieces of evidence favour the idea that Newtonian gravity breaks down where the acceleration is small, and this occurs below a very precise acceleration scale set by observations (e.g. [42, 43, 44]). This could strongly support MOND with respect to RG, since the same could not be said for low density regions and the critical density.

Still concerning the comparison between the RG and MOND theories of gravity, it is also interesting to discuss the differences between RG and the dipole DM model. In the dipole DM model [311, 312, 313, 314, 315] the phenomenology described by MOND is reproduced by a framework that includes both standard CDM particles and a dark fluid subjected to a polarisation in a gravitational field, similar to the electrostatic polarisation of a dielectric medium, induced by the presence of a vector field [315]. Even if both the dipole DM model and RG refer to electrodynamics, they are based on two completely different approaches. Indeed, whereas in RG the connection to electrodynamics does not go beyond the phenomenological formulation of the modified Poisson equation (3.3), in the dipole DM model the polarisation is a real phenomenon.

3.5 A covariant extension of RG

Recently, Sanna, Matsakos and Diaferio have worked on a relativistic formulation of RG [301]. The formulation of RG offers another advantage with respect to MOND. The transition from a Newtonian regime to a regime of modified gravity driven by the gravitational acceleration has made the construction of a covariant formulation of MOND considerably challenging (e.g. [253]). Instead, the adoption of a scalar quantity, like the mass density, appears to make RG expandable in a covariant sense. RG might be reformulated as a scalar-tensor theory (see Sect. 2.2.1) which includes the presence of a single scalar field, φ, nonminimally coupled to the gravitational field. The RG Poisson equation (3.3) can be recovered as the weak field limit of the modified Einstein equations derived from the scalar-tensor action if φ coincides with the gravitational permittivity $\epsilon(\rho)$. Being associated with the gravitational permittivity, the scalar field is responsible for the phenomenology that in Newtonian gravity is associated to DM. The same field is also responsible for the accelerated expansion of the Universe, that is it explains the phenomenology that in GR is attributed to DE [301].

The fact that a single scalar field can mimic both the behaviours that in GR are due to DE and DM, classifies RG in the group of theories of modified gravity involving the unified dark sector (see Sect. 2.2.2). Moreover, the fact that in RG the modification of gravity depends on the local density and that, in particular, Newtonian gravity is recovered in high-density regions, reminds the screening mechanism, which hide the effect of the fifth force mediated by the scalar field in the same regions (see Sect. 2.2.1). Given the present formulation of relativistic RG, this theory should employ the Vainshtein screening mechanism (see Sect. 2.2.1), which prevents the theory to violate the weak equivalence principle [301, 316].

In this work, we intend to study if RG can model the dynamics of real galaxies. This is an essential test to perform, before investigating RG in its relativistic version. Specifically, we model, at the same time, the rotation curves and the vertical velocity dispersions of 30 disk galaxies in the DiskMass Survey (DMS) [317, 97], and the velocity dispersions of stars and GCs of three elliptical E0 galaxies in the SLUGGS survey [76, 318]. In the

sections below, we present the results of these two analyses, where we adopt the Hubble constant $H_0 = 73$ km s^{-1} Mpc^{-1} [319, 320]. This value of the Hubble constant is adopted by Martinsson and coauthors for their analysis with DMS galaxies [320].

Chapter 4

Dynamics of disk galaxies in RG: the DiskMass Survey[1]

To test the viability of RG, we model the observed dynamics of disk galaxies. To provide the most stringent tests of the full dynamics of a disk galaxy, rather than modelling rotation curves alone, we consider a sample of galaxies where both the rotation curves and the velocity dispersion profiles, in the direction perpendicular to the disk, are available. The DMS [317, 321, 322, 323, 320, 324] provides a sample that is fitting for our purpose: it contains 46 galaxies from the Uppsala General Catalogue (UGC) whose disks appear close to face-on and for 30 galaxies the measures of both the rotation curves and the vertical velocity dispersion profiles are publicly available.

The dynamics of this galaxy sample was already modelled with other theories of gravity. The DMS collaboration performed the modelling in Newtonian gravity, by adopting the disk-scale heights derived from the observations of edge-on galaxies [321], obtaining sub-maximal disks, with mass-to-light ratios systematically smaller than the predictions from stellar population synthesis (SPS) models [325]. Instead, Angus and coauthors used the DMS sample to test MOND [326]. MOND reproduces the kinematic profiles of these galaxies with mass-to-light ratios in agreement with the SPS values but with disk-scale heights systematically smaller than those inferred from the observations of edge-on galaxies. Milgrom [327], however, pointed out that this inconsistent disk thickness might originate from an observational bias: the measured velocity dispersion is inferred from the absorption lines near the V-band of the integrated spectra, which are dominated by the younger stellar population [328]; this measured velocity dispersion is thus smaller than the velocity dispersion of the older stellar population which sets the estimate of the disk-scale height from near infrared photometry of edge-on galaxies [329, 330, 331, 332, 333, 321]. This bias would also explain the low mass-to-light ratios estimated by the DMS collaboration because the disk surface mass density is proportional to the ratio between the velocity dispersion and the disk-scale height and it is thus underestimated [328]. The analysis of the dynamics of DMS galaxies that we present here could also be affected by this bias.

To test RG, we first model the rotation curves of the DMS galaxies alone and then we provide a unique constraint of RG parameters from both the rotation curves and the vertical velocity dispersions at the same time. Moreover, to further test RG theory, we also model the RAR of DMS galaxies, since the RAR very clearly quantifies the mass discrepancy on galaxy scale. In the following sections, we detail the analysis we perform to investigate the dynamics of DMS galaxies in RG.

[1] The results in this chapter are published in [97].

4.1 Modelling the rotation curves alone of the DMS galaxies

To test whether RG can describe the dynamics of disk galaxies, we first consider the rotation curves of the 30 published galaxies of the DMS catalogue on their own [317, 321, 322, 323, 320, 324].

Disk galaxies can be modelled as axisymmetric systems. For an axisymmetric mass density distribution $\rho(R, z)$, the Poisson equation (3.3) returns the gravitational potential $\phi(R, z)$ that, in turn, yields the rotation curve (2.2) on the disk plane, $z = 0$.

We model each disk galaxy with a stellar disk, a stellar bulge, and an interstellar gas disk separated into an atomic and a molecular component. The stellar disk is described by a linear interpolation of the measured radial surface brightness and by an exponentially decreasing density profile along the vertical axis. The stellar bulge is described by a Sérsic profile. The details of our model of the mass distribution are given in Appendix A.

To model the galaxy rotation curves, we estimate the RG potential by numerically solving the Poisson equation (3.3) with a successive over relaxation algorithm described in Appendix B. We then perform the numerical derivative of the potential to obtain the rotation curve from Eq. (2.2). In our model, the rotation curve depends on two parameters describing the galaxy, namely the disk mass-to-light ratio, Υ, and the disk-scale height, h_z, and on the three parameters of the RG gravitational permittivity: ϵ_0, Q, and ρ_c.

We adopt the same mass-to-light ratio for the bulge and the stellar disk because, in our sample, the galaxy luminosity is dominated by the disk (see Appendix A); assuming a different mass-to-light ratio for the bulge only introduces an additional free parameter without substantially improving the galaxy model. We explore this five-dimensional parameter space with a Monte Carlo Markov Chain (MCMC) algorithm.

We assume a Gaussian prior for the two galaxy parameters Υ and h_z and a flat prior for the three RG parameters. Specifically:

1. For the mass-to-light ratio Υ in the K-band, adopted for the measurement of the surface brightness of the DMS galaxies, we use a Gaussian prior; the first moment of the Gaussian is the value derived from the SPS models of [325] applied to the DMS galaxies; for these galaxies the $B - K$ colour ranges from 2.7 (UGC 7244) to 4.2 (UGC 4458) (see Table 1 in [320]). We set the second moment of the Gaussian to three times the maximum errors derived from the SPS models for each galaxy. This choice yields a second moment in the range of 0.21-0.36 dex.[2] We set the Gaussian tail to zero where $\Upsilon < 0$.

2. For the disk-scale height h_z, we adopt a Gaussian prior with mean $h_{z,\mathrm{SR}}$, where $h_{z,\mathrm{SR}}$ is the disk-scale height derived from the relation, reported in Eq. (A.12) in Appendix A, between the observed disk-scale heights and the disk-scale lengths, inferred from the observations of edge-on galaxies [321]. We set the standard deviation of the Gaussian to three times the errors on $h_{z,\mathrm{SR}}$, which basically coincide with the intrinsic scatter of the relation (A.12). On average, the error on $h_{z,\mathrm{SR}}$ is 0.11 kpc for the DMS galaxies. We set the Gaussian tail to zero where $h_z < 0$.

3. For the vacuum permittivity ϵ_0, we adopt a flat prior in the range of $[0.10, 1]$. In principle, the full allowed range is $[0, 1]$; however, we do not explore values smaller than 0.10 because the boost of the gravitational field would yield unphysically large rotation velocities, of the order of $\sim 600 - 1000$ km s^{-1}.

4. For Q, we adopt a flat prior in the range of $[0.01, 2]$. This parameter regulates the steepness of the transition between the Newtonian and the RG regimes. Our range

[2] Setting the second moment of the Gaussian to three times the error from the SPS models, rather than just the error, enables the MCMC analysis to explore a sufficiently extended range of Υ; in fact, the relative error on the SPS Υ's is 16%, on average, and, with the second moment of the Gaussian set to this value, the preferred value suggested by the MCMC analysis would often be forced to be close to the SPS value, independently of the theory of gravity we want to test. The same argument holds for the disk-scale height $h_{z,\mathrm{SR}}$, whose relative error is 22%, on average.

explores from very smooth ($Q = 0.01$) to very steep transitions ($Q = 2$).

5. For $\log_{10}\rho_c$, we adopt a flat prior in the range of $[-27, -23]$, with the critical density ρ_c in units of g cm^{-3}. This range includes the two extreme values -27 and -24 considered by [300].

We adopt the Metropolis-Hastings acceptance criterion in our MCMC algorithm. The random variate $\mathbf{x}$ at step $i+1$ is drawn from the probability density $G(\mathbf{x}|\mathbf{x}_i)$, which depends on the random variate $\mathbf{x}_i$ at the previous step. For the probability density $G(\mathbf{x}|\mathbf{x}_i)$, we adopt a multi-variate Gaussian density distribution with mean value $\mathbf{x}_i$; its multiple standard deviations are 1/3 the standard deviation of the Gaussian priors, for Υ and h_z, and 10% of the prior ranges, for the three RG parameters. In our case, $\mathbf{x}$ is the five-dimensional vector $\mathbf{x} = (\Upsilon, h_z, \epsilon_0, Q, \log_{10}\rho_c)$. We adopt the likelihood,

$$\mathcal{L}(\mathbf{x}) = \exp\left[-\frac{\chi^2_{\rm red,RC}(\mathbf{x})}{2}\right], \tag{4.1}$$

where,

$$\chi^2_{\rm red,RC}(\mathbf{x}) = \frac{1}{n_{\rm dof,RC}}\sum_{i=1}^{N_{\rm RC}}\frac{[v_{\rm mod}(R_i;\mathbf{x}) - v_{\rm data}(R_i)]^2}{v^2_{\rm data,err}(R_i)}, \tag{4.2}$$

$N_{\rm RC}$ is the number of data points of the rotation curve, $v_{\rm data}$ are the velocity measures at the projected distance R_i with their uncertainty $v_{\rm data,err}$, $v_{\rm mod}$ is estimated with Eq. (2.2) and $n_{\rm dof,RC} = N_{\rm RC} - 5$ is the number of degrees of freedom. If $p(\mathbf{x})$ is the product of the priors of the components of $\mathbf{x}$, the Metropolis-Hastings ratio is:

$$A = \frac{p(\mathbf{x})\times\mathcal{L}(\mathbf{x})}{p(\mathbf{x}_i)\times\mathcal{L}(\mathbf{x}_i)}\frac{G(\mathbf{x}|\mathbf{x}_i)}{G(\mathbf{x}_i|\mathbf{x})}. \tag{4.3}$$

If $A \geq 1$, we set $\mathbf{x}_{i+1} = \mathbf{x}$, otherwise we set either $\mathbf{x}_{i+1} = \mathbf{x}$, with probability A, or $\mathbf{x}_{i+1} = \mathbf{x}_i$, with probability $1 - A$.

For the chain starting points, we adopt the values found by the DMS collaboration for Υ and h_z (see Table 1 of [326]); for the three RG parameters ϵ_0, Q and $\log_{10}\rho_c$, we set 0.30, 1.00, and -24.0, respectively. We run the MCMC algorithm for 19000 steps, after a burn-in chain of 1000 steps. This number of steps guarantees the achievement of the chain convergence. We check the chain convergence using the Geweke diagnostic [334]: we compare the means of the first 10% of the chain steps, after the burn-in, with the last 50% of the chain steps; we compare the means with a Gaussian test, adopting the standard deviations of the two portions of the chains as the errors on the two means. In every case, the Gaussian test shows that the two means coincide at a significant level larger than 5%, suggesting that the chains converge.

As an example, Fig. 4.1 shows the posterior distributions for four galaxies. The posterior distributions for the remaining galaxies are qualitatively very similar. The posterior distributions show a single peak and we can thus adopt the medians of the posterior distributions as our parameter estimates; the range between the 15.9 and the 84.1 percentiles, thus including 68% of the posterior cumulative distribution centred on the median, defines our 1σ uncertainty range on the parameter estimates. Table 4.1 lists the medians of the parameters and their associated uncertainties.

We use these parameters to compute our rotation curve models. We collect all the figures showing our results in Appendix E. We arrange the figures by galaxy, so that the outcomes of the various analyses we perform here can be compared more easily.

The rotation curves estimated in this section are shown in sub-panels (d) of Figs. E.1–E.7 as blue solid lines. The red dots with error bars are the DMS data. The vertical lines show the size of the bulge we adopt. In some galaxies, the presence of the bulge produces, at small radii, a relevant spike in the modelled rotation curve that is not present in the

data. Other than these cases, the observed rotation curves are modelled relatively well. Because we model the surface brightness of the disk with a linear interpolation of the data (Appendix A), the model rotation curves capture some of the features appearing in the measured rotation curves that have a correspondence in the surface brightness profile of the disk (Renzo's rule [335]); the galaxies UGC 1635, UGC 4555, UGC 6903, or UGC 7244 are some examples of this correspondence. Nevertheless, the rotation curves of a few galaxies still have some features that are not described by the model, for example UGC 4036, UGC 4622 or UGC 8196.

The $\chi^2_{\rm red,RC}$ of Eq. (4.2) are listed in Table 4.1; they quantify the quality of the RG model. In most cases, the large values of $\chi^2_{\rm red,RC}$ originate from a possible underestimation of the error bars of the data, as suggested by the visual inspection of the sub-panels (d) of Figs. E.1–E.7, rather than from an inappropriate modelling. The goodness of the modelling does not show any significant trend with galaxy properties, like the value of the central density or the bulge-to-disk luminosity ratio, and with the radial coverage of the kinematic data, that goes from $1.88h_R$ (UGC 1862) to $12.14h_R$ (UGC 4368).

Table 4.1 also lists the mass-to-light ratio $\Upsilon_{\rm SPS}$ that we estimate for each galaxy with the SPS models of [325] from the $B-K$ colours listed in Table 1 of [320].[3] Specifically, we adopt the SPS model with a mass-dependent formation epoch with bursts and a scaled Salpeter initial mass function (IMF) (see Table 1 of [325]). According to [325], this model better reproduces (1) the trends in colour-based stellar ages and metallicities [338], (2) the decrease in the colour-stellar mass-to-light ratio slope caused by modest bursts of star formation, and (3) it has an IMF consistent with maximum disk constraints.

To somehow quantify the uncertainty on $\Upsilon_{\rm SPS}$, for the error bar we adopt the range covered by all the different models investigated by [325] based on a scaled Salpeter IMF (see Table A3 of [325]). The resulting uncertainties are asymmetric and, except for three galaxies, the lower limit of the error bar is 0 because, in these cases, our preferred SPS model yields the smallest mass-to-light ratio among all the other models with the same IMF. We neglect the models that adopt different IMFs, under the assumption that the scaled Salpeter IMF can reasonably be considered universal [325]. We do not estimate the SPS mass-to-light ratio for the galaxy UGC 3997, since [320] does not provide its $B-K$ colour.

The two mass-to-light ratios for each galaxy, namely, the $\Upsilon_{\rm SPS}$ and Υ derived from our RG model, are shown in the left panel of Fig. 4.2. In Table 4.1 we list the difference between these ratios in units of the uncertainties on the mass-to-light ratios. Our Υ's nearly cover the same range as the $\Upsilon_{\rm SPS}$'s and the two mass-to-light ratios for the same galaxy tend to agree with each other: for 23 out of 29 galaxies, they agree within 2σ; for an additional five galaxies, they agree within 2.5 to 3.5σ; and for only one galaxy, they are discrepant at more than 6.5σ.

The disk-scale height h_z derived in RG tends to be larger than the scale height $h_{z,\rm SR}$ calculated with Eq. (A.12), as shown in the left panel of Fig. 4.3. Table 4.1 also lists their ratios. Specifically, the RG h_z is larger than $h_{z,\rm SR}$ for 20 galaxies out of 30, and for nine galaxies $h_z/h_{z,\rm SR} \geq 2$; among these nine galaxies, two have $h_z/h_{z,\rm SR} \geq 5$. The ten galaxies with $h_z/h_{z,\rm SR} < 1$ have thinner disks than expected because their gravitational potential wells are shallow: in fact, their central disk surface brightness $I_{\rm d0}$ and their disk-scale length h_R are among the smallest in the sample, similarly to their rotation velocity and vertical velocity dispersion profiles.

[3] We adopt the SPS models of [325], rather than more recent models of the relations between mass-to-light and colours (e.g. [336, 337]) because [325] specifically compute these relations for the $B-K$ colour, which is available in the DMS sample.

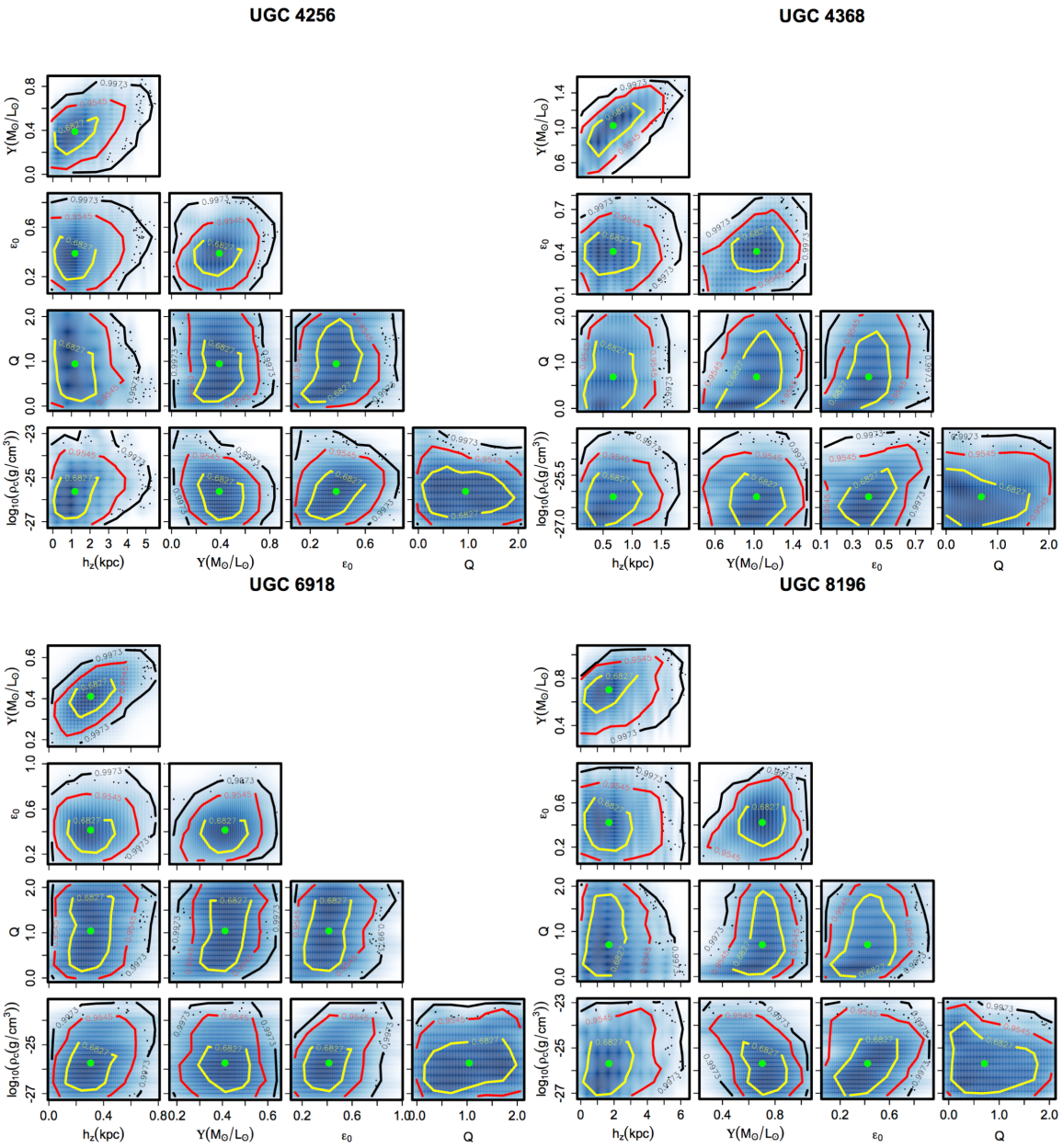

Figure 4.1: Examples of the posterior distributions for four galaxies. The quantities plotted are the two galaxy parameters and the three RG parameters estimated from the rotation curves alone. The green dots locate the median values and the yellow, red and black contours limit the 1σ, 2σ and 3σ regions, respectively.

4.2 Modelling the rotation curves and the vertical velocity dispersion profiles

The DMS sample enables a more comprehensive investigation of the dynamics of disk galaxies because, in addition to the rotation curves, we have a measurement of their stellar vertical velocity dispersion profiles. In fact, the DMS galaxies are close to face-on: as illustrated in Appendix A, based on the Tully-Fisher relation (Eqs. (A.5) and (A.6)), the estimated inclinations of the DMS galaxies are in the range of $5.8 - 45.3\,\mathrm{deg}$ (see Table 5 of [320]). Therefore, combining the two kinematic pieces of information can provide unique constraints on the dynamical properties of the galaxies and can represent a stringent test for theories of modified gravity.

To model the stellar vertical velocity dispersion profile, we use the fact that our axisymmetric model of the galaxy, illustrated in Appendix A, is described by a two-integral distribution function $f(E, L_z)$ and thus the velocity dispersions, $\sigma(R, z)$, along the ver-

Table 4.1: Parameters estimated from the rotation curves alone.

UGC	$\Upsilon\ \left[\frac{M_\odot}{L_\odot}\right]$	$\Upsilon_{SPS}\ \left[\frac{M_\odot}{L_\odot}\right]$	$\frac{\Upsilon_{fit}-\Upsilon_{SPS}}{\sqrt{\sigma^2_{\Upsilon_{fit}}+\sigma^2_{\Upsilon_{SPS}}}}$	h_z [kpc]	$\frac{h_z}{h_{z,SR}}$	ϵ_0	Q	$\log_{10}\left(\rho_c\ \left[\frac{g}{cm^3}\right]\right)$	$\chi^2_{red,RC}$
(1)	(2)	(3)	(4)	(5)	(6)	(7)	(8)	(9)	(10)
448	$1.06^{+0.12}_{-0.16}$	$0.64^{+0.07}_{-0.00}$	$+2.88$	$0.52^{+0.65}_{-0.31}$	1.13	$0.62^{+0.24}_{-0.31}$	$0.78^{+0.84}_{-0.65}$	$-26.03^{+1.06}_{-0.58}$	8.03
463	$0.66^{+0.08}_{-0.08}$	$0.64^{+0.07}_{-0.00}$	$+0.22$	$0.66^{+0.60}_{-0.34}$	1.43	$0.89^{+0.08}_{-0.14}$	$0.92^{+0.73}_{-0.73}$	$-25.37^{+1.82}_{-1.17}$	10.93
1081	$0.61^{+0.21}_{-0.17}$	$0.52^{+0.10}_{-0.00}$	$+0.46$	$0.30^{+0.56}_{-0.18}$	0.77	$0.55^{+0.16}_{-0.16}$	$1.34^{+0.40}_{-0.74}$	$-23.72^{+0.55}_{-1.65}$	16.34
1087	$0.85^{+0.25}_{-0.32}$	$0.58^{+0.08}_{-0.00}$	$+0.92$	$0.22^{+0.32}_{-0.13}$	0.56	$0.52^{+0.10}_{-0.11}$	$0.78^{+0.56}_{-0.65}$	$-25.78^{+1.81}_{-0.81}$	10.67
1529	$1.09^{+0.11}_{-0.13}$	$0.70^{+0.08}_{-0.00}$	$+3.08$	$0.85^{+0.44}_{-0.31}$	1.93	$0.79^{+0.12}_{-0.16}$	$0.86^{+0.83}_{-0.74}$	$-25.86^{+1.09}_{-0.85}$	42.03
1635	$0.88^{+0.18}_{-0.14}$	$0.61^{+0.07}_{-0.00}$	$+1.64$	$0.18^{+0.27}_{-0.10}$	0.44	$0.70^{+0.15}_{-0.16}$	$0.60^{+0.79}_{-0.51}$	$-24.48^{+1.19}_{-1.01}$	8.58
1862	$0.74^{+0.38}_{-0.33}$	$0.52^{+0.10}_{-0.00}$	$+0.61$	$0.06^{+0.06}_{-0.03}$	0.23	$0.64^{+0.19}_{-0.17}$	$0.89^{+0.82}_{-0.75}$	$-25.22^{+1.27}_{-1.34}$	23.16
1908	$0.29^{+0.04}_{-0.04}$	$0.67^{+0.07}_{-0.00}$	-6.72	$2.91^{+1.11}_{-1.27}$	5.37	$0.39^{+0.04}_{-0.04}$	$1.86^{+0.13}_{-0.28}$	$-23.86^{+0.10}_{-0.07}$	32.02
3091	$0.87^{+0.21}_{-0.29}$	$0.48^{+0.10}_{-0.00}$	$+1.53$	$0.40^{+0.65}_{-0.23}$	0.95	$0.52^{+0.12}_{-0.22}$	$1.06^{+0.75}_{-0.87}$	$-23.58^{+0.48}_{-1.41}$	11.62
3140	$0.85^{+0.11}_{-0.13}$	$0.64^{+0.07}_{-0.00}$	$+1.66$	$0.65^{+0.46}_{-0.34}$	1.55	$0.78^{+0.13}_{-0.17}$	$0.77^{+0.82}_{-0.64}$	$-25.63^{+1.70}_{-1.07}$	8.75
3701	$0.70^{+0.24}_{-0.20}$	$0.45^{+0.11}_{-0.00}$	$+1.10$	$0.54^{+0.63}_{-0.37}$	1.26	$0.25^{+0.07}_{-0.06}$	$0.87^{+0.67}_{-0.49}$	$-23.79^{+0.32}_{-1.27}$	2.13
3997	$0.32^{+0.21}_{-0.10}$	-	-	$0.19^{+0.41}_{-0.12}$	0.33	$0.23^{+0.14}_{-0.06}$	$1.24^{+0.35}_{-0.20}$	$-23.28^{+0.13}_{-0.21}$	22.90
4036	$0.79^{+0.20}_{-0.22}$	$0.50^{+0.10}_{-0.00}$	$+1.34$	$0.54^{+0.48}_{-0.31}$	1.32	$0.55^{+0.19}_{-0.17}$	$0.70^{+0.77}_{-0.55}$	$-25.52^{+1.61}_{-1.07}$	4.62
4107	$0.82^{+0.18}_{-0.21}$	$0.58^{+0.08}_{-0.00}$	$+1.18$	$0.17^{+0.25}_{-0.08}$	0.40	$0.81^{+0.11}_{-0.14}$	$0.94^{+0.82}_{-0.62}$	$-24.98^{+1.38}_{-1.45}$	8.06
4256	$0.39^{+0.11}_{-0.12}$	$0.52^{+0.10}_{-0.00}$	-1.00	$1.19^{+0.95}_{-0.62}$	2.43	$0.39^{+0.12}_{-0.13}$	$0.95^{+0.64}_{-0.57}$	$-25.63^{+0.77}_{-0.79}$	2.08
4368	$1.03^{+0.15}_{-0.21}$	$0.45^{+0.11}_{-0.00}$	$+3.06$	$0.67^{+0.31}_{-0.26}$	1.86	$0.40^{+0.09}_{-0.13}$	$0.68^{+0.74}_{-0.53}$	$-26.16^{+0.65}_{-0.58}$	12.25
4380	$0.96^{+0.25}_{-0.32}$	$0.52^{+0.10}_{-0.00}$	$+1.50$	$1.06^{+0.93}_{-0.67}$	1.96	$0.47^{+0.18}_{-0.19}$	$0.83^{+0.82}_{-0.74}$	$-24.06^{+0.92}_{-2.06}$	22.07
4458	$0.55^{+0.04}_{-0.05}$	$0.85^{+0.09}_{-0.06}$	-3.18	$4.20^{+3.84}_{-2.65}$	5.25	$0.77^{+0.15}_{-0.28}$	$0.76^{+0.79}_{-0.56}$	$-25.78^{+1.62}_{-0.95}$	2.83
4555	$0.73^{+0.25}_{-0.30}$	$0.48^{+0.10}_{-0.00}$	$+0.88$	$0.12^{+0.15}_{-0.05}$	0.29	$0.91^{+0.05}_{-0.19}$	$1.28^{+0.51}_{-0.86}$	$-24.53^{+0.97}_{-1.10}$	18.91
4622	$0.69^{+0.33}_{-0.24}$	$0.55^{+0.09}_{-0.00}$	$+0.48$	$2.58^{+2.09}_{-1.53}$	3.69	$0.45^{+0.18}_{-0.14}$	$1.06^{+0.62}_{-0.95}$	$-23.49^{+0.30}_{-1.24}$	15.47
6903	$0.67^{+0.27}_{-0.13}$	$0.52^{+0.10}_{-0.00}$	$+0.73$	$0.10^{+0.07}_{-0.03}$	0.18	$0.37^{+0.26}_{-0.10}$	$0.62^{+0.42}_{-0.39}$	$-25.95^{+1.76}_{-0.59}$	7.08
6918	$0.41^{+0.06}_{-0.06}$	$0.52^{+0.10}_{-0.00}$	-1.41	$0.31^{+0.13}_{-0.09}$	1.48	$0.41^{+0.12}_{-0.11}$	$1.04^{+0.64}_{-0.60}$	$-25.75^{+0.87}_{-0.72}$	4.13
7244	$0.51^{+0.24}_{-0.19}$	$0.41^{+0.12}_{-0.00}$	$+0.44$	$0.72^{+0.53}_{-0.39}$	1.67	$0.23^{+0.06}_{-0.06}$	$0.79^{+0.69}_{-0.42}$	$-24.74^{+0.73}_{-1.20}$	2.00
7917	$0.97^{+0.14}_{-0.17}$	$0.81^{+0.09}_{-0.04}$	$+0.92$	$1.45^{+1.47}_{-0.91}$	2.10	$0.85^{+0.11}_{-0.16}$	$0.78^{+0.88}_{-0.64}$	$-25.59^{+1.85}_{-1.06}$	7.14
8196	$0.70^{+0.09}_{-0.11}$	$0.77^{+0.08}_{-0.03}$	-0.60	$1.69^{+1.18}_{-0.83}$	2.91	$0.42^{+0.16}_{-0.15}$	$0.71^{+0.76}_{-0.48}$	$-25.69^{+0.99}_{-0.86}$	4.72
9177	$0.83^{+0.38}_{-0.26}$	$0.43^{+0.11}_{-0.00}$	$+1.23$	$2.22^{+2.11}_{-1.44}$	3.26	$0.46^{+0.19}_{-0.11}$	$1.41^{+0.36}_{-0.63}$	$-23.33^{+0.21}_{-0.69}$	11.46
9837	$0.67^{+0.18}_{-0.14}$	$0.64^{+0.07}_{-0.00}$	$+0.18$	$0.76^{+1.38}_{-0.70}$	1.27	$0.29^{+0.18}_{-0.07}$	$0.93^{+0.39}_{-0.34}$	$-23.47^{+0.34}_{-0.20}$	17.11
9965	$0.83^{+0.18}_{-0.22}$	$0.50^{+0.10}_{-0.00}$	$+1.60$	$0.37^{+0.38}_{-0.17}$	0.86	$0.78^{+0.15}_{-0.16}$	$0.81^{+0.80}_{-0.63}$	$-25.43^{+1.52}_{-1.05}$	3.16
11318	$0.70^{+0.12}_{-0.13}$	$0.67^{+0.07}_{-0.00}$	$+0.22$	$1.40^{+1.05}_{-0.79}$	2.75	$0.66^{+0.23}_{-0.31}$	$0.89^{+0.74}_{-0.63}$	$-25.52^{+1.59}_{-1.00}$	2.87
12391	$0.99^{+0.13}_{-0.14}$	$0.50^{+0.10}_{-0.00}$	$+3.30$	$1.29^{+0.64}_{-0.46}$	2.87	$0.37^{+0.26}_{-0.12}$	$1.18^{+0.57}_{-0.66}$	$-25.60^{+0.76}_{-0.80}$	11.58

Column 1: UGC number; Cols. 2, 5, 7, 8, 9: medians of the posterior distributions of the model parameters estimated from the rotation curves alone; Col. 3: mass-to-light ratio derived with the SPS model; Col. 10: reduced chi-square, $\chi^2_{red,RC}$, from Eq. (4.2).

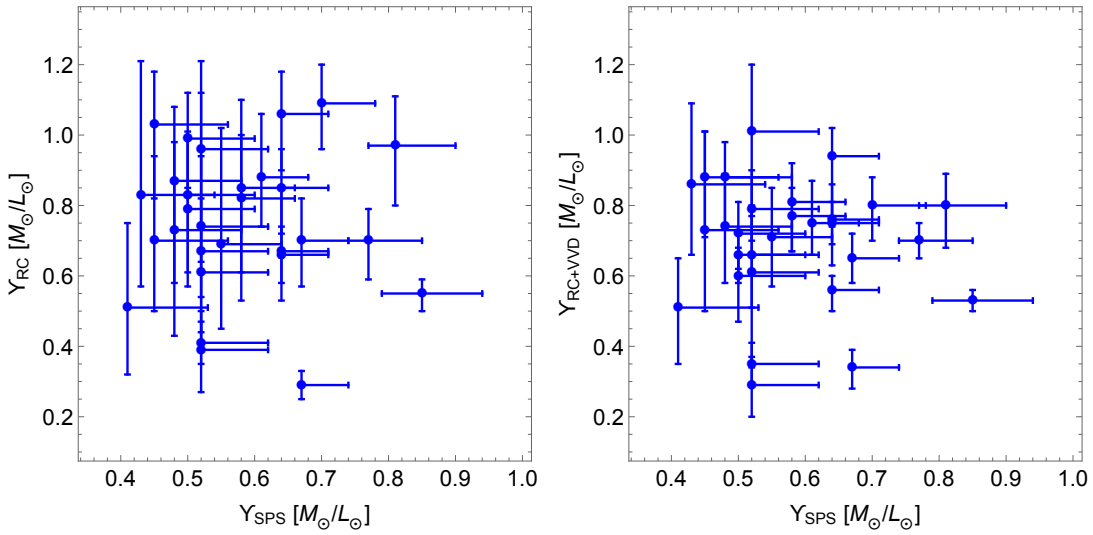

Figure 4.2: Mass-to-light ratios estimated with RG from the measured rotation curves alone (Υ_{RC} - *left panel*) and with the rotation curves and the vertical velocity dispersion profiles (Υ_{RC+VVD} - *right panel*) compared with the mass-to-light ratios derived with the SPS model (Υ_{SPS}), for each DMS galaxy. The black dashed line is the line of equality.

tical and radial axes, z and R, coincide [339, 340]. The system also satisfies the Jeans

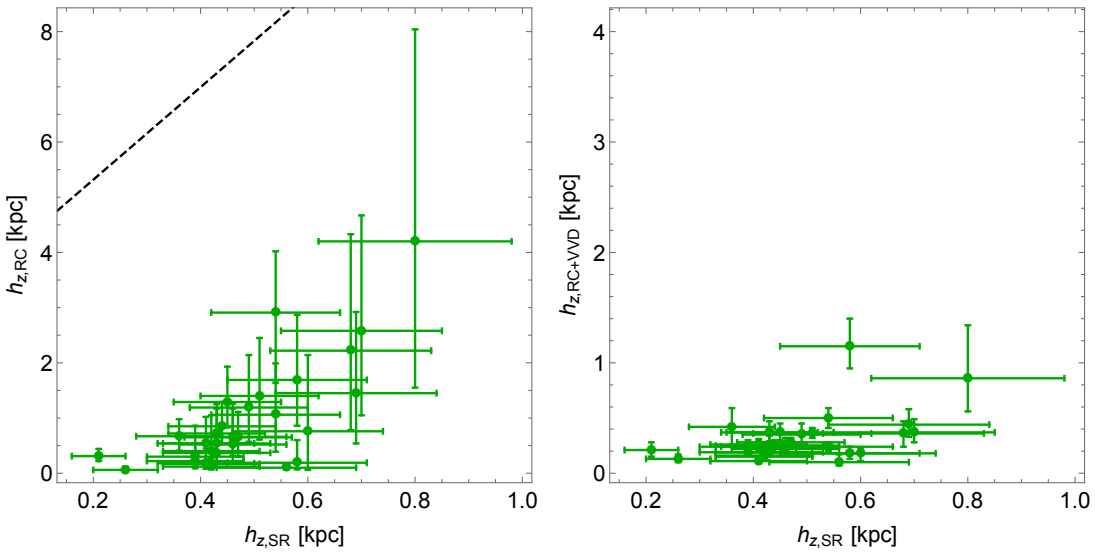

Figure 4.3: Disk-scale heights estimated with RG from the measured rotation curves alone ($h_{z,\mathrm{RC}}$ - *left panel*) and with the rotation curves and the vertical velocity dispersion profiles ($h_{z,\mathrm{RC+VVD}}$ - *right panel*) compared with the disk-scale heights inferred from the observations of edge-on galaxies ($h_{z,\mathrm{SR}}$, see Eq. (A.12) in Appendix A), for each DMS galaxy. The black dashed line is the line of equality.

equation,

$$\frac{\partial[\rho(R,z)\sigma^2(R,z)]}{\partial z} + \rho(R,z)\frac{\partial\phi(R,z)}{\partial z} = 0 \ , \tag{4.4}$$

where $\rho(R,z)$ is the stellar density. The observed vertical velocity dispersion profile, weighted by the local stellar surface density $\Sigma_*(R)$, is

$$\sigma_z^2(R) = \frac{1}{\Sigma_*(R)}\int_{-\infty}^{+\infty}\rho(R,z)\sigma^2(R,z)dz \ . \tag{4.5}$$

By considering the contribution of the disk alone to $\Sigma_*(R)$ and $\rho(R,z)$, thus neglecting the luminosity contribution of the bulge (see Appendix A), the stellar surface mass density profile is:

$$\Sigma_*(R) = \int_{-\infty}^{+\infty}\rho_*(R,z)dz = \Upsilon_\mathrm{d} I_\mathrm{d}(R) \ , \tag{4.6}$$

where $\rho(R,z) = \rho_*(R,z)$ is our disk model, namely the surface brightness profile $I_\mathrm{d}(R)$ multiplied by $\exp(-|z|/h_z)/(2h_z)$ (Appendix A.1). Thus, combining Eqs. (4.5), (4.6), and (4.4) yields:

$$\sigma_z^2(R) = \frac{1}{h_z}\int_0^{+\infty}\left[\int_z^{+\infty}\exp\left(-\frac{|z'|}{h_z}\right)\frac{\partial\phi(R,z')}{\partial z'}dz'\right]dz \ . \tag{4.7}$$

We model the two kinematic profiles, the rotation curve (Eq. (2.2)), and the vertical velocity dispersion profile (Eq. (4.7)), with the same MCMC algorithm illustrated in Sect. 4.1. We adopt the same priors of Sect. 4.1.

The MCMC analysis considers the two kinematic profiles at the same time. We thus define the single figure of merit,

$$\chi^2_{\mathrm{red,tot}}(\mathbf{x}) = \frac{\chi^2_\mathrm{RC}(\mathbf{x}) + \chi^2_\mathrm{VVD}(\mathbf{x})}{n_{\mathrm{dof,tot}}} \ , \tag{4.8}$$

where χ^2_RC is Eq. (4.2) multiplied by $n_{\mathrm{dof,RC}}$, and

$$\chi^2_\mathrm{VVD}(\mathbf{x}) = \sum_{j=1}^{N_\mathrm{VVD}}\frac{[\sigma_{z,\mathrm{mod}}(R_j,\mathbf{x}) - \sigma_{z,\mathrm{data}}(R_j)]^2}{\sigma^2_{z,\mathrm{data,err}}(R_j)} \tag{4.9}$$

is derived from the vertical velocity dispersion profile, with $N_{\rm VVD}$ the number of data points of the vertical velocity dispersion profile, $\sigma_{z,\rm data}$ the velocity dispersion measured at the projected distance R_j with their uncertainty $\sigma_{z,\rm data,err}$, and $\sigma_{z,\rm mod}$ the velocity dispersion model estimated with Eq. (4.7); finally $n_{\rm dof,tot} = N_{\rm RC} + N_{\rm VVD} - 5$ is the total number of degrees of freedom.

We estimate the vertical velocity dispersion error bars, $\sigma_{z,\rm data,err}$, by summing their random ($\sim 0.1 - 10$ km s^{-1}) and systematic ($\sim 1 - 10$ km s^{-1}) uncertainties in quadrature [324].

Figure 4.4 shows the posterior distributions for the same four galaxies shown in Fig. 4.1 for comparison. For the remaining galaxies, the posterior distributions are qualitatively similar. Because the posterior distributions show a single peak, we adopt the medians of the posterior distributions as our parameter estimates as in Sect. 4.1.

Table 4.2 lists the medians and the 15.9 and the 84.1 percentiles of the posterior distributions. We adopt these percentiles as the 1σ uncertainty range. The blue solid lines in the sub-panels (e) and (f) in Figs. E.1–E.7 in Appendix E show the model rotation curves and the vertical velocity dispersion profiles with the median parameters listed in Table 4.2. The red dots with error bars show the DMS data. As in Sect. 4.1, the features of the observed rotation curves are captured by the models in most cases although some discrepancies remain. Remarkably, the modelling of the rotation curves generally improves, like in UGC 1087, UGC 3997, and UGC 9837. Also in this case, the quality of the RG models does not present any trend either with the galaxy properties or with the radial coverage of the kinematic data.

The right panel of Fig. 4.3 shows that the disk-scale heights h_z required to model the rotation curves and the vertical velocity dispersion profiles are substantially smaller than the disk-scale heights $h_{z,\rm SR}$ derived from Eq. (A.12), suggested by the observations of edge-on galaxies. In sub-panels (f) of Figs. E.1–E.7, the cyan solid lines are the vertical velocity dispersion profiles when we adopt the parameters of Table 4.2 except for h_z replaced by $h_{z,\rm SR}$. Comparing the left and the right panels of Fig. 4.3 confirms that including the vertical velocity dispersion profiles in the modelling is responsible for requiring substantially thinner disks than $h_{z,\rm SR}$; in fact, modelling the rotation curves alone actually requires, sometimes, disks thicker than expected from Eq. (A.12).

This comparison supports the conclusion that the discrepancies between $h_{z,\rm RC+VVD}$ and $h_{z,\rm SR}$ are derived from the fact that the two scale heights are inferred from two different stellar populations: a younger stellar population dominating the observed vertical velocity dispersion, hence $h_{z,\rm RC+VVD}$, and an older stellar population dominating the surface brightness in the edge-on galaxy sample, hence $h_{z,\rm SR}$ [328].

The general agreement between our results and those found by [326] for MOND also confirms that, as anticipated in the introduction of this chapter, if this disagreement between $h_{z,\rm RC+VVD}$ and $h_{z,\rm SR}$ is derived from an overlooked observational bias, it does not suggest a possible tension between the data and the theory of gravity, either MOND or RG.

This observational bias in the vertical velocity dispersion measure brings on consequences for the estimate of the mass-to-light ratio. In fact, the velocity dispersion increases with the disk thickness and with the intensity of the gravitational field originated by the baryonic mass. By reducing the disk thickness, a larger mass must be attributed to the baryonic component to reproduce the observed velocity dispersion field. Therefore, our mass-to-light ratios are larger than the DMS values, as also occurs in MOND [326]. In fact, our mass-to-light ratios agree with the MOND ratios within 2σ for 29 out of 30 galaxies and within 2.13σ for UGC 11318.

Our estimated mass-to-light ratios are corroborated by the comparison with the SPS values (Sect. 4.1). The right panel of Fig. 4.2 compares the mass-to-light ratios required to model the rotation curves and the vertical velocity dispersion profiles with the mass-to-light ratios derived from the SPS model. The RG mass-to-light ratios span the same

range ($\sim 0.3 - 1.2\ M_\odot/L_\odot$) as the RG ratio derived by modelling the rotation curve alone (left panel of Fig. 4.2), which nearly coincides with the range covered by the mass-to-light ratios derived from the SPS models. For each individual galaxy, our estimated mass-to-light ratio agrees with the mass-to-light ratio derived from the SPS model most of the time: for 20 out of 29 galaxies, the two values agree within 2σ; for six galaxies, they agree within 2 to 3σ; and for the remaining three galaxies, they are consistent within 3 to 5σ. The largest discrepancy, 4.6σ, occurs for UGC 1908; this discrepancy is smaller, however, than the 6.7σ discrepancy found in Sect. 4.1 with the modelling of the rotation curve alone.

On the contrary, for 70% of the galaxy sample, the mass-to-light ratios estimated by the DMS collaboration are at least a factor of 2 smaller than the SPS values and their disks turn out to be sub-maximal [326, 328]. Despite these discrepancies, the large error bars associated with the DMS mass-to-light ratios make them agree within 3σ with the SPS values (see Table 1 of [326]).

To test RG, we have modeled the rotation curves alone and the rotation curves and the vertical velocity dispersion profiles at the same time, for each DMS galaxy. Instead, we have not considered the only vertical velocity dispersion profiles, which is an additional consistency check that should be taken into account in future works. However, given the limited radial extension of the vertical velocity dispersion profiles that in some cases cover regions of densities above ρ_c, this kinematic piece of information would not be so relevant to constrain the property of the theory. Indeed, we can see by comparing the values of Tables 4.1 and 4.2 that the RG parameters are weakly affected by the introduction of the vertical velocity dispersions in the modelling.

4.2.1 The observational bias in the vertical velocity dispersion profile

As mentioned above, the estimate of the vertical velocity dispersion profile is likely to be affected by an observational bias. Therefore, the disk thickness obtained by modelling this profile might give a severe underestimation of the real value. Here, we want to quantify how correcting the vertical velocity dispersions by an appropriate factor can give disk thicknesses that are consistent with the observations of edge-on galaxies and with mass-to-light ratios still consistent with the SPS models.

Aniyan and coauthors [328] model what we would observe in the disk of a typical external face-on galaxy by selecting a sample of giant stars simulated in the Milky Way from the on-line Besançon model [341]. This model describes the main structural components and stellar populations of the Milky Way and includes recipes for galactic reddening, star formation history, and dynamical evolution [341, 328]. For their simulated star sample, Aniyan and collaborators [328] choose giant stars of spectral type G8III - K5III, with luminosity in the range of $-3 \leq M_V \leq +3$, and colour in the range of $0.8 \leq B - V \leq 1.8$, within a cylindric volume, centred on the Sun and perpendicular to the Galactic disk, of radius 2 kpc and height 10 kpc. They assume a star formation and a dynamical history similar to the solar neighbourhood.

From the simulated sample, they extract the vertical velocity dispersion integrated vertically through the disk by considering either the entire stellar population (σ_1) or the dynamically hotter and older giant component alone (σ_2). They estimate that $\eta = \sigma_2/\sigma_1 = 1.55 \pm 0.02$. Now, observationally, the disk-scale heights are inferred from measures of the surface brightness that is dominated by the old hot giants, which have a larger vertical velocity dispersion, whereas the younger stellar population mostly contributes to the spectral signal used to derive the observed velocity dispersion. Therefore, according to the result of [328], assuming a single stellar population to interpret the vertical velocity dispersions and the disk-scale height at the same time introduces a bias that originates an underestimate of the disk thickness.

Here, we estimate this observational bias with the ratio between the expected vertical

Table 4.2: Parameters estimated from the rotation curves and the vertical velocity dispersion profiles.

UGC	$\Upsilon\ \left[\frac{M_\odot}{L_\odot}\right]$	$\Upsilon_{SPS}\ \left[\frac{M_\odot}{L_\odot}\right]$	$\frac{\Upsilon_{fit}-\Upsilon_{SPS}}{\sqrt{\sigma^2_{\Upsilon_{fit}}+\sigma^2_{\Upsilon_{SPS}}}}$	h_z [kpc]	$\frac{h_z}{h_{z,SR}}$	ϵ_0	Q	$\log_{10}\left(\rho_c\ \left[\frac{g}{cm^3}\right]\right)$	$\chi^2_{red,tot}$
(1)	(2)	(3)	(4)	(5)	(6)	(7)	(8)	(9)	(10)
448	$0.94^{+0.08}_{-0.20}$	$0.64^{+0.07}_{-0.00}$	+2.06	$0.22^{+0.06}_{-0.05}$	0.48	$0.60^{+0.26}_{-0.37}$	$0.57^{+0.72}_{-0.51}$	$-25.82^{+1.07}_{-0.80}$	5.32
463	$0.56^{+0.04}_{-0.06}$	$0.64^{+0.07}_{-0.00}$	−1.25	$0.25^{+0.07}_{-0.07}$	0.54	$0.90^{+0.07}_{-0.12}$	$1.09^{+0.60}_{-0.70}$	$-25.07^{+1.29}_{-1.42}$	6.71
1081	$0.66^{+0.13}_{-0.15}$	$0.52^{+0.10}_{-0.00}$	+0.94	$0.24^{+0.06}_{-0.05}$	0.62	$0.53^{+0.19}_{-0.15}$	$0.92^{+0.76}_{-0.59}$	$-24.54^{+1.02}_{-1.57}$	8.38
1087	$0.81^{+0.11}_{-0.14}$	$0.58^{+0.08}_{-0.00}$	+1.69	$0.19^{+0.04}_{-0.03}$	0.49	$0.52^{+0.14}_{-0.13}$	$0.85^{+0.63}_{-0.67}$	$-25.53^{+1.20}_{-0.91}$	3.53
1529	$0.80^{+0.08}_{-0.10}$	$0.70^{+0.08}_{-0.00}$	+1.02	$0.24^{+0.06}_{-0.05}$	0.55	$0.74^{+0.09}_{-0.07}$	$1.11^{+0.55}_{-0.75}$	$-25.02^{+0.96}_{-1.35}$	16.35
1635	$0.75^{+0.12}_{-0.09}$	$0.61^{+0.07}_{-0.00}$	+1.20	$0.11^{+0.02}_{-0.02}$	0.27	$0.66^{+0.18}_{-0.14}$	$0.76^{+0.59}_{-0.51}$	$-25.39^{+1.68}_{-1.29}$	4.91
1862	$1.01^{+0.19}_{-0.24}$	$0.52^{+0.10}_{-0.00}$	+2.17	$0.13^{+0.04}_{-0.03}$	0.50	$0.46^{+0.22}_{-0.17}$	$0.84^{+0.74}_{-0.65}$	$-24.28^{+0.94}_{-1.68}$	6.23
1908	$0.34^{+0.05}_{-0.06}$	$0.67^{+0.07}_{-0.00}$	−4.57	$0.50^{+0.09}_{-0.09}$	0.93	$0.37^{+0.09}_{-0.09}$	$0.59^{+0.71}_{-0.32}$	$-25.51^{+0.84}_{-0.98}$	16.91
3091	$0.74^{+0.15}_{-0.16}$	$0.48^{+0.10}_{-0.00}$	+1.55	$0.15^{+0.03}_{-0.02}$	0.36	$0.53^{+0.18}_{-0.14}$	$0.82^{+0.80}_{-0.66}$	$-24.86^{+1.22}_{-1.58}$	2.82
3140	$0.75^{+0.06}_{-0.06}$	$0.64^{+0.07}_{-0.00}$	+1.53	$0.28^{+0.04}_{-0.04}$	0.67	$0.78^{+0.13}_{-0.15}$	$0.76^{+0.74}_{-0.56}$	$-25.91^{+1.52}_{-0.83}$	8.90
3701	$0.73^{+0.28}_{-0.23}$	$0.45^{+0.11}_{-0.00}$	+1.05	$0.25^{+0.09}_{-0.07}$	0.58	$0.26^{+0.09}_{-0.07}$	$0.78^{+0.79}_{-0.45}$	$-24.15^{+0.64}_{-1.10}$	2.09
3997	$0.97^{+0.31}_{-0.23}$	-	-	$0.18^{+0.06}_{-0.05}$	0.31	$0.47^{+0.17}_{-0.11}$	$1.27^{+0.51}_{-0.66}$	$-23.68^{+0.48}_{-1.39}$	13.63
4036	$0.72^{+0.09}_{-0.10}$	$0.50^{+0.10}_{-0.00}$	+1.97	$0.26^{+0.05}_{-0.05}$	0.63	$0.58^{+0.19}_{-0.13}$	$0.97^{+0.67}_{-0.68}$	$-25.94^{+1.03}_{-0.78}$	5.20
4107	$0.77^{+0.08}_{-0.10}$	$0.58^{+0.08}_{-0.00}$	+1.93	$0.16^{+0.03}_{-0.03}$	0.38	$0.78^{+0.14}_{-0.14}$	$0.62^{+0.82}_{-0.49}$	$-25.45^{+1.82}_{-1.12}$	5.84
4256	$0.29^{+0.08}_{-0.09}$	$0.52^{+0.10}_{-0.00}$	−2.23	$0.35^{+0.10}_{-0.07}$	0.71	$0.37^{+0.13}_{-0.11}$	$0.99^{+0.65}_{-0.64}$	$-25.99^{+0.74}_{-0.63}$	2.10
4368	$0.88^{+0.13}_{-0.17}$	$0.45^{+0.11}_{-0.00}$	+2.66	$0.42^{+0.17}_{-0.16}$	1.17	$0.43^{+0.07}_{-0.07}$	$0.84^{+0.78}_{-0.52}$	$-26.05^{+0.72}_{-0.64}$	9.20
4380	$0.79^{+0.11}_{-0.09}$	$0.52^{+0.10}_{-0.00}$	+2.41	$0.24^{+0.04}_{-0.04}$	0.44	$0.54^{+0.18}_{-0.15}$	$0.28^{+0.92}_{-0.20}$	$-25.98^{+1.27}_{-0.73}$	8.40
4458	$0.53^{+0.03}_{-0.03}$	$0.85^{+0.09}_{-0.06}$	−3.75	$0.86^{+0.48}_{-0.30}$	1.08	$0.77^{+0.15}_{-0.22}$	$1.02^{+0.64}_{-0.72}$	$-26.08^{+1.24}_{-0.73}$	3.08
4555	$0.88^{+0.10}_{-0.14}$	$0.48^{+0.10}_{-0.00}$	+3.08	$0.19^{+0.09}_{-0.06}$	0.45	$0.89^{+0.09}_{-0.10}$	$0.89^{+0.89}_{-0.60}$	$-25.33^{+1.69}_{-0.89}$	11.55
4622	$0.71^{+0.14}_{-0.14}$	$0.55^{+0.09}_{-0.00}$	+1.08	$0.37^{+0.12}_{-0.09}$	0.53	$0.58^{+0.17}_{-0.12}$	$1.30^{+0.47}_{-0.53}$	$-25.14^{+1.05}_{-1.15}$	6.06
6903	$0.61^{+0.19}_{-0.27}$	$0.52^{+0.10}_{-0.00}$	+0.38	$0.10^{+0.07}_{-0.03}$	0.18	$0.33^{+0.14}_{-0.10}$	$1.11^{+0.84}_{-0.57}$	$-25.04^{+1.38}_{-0.58}$	8.47
6918	$0.35^{+0.06}_{-0.06}$	$0.52^{+0.10}_{-0.00}$	−2.18	$0.21^{+0.07}_{-0.06}$	1.00	$0.42^{+0.15}_{-0.12}$	$0.96^{+0.66}_{-0.59}$	$-25.71^{+0.99}_{-0.79}$	4.10
7244	$0.51^{+0.14}_{-0.16}$	$0.41^{+0.12}_{-0.00}$	+0.62	$0.37^{+0.10}_{-0.08}$	0.86	$0.22^{+0.07}_{-0.06}$	$0.85^{+0.64}_{-0.49}$	$-25.17^{+0.75}_{-1.16}$	3.41
7917	$0.80^{+0.09}_{-0.12}$	$0.81^{+0.09}_{-0.04}$	−0.08	$0.44^{+0.14}_{-0.11}$	0.64	$0.81^{+0.14}_{-0.19}$	$1.01^{+0.61}_{-0.74}$	$-25.86^{+1.02}_{-0.76}$	4.60
8196	$0.70^{+0.05}_{-0.05}$	$0.77^{+0.08}_{-0.03}$	−0.90	$1.15^{+0.25}_{-0.20}$	1.98	$0.43^{+0.17}_{-0.13}$	$1.07^{+0.60}_{-0.60}$	$-26.17^{+0.63}_{-0.56}$	12.51
9177	$0.86^{+0.23}_{-0.20}$	$0.43^{+0.11}_{-0.00}$	+1.89	$0.36^{+0.11}_{-0.12}$	0.53	$0.55^{+0.20}_{-0.10}$	$1.25^{+0.51}_{-0.62}$	$-24.65^{+1.05}_{-1.78}$	6.39
9837	$0.76^{+0.13}_{-0.10}$	$0.64^{+0.07}_{-0.00}$	+0.95	$0.18^{+0.05}_{-0.07}$	0.30	$0.35^{+0.06}_{-0.04}$	$1.11^{+0.54}_{-0.41}$	$-23.57^{+0.29}_{-0.16}$	3.24
9965	$0.66^{+0.07}_{-0.08}$	$0.50^{+0.10}_{-0.00}$	+1.70	$0.19^{+0.04}_{-0.03}$	0.44	$0.75^{+0.15}_{-0.17}$	$0.88^{+0.56}_{-0.60}$	$-25.67^{+1.32}_{-0.85}$	2.21
11318	$0.65^{+0.07}_{-0.07}$	$0.67^{+0.07}_{-0.00}$	−0.25	$0.36^{+0.05}_{-0.04}$	0.71	$0.72^{+0.17}_{-0.29}$	$1.37^{+0.44}_{-0.65}$	$-25.68^{+0.81}_{-0.96}$	37.53
12391	$0.60^{+0.08}_{-0.13}$	$0.50^{+0.10}_{-0.00}$	+0.83	$0.37^{+0.08}_{-0.07}$	0.82	$0.39^{+0.09}_{-0.12}$	$0.61^{+0.71}_{-0.42}$	$-25.67^{+0.99}_{-0.83}$	8.02

Column 1: UGC number; Cols. 2, 5, 7, 8, 9: medians of the posterior distributions of the model parameters estimated from the rotation curves and the vertical velocity dispersion profiles; Col. 3: mass-to-light ratio derived with the SPS model; Col. 10: $\chi^2_{red,tot}$ (Eq. 4.8).

velocity dispersions computed with the parameters inferred from the rotation curves alone (Table 4.1) and the measured vertical velocity dispersion profiles. We adopt the following procedure: (1) for each galaxy, we use Eq. (4.7) to compute the expected vertical velocity dispersion, according to the parameters of Table 4.1; (2) at each radial coordinate, we compute the ratio between the expected and the measured vertical velocity dispersions and we estimate the mean of these ratios along the radial profile of each of the 30 galaxies; (3) we then estimate the mean, η', of these 30 means and their standard deviation. Thus, we obtain $\eta' = 1.63 \pm 0.65$, which agrees within 0.12σ with the value 1.55 ± 0.02 found by [328].

To quantify the effect of this bias on the estimate of the disk thickness, we now repeat the analysis presented in Sect. 4.2 for five galaxies where we artificially increase the vertical velocity dispersion profile by a factor of 1.63. We choose five galaxies with a h_z-to-$h_{z,SR}$ ratio smaller than 0.5: UGC 1635, UGC 3091, UGC 4107, UGC 4555, and UGC 9965. We also model the kinematics of these galaxies in MOND where, as free parameters, we only have the galactic parameters Υ and h_z. For the MCMC analysis, we use the same priors as above.

To model the galaxies in MOND, we derive the MOND potential by solving the Poisson equation in the QUMOND formulation of MOND [243]:

$$\nabla^2\phi = \nabla\cdot\left[\nu\left(\frac{|\nabla\phi_N|}{a_0}\right)\nabla\phi_N\right], \tag{4.10}$$

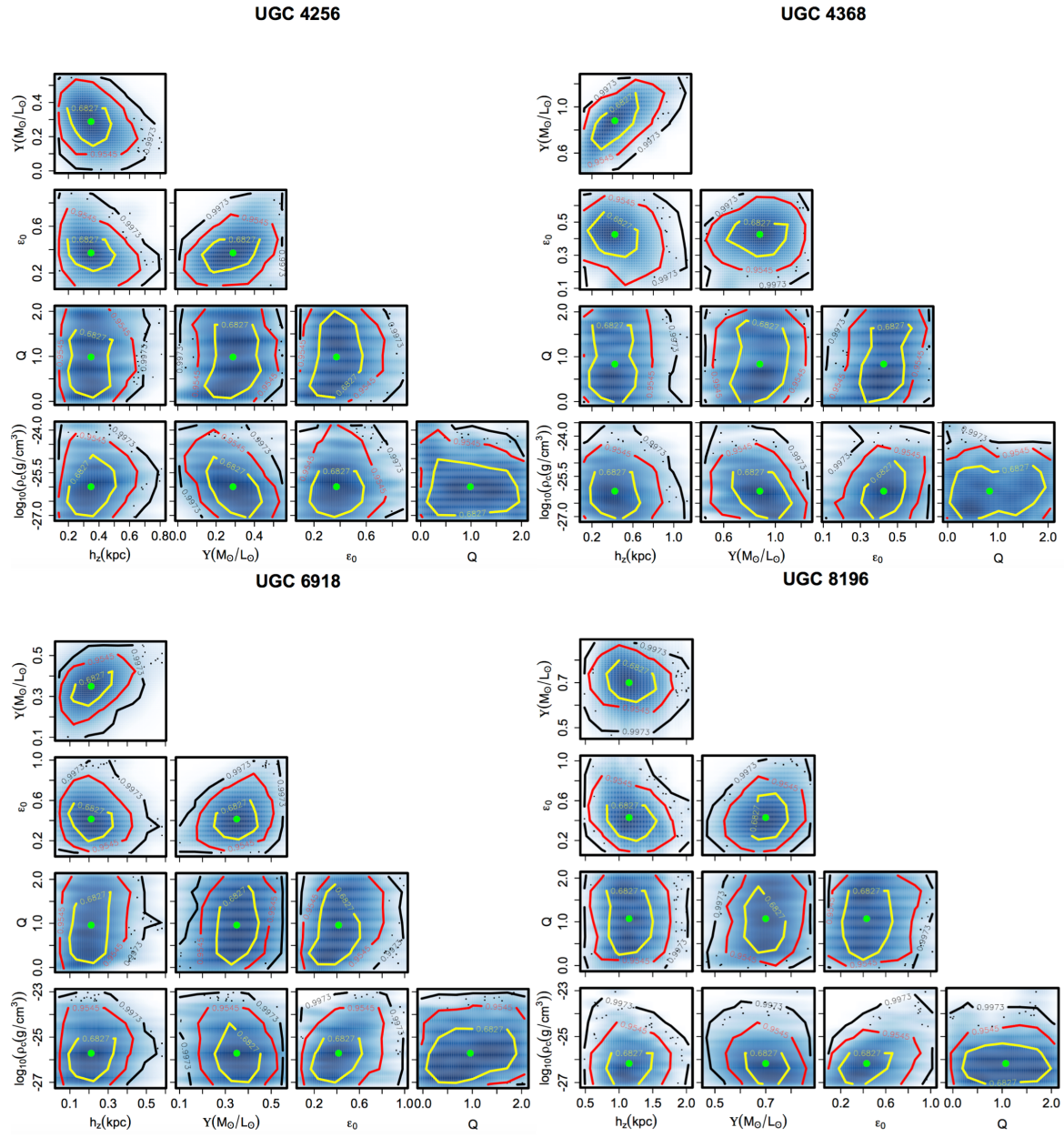

Figure 4.4: Four examples of posterior distributions of the two galaxy parameters and of the three RG parameters estimated from the rotation curves and the vertical velocity dispersion profiles at the same time. The green dots locate the median values and the yellow, red and black contours show the 1σ, 2σ and 3σ levels, respectively.

where $\phi_{\rm N}$ is the Newtonian potential, $a_0 = 1.2\times10^{-10}$ m s^{-2} $= 3600$ kpc^{-1} (km s^{-1})^2 is the MOND critical acceleration, and ν is the interpolating function regulating the transition between the Newtonian and the MOND regimes. We use the 'simple ν-function' [54, 326],

$$\nu(y) = \frac{1}{2}\left(1+\sqrt{1+\frac{4}{y}}\right) \ . \tag{4.11}$$

Tables 4.3 and 4.4 list the medians and percentile ranges of the posterior distributions in RG and QUMOND, respectively. As expected, h_z increases by a factor between 2.07 (found for UGC 3091 in QUMOND) and 2.89 (found for UGC 4555 in QUMOND) with respect to the values obtained in Sect. 4.2 (see Tables 4.2, 4.3, and 4.4). For UGC 1635 and UGC 3091, the disk-scale heights are still smaller than the values expected from the observations of edge-on galaxies, but their h_z-to-$h_{z,\rm SR}$ ratios still increase to values greater than 0.5.

The agreement between the RG mass-to-light ratios estimated in the current section

and the SPS values worsens compared to Sect. 4.2, but for four out of five galaxies, it is within 4σ. QUMOND mass-to-light ratios tend to be closer to the SPS values than the RG mass-to-light ratios: their agreement with their SPS expectations is within 3σ for four out of five galaxies. However, since the QUMOND mass-to-light ratios uncertainties are smaller than in RG, the agreement between the QUMOND mass-to-light ratios and the SPS values is formally worse than in RG for two out of five galaxies (UGC 1635 and UGC 3091).

The sub-panels (i)-(l) of Figs. E.6–E.7 in Appendix E show the RG and QUMOND models of the rotation curves and vertical velocity dispersion profiles (blue solid lines). The vertical velocity dispersion data are increased by the factor 1.63 (red dots with error bars). RG describes the rotation curves slightly better than QUMOND whereas both theories describe the vertical velocity dispersion profiles equally well. Clearly, this better performance of RG follows from the version of RG we adopt at this stage that, for each galaxy, has three more free parameters than QUMOND.

Our QUMOND results of these five galaxies are comparable to the results of [326]. Specifically, we also find that the QUMOND rotation curves of UGC 3091 and UGC 9965 properly describe the data, whereas the QUMOND rotation curves of UGC 1635, UGC 4107 and UGC 4555 tend to underestimate the inner profile and to overestimate the outer profile. Our vertical velocity dispersions are also comparable to [326], although their models slightly uderestimate the most inner data point of UGC 1635 and UGC 3091.

Figure 4.5 compares the parameters estimated with RG with the original values of the vertical velocity dispersion profile, $\sigma_z(R)$ (Sect. 4.2), with the parameters obtained with $\sigma_z(R)$ increased by the factor of 1.63. These figures show that the three RG parameters are not systematically affected by the increase of $\sigma_z(R)$, whereas both Υ and h_z tend to be larger. Figure 4.6 compares Υ and h_z obtained in RG and QUMOND with the $\sigma_z(R)$ values increased by the factor 1.63. The disk-scale heights are comparable in the two theories of gravity whereas the mass-to-light ratios in RG are systematically larger than in QUMOND. This systematic difference will be relevant in describing the RAR we illustrate in Sect. 4.4.

Table 4.3: Parameters estimated in RG from the rotation curves and the vertical velocity dispersion profiles increased by the factor 1.63.

UGC	$\Upsilon\ \left[\frac{M_\odot}{L_\odot}\right]$	$\Upsilon_{SPS}\ \left[\frac{M_\odot}{L_\odot}\right]$	$\frac{\Upsilon_{fit}-\Upsilon_{SPS}}{\sqrt{\sigma^2_{\Upsilon_{fit}}+\sigma^2_{\Upsilon_{SPS}}}}$	h_z [kpc]	$\frac{h_z}{h_{z,SR}}$	ϵ_0	Q	$\log_{10}\left(\rho_c\ \left[\frac{g}{cm^3}\right]\right)$	$\chi^2_{red,tot}$
(1)	(2)	(3)	(4)	(5)	(6)	(7)	(8)	(9)	(10)
1635	$0.82^{+0.15}_{-0.14}$	$0.61^{+0.07}_{-0.00}$	+1.35	$0.27^{+0.05}_{-0.04}$	0.66	$0.56^{+0.11}_{-0.13}$	$1.11^{+0.65}_{-0.69}$	$-23.58^{+0.39}_{-0.86}$	5.66
3091	$0.94^{+0.18}_{-0.21}$	$0.48^{+0.10}_{-0.00}$	+2.23	$0.33^{+0.04}_{-0.05}$	0.79	$0.56^{+0.13}_{-0.12}$	$0.99^{+0.70}_{-0.67}$	$-23.82^{+0.63}_{-1.60}$	5.07
4107	$0.96^{+0.09}_{-0.16}$	$0.58^{+0.08}_{-0.00}$	+2.79	$0.41^{+0.07}_{-0.08}$	0.98	$0.78^{+0.14}_{-0.22}$	$0.99^{+0.69}_{-0.84}$	$-24.82^{+1.49}_{-1.59}$	7.82
4555	$1.07^{+0.08}_{-0.11}$	$0.48^{+0.10}_{-0.00}$	+5.28	$0.52^{+0.16}_{-0.14}$	1.24	$0.88^{+0.08}_{-0.16}$	$0.88^{+0.70}_{-0.77}$	$-25.10^{+1.47}_{-1.21}$	13.77
9965	$0.88^{+0.07}_{-0.10}$	$0.50^{+0.10}_{-0.00}$	+3.69	$0.48^{+0.08}_{-0.06}$	1.12	$0.68^{+0.21}_{-0.23}$	$0.77^{+0.81}_{-0.59}$	$-25.88^{+1.24}_{-0.83}$	4.42

Column 1: UGC number; Cols. 2, 5, 7, 8, 9: medians of the posterior distributions of the parameters estimated simultaneously, in RG, from the observed rotation curves and the vertical velocity dispersion profiles increased by the factor 1.63; Col. 3: mass-to-light ratio derived with the SPS model; Col. 10: $\chi^2_{red,tot}$ (Eq. 4.8).

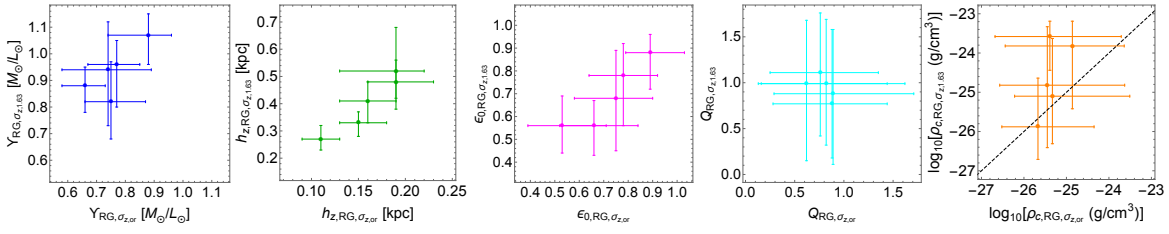

Figure 4.5: Comparison between the parameters estimated with RG from the two kinematic profiles of five DMS galaxies with the original values of $\sigma_z(R)$ (Sect. 4.2) and the parameters estimated with RG from the two kinematic profiles with $\sigma_z(R)$ increased by the factor 1.63 (Sect. 4.2.1). The black dashed lines show the lines of equality.

Table 4.4: Parameters estimated in QUMOND from the rotation curves and the vertical velocity dispersion profiles increased by the factor 1.63.

UGC	$\Upsilon\ \left[\frac{M_\odot}{L_\odot}\right]$	$\Upsilon_{SPS}\ \left[\frac{M_\odot}{L_\odot}\right]$	$\frac{\Upsilon_{fit}-\Upsilon_{SPS}}{\sqrt{\sigma^2_{\Upsilon_{fit}}+\sigma^2_{\Upsilon_{SPS}}}}$	h_z [kpc]	$\frac{h_z}{h_{z,SR}}$	$\chi^2_{red,tot}$
(1)	(2)	(3)	(4)	(5)	(6)	(7)
1635	$0.70^{+0.04}_{-0.05}$	$0.61^{+0.07}_{-0.00}$	+1.41	$0.26^{+0.04}_{-0.04}$	0.63	7.58
3091	$0.73^{+0.04}_{-0.04}$	$0.48^{+0.10}_{-0.00}$	+3.90	$0.31^{+0.05}_{-0.05}$	0.74	6.09
4107	$0.60^{+0.04}_{-0.04}$	$0.58^{+0.08}_{-0.00}$	+0.35	$0.42^{+0.08}_{-0.07}$	1.00	12.91
4555	$0.62^{+0.04}_{-0.03}$	$0.48^{+0.10}_{-0.00}$	+2.19	$0.55^{+0.19}_{-0.15}$	1.31	27.83
9965	$0.52^{+0.04}_{-0.04}$	$0.50^{+0.10}_{-0.00}$	+0.31	$0.45^{+0.06}_{-0.05}$	1.05	5.74

Column 1: UGC number; Cols. 2, 5: medians of the posterior distributions of the parameters estimated simultaneously, in QUMOND, from the observed rotation curves and the vertical velocity dispersion profiles increased by the factor 1.63; Col. 3: mass-to-light ratio derived with the SPS model; Col. 7: $\chi^2_{red,tot}$ (Eq. 4.8), with $n_{dof,tot} = N_{RC} + N_{VVD} - 2$ degrees of freedom.

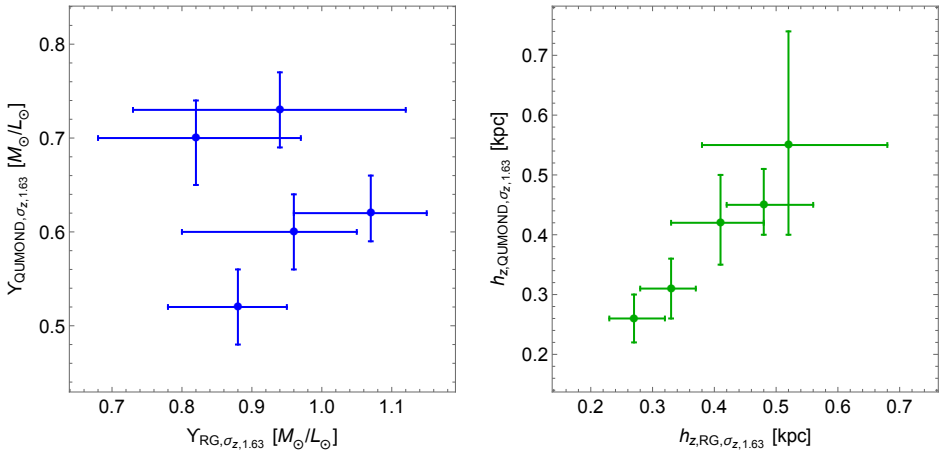

Figure 4.6: Comparison between the RG and QUMOND Υ and h_z estimated from the two kinematic profiles of five DMS galaxies where $\sigma_z(R)$ is increased by the factor 1.63 (Sect. 4.2.1). The black dashed lines show the lines of equality.

4.2.2 On the error bars of the rotation curves

We conclude this section with a digression on the rotation curve error bars. In their modelling of the DMS data with MOND, rather than maintaining the original DMS error bars as we do here, [326] arbitrarily increase the error bars from $\sim 1-5$ km s^{-1} to 10 km s^{-1}. Angus and coauthors [326] were concerned by the possibility that disk warping could introduce systematic errors which can indeed affect the rotation curves; by this approach, Angus and coauthors [326] clearly intend to increase the statistical weight of the vertical velocity dispersion profiles which are more dependent on the disk thickness.

We verified that this modification is in fact unnecessary. By setting the rotation curves error bars to 10 km s^{-1} and performing once again the MCMC analysis described above, we find that the new disk-scale heights, h_z, substantially agree with our original results: the distributions of the ratios between the new and the original h_z is peaked around $\sim$1, with median $1.09^{+0.11}_{-0.20}$, where the uncertainties are the 15.9 and 84.1 percentiles. Similarly, the mass-to-light ratios remain unbiased, with their ratios between the new and the original values having median $0.95^{+0.09}_{-0.11}$.

4.3 A universal combination of the RG parameters

In the formulation of RG, ϵ_0, Q and ρ_c are universal parameters. Here we show that, in principle, a single set of these parameters could indeed be able to model the dynamics of our entire sample of disk galaxies.

For this task, the ideal approach would be to use the MCMC algorithm to explore the

63-dimensional space of these three RG parameters and the 2×30 parameters describing the galaxies, namely the mass-to-light ratios Υ and the disk-scale heights h_z. However, this approach requires an extraordinary computational effort which, at this stage of our investigation of the RG viability, appears unreasonably large.

We prefer a simpler strategy. Our analyses above show that modelling each individual galaxy by keeping the three RG parameters free returns values of these parameters that are roughly consistent from galaxy to galaxy. In fact, the ϵ_0, Q and $\log_{10}\rho_\mathrm{c}$ values listed in Table 4.2, whose distributions are shown in Fig. 4.7, have mean and standard deviations $\epsilon_0 = 0.56 \pm 0.19$, $Q = 0.92 \pm 0.24$, and $\log_{10}[\rho_\mathrm{c}\,(\mathrm{g/cm^3})] = -25.30 \pm 0.70$. These standard deviations are either smaller than or comparable to the mean uncertainties of the values listed in Table 4.2, which are 0.16, 0.71, and 1.22, for ϵ_0, Q and $\log_{10}\rho_\mathrm{c}$, respectively. We can thus reasonably conclude that the different values that we find for different galaxies can in principle be ascribed to statistical fluctuations.

Therefore, to check whether a single set of RG parameters could be able to describe the entire galaxy sample, rather than performing the computationally demanding exploration of the 63-dimensional parameter space, we assume that the values of the mass-to-light ratios Υ and the disk-scale heights h_z for each galaxy, estimated in our previous analysis, are appropriate, and we only explore the 3-dimensional space of the parameters ϵ_0, Q and $\log_{10}\rho_\mathrm{c}$ for the entire galaxy sample at the same time.

We adopt the priors for the three RG parameters as in Sects. 4.1 and 4.2. The figure of merit is now:

$$\chi^2_\mathrm{red}(\mathbf{x}) = \sum_{i=1}^{N_\mathrm{gal}} \chi^2_{\mathrm{red,tot},i}(\mathbf{x}) \;, \tag{4.12}$$

where $\mathbf{x} = (\epsilon_0, Q, \log_{10}\rho_\mathrm{c})$, N_gal is the number of DMS galaxies and $\chi^2_{\mathrm{red,tot},i}(\mathbf{x})$ is Eq. (4.8) where the number of free parameters is now equal to three instead of five.

As in Sects. 4.1 and 4.2, we run the MCMC for 19000 steps in addition to the 1000 burn-in steps.[4] To better assess the convergence of the chains, we run three chains with three different starting points and we test their convergence with the variance ratio method of Gelman and Rubin [344], described in Appendix D. We find that 13000 steps are already sufficient to have the chains converging. We also test that each chain converges according to the Geweke diagnostic [334].

Figure 4.8 shows the posterior distributions of the three parameters. The green dots show the median values, and the yellow, red, and black curves show the 1, 2, and 3σ contour levels. The medians and 68% confidence intervals are $\epsilon_0 = 0.661^{+0.007}_{-0.007}$, $Q = 1.79^{+0.14}_{-0.26}$ and $\log_{10}\rho_\mathrm{c} = -24.54^{+0.08}_{-0.07}$. The purple points show the means of the three distributions shown in Fig. 4.7; the error bars show the mean errors listed in Table 4.2.

As expected, the posterior distributions in Fig. 4.8 show that considering all the DMS galaxies at the same time provides much tighter constraints on the RG parameters than in our previous analyses. Because of the large errors found in Sect. 4.2, the universal parameters estimated here are consistent with our previous analyses: the means of the distributions of Fig. 4.7 agree within 0.63, 1.19 and 0.62σ with the medians, found here, of ϵ_0, Q and $\log_{10}\rho_\mathrm{c}$, respectively.

However, the agreement between the data and the models of the rotation curves and the vertical velocity dispersion profiles derived with the mass-to-light ratios and disk-scale heights listed in Table 4.2 and the universal combination of RG parameters found here worsens with respect to the agreement obtained with the individual RG parameters found in Sect. 4.2 as shown in sub-panels (g) and (h) of Figs. E.1–E.7. Figure 4.9 compares the reduced χ^2 found in Sect. 4.2 with the reduced χ^2 found here. Despite the presence of a

[4] To explore the parameter space, we consider all the galaxies at the same time and we thus need to run the Poisson solver 2×30 times at each MCMC iteration. To reduce the computational effort, we parallelised our code with OpenMP, an application programming interface, which supports multiplatform shared memory multiprocessing programming in different languages. The C++ code we used, named astroMP, is publicly available at `https://github.com/alpha-unito/astroMP` and it is described in [342] and [343]. We report the description and the scaling properties of this code in Appendix C.2.

number of galaxies whose χ^2 substantially increases, the bulk of the sample maintains its χ^2 close to, albeit still larger than, the original χ^2.

The increase of the χ^2 compared to Sect. 4.2 is mainly due to the rotation curves. In fact, all the vertical velocity dispersion profiles are rather well interpolated with this universal combination of RG parameters: their χ^2 are close to those of Sect. 4.2, except for a few outliers, like UGC 3701 and UGC 3997. On the contrary, the rotation curves of only about half of the sample are still well described with this unique combination of RG parameters (e.g. UGC 1081, UGC 1635, UGC 4036, UGC 4380 and UGC 9965), whereas the models worsen for the remaining sample.

The good agreement of this universal combination of RG parameters with the parameters of Sect. 4.2 and the somewhat limited worsening of the χ^2 shown in Fig. 4.9 suggest that finding a unique set of RG parameters that accurately describes the kinematics of the DMS galaxies might be feasible. This simple exercise in fact appears to indicate that properly exploring the full 63-dimensional parameter space might return substantially smaller χ^2 with still reasonable, albeit different from the results of Sect. 4.2, mass-to-light ratios and disk-scale heights of the galaxies. We might also expect that the unique set of RG parameters will be statistically equivalent to the set we find here.

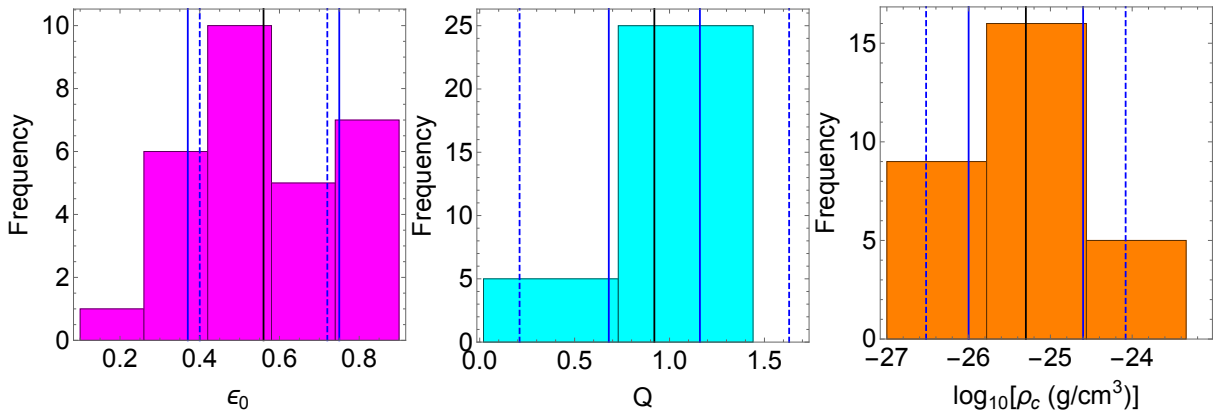

Figure 4.7: Distributions of the three RG parameters ϵ_0, Q, and $\log_{10}\rho_c$ listed in Table 4.2. The bin sizes are of the order of the mean uncertainties. The means of the distributions are shown as black solid lines; the two blue solid lines show the standard deviations of the distributions; the two blue dashed lines show the mean uncertainties of the parameters listed in Table 4.2.

4.4 The Radial Acceleration Relation

To test the viability of RG as a gravity theory describing the dynamics of disk galaxies, we need to consider an additional relevant observational piece of evidence that very clearly quantifies the mass discrepancy on galaxy scales: the RAR. McGaugh et al. [44] and Lelli et al. [246] pointed out that the observed centripetal acceleration traced by the rotation curves,

$$g_{\rm obs}(R) = v^2_{\rm obs}(R)/R\ , \tag{4.13}$$

is tightly correlated with the Newtonian acceleration $g_{\rm bar}(R)$ due to the baryonic matter distribution alone.

McGaugh et al. [44] found that the function:

$$g_{\rm obs}(R) = \frac{g_{\rm bar}(R)}{1-\exp\left(-\sqrt{\frac{g_{\rm bar}(R)}{g_\dagger}}\right)} \tag{4.14}$$

provides a good fit for the entire SPARC sample, made of 153 galaxies [345]. The fit has only one free parameter $g_\dagger$ whose single value $g_\dagger = 1.20 \pm 0.02$ (random) ± 0.24

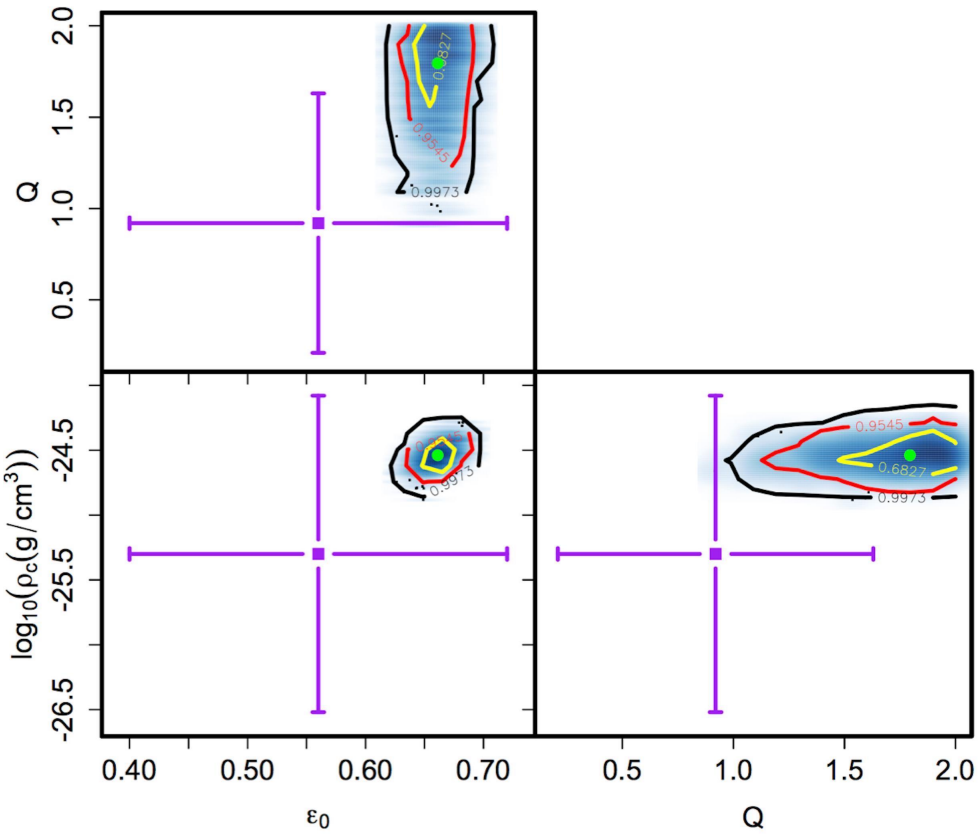

Figure 4.8: Posterior distributions of the three RG parameters. The green dots locate the median values and the yellow, red, and black contours show the 1σ, 2σ, and 3σ levels, respectively. The purple points and error bars show the means of the distributions of the RG parameters and their mean uncertainties found in Sect. 4.2 and reported in Fig. 4.7.

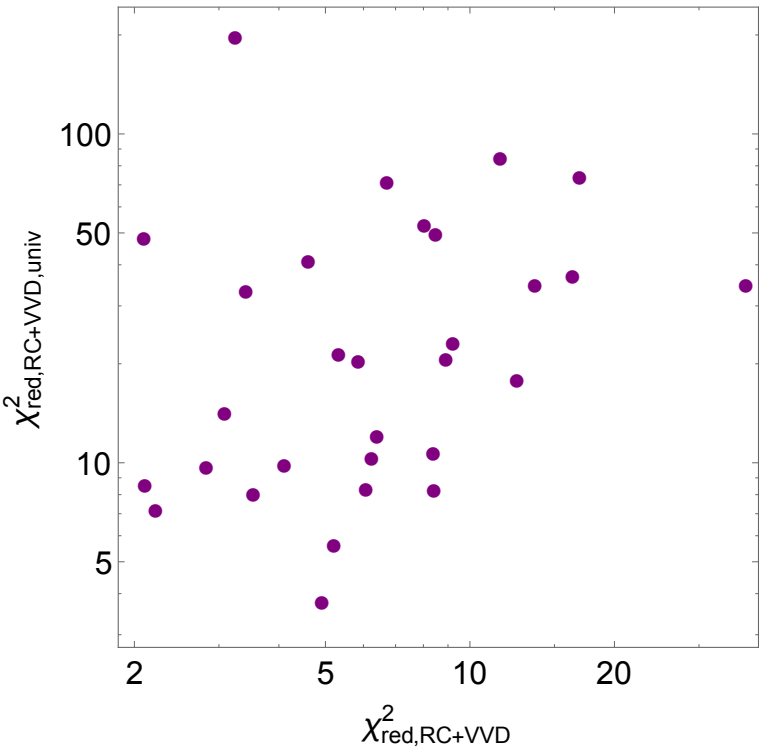

Figure 4.9: Comparison between the reduced χ^2 (Eq. 4.8) for each galaxy by adopting the universal (Sect. 4.3) or the individual (Sect. 4.2, Table 4.2) set of the RG parameters. The one-to-one line is shown as a black dashed line, for comparison.

(systematic) $\times 10^{-10}$ m s^{-2} is appropriate for all the galaxies in the sample. This value is also consistent with the MOND acceleration scale a_0. The asymptotic limit of Eq. (4.14) for small $g_{\rm bar}$ returns the acceleration in the MOND regime $g_{\rm obs} \sim \sqrt{g_{\rm bar}(R) a_0}$.

For the galaxies of the SPARC sample, this correlation has a relatively small root-mean-square scatter of 0.13 dex, mostly due to possible variations of the stellar mass-to-light ratio from galaxy to galaxy and to observational uncertainties [44, 246]. Indeed, for this result, McGaugh et al. [44] adopt a single 3.6 μm mass-to-light ratio of 0.50 $M_\odot/L_\odot$ for all the galaxy disks, under the assumption that the stellar mass-to-light ratio does not vary much in this band [336, 346, 347, 348]. Similarly, for the galaxy bulges, which are present in 31 out of 153 galaxies, McGaugh et al. [44] adopt a mass-to-light ratio equal to 0.70 $M_\odot/L_\odot$.

To explore the intrinsic scatter of the RAR due to the mass-to-light ratio variations, Li and coauthors [56] fit galaxy mass-to-light ratios to individual galaxies with Eq. (4.14) and $g_\dagger$ fixed to 1.2×10^{-10} m s^{-2}. They find a RAR tighter than [44], with an intrinsic root-mean-square scatter of 0.057 dex and mass-to-light ratios generally consistent with the SPS model predictions.

Here, we estimate the RAR for our DMS sample. The observed acceleration, $g_{\rm obs}$, is directly derived from the measured rotation curve according to Eq. (4.13). The Newtonian acceleration attributed to the baryonic matter alone, $g_{\rm bar} = |-\partial\phi/\partial R|$, is derived from the numerical solution of the Newtonian Poisson equation (2.11) where the density, $\rho(R, z)$, is Eq. (A.10). For the galaxy disk-scale height, h_z, which appears in $\rho(R, z)$, we use the values derived from Eq. (A.12) inferred from the observations of edge-on galaxies (see Appendix A.3). For the numerical solution of the Poisson equation, we adopt the successive over relaxation algorithm described in Appendix B.

To estimate the mass density $\rho(R, z)$ from the galaxy surface brightness, we adopt the mass-to-light ratios derived with our MCMC analysis (Sect. 4.2) and listed in Table 4.2. As discussed above, for 26 galaxies out of 29, these values agree within 3σ with the values of the SPS models (see Table 1 of [325]) and for all the galaxies, the difference is within 5σ.

Red symbols and error bars in both panels of Fig. 4.10 show the RAR of all the DMS galaxies in our sample. The black curve is Eq. (4.14). The blue curves in the left panel of Fig. 4.10 are the RAR of each DMS galaxy obtained from the RG parameters, the mass-to-light ratios and the disk-scale heights derived from our MCMC analysis of the rotation curves and vertical velocity dispersion profiles (Sect. 4.2). The blue curves are not fits to the observed RAR, but just the relations between the Newtonian $g_{\rm bar}$ and the expected RG centripetal acceleration $g_{\rm obs}$ based on the galaxy parameters estimated with our previous analysis. The dashed line shows the relation $g_{\rm obs} = g_{\rm bar}$ for comparison.

We also estimate the RAR expected in MOND, adopting the QUMOND formulation described in Sect. 4.2.1. For QUMOND, we adopt the mass-to-light ratios Υ and the disk-scale heights h_z that we derive for RG in Sect. 4.2. These mass-to-light ratios agree within 2σ with the values estimated by [326], who model the rotation curves and vertical velocity dispersions in QUMOND with the simple interpolating function (Eq. (4.11)). Similarly, their values of h_z agree with our estimates within 1σ. The QUMOND RAR curves are shown as green solid lines in the right panel of Fig. 4.10.

RG correctly reproduces the asymptotic limits of the observed RAR and, on average, it interpolates the data, although it tends to underestimate the relation (4.14) at low $g_{\rm bar}$; on the contrary, QUMOND properly reproduces the shape of the RAR relation (4.14) along the entire range of $g_{\rm bar}$. The fact that RG slightly underestimates the observed RAR while at the same time providing a good fit to the kinematics of the individual galaxies, as shown in the previous sections, suggests that RG might attribute more mass to the luminous matter than QUMOND. In fact, Fig. 4.11 shows that the RG mass-to-light ratios are systematically larger than in QUMOND, although the mass-to-light ratios in the two models agree with each other within 2σ. This result is consistent with the left

panel of Fig. 4.6 of Sect. 4.2.1.

A more serious issue for RG is the scatter of the curves along the $g_{\rm obs}$ axis. Figure 4.12 shows the distributions of the deviations of each curve from Eq. (4.14). We only consider the deviations of each curve from Eq. (4.14) within the horizontal axis range of $\log_{10}[g_{\rm bar}({\rm m/s^2})] = [-11.28, -8.81]$ covered by the data. This approach makes the comparison with the data more sensible. In passing, we note that we use the disk-scale heights $h_{z,{\rm SR}}$ for the data and our estimated h_z for the models. These values can be different by a factor of two, as shown in the right panel of Fig. 4.3 and in Table 4.2. However, adopting, for the models, $h_{z,{\rm SR}}$ rather than h_z, leaves the distributions of the deviations basically unaffected.

The width of the residual distribution in Fig. 4.12 for the data, which quantifies the observed scatter of the RAR, is 0.12 dex. We estimate this scatter by removing four outlying points, clearly visible in the right part of both panels of Fig. 2.11. These points belong to the galaxies UGC 1081, UGC 1862, UGC 3997, and UGC 6903, and they correspond to the innermost point of their rotation curves; these values are 17.00, 0.05, 1.19, and 17.69 km s^{-1}, which are unusually small. If we include these four points, the root-mean-square scatter increases from 0.12 dex to 0.32 dex. The observed scatter of the DMS sample is thus comparable to the value 0.13 dex found by [44] and [246].

The widths of the distributions of the residuals for the RG and QUMOND models shown in Fig. 4.12 are 0.11 and 0.017 dex, respectively. We can identify these widths with the intrinsic scatter of the RAR predicted by the two models. The small intrinsic scatter predicted by QUMOND, consistent with the expectations [246, 247], is almost an order of magnitude smaller than the RG scatter. MOND actually appears with different formulations: in the version of modified inertia, which modifies the Newtonian second law of dynamics, the intrinsic scatter is predicted to be zero if the orbits are circular [244]; similarly, in the version of modified gravity, which modifies the Poisson equation, like QUMOND does, the intrinsic scatter is predicted to be zero only for spherically symmetric systems [237], whereas in flat systems, like disk galaxies, a small not-null intrinsic scatter should appear (see also Sect. 2.2.2).

To investigate the nature of the intrinsic scatter predicted by RG, we explore the possible correlation of the RAR residuals with the global and the radially-dependent properties of the galaxies. We plot these residuals in Figs. 4.13 and 4.14. The first column shows, in cyan, the residuals of the RG models. The second and the third columns show the residuals for QUMOND, in green, and the DMS data, in pink.[5]

Table 4.5 lists the Kendall statistic τ [349] and the Spearman statistic ρ [350] with their corresponding p-values, namely, the significance levels of the lack of correlation. For large size N of the sample, the density distributions of the random variates τ and ρ are excellently approximated by the Gaussian distribution with zero mean and variance $(4N+10)/(9N^2-9N)$ and $1/(N-1)$ for τ and ρ, respectively [351, 352]. In our analysis of RG, $N = 4560$ and, assuming Gaussian distributions, the corresponding standard deviations σ's are $\langle\tau^2\rangle^{1/2} = 0.0099$ and $\langle\rho^2\rangle^{1/2} = 0.0148$.

We can interpret the results of Table 4.5 by arbitrarily choosing the threshold $\log_{10} p = -3$: p-values smaller than the threshold of $p = 10^{-3}$ indicate that the listed values of τ or ρ have a probability smaller than 0.1% of occurring by chance for an uncorrelated sample. For this probability, the values $|\tau| > 0.033$ and $|\rho| > 0.049$ are thus more than 3.3σ away from the expected means $\langle\tau\rangle = 0$ and $\langle\rho\rangle = 0$. For RG, the only two parameters that have p-values larger than 10^{-3}, namely, $-\log_{10} p < 3$, and therefore their uncorrelation with the residuals is statistically significant, are the central surface brightness $I_{\rm d0}$ of the disk and its scale length h_R. The remaining parameters show significant correlations. This

[5]The residuals for the four outlying points of the DMS data that we mention above do not appear in the plots because they lie beyond the range of the vertical axis. They are however included in our statistical tests we describe below. These four outliers do not drive the correlations of the DMS data that we find: if we remove them when performing the statistical tests, the statistical significance of the correlations actually increases.

result might appear at odds with the observed RAR because the observed residuals do not seem to correlate with the galaxy properties in the SPARC sample [246].

This issue requires additional clarification. In fact, unlike the SPARC sample, the DMS sample also shows some correlations: the p-values listed in Table 4.5 indicate that the RAR residuals are not significantly correlated ($-\log_{10} p < 3$) only with h_R, $I_{\rm d0}$, $R_{\rm e}$, and the stellar surface brightness profile, $\Sigma_*(R)$ (see also Figs. 4.13 and 4.14). Moreover, similarly to RG, correlations are found between the residuals of the QUMOND models and all the galaxy properties but the bulge central surface brightness $I_{\rm e}$.[6] For QUMOND, this result might not be surprising, however, because QUMOND is a modified-gravity version of MOND, where a non-null intrinsic scatter for the RAR, and thus correlated residuals, are expected for nonspherical systems, unlike modified-inertia versions of MOND, that predict a null intrinsic scatter, and thus uncorrelated residuals [237].

The correlations we find for the residuals of the DMS data might partly generate the correlations we find for the RG residuals. In addition, the correlations for the DMS data, at odds with the claimed uncorrelations for the SPARC sample, might suggest a difference between the DMS and the SPARC samples. Unfortunately, we cannot quantify this difference here, if there even is any, because Lelli and coauthors [246] only mention in their analysis that the Kendall and Spearman coefficients are in the range of $[-0.2, 0.1]$ but they do not report their corresponding significance levels, namely their p-values. Therefore, we cannot assess the statistical significance of the lack of correlation. In fact, many coefficients in Table 4.5 from our analysis are in the range of $[-0.2, 0.1]$, but their p-values clearly indicate that they are at many σ's away from the null expected means and, thus, they demonstrate the presence of a statistically significant correlation.

The significance levels listed in Table 4.5 suggest that the correlations for the RG models are much stronger than for the DMS data for all the galaxy properties but $I_{\rm d0}$. In addition, RG shows a very strong correlation, at largely more than 5σ, namely $-\log_{10} p > 6.24$, with the radially-dependent properties of the galaxies, whereas the data show a significant correlation, between 4 and 5σ, namely $4.20 < -\log_{10} p < 6.24$, for R and $f_{\rm gas}(R)$, but no correlation for $\Sigma_*(R)$.

Therefore, a possible serious tension between RG and the data might indeed be present. However, given the possible tension between the DMS and the SPARC samples, which is yet to be confirmed, we conclude that this issue remains open at this stage of our testing of RG. Further investigations with multiple data samples are necessary to clarify whether reproducing the observed properties of the RAR is indeed a challenge for RG.

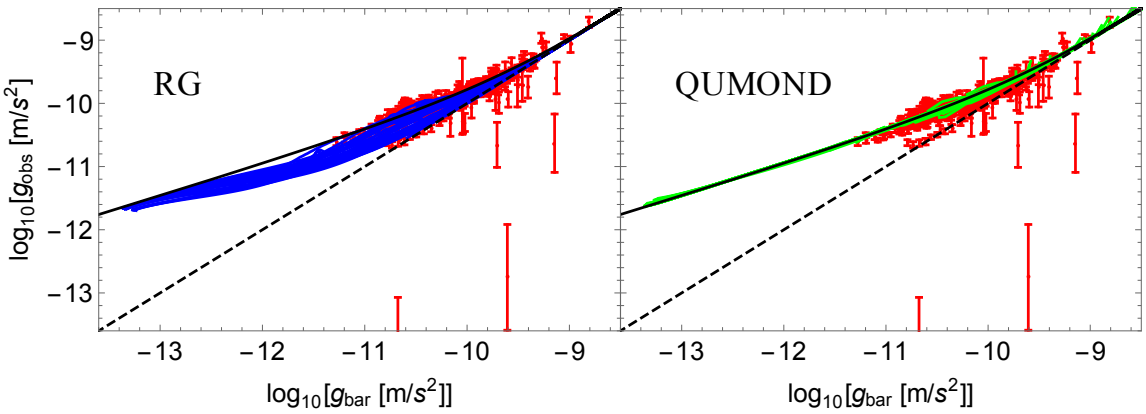

Figure 4.10: RG (left panel) and QUMOND (right panel) models of the RAR obtained for each galaxy with the parameters derived from the MCMC analysis of the rotation curves and vertical velocity dispersion profiles (Sect. 4.2). Red points with error bars are the DMS measures. The black solid line is Eq. (4.14). The black dashed line is $g_{\rm obs} = g_{\rm bar}$.

[6] In passing, we emphasise that the statistical significance of the correlation is quantitatively supported by the p-values listed in Table 4.5: from a qualitative visual inspection of Figs. 4.13 and 4.14, one might draw the incorrect conclusion that the residuals of QUMOND generally show a weaker correlation, if any, than the DMS data.

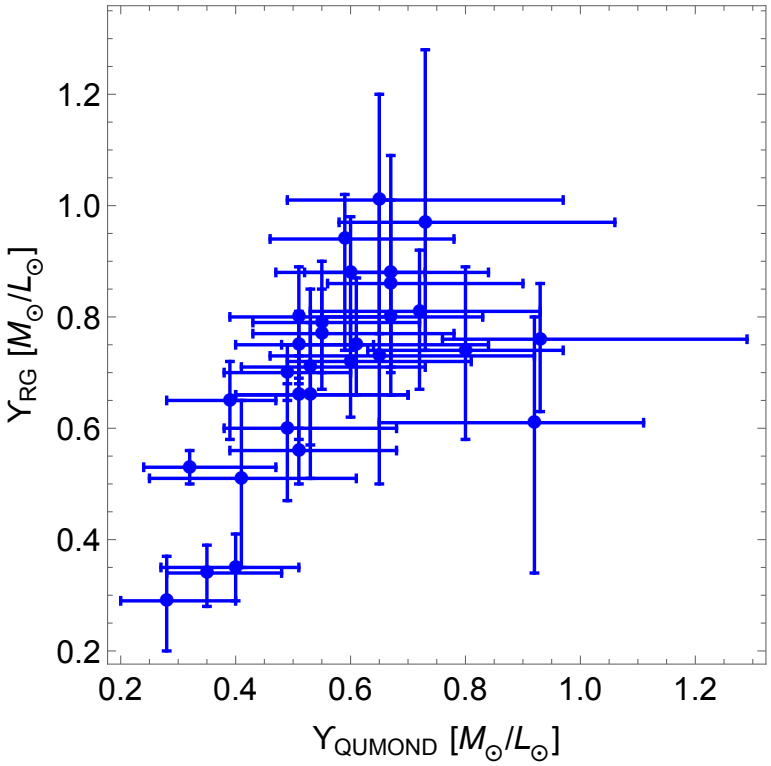

Figure 4.11: Mass-to-light ratios estimated with RG, $\Upsilon_{\rm RG}$ (Table 4.2), and with QUMOND, $\Upsilon_{\rm QUMOND}$ (Table 1, [326]). The black dashed line is the line of equality.

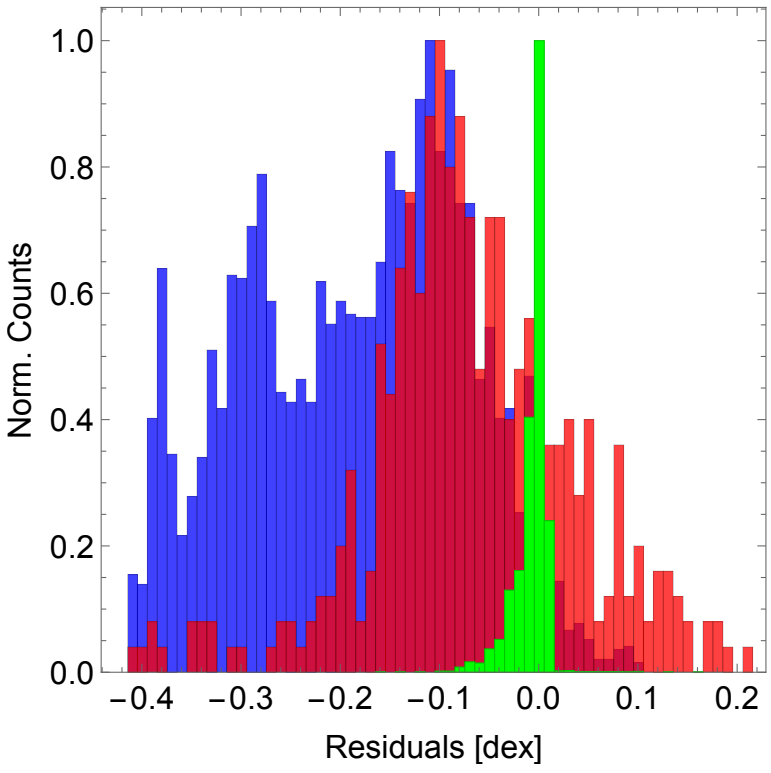

Figure 4.12: Distributions of the residuals of the RG models (blue), the QUMOND models (green) and the data (red) of the RAR with respect to relation (4.14).

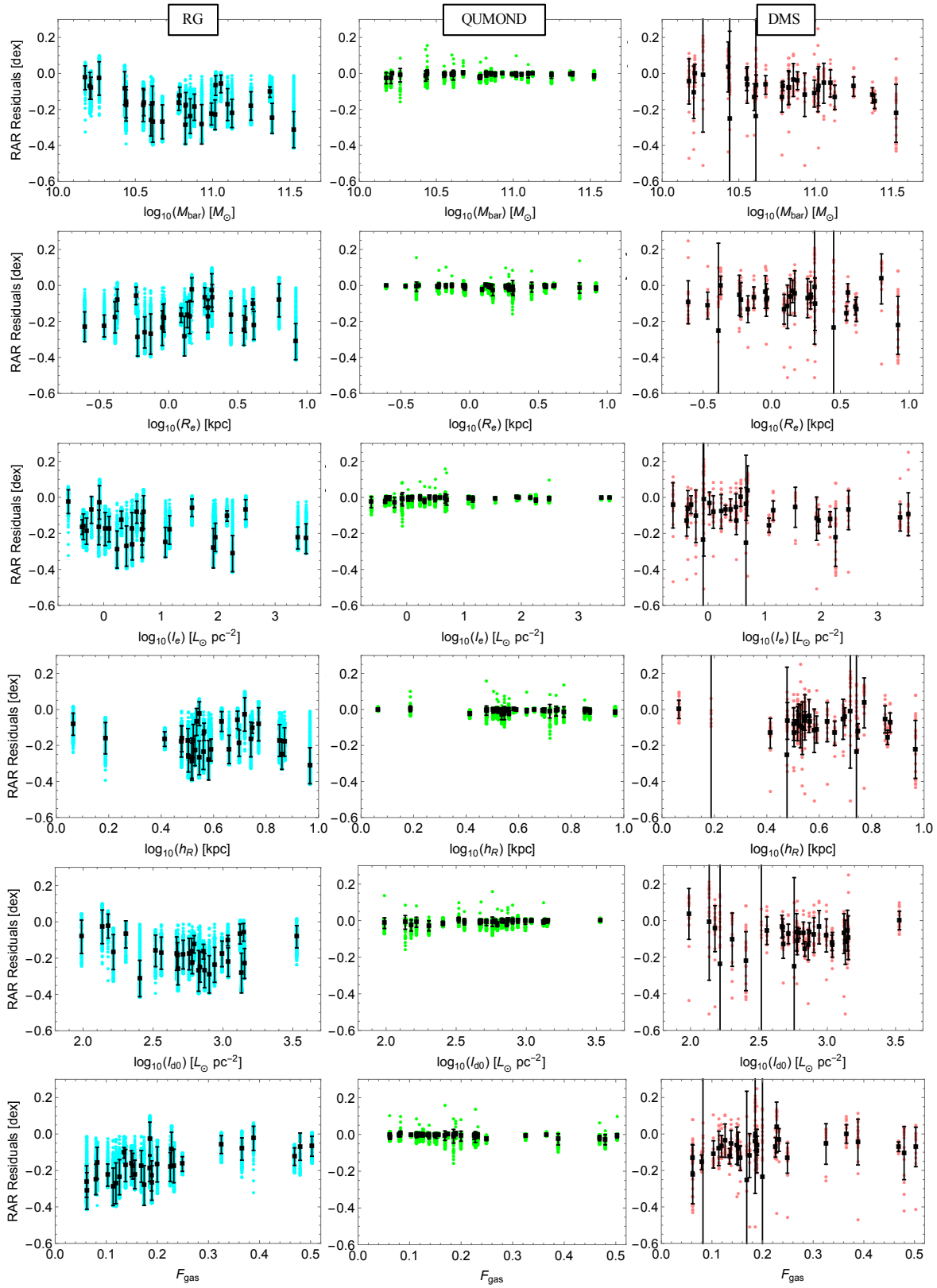

Figure 4.13: Residuals of the modelled or estimated RAR from the relation (4.14) as a function of the global properties of the galaxies. Left, middle and right columns show the RG, QUMOND, and DMS residuals, respectively. From top to bottom the residuals are plotted against the total baryonic mass, bulge effective radius, bulge effective surface brightness, disk-scale length, central disk surface brightness, and total gas fraction. To guide the eye, solid squares with error bars show the means and standard deviations of binned residuals.

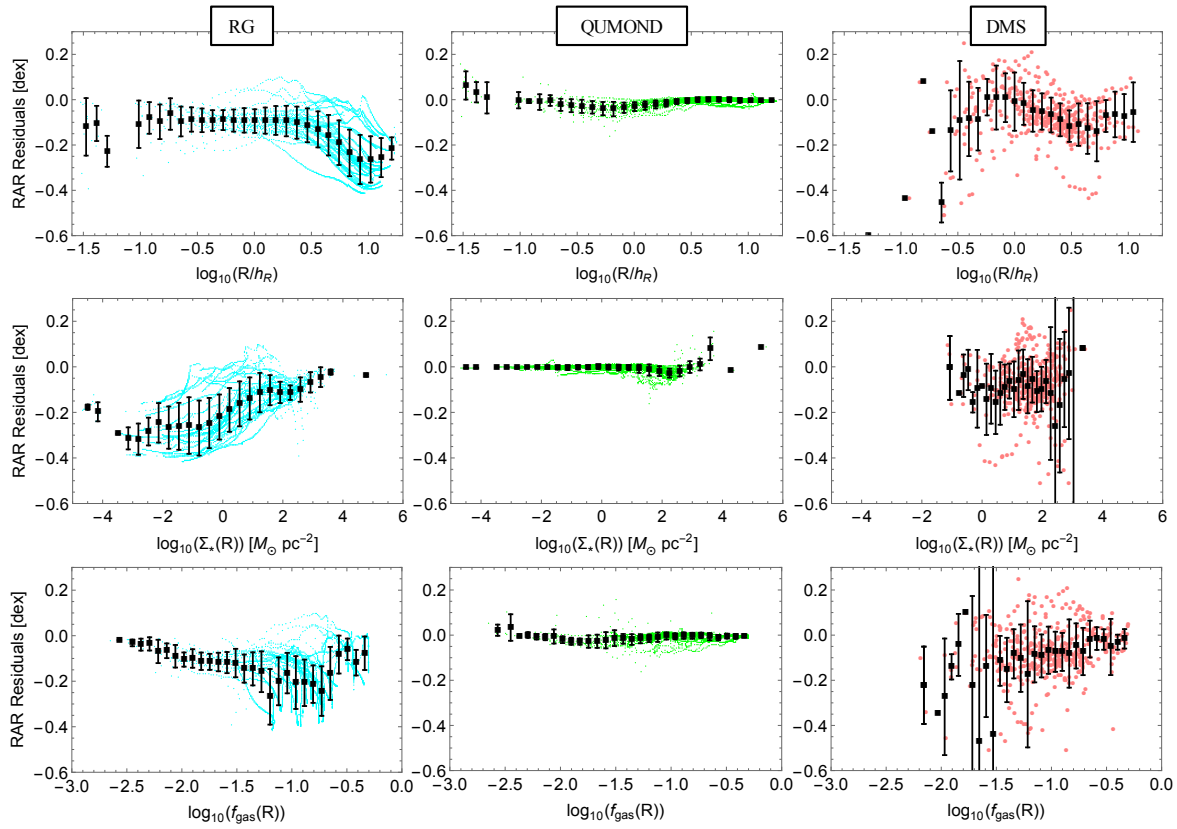

Figure 4.14: Same as Fig. 4.13 for three radially-dependent properties of the galaxies. From top to bottom the residuals are plotted against the radius, the stellar surface density profile, and the gas fraction profile.

Table 4.5: Correlations of the RAR residuals of RG models, QUMOND models, and DMS data with the galaxy properties.

Galaxy	**RG**				**QUMOND**				**DMS**			
property (1)	τ (2)	$-\log_{10} p_\tau$ (3)	ρ (4)	$-\log_{10} p_\rho$ (5)	τ (6)	$-\log_{10} p_\tau$ (7)	ρ (8)	$-\log_{10} p_\rho$ (9)	τ (10)	$-\log_{10} p_\tau$ (11)	ρ (12)	$-\log_{10} p_\rho$ (13)
h_R [kpc]	−0.030	2.62	−0.038	1.96	−0.065	9.85	−0.094	9.72	−0.042	0.68	−0.060	0.66
$I_{\rm d0}$ $\left[\frac{\rm L_\odot}{\rm pc^2}\right]$	+0.0083	0.39	+0.0052	0.14	+0.049	5.92	+0.073	6.10	−0.099	2.55	−0.15	2.64
$M_{\rm bar}$ $[\rm M_\odot]$	−0.16	56.6	−0.23	54.4	−0.053	6.77	−0.074	6.26	−0.27	15.7	−0.38	15.2
$R_{\rm e}$ [kpc]	+0.046	5.14	+0.061	4.18	−0.094	19.0	−0.14	20.3	+0.0020	0.022	−0.012	0.086
$I_{\rm e}$ $\left[\frac{\rm L_\odot}{\rm pc^2}\right]$	−0.10	22.6	−0.15	23.6	−0.00023	0.0088	+0.011	0.31	−0.15	5.21	−0.23	5.41
$F_{\rm gas}$	+0.33	237	+0.48	256	−0.11	29.0	−0.17	31.6	+0.21	9.82	+0.31	10.1
R [kpc]	−0.41	377	−0.59	419	+0.15	53.9	+0.27	76.1	−0.16	6.10	−0.21	4.89
$\Sigma_*(R)$ $\left[\frac{\rm M_\odot}{\rm pc^2}\right]$	+0.41	368	+0.57	395	−0.17	62.6	−0.28	84.5	+0.033	0.49	+0.041	0.40
$f_{\rm gas}(R)$	+0.073	12.9	+0.12	16.6	+0.14	42.0	+0.20	43.2	+0.16	6.10	+0.24	6.12

Column 1: Name of the galaxy property; Cols 2-5: correlations of the RAR residuals of RG models with the galaxy properties; Cols. 6-9: correlations of the RAR residuals of QUMOND models with the galaxy properties; Cols. 10-13: correlations of the RAR residuals of DMS data with the galaxy properties. τ and ρ are the Kendall and Spearman correlation coefficients, respectively; p_τ and p_ρ the corresponding significance levels of the lack of correlation.

Chapter 5

Dynamics of elliptical galaxies in RG: the case of three nearby E0 galaxies[1]

In Chapter 4 we show that the bending of the gravitational field lines occurring in RG is sufficient to describe the kinematic profiles of flat systems, namely 30 disk galaxies in the DMS, without resorting to DM. RG describes the kinematics of the entire DMS sample with a single set of permittivity parameters, ϵ_0, Q, and ρ_c, supporting the expectation that these parameters should be universal. These encouraging results on flat systems motivate us to test whether RG is also able to describe, with the same set of parameters, the dynamics of spherical systems, where the RG field lines remain radial and the gravitational field is enhanced with respect to Newtonian case by the inverse of the gravitational permittivity (see Chapter 3). In other words, we wish to probe that the boost of the gravitational field can be set by the gravitational permittivity alone, independently of the redirection of the field lines.

Here, we illustrate the result of this test on three E0 galaxies, that are approximately spherical. We consider NGC 1407, NGC 4486, alias M87, and NGC 5846 from the SLUGGS survey[2] [76, 353, 354]. In elliptical galaxies, the baryonic matter within R_e, the effective radius at half projected luminosity, suffices to describe the galaxy dynamics with Newtonian gravity (e.g. [355, 356, 75, 77]). To probe RG, we thus need kinematic information in the outer regions, where Newtonian gravity breaks down unless DM is assumed to exist. X-ray emitting gas, planetary nebulae, and GCs have been adopted as kinematic tracers in these regions, out to $\sim 10 R_e$, where the stellar luminosity fades out [357, 358, 359, 76, 80]. In addition, GCs usually appear separated into two distinct populations, according to their colour. Red GCs tend to be more spatially concentrated and to have smaller velocity dispersions than blue GCs [360, 361, 362, 363, 364, 365, 366, 367, 76]. In particular, the kinematics of the red GCs is typically similar to the one of the stars in the host galaxy [368, 365], which could be explained by a similar formation history of the two populations [369]. By adopting GCs as tracers of the velocity field in the outer regions of ellipticals, we thus actually have two tracers rather than one and they can thus more strongly constrain the model. The SLUGGS survey thus provides the ideal dataset for our study.

Studying the outer regions of ellipticals might be, however, particularly insidious. Here, we will model each galaxy as an isolated system. However, ellipticals tend to live in dense environments: NGC 1407 and NGC 5846 are within groups and NGC 4486 is the central galaxy of the Virgo cluster. Therefore, their outer regions are subject to the gravitational field of nearby galaxies and of the hosting system as a whole. As a consequence, our simple model might overlook relevant effects. We will actually see that, although the environment might indeed be responsible for some discrepancies that we find, RG can satisfactorily describe the dynamics of these elliptical galaxies.

[1] The results in this chapter are presented in [318].

[2] `https://sluggs.swin.edu.au/Start.html`

5.1 Photometric data

In this section, we describe the observables that enter our mass model of each galaxy: the surface brightness of the stars, the surface number densities of the GCs populations, the mass density of the hot X-ray emitting gas, and the mass of the central supermassive black hole (SMBH). Table 5.1 lists the quantities characterising the three galaxies and the colour cut that we adopt in Sect. 5.2.2 to separate the GC samples into the red and blue populations.

NGC 1407, NGC 4486, and NGC 5846 are at redshift $z < 0.007$.[3] We can thus neglect any k-correction in the photometric measures and in the distance modulus $m - M = 5\log_{10}[D(\mathrm{pc})] - 5$, with m and M the apparent and the absolute magnitudes of the source. Similarly, to convert the radial coordinate R projected on the sky from angular units, in arcsec, to physical units, in kpc, we adopt the relation, valid in a nonexpanding Euclidean geometry,

$$R(\mathrm{kpc}) = 4.84814 \times 10^{-6} D(\mathrm{kpc}) R(\mathrm{arcsec})\,, \tag{5.1}$$

with D the distance to the galaxy. For elliptical galaxies, the radial coordinate R is

$$R = \sqrt{qx'^2 + \frac{y'^2}{q}}, \tag{5.2}$$

where q is the minor-to-major axis ratio of the galaxy on the sky, and the x' and y' coordinates are oriented along the galaxy major and minor axes, respectively (e.g. [370, 77, 371, 76, 81]).

Table 5.1: General properties of NGC 1407, NGC 4486, and NGC 5846.

NGC	D [Mpc]	z	q	N_{GCs}	$N_{\mathrm{GCs,Blue}}$	$N_{\mathrm{GCs,Red}}$	V_{hel} $[\mathrm{km\ s^{-1}}]$	$(g-i)_{\mathrm{TH}}$
(1)	(2)	(3)	(4)	(5)	(6)	(7)	(8)	(9)
1407	28.05	0.0068	0.95	379	153	148	1779 ± 9	0.98
4486	17.2	0.0042	0.86	737	480	199	1284 ± 5	0.93
5846	24.2	0.0059	0.92	195	91	102	1712 ± 5	0.95

Column 1: galaxy name; Col. 2: distance; Col. 3: redshift; Col. 4: minor-to-major axis ratio; Col. 5: number of confirmed GCs; Cols. 6–7: number of blue and red GCs in the final sample (see text). Col. 8: heliocentric (recession) velocity; Col. 9: $(g-i)$ colour threshold separating the GC population. The distance and the number of confirmed GCs of NGC 1407 are from [81], whereas the distance and the number of confirmed GCs of NGC 4486 and NGC 5846 are from [76]. The distances are derived with the method of the surface brightness fluctuations, from the SBF survey [372], subtracting 0.06 mag to the distance modulus [373] (NGC 1407 and NGC 5846), and from the ACS Virgo cluster survey [373] (NGC 4486). The number of blue and red GCs of NGC 1407 are from [81], whereas the number of blue and red GCs of NGC 4486 and NGC 5846 are determined from our analysis. The minor-to-major axis ratio and the heliocentric velocities of the three galaxies are from [76], as well as the $(g-i)$ colour thresholds for NGC 1407 and NGC 5846. The $(g-i)$ colour threshold for NGC 4486 is from [365].

5.1.1 Stellar surface brightness profiles

For the surface brightness of the stars, we adopt the models derived by [81] for NGC 1407 and by [374] for NGC 4486 and NGC 5846.

NGC 1407

The stellar surface brightness profile of NGC 1407 is measured in the B-band with the *Hubble Space telescope*/ACS [375, 376] and in the g-band with the Subaru/Suprime-Cam [76].

[3] The redshifts are computed as $z = H_0 D/c$, where H_0 is the Hubble parameter, D is the distance, and c is the speed of light. This formula neglects the contribution of peculiar velocities to the recession velocity V_{hel} of the galaxy. However, the redshifts calculated as $z = V_{\mathrm{hel}}/c$ are at most within 13% (NGC 1407) from the redshifts calculated as $z = H_0 D/c$, suggesting that the Hubble flow dominates peculiar velocities.

The B and g-bands largely overlap; therefore, Pota and collaborators [81] derive a unique surface brightness profile in the B-band by a proper transformation of the g-band data. NGC 1407 has ellipticity $\varepsilon = 1 - q = 0.05$. Pota and collaborators [81] model the surface brightness profile with the Sérsic profile

$$I_*(R) = I_\mathrm{e} \exp\left\{-b_{n_\mathrm{s}}\left[\left(\frac{R}{R_\mathrm{e}}\right)^{\frac{1}{n_\mathrm{s}}} - 1\right]\right\}, \tag{5.3}$$

where the effective radius R_e encloses half of the total luminosity of the stellar distribution, I_e is the surface brightness at radius R_e, n_s is the Sérsic index, and

$$b_{n_\mathrm{s}} = 2n_\mathrm{s} - \frac{1}{3} + \frac{4}{405n_\mathrm{s}} + \frac{46}{25515n_\mathrm{s}^2} \tag{5.4}$$

[377]. After deconvolving for the seeing, Pota and collaborators [81] derive $R_\mathrm{e} = (100 \pm 3)$ arcsec, $I_\mathrm{e} = 3.5 \times 10^5\ L_{\odot,B}\ \mathrm{arcsec}^{-2}$, and $n_\mathrm{s} = 4.67 \pm 0.15$.

NGC 4486 and NGC 5846

Scott and collaborators [374] measure the surface brightness of NGC 4486 and NGC 5846 in the *ugriz* bands from the Sloan Digital Sky Survey DR7 [378] and the Wide Field Camera on the 2.5-m Isaac Newton Telescope at the Roque de los Muchachos observatory. Scott and collaborators [374] model the two-dimensional map of the surface brightness in the r-band; this band reduces the dust contamination and provides images with the optimal signal-to-noise value [77]. They adopt the axisymmetric Multi-Gaussian Expansion (MGE) approach [379], which yields the surface brightness map [370, 77]

$$I_*(x', y') = \sum_{k=1}^{N} \frac{L_k}{2\pi\sigma_k^2 q_k'} \exp\left[-\frac{1}{2\sigma_k^2}\left(x'^2 + \frac{y'^2}{q_k'^2}\right)\right], \tag{5.5}$$

where N is the number of Gaussian components in the MGE fit, and L_k, σ_k, and $0 \leq q_k' \leq 1$ are the luminosity, the standard deviation along the major axis, and the observed minor-to-major axis ratio of each Gaussian, respectively; x' and y' are the coordinates on the plane of the sky, where the x'-axis is oriented along the major axis of the galaxy. Scott and collaborators [374] find $q_k' = 1$ within 5% for almost all the Gaussians of the model of each galaxy[4]. Indeed, NGC 4486 has ellipticity $\varepsilon = 1 - q = 0.14$, and NGC 5846 has $\varepsilon = 0.08$. We thus model these galaxies as spherical systems, set $q_k' = 1$ for all the Gaussians, and adopt the parameters L_k and σ_k determined by [374] for Eq. (5.5) in the surface brightness profile [370]

$$I_*(R) = \sum_{k=1}^{N} \frac{L_k}{2\pi\sigma_k^2} \exp\left(-\frac{R^2}{2\sigma_k^2}\right). \tag{5.6}$$

Scott and collaborators [374] find $N = 9$ and $N = 7$ Gaussian components for NGC 4486 and NGC 5846, respectively. Tables 5.2 and 5.3 list L_k and σ_k after deconvolving for the seeing. Finally, the total stellar luminosity of the galaxy is [77]

$$L_{*,\mathrm{tot}} = \sum_{k=1}^{N} L_k. \tag{5.7}$$

[4]Specifically, for NGC 5846 $q_k' = 1$ within 5% for 5 out of 7 Gaussians and within 9% for all the Gaussians. For NGC 4486, $q_k' = 1$ within 5% for 7 out of 9 Gaussians, within 10% for 8 out of 9 Gaussians, and within 20% for all the Gaussians.

Table 5.2: Parameters of the stellar surface brightness profile of NGC 4486.

L_k $[L_\odot]$ (1)	σ_k [arcsec] (2)
3.26333×10^7	0.31847133
6.31462×10^7	0.85316859
1.42502×10^8	1.9878101
1.20241×10^9	4.3688105
2.92993×10^9	7.0315581
6.16303×10^9	11.941329
1.08416×10^{10}	21.809295
2.11184×10^{10}	48.869046
3.15170×10^{10}	120.71397

Table 5.3: Parameters of the stellar surface brightness profile of NGC 5846.

L_k $[L_\odot]$ (1)	σ_k [arcsec] (2)
3.09594×10^8	1.3004914
6.31938×10^8	2.0720509
2.52404×10^9	4.7753466
2.41652×10^9	8.9026766
8.05893×10^9	16.353135
9.26616×10^9	32.666416
2.29889×10^{10}	78.813294

Stellar 3D luminosity density profiles

For NGC 1407, the three-dimensional (3D) luminosity density of the stars is the Abel integral, valid in spherical symmetry,

$$\nu_*(r) = -\frac{1}{\pi} \int_r^{+\infty} \frac{\mathrm{d}I_*}{\mathrm{d}R} \frac{\mathrm{d}R}{\sqrt{R^2 - r^2}}\,, \tag{5.8}$$

where $I_*(R)$ is given by Eq. (5.3) and r is the radial coordinate in three dimensions. For NGC 4486 and NGC 5846, the deprojected MGE 3D luminosity density is [370]

$$\nu_*(r) = \sum_{k=1}^{N} \frac{L_k}{(\sqrt{2\pi}\sigma_k)^3} \exp\left(-\frac{r^2}{2\sigma_k^2}\right). \tag{5.9}$$

The 3D luminosity density of the stars, $\nu_*(r)$, yields the stellar luminosity profile

$$L_*(r) = 4\pi \int_0^r \nu_*(r') r'^2 \, \mathrm{d}r'. \tag{5.10}$$

The total stellar luminosity, $L_{*,\mathrm{tot}}$, is formally obtained by setting $r = \infty$. However, $L_*(r)$ rapidly converges to $L_{*,\mathrm{tot}}$. By setting $R = 4800$ arcsec, we obtain $L_*(R) = 8.51 \times 10^{10}\ L_\odot$ for NGC 1407, $L_*(R) = 7.39 \times 10^{10}\ L_\odot$ for NGC 4486, and $L_*(R) = 4.59 \times 10^{10}\ L_\odot$ for NGC 5846. These total luminosities are consistent with the total galaxy luminosities $L_{*,\mathrm{tot}} = 8.53 \times 10^{10}\ L_\odot$, found by [81] for NGC 1407, and $L_{*,\mathrm{tot}} = 7.40 \times 10^{10}\ L_\odot$ and $L_{*,\mathrm{tot}} = 4.62 \times 10^{10}\ L_\odot$, found by [374] with Eq. (5.7), for NGC 4486 and NGC 5846, respectively. This result supports our spherical approximation and our choice of $R = 4800$ arcsec as the extension of the radial grid that we will adopt in our dynamical model in Sect. 5.3.1.

5.1.2 Number density profiles of GCs

The number density profiles of GCs are from [81] for NGC 1407, from [365] for NGC 4486, and from [76] for NGC 5846. Each GC sample is separated into a blue and a red sample according to the colour thresholds listed in Table 5.1. To ensure the magnitude completeness

of the GC samples in all the three galaxies, Pota and collaborators [76] remove the sources fainter than $M_i = -8.0$ in the i-band. This magnitude limit corresponds to the peak of the GC luminosity function that has a roughly Gaussian shape (e.g. [380, 381, 382]). Moreover, the samples might be contaminated by ultracompact dwarf galaxies (UCDs), that are a kinematically and spatially distinct population from the GCs. Therefore, Pota and collaborators [76] remove the sources brighter than $M_i = -11.6$. This luminosity is 1 mag brighter than ω Cen, the brightest GC in the Milky Way, and brighter objects are likely to be UCDs. NGC 1407, NGC 4486, and NGC 5846 have 379, 737, and 195 confirmed GCs, respectively (Table 5.1). Imposing the magnitude range $-11.6 < M_i < -8.0$ removes 72 objects from the NGC 1407 sample, and 53 objects from the NGC 4486 sample, whereas the NGC 5846 sample remains unaffected.

In addition to this photometric selection, Pota and collaborators [76, 81] apply a kinematic selection on the two separated populations of blue and red GCs. Despite Galactic stars and GCs are two populations whose velocity distributions are usually well distinct, sometimes the population of stars might have a low-velocity tail so that a Galactic star could erroneously be identified as a GC. Pota and collaborators [76, 81] thus remove the sources whose velocity is more than 3σ discrepant from the mean velocity of the 20 closest neighbours in the GC sample, where σ is the velocity dispersion of these 20 neighbours [383]. This kinematic criterion removes 6, 5, and 2 objects from the NGC 1407, NGC 4486, and NGC 5846 samples, respectively. The sizes of the final samples of blue and red GCs for each galaxy are listed in Table 5.1.

Each GC sample is binned in circular annuli around the galaxy centre. The background-subtracted surface number density profiles, along with their Poissonian uncertainties, are shown in Fig. 5.1.

NGC 5846

We model the profiles of the blue and red GCs in NGC 5846 with the Sérsic profile

$$N_{\rm GC}(R) = N_{\rm e} \exp\left\{-b_{n_{\rm s}}\left[\left(\frac{R}{R_{\rm e}}\right)^{\frac{1}{n_{\rm s}}} - 1\right]\right\}, \tag{5.11}$$

where the parameters $R_{\rm e}$, $N_{\rm e}$, and $n_{\rm s}$ have similar meaning of those in Eq. (5.3).

We estimate the free parameters of the surface number density profiles of the blue and red GCs with a MCMC method with a Metropolis–Hastings acceptance criterion. Details of this algorithm are in Sect. 5.3.2. We run the MCMC for 2×10^6 steps with 10^5 burn-in elements to achieve the convergence of the chains, according to the Geweke diagnostics [334]. We adopt flat priors on the free parameters of the model in the ranges listed in Table 5.4. The upper limit of $R_{\rm e}$ is the radius of the most external data point of the surface number density; the upper limit of $N_{\rm e}$ is slightly larger than the data point with the smallest R. Therefore, the upper limits of the priors for $R_{\rm e}$ and $N_{\rm e}$ are different for the two GC populations. Our posterior distributions are single-peaked. We thus adopt their medians as our parameter estimates and the range between the 15.9 and 84.1 percentiles, which includes 68% of the posterior cumulative distribution, as our parameter uncertainties. These parameters are listed in Table 5.5. They provide the curves shown in Fig. 5.1.

NGC 1407 and NGC 4486

We model the surface number densities of the two GC populations in NGC 1407 and NGC 4486 with a Sérsic profile, adopting the parameters obtained by [81] and [365] for the two galaxies, respectively. Pota and coauthors [81] model their data with Eq. (5.11). Strader

and coauthors [365] adopt the slightly different parametrisation

$$N_{\rm GC}(R) = N_0 \exp\left[-\left(\frac{R}{R_{\rm s}}\right)^{\frac{1}{m}}\right]. \tag{5.12}$$

Table 5.5 lists the parameters of the models shown in Fig. 5.1.

For the three galaxies, the 3D number density of the GCs is

$$\nu_{\rm GC}(r) = -\frac{1}{\pi}\int_r^{+\infty} \frac{{\rm d}N_{\rm GC}}{{\rm d}R}\frac{{\rm d}R}{\sqrt{R^2-r^2}}. \tag{5.13}$$

Table 5.4: Priors of the parameters of the GC surface number density models of NGC 5846.

GC sample	$N_{\rm e}$ $\left[\frac{\rm GCs}{\rm arcmin^2}\right]$	$R_{\rm e}$ [arcsec]	$n_{\rm s}$
(1)	(2)	(3)	(4)
Blue	$U(0.00, 2.24]$	$U(0.00, 833]$	$U(0.00, 3.00]$
Red	$U(0.00, 2.55]$	$U(0.00, 714]$	$U(0.00, 3.00]$

U stands for uniform distribution.

Table 5.5: Parameters of the models of the surface number density of the GCs.

NGC	GC sample	$N_{\rm e}$, N_0 $\left[\frac{\rm GCs}{\rm arcmin^2}\right]$	$R_{\rm e}$, $R_{\rm s}$ [arcsec]	$n_{\rm s}$, m	$\chi^2_{{\rm red},\nu}$
(1)	(2)	(3)	(4)	(5)	(6)
1407	Blue	7 ± 1	346 ± 29	1.6 ± 0.2	0.90
	Red	20 ± 2	169 ± 7	1.6 ± 0.2	1.29
4486	Blue	$(6.10 \pm 2.88) \times 10^2$	1 ± 2	3.69 ± 0.47	0.54
	Red	$(5.08 \pm 1.59) \times 10^4$	$(1.6 \pm 1.7) \times 10^{-3}$	5.33 ± 0.24	0.28
5846	Blue	$0.65^{+0.57}_{-0.37}$	324^{+171}_{-100}	$1.39^{+1.02}_{-0.82}$	1.64
	Red	$0.91^{+0.30}_{-0.30}$	268^{+43}_{-35}	$0.95^{+0.87}_{-0.38}$	1.88

Column 1: galaxy name; Col. 2: colour of the GC population; Cols. 3–5: parameters of the model of the surface number density; Col. 6: reduced chi-square, $\chi^2_{{\rm red},\nu}$, for ν degrees of freedom. The parameters $\{N_{\rm e}, R_{\rm e}, n_{\rm s}\}$, adopted for NGC 1407 and NGC 5846, refer to Eq. (5.11) and are from [81] and our MCMC analysis, respectively; the parameters $\{N_0, R_{\rm s}, m\}$, adopted for NGC 4486, refer to Eq. (5.12) and are from [365].

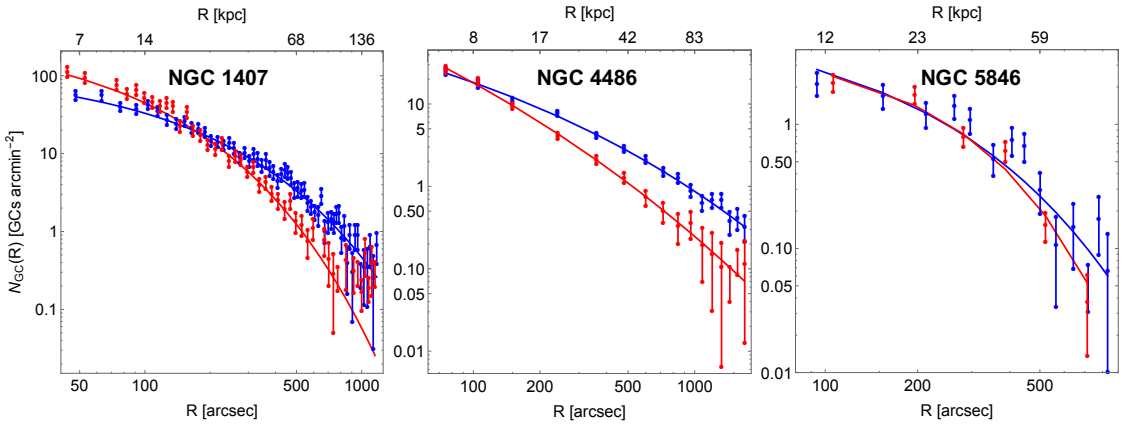

Figure 5.1: Surface number density profiles of blue (blue symbols and blue lines) and red (red symbols and red lines) GCs. Blue and red dots with error bars show the measured profiles; the solid lines are the models.

5.1.3 Mass density profiles of the X-ray gas

NGC 1407

For the 3D mass density of the hot X-ray emitting gas, we adopt the model parameters derived by [384]. They assume spherical symmetry and model the 3D number density profile of the gas, $n_{\rm g}(r)$, with the two-β function

$$n_{\rm g}^2(r) = n_{\rm g,1}^2 \left[1 + \left(\frac{r}{R_{\rm c,1}}\right)^2\right]^{-3\beta_1} + n_{\rm g,2}^2 \left[1 + \left(\frac{r}{R_{\rm c,2}}\right)^2\right]^{-3\beta_2} . \tag{5.14}$$

If we assume hydrodynamic equilibrium and an ideal and thermalised gas, $n_{\rm g}^2(r)$ enters the observed X-ray surface brightness profile

$$S_{\rm g}(R) = S_0 \int_R^{+\infty} \Lambda(T,Z) n_{\rm g}^2(r) \frac{r{\rm d}r}{\sqrt{r^2 - R^2}} + S_{\rm bkg} \, , \tag{5.15}$$

where $T(r)$ and $Z(r)$ are the temperature and the metallicity profiles, $\Lambda(T,Z)$ is the cooling function, and $S_{\rm bkg}$ is the background contamination level. The observed $S_{\rm g}(R)$ was measured with *Chandra* ACIS in the 0.7–7 keV band and with *ROSAT* PSPC in the 0.2–2 keV band. Zhang and collaborators [384] fit Eq. (5.15) to the data and obtain $n_{\rm g,1} = 0.1$ cm^{-3}, $n_{\rm g,2} = 3.65 \times 10^{-3}$ cm^{-3}, $R_{\rm c,1} = (8.42 \pm 0.70)$ arcsec, $R_{\rm c,2} = (58.3 \pm 0.7)$ arcsec, $\beta_1 = 0.70 \pm 0.01$, and $\beta_2 = 0.45 \pm 0.01$. They report $n_{\rm g,1}$ and $n_{\rm g,2}$ without uncertainty.

The 3D density profile of the gas entering our model is

$$\rho_{\rm g}(r) = \mu m_{\rm H} n_{\rm g}(r) \, , \tag{5.16}$$

where $m_{\rm H} = 1.66054 \times 10^{-27}$ kg is the atomic unit mass and $\mu = 0.6$ is the mean molecular weight, which assumes a completely ionised gas and a chemical composition with zero metallicity.[5] The normalisations $n_{\rm g,1}$ and $n_{\rm g,2}$ yield $\rho_{\rm g,1} = 9.96 \times 10^{-26}$ g cm^{-3} and $\rho_{\rm g,2} = 3.64 \times 10^{-27}$ g cm^{-3}.

NGC 5846

We derive our analytic model of the gas mass density profile from the measurements of [386]. They use the data from the X-ray observations of the *Chandra* ACIS and *XMM-Newton* MOS instruments. Paggi and coauthors [386] model the galaxy as a spherical system and fit the galaxy spectrum of each concentric circular annulus around the galaxy centre with the Astrophysical Plasma Emission Code (APEC) [387]. Each circular annulus has a minimum width of 1 arcsec, for *Chandra* data, and of 30 arcsec, for *XMM*-MOS data; this choice yields a finer grid in the innermost galaxy region where most of the *Chandra* data are. The inner and the outer radii of each annulus are chosen to achieve a minimum signal-to-noise $S/N = 100$, for *Chandra* ACIS data, and $S/N = 50$, for XMM-MOS data. The spectrum in each circular annulus is the integral of the emission from all the 3D spherical shells along the line of sight. For a source at redshift z and angular diameter distance D_A, the APEC parameters include the temperature of the plasma in each spherical shell, its element abundances, and its normalisation

$${\rm EM} = \frac{10^{-14}}{4\pi[(1+z)D_A]^2} \int n_{\rm e}(r) n_{\rm H}(r) {\rm d}V \, , \tag{5.17}$$

where the integral is taken over the volume of the 3D spherical shell. The equation above returns EM in cm^{-5}, when D_A is in cm, $n_{\rm e}$ and $n_{\rm H}$ in cm^{-3}, and the volume V in cm^3. In

[5] Zhang and collaborators [384] assume a non-null metallicity, in the range $[0.21, 1.40]$ $Z_\odot$, where $Z_\odot = 0.0169$ [385]. Within this range, μ is basically insensitive to Z. Indeed, assuming solar hydrogen and helium mass fractions from [385] ($X_\odot = 0.7345$ and $Y_\odot = 0.2485$), as in [384], and adopting $Z = 1.40$ $Z_\odot$ yields $\mu = 0.5998$.

Eq. (5.17), $n_{\rm e}$ and $n_{\rm H}$ are the electron and hydrogen number densities. For a fully ionised gas, $\eta = n_{\rm e}/n_{\rm H} = 1.2$. In addition, for NGC 5846, Paggi and coauthors [386] assume that $n_{\rm e}$ and $n_{\rm H}$ are constant within the shell. Therefore, $4\pi[(1+z)D_A]^2{\rm EM} = 10^{-14}\eta n_{\rm H}^2 V$, where V is the volume of the spherical shell. In each spherical shell, the mass density is thus

$$\rho_{\rm g} = \mu m_{\rm H} n_{\rm H} = 10^7 \mu m_{\rm H}(1+z)D_A \left[\frac{4\pi{\rm EM}}{\eta V}\right]^{1/2} \ [{\rm g\,cm^{-3}}]\,, \tag{5.18}$$

where Paggi and collaborators [386] assume $\mu = 0.62$ to account for the metallicity $Z > 0$ of the gas of NGC 5846.[6]

We model the set of data points of the gas mass density in each spherical shell provided by [386] with the function in Eq. (5.14), where the two normalisation constants are now $\rho_{\rm g,1}$ and $\rho_{\rm g,2}$. We estimate the parameters of the gas mass density with the MCMC method described in Sect. 5.3.2 adopting the Metropolis-Hasting acceptance criterion. Running the chains for 2×10^4 steps with 10^3 burn-in elements is sufficient to reach the convergence of the chains, according to the Geweke diagnostics [334]. We adopt uniform priors in the intervals listed in Table 5.6. The upper limits of $R_{\rm c,1}$ and $R_{\rm c,2}$ are the radii of the most external data point of the gas mass density profile in Eq. (5.18). The upper limits of $\rho_{\rm g,1}$ and $\rho_{\rm g,2}$ are slightly larger than the data point with the smallest R. Our posterior distributions are single-peaked, and we thus adopt the medians of the posterior distributions as our parameter estimates and the range between the 15.9 and 84.1 percentiles as our parameter uncertainties. The parameters of the model, along with their uncertainties, are listed in Table 5.6 and they provide the curve shown in Fig. 5.2.

Table 5.6: Priors and parameters of the 3D mass density model of the hot X-ray emitting gas of NGC 5846.

$\rho_{\rm g,1}$ $\left[10^{-26}\frac{\rm g}{\rm cm^3}\right]$	$\rho_{\rm g,2}$ $\left[10^{-26}\frac{\rm g}{\rm cm^3}\right]$	$R_{\rm c,1}$ [arcsec]	$R_{\rm c,2}$ [arcsec]	β_1	β_2
(1)	(2)	(3)	(4)	(5)	(6)
$U(0, 12.6]$	$U(0, 12.6]$	$U(0, 368]$	$U(0, 368]$	$U(0, 3]$	$U(0, 3]$
$3.21^{+0.62}_{-1.21}$	$6.05^{+0.69}_{-0.68}$	34^{+13}_{-9}	18^{+4}_{-5}	$0.4985^{+0.0026}_{-0.0007}$	$0.95^{+0.52}_{-0.47}$

U stands for uniform distribution.

NGC 4486

We adopt the model derived by [388]. They model the X-ray surface brightness profile of the gas, $S_{\rm g}(R)$, measured in the 0.7–3.0 keV energy band with the *Einstein Observatory*, with

$$S_{\rm g}(R) = \frac{S_0}{(1 + bR^2 + cR^4 + dR^6)^n}, \tag{5.19}$$

where $b = 1.009$ arcmin^{-2}, $c = 2.386 \times 10^{-3}$ arcmin^{-4}, $d = 1.845 \times 10^{-7}$ arcmin^{-6}, and $n = 0.68$. To obtain the 3D mass density profile, they numerically invert Eq. (5.19), assuming an isothermal gas. They adopt zero metallicity, with a mean molecular weight $\mu = 0.6$, and model the numerical deprojected density distribution with the function

$$\rho(r) = \frac{\rho_0}{(1 + b'r^2 + c'r^4 + d'r^6)^{n'}}\,, \tag{5.20}$$

where $b' = 9.724 \times 10^{-1}$ arcmin^{-2}, $c' = 3.810 \times 10^{-3}$ arcmin^{-4}, $d' = 2.753 \times 10^{-8}$ arcmin^{-6}, $n' = 0.59$, and $\rho_0 = 1.0 \times 10^{-25}$ g cm^{-3}. These parameters are provided without uncertainty.

[6] In fact, assuming a null metallicity, and thus $\mu = 0.6$, leaves our results unaffected.

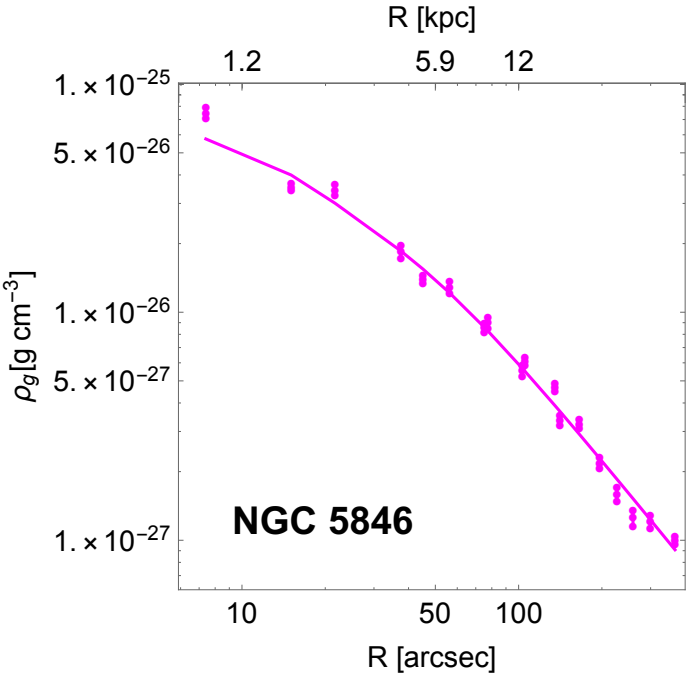

Figure 5.2: Mass density profile of the X-ray gas in NGC 5846. Magenta dots with error bars show the measured profile; the solid line is the model.

5.1.4 SMBH mass

We include the contribution of the central SMBH in our mass model. We adopt the SMBH masses provided by [376]: $M_\bullet = 4.5^{+0.9}_{-0.4} \times 10^9\ M_\odot$, $6.2^{+0.4}_{-0.5} \times 10^9\ M_\odot$, and $1.1^{+0.1}_{-0.1} \times 10^9\ M_\odot$ for NGC 1407, NGC 4486, and NGC 5846, respectively. We model the mass density of the SMBH as

$$\rho_\bullet(r) = \frac{M_\bullet}{4\pi r^2}\delta(r) \tag{5.21}$$

where δ is the Dirac δ function. The cumulative mass profile is thus $M(r) = M_\bullet$.

5.2 Spectroscopic data

5.2.1 Stellar velocity dispersion profiles

NGC 1407

For NGC 1407, we use the root-mean-square velocity dispersion profile of the stars measured by [81]. They derive the profile from two different data sets, depending on the radial range. For radii in the range of $[0, 30]$ arcsec, they use the long-slit data, along the major axis of the galaxy, from the European Southern Observatory Faint Object Spectrograph and Camera (v.2) (EFOSC2) [75]. For radii in the range of $[40, 110]$ arcsec, they use the multislit Keck/DEIMOS data [389], again along the galaxy major axis. In the overlapping range of $[30, 40]$ arcsec, they keep both data sets.

The root-mean-square velocity dispersion profile of the stars at the circularised projected radius R is

$$V_{\rm rms}(R) = \left[V^2_{\rm rot}(R) + \sigma^2(R)\right]^{1/2}\ , \tag{5.22}$$

where $\sigma(R)$ is the stellar velocity dispersion and $V_{\rm rot}(R) = V(R) - V_{\rm sys}$ is the major axis stellar rotation velocity in the galaxy frame, properly corrected for the angle between the major rotation axis and the galaxy region considered (see [75] for details), with $V(R)$ the observed rotation velocity, and $V_{\rm sys}$ the galaxy systemic velocity mainly due to the

Hubble flow (peculiar velocities are subdominant as stated in Sect. 5.1), given by $V_{\rm hel}$ in Table 5.1.

$V_{\rm rot}(R)$ and $\sigma(R)$ are estimated from the mean and the standard deviation of the Gaussian distribution that best fits the line-of-sight velocity distribution (LOSVD) of the stars derived from the spectral line profile [370, 77]. Cappellari and collaborators [390, 391] use semi-analytic dynamical models to show that $V_{\rm rms} = (V_{\rm rot}^2 + \sigma^2)^{1/2}$ obtained from this Gaussian fit is a better estimator of the second moment of the velocity distribution than the second moment estimated with the integral of the LOSVD modelled with a Gauss-Hermite parametrisation [392, 393]. This result is due to the sensitivity of $V_{\rm rot}$ and σ to the tails of the LOSVD, which are affected by large observational uncertainties [370, 77].

The analysis of [75] confirms that NGC 1407 is a slow rotator, namely $V_{\rm rot} \ll \sigma$; therefore, Eq. (5.22) yields $V_{\rm rms}(R) \approx \sigma(R)$. To obtain the final $V_{\rm rms}(R)$ profile, Pota and coauthors [81] fold and average the data with respect to the galaxy centre.

In our dynamical model described in Sect. 5.3, we assume an orbital anisotropy parameter β independent of 3D radius r, as [81] do. However, by fitting Schwarzschild orbit-superposition models to their kinematic data, Thomas and collaborators [394] infer a variable $\beta(r)$ within $R = 2$ arcsec of NGC 1407. Therefore, Pota and coauthors [81] only consider the $V_{\rm rms}$ profile beyond $R = 2$ arcsec $= 0.272$ kpc. The top-left panel of Fig. 5.3 shows the $V_{\rm rms}(R)$ profile of the stars obtained by [81].

NGC 4486 and NGC 5846

For NGC 4486 and NGC 5846, we derive $V_{\rm rms}(R)$ from the ATLAS$^{\rm 3D}$ survey [71]. All the data are publicly available on the ATLAS$^{\rm 3D}$ website.[7]

The available data provide the two-dimensional map of V and σ of the galaxy on the plane of the sky, where V and σ are the observed rotation velocity and velocity dispersion of the stars. In NGC 4486 and NGC 5846, 99.6% and 97.9% of the data points, respectively, have $V/\sigma \leq 0.2$. Therefore these galaxies, like NGC 1407, are slow rotators, and we have $V_{\rm rms} \approx \sigma$.

We rotate the galaxy map counter-clockwise in the new Cartesian coordinates $(x'_{\rm rot}, y'_{\rm rot})$, such that the photometric major axis of the galaxy is aligned with the east-west direction [395]. We iteratively remove the values of $V_{\rm rms}(x'_{\rm rot}, y'_{\rm rot})$ that deviate more than 3 standard deviations from the mean $V_{\rm rms}$ of the entire map [77]. For NGC 4486 and NGC 5846, the procedure converges after 7 and 6 iterations and removes 155 and 201 data points, respectively. This removal is necessary because some data points could be spurious, because of the presence of Milky Way stars or problematic bins at the edge of the field of view [77]. Finally, we transform the two-dimensional map $V_{\rm rms}(x'_{\rm rot}, y'_{\rm rot})$ in a one-dimensional profile, $V_{\rm rms}(R)$, by folding and averaging the data with respect to the galaxy centre.

This procedure yields $V_{\rm rms}(R)$ profiles with 2444 and 1752 data points for NGC 4486 and NGC 5846, respectively. These profiles are shown in the upper middle and right panels of Fig. 5.3. These numbers are $\sim$2 orders of magnitude larger than the number of data points in the kinematic profiles of the GC populations of the two galaxies (see Sect. 5.2.2). As confirmed by preliminary tests, with these unbalanced datasets the dynamical models are driven by the $V_{\rm rms}(R)$ of the stars and are basically insensitive to the GC kinematic profiles. To overcome this problem, we bin the stellar kinematic data. Each bin contains a constant number of data points: $N = 111$ for NGC 4486 and $N = 103$ for NGC 5846. NGC 4486 and NGC 5846 have now 22 and 17 binned data, respectively. These binned data are the medians, both in the $V_{\rm rms}$ and R directions, of the values of the N data points in the bin. The uncertainties are the semi-interval between the 15.9 and the 84.1 percentiles of the distributions, which are nearly symmetric, of the data points in the bin.

[7] http://www-astro.physics.ox.ac.uk/atlas3d/

In general, massive early-type galaxies, like these two galaxies, show negative orbital anisotropy parameters in their central regions, indicating tangential orbits; on the contrary, in the outer regions, the orbits appear radial [394, 396]. Numerical simulations show that this difference in the stellar orbits might originate if massive elliptical galaxies form from the merging of two progenitors with mass ratios larger than 1/3 [396]: at the centre of the new-born galaxy, the gravitational torques caused by the merging of the SMBHs of the two parent galaxies cause a reversal of the orbit behaviour, from radial to tangential. Therefore, because we assume below an orbital anisotropy parameter β independent of radius r, we exclude the innermost 2 arcsec in the kinematic profiles of NGC 4486 and NGC 5846. This projected radius corresponds to 0.167 kpc and 0.235 kpc for NGC 4486 and NGC 5846, respectively.

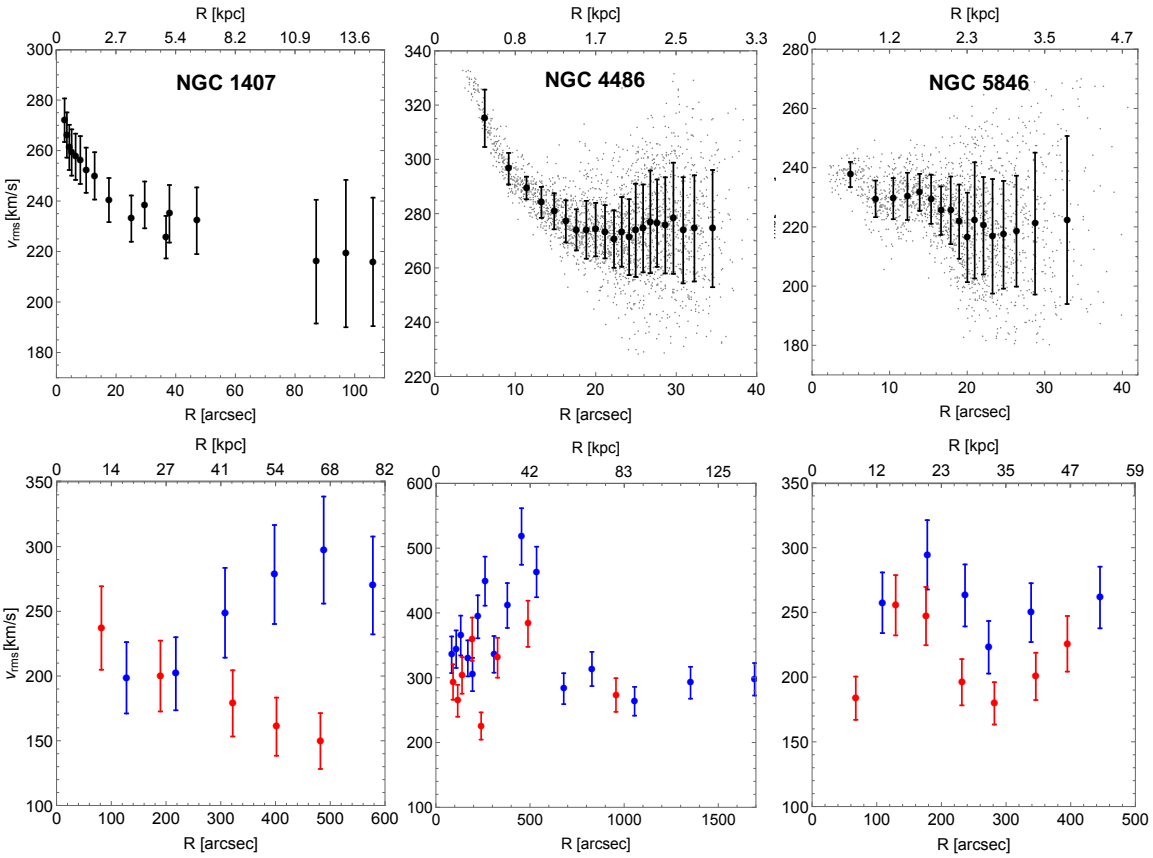

Figure 5.3: Root-mean-square velocity dispersion profiles of the stars (upper panels) and of the GCs (lower panels). Each column refers to the galaxy indicated in the upper panels. In the upper middle and right panels, the grey dots and the black dots with error bars show the unbinned and binned profiles, respectively. In the lower panels, the red and blue dots with error bars refer to the blue and red GC populations, respectively. Note the different radial and velocity ranges of the panels.

5.2.2 Velocity dispersion profiles of the GCs

NGC 4486 and NGC 5846

We derive the $V_{\rm rms}$ profiles of the GCs in NGC 4486 and NGC 5846 following the procedure of [76] and [81]. As already specified in Sect. 5.1.2, our samples of GCs contain 480 blue GCs and 199 red GCs in NGC 4486 and 91 blue GCs and 102 red GCs in NGC 5846.

We bin each GC population into circular annuli centred on the galaxy centre. Each annulus contains the same number of GCs. Specifically, each bin contains $N = 30$ and $N = 25$ GCs for the blue and red populations in NGC 4486 and $N = 26$ GCs for both populations in NGC 5846. These N's are a trade-off between too poor bins and a too coarse profile. For NGC 4486, we obtain 16 and 8 bins for the blue and the red

GCs, respectively. In NGC 5846, we obtain 6 and 7 bins for the blue and the red GCs, respectively. In NGC 5846, some GCs are common to contiguous bins, so that we have a sufficient number of bins despite the small total number of GCs. The radius R of each bin is the median of the radial coordinates of the GCs in the bin. The $V_{\rm rms}$ of the GCs in each bin is [76, 81]

$$V_{\rm rms}^2 = \frac{1}{N}\sum_{i=1}^{N}(V_{{\rm rad},i} - V_{\rm sys})^2 - (\Delta V_{{\rm rad},i})^2\,, \tag{5.23}$$

where $V_{{\rm rad},i}$ is the radial velocity of the i-th GC in the radial bin and $\Delta V_{{\rm rad},i}$ is its uncertainty [397, 398]. We take $V_{\rm rad}$ and $\Delta V_{\rm rad}$ from [365], for NGC 4486, and [76], for NGC 5846. To estimate the errors on each value of $V_{\rm rms}$ we use the procedure reported in [398], as performed by [81]. For convenience, we report this procedure in Appendix F.

The kinematic profiles of the GCs are shown in Fig. 5.3. These profiles are ∼48 and ∼13 times more extended than the kinematic profiles of the stars for NGC 4486 and NGC 5846, respectively. In NGC 4486, the root-mean-square velocity dispersion profiles of the GC populations show a bell-like shape that peaks at large radii, around ∼500 arcsec = ∼42 kpc. This feature suggests that the GC kinematics is influenced by the gravitational potential well of the Virgo cluster whose central giant elliptical galaxy is exactly NGC 4486 [365]. This shape is common to the stellar velocity dispersion profiles of other elliptical galaxies located at the centre of galaxy clusters, like the brightest cluster galaxy of Abell 383 [399].

NGC 1407

We extract the $V_{\rm rms}(R)$ profiles of the two populations of GCs in NGC 1407 from Fig. 5 of [81]. They derive the profiles with the same procedure that we adopt here for NGC 4486 and NGC 5846. Pota and coauthors [81] obtain their kinematic data from nine DEIMOS masks in [76] and an additional DEIMOS mask in [81]. They have a total sample of 379 GCs. After applying the photometric and kinematic selection criteria detailed in Sect. 5.1.2, Pota and coauthors [81] obtain a sample with 153 blue GCs and 148 red GCs. The kinematic profiles of the blue and red GC populations in NGC 1407 are shown in Fig. 5.3 and are ∼5 times more extended than the star profile.

5.3 Dynamical model

5.3.1 Basic equations

We model the kinematics of the three E0 galaxies by assuming spherical symmetry and no net rotation, as suggested by the observed slow rotation of the galaxies. We model the velocity dispersion profile of each dynamical tracer $\mathrm{t} = \{*, R, B\}$, namely stars, red GCs, and blue GCs, as

$$V_{\rm rms,t}^2(R) = \frac{2}{I_{\rm t}(R)}\int_R^{+\infty} K\left(\beta_{\rm t}, \frac{r}{R}\right)\nu_{\rm t}(r)\frac{{\rm d}\phi}{{\rm d}r}r\ {\rm d}r\,, \tag{5.24}$$

which is the solution to the spherical Jeans equations [400, 370, 356, 81]. In Eq. (5.24), R is the circularised radius projected onto the sky according to Eq. (5.2), whereas r is the 3D radius; $I_{\rm t}(R)$ is the surface brightness of the stars or the surface number density of GCs; $\nu_{\rm t}(r)$ is the 3D luminosity density of the stars or the 3D number density of GCs; $\phi(r)$ is the gravitational potential; and $\beta_{\rm t} = 1 - \sigma_\theta^2/\sigma_r^2$ is the orbital anisotropy parameter, with σ_θ and σ_r, the velocity dispersions in the tangential and the radial directions, respectively.

We assume β_t to be independent of r. K is the kernel

$$\begin{aligned} K\left(\beta_\mathrm{t}, \frac{r}{R}\right) =& \frac{1}{2}\left(\frac{r}{R}\right)^{2\beta_\mathrm{t}-1}\left[\left(\frac{3}{2}-\beta_\mathrm{t}\right)\right]\sqrt{\pi}\frac{\Gamma(\beta_\mathrm{t}-\frac{1}{2})}{\Gamma(\beta_\mathrm{t})} \\ &+ \beta_\mathrm{t} B_{\frac{R^2}{r^2}}\left(\beta_\mathrm{t}+\frac{1}{2},\frac{1}{2}\right) - B_{\frac{R^2}{r^2}}\left(\beta_\mathrm{t}-\frac{1}{2},\frac{1}{2}\right), \end{aligned} \tag{5.25}$$

where $\Gamma(z) = \int_0^{+\infty} t^{z-1}e^{-t}\,\mathrm{d}t$ is the Euler Γ function and $B_x(a,b) = \int_0^x t^{a-1}(1-t)^{b-1}\,\mathrm{d}t$ is the incomplete beta function (see Eq. A16 in [356]). By inserting the RG gravitational field obtained in spherical symmetry, Eq. (3.6), into Eq. (5.24), we obtain

$$V^2_{\mathrm{rms,t}}(R) = \frac{2G}{I_\mathrm{t}(R)}\int_R^{+\infty} K\left(\beta_\mathrm{t}, \frac{r}{R}\right)\nu_\mathrm{t}(r)\frac{M(r)}{\epsilon(\rho)}\frac{\mathrm{d}r}{r}\,. \tag{5.26}$$

In our model, $M(r)$ is the baryonic mass alone, namely

$$M(r) = M_*(r) + M_\mathrm{g}(r) + M_\bullet(r) + M_\mathrm{GC}(r)\,, \tag{5.27}$$

where $M_*(r)$, $M_\mathrm{g}(r)$, $M_\bullet(r)$, and $M_\mathrm{GC}(r)$ are the cumulative mass profiles of the stars, X-ray emitting gas, SMBH, and GCs, respectively. We estimate the mass profile of the stars as

$$M_*(r) = \Upsilon L_*(r)\,, \tag{5.28}$$

where $L_*(r)$ is the luminosity profile, Eq. (5.10), and Υ is the stellar mass-to-light ratio that we assume to be independent of r. In our dynamical model, Υ is a free parameter in the ranges predicted by the SPS models of [401] and [384], in the B-band, and [402] and [403], in the r-band. These ranges depend on the initial mass function. For the B-band, the range is $[4.0, 11.2]$ $M_\odot/L_\odot$ and the lower and upper limits are set by the Kroupa [404] and Salpeter [405] initial mass functions, respectively. For the r-band, the range is $[1.7, 5.5]$ $M_\odot/L_\odot$ and the lower and upper limits are set by the Bottema [406] and Salpeter [405] initial mass functions, respectively.

The mass profile of the gas, $M_\mathrm{g}(r)$, derives from the integration of its density profile. This density profile is indicated in Eq. (5.14), for NGC 1407 and NGC 5846, and in Eq. (5.20) for NGC 4486. For each galaxy, the mass of the SMBH, $M_\bullet$, is the value reported in Sect. 5.1.4. For the cumulative mass profile of GCs, we adopt

$$M_\mathrm{GC}(r) = M_\mathrm{GC} \times 4\pi\int_0^r \nu_\mathrm{GC}(r')r'^2\,\mathrm{d}r'\,, \tag{5.29}$$

where $\nu_\mathrm{GC}(r)$ is the 3D number density of GCs, Eq. (5.13), and M_GC is a constant in the range of $[10^4 - 10^6]M_\odot$, according to the typical mass function of GCs [407, 408].

Figure 5.4 shows the mass profile of each component. The stars provide the largest contribution to the total mass of each galaxy in most radial range, except in the very centre, where the SMBH dominates, and in the outskirts of NGC 4486 and NGC 5846, where the gas contribution overcomes the star contribution. The contribution of GCs to the total galaxy mass is always smaller than 1% and we thus ignore it hereafter. Therefore, in the velocity dispersion profile of Eq. (5.26), we also ignore the GC contribution to the density profile

$$\rho(r) = \rho_*(r) + \rho_\mathrm{g}(r) + \rho_\bullet(r)\,, \tag{5.30}$$

which appears as the argument of the permittivity of Eq. (3.5).

We solve Eq. (5.26) by adopting two independent linear grids in the R and the r coordinates. Both grids cover the range $[10^{-4}, 4800]$ arcsec, with a step of 4 arcsec.

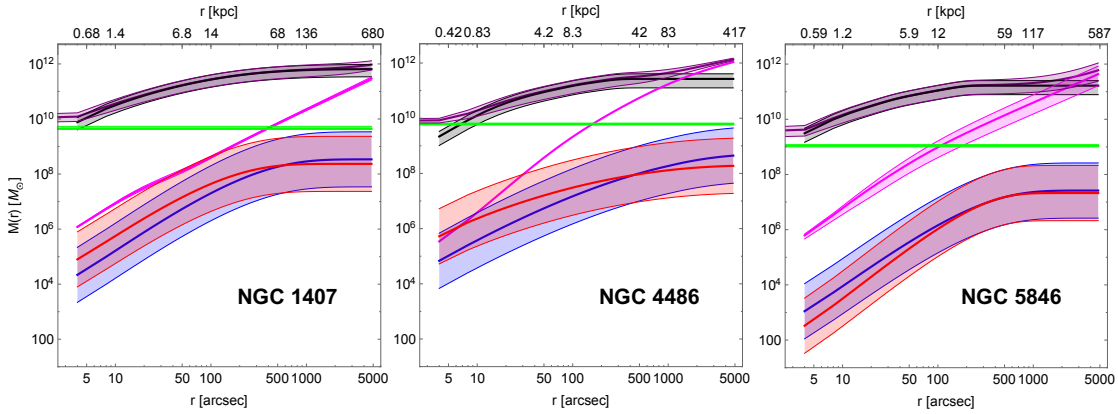

Figure 5.4: Cumulative mass profiles of the baryonic component of each galaxy: stars (black solid line), blue GCs (blue solid line), red GCs (red solid line), hot X-ray emitting gas (magenta solid line), and SMBH (green solid line). The purple solid line shows the sum of all the mass contributions. The stellar mass profiles assume $\Upsilon = 7.6\ M_\odot/L_\odot$ for NGC 1407, and $\Upsilon = 3.6\ M_\odot/L_\odot$ for NGC 4486 and NGC 5846. The grey shaded area around the star mass profiles shows the mass variation by adopting mass-to-light ratios in the range of $[4.0, 11.2]\ M_\odot/L_\odot$, for NGC 1407, and of $[1.7, 5.5]\ M_\odot/L_\odot$, for NGC 4486 and NGC 5846, in the B- and r-band, respectively. The mass profiles of blue and red GCs assume a GC mass $M_{\rm GC} = 10^5\ M_\odot$; the blue and red shaded areas show the mass variation by adopting $M_{\rm GC}$ in the range of $[10^4, 10^6]\ M_\odot$. The gas mass profile of NGC 4486 has no shaded area because the uncertainties on the adopted mass density profile are unavailable. The green solid lines and shaded areas are the masses of the SMBH and their uncertainties. The purple shaded areas show the uncertainty on the total baryonic mass profile.

5.3.2 The MCMC approach

For each galaxy, the dynamical model has seven free parameters: four parameters, Υ, ϵ_0, Q and $\rho_{\rm c}$, contribute to the gravitational potential well of the galaxy and are common to the three tracers, and three parameters, β_*, $\beta_{\rm B}$ and $\beta_{\rm R}$, are specific for each tracer. Note that the contributions of the X-ray emitting gas and the SMBH to the gravitational potential have no free parameters. For convenience, hereafter, we use the parameters $\mathcal{B}_* = -\log_{10}(1-\beta_*)$, $\mathcal{B}_{\rm B} = -\log_{10}(1-\beta_{\rm B})$, $\mathcal{B}_{\rm R} = -\log_{10}(1-\beta_{\rm R})$, and $\mathcal{P}_{\rm c} = \log_{10}[\rho_{\rm c}\,({\rm g/cm^3})]$. Tangential and radial orbits correspond to $\mathcal{B}_{\rm t} < 0$ and $\mathcal{B}_{\rm t} > 0$, respectively, where ${\rm t} = (*, {\rm B}, {\rm R})$.

We explore this seven-dimensional parameter space with a MCMC algorithm, where we adopt a Metropolis-Hastings acceptance criterion: the random variate $\vec{x}_{i+1} = (\Upsilon_*, \epsilon_0, Q, \mathcal{P}_{\rm c}, \mathcal{B}_*, \mathcal{B}_{\rm B}, \mathcal{B}_{\rm R})$, at step $i+1$ of the chain, is obtained from the probability density $G(\vec{x}_{i+1}|\vec{x}_i)$, which depends on the random variate $\vec{x}_i$ at the previous step. For $G(\vec{x}|\vec{x}_i)$, we adopt a multi-variate Gaussian density distribution with mean value $\vec{x}_i$. We choose the standard deviation of this Gaussian distribution according to the priors: when we adopt uniform priors, the standard deviation is 10% of the ranges of the prior; when we adopt Gaussian priors, the standard deviation is 1/3 of the standard deviation of the prior.

We adopt the likelihood

$$\mathcal{L}(\vec{x}) = \exp\left[-\frac{\chi^2_{\rm red,tot}(\vec{x})}{2}\right], \tag{5.31}$$

where

$$\chi^2_{\rm red,tot}(\vec{x}) = \frac{\chi^2_*(\vec{x}) + \chi^2_{\rm B}(\vec{x}) + \chi^2_{\rm R}(\vec{x})}{n_{\rm dof,tot}}, \tag{5.32}$$

and

$$\chi^2_{\rm t}(\vec{x}) = \sum_{i=1}^{N_{\rm t}} \frac{\left[V_{\rm rms,mod,t}(R_i,\vec{x}) - V_{\rm rms,data,t}(R_i)\right]^2}{\Delta V^2_{\rm rms,data,t}(R_i)}, \tag{5.33}$$

where ${\rm t} = (*, {\rm B}, {\rm R})$, $N_{\rm t}$ is the number of data points of the tracer, $V_{\rm rms,data,t}$ and $\Delta V_{\rm rms,data,t}$ are the measured root-mean-square velocity dispersions at the projected distances R_i, and their uncertainties, and $V_{\rm rms,mod,t}$ is the root-mean-square velocity dispersion model

derived from Eq. (5.26). The total number of degrees of freedom is

$$n_{\rm dof,tot} = N_* + N_{\rm B} + N_{\rm R} - N_{\rm par}, \tag{5.34}$$

where $N_{\rm par} = 7$ is the number of the free parameters of the model.

The Metropolis–Hastings ratio is

$$A = \frac{p(\vec{x}) \times \mathcal{L}(\vec{x})}{p(\vec{x}_i) \times \mathcal{L}(\vec{x}_i)} \frac{G(\vec{x}|\vec{x}_i)}{G(\vec{x}_i|\vec{x})}, \tag{5.35}$$

where $p(\vec{x})$ is the product of the priors of the components of $\vec{x}$. If $A \geq 1$, we accept the proposed combination of free parameters and we thus set $\vec{x}_{i+1} = \vec{x}$; otherwise, we either set $\vec{x}_{i+1} = \vec{x}$, with probability A, or $\vec{x}_{i+1} = \vec{x}_i$, with probability $1 - A$. We adopt 2×10^4 steps for our MCMC, a number sufficient to achieve the chain convergence, according to the Geweke diagnostics [334]. The first 10^3 elements are discarded as part of the burn-in chains.

5.4 Results

5.4.1 Priors

To model each galaxy with our MCMC analysis, we need to adopt a prior for each of our seven free parameters. For NGC 1407, the photometric information available in the B-band suggests the uniform prior $[4.0, 11.2]$ $M_\odot/L_\odot$ for Υ. For NGC 4486 and NGC 5846, with photometric information in the r-band, we adopt the uniform prior $[1.7, 5.5]$ $M_\odot/L_\odot$. We choose both prior ranges according to the ranges expected from the SPS models mentioned in Sect. 5.3 [401, 384, 402, 403]. For all the three orbital anisotropy parameters, $\mathcal{B}_*$, $\mathcal{B}_{\rm B}$, and $\mathcal{B}_{\rm R}$, we adopt the uniform prior $[-1.5, 1.0]$, thus including almost all possible orbits, from very tangential to very radial. Except for the prior of Υ in the r-band for NGC 4486 and NGC 5846, our priors coincide with those adopted by [81], who model the kinematics of NGC 1407 in Newtonian gravity with a generalised Navarro-Frenk-White DM halo [409, 410].

For the three permittivity parameters, we adopt uniform priors in the ranges $(0, 1]$, $[0.01, 2]$, and $[-27, -23]$, for ϵ_0, Q, and $\mathcal{P}_{\rm c}$, respectively. These priors are those adopted in [97], except for ϵ_0: our range here is wider, compared to the range $[0.1, 1]$ of [97].

5.4.2 Refining the priors

Figures 5.5–5.7 show the posterior distributions of the parameters of the model for each galaxy and Fig. 5.8 shows the models of the $V_{\rm rms}$ profiles whose parameters are the medians of the posterior distributions. The description of the kinematics of NGC 4486 and NGC 5846 shown in Fig. 5.8 appears satisfactory. However, this result is not shared by NGC 1407, despite the convergence of its MCMC: the model of the blue GCs severely underestimates the corresponding kinematic data. The corner plots in Fig. 5.5 show that the nearly flat posterior distribution of Q, the broad posterior distributions of ϵ_0, $\mathcal{B}_{\rm B}$, and $\mathcal{B}_{\rm R}$ without distinct peaks, and the substantial uncorrelation between several pairs of parameters, complicate the identification of the best values of ϵ_0, Q, $\mathcal{B}_{\rm B}$, and $\mathcal{B}_{\rm R}$; therefore, adopting the medians of the posterior distribution for these values is unconvincing.

This conclusion also applies to NGC 4486 and NGC 5846, despite the fact that the estimated parameters appear to provide a proper modelling of their kinematic profiles. Indeed, Figs. 5.6 and 5.7 show that the one-dimensional posterior distributions of Q and $\mathcal{B}_{\rm R}$ of both galaxies are broad and their medians do not coincide with their peaks. In addition, the posterior distributions show that most parameters are independent of each other.

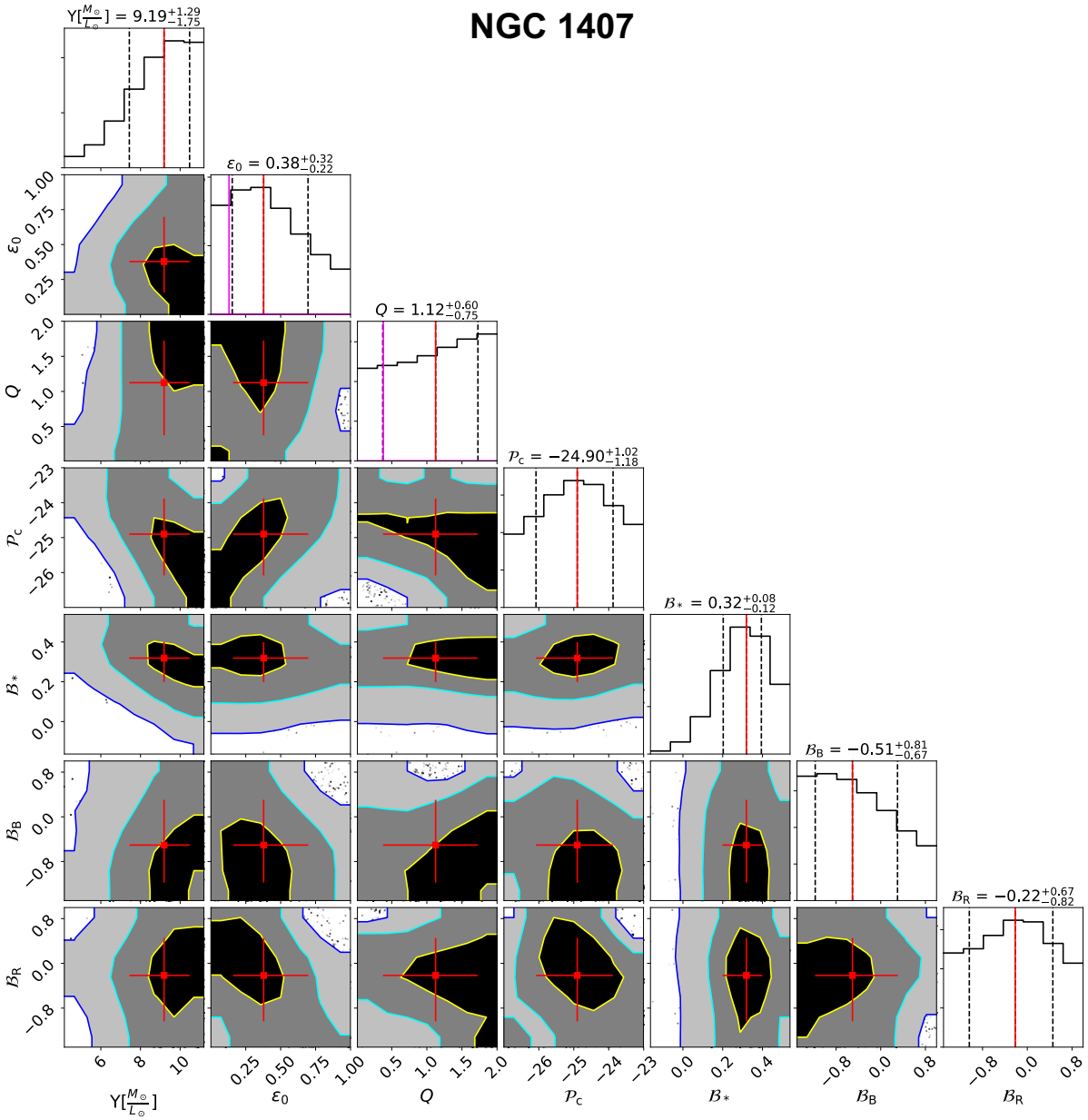

Figure 5.5: Posterior distributions of the seven parameters of our first MCMC analysis adopting uniform priors for NGC 1407. The parameters are the stellar mass-to-light ratio, Υ, the anisotropy parameters of the three tracers, $\mathcal{B}_*$, $\mathcal{B}_B$, $\mathcal{B}_R$, and the three permittivity parameters, ϵ_0, Q, and $\mathcal{P}_c$. The red squares with error bars show the medians and their uncertainties, set by the 15.9 and 84.1 percentiles of the posterior distributions. The yellow, cyan, and blue contours limit the 1σ, 2σ, and 3σ regions, respectively. The medians and their uncertainties are also reported above each column and in the one-dimensional posterior distributions in the top panels of each column as red solid and black dashed lines, respectively. The magenta solid lines in the one-dimensional posterior distributions of ϵ_0 and Q show the means of the Gaussian priors that we adopt in our second MCMC analysis.

We thus perform a second MCMC analysis with refined prior distributions as follows. For NGC 1407, the first MCMC analysis shows that the values $\epsilon_0 = 0.13$ and $Q = 0.38$ yield a reasonable description of the kinematic data, almost independently of the values of $\mathcal{P}_c$ and of the other parameters. In our second MCMC analysis, for ϵ_0 and Q, we thus adopt Gaussian priors with means and standard deviations $\epsilon_0 = 0.13 \pm 0.05$ and $Q = 0.38 \pm 0.05$. These two means are approximately 1σ smaller than the medians of the posterior distributions of the first MCMC analysis (Fig. 5.5). For the other parameters, we keep the flat priors of the first analysis. Peaking the priors of the three permittivity parameters to the global values found from the DMS sample, listed in Sect. 4.3, would apparently be more sensible and unbiased. Yet, since a $\epsilon_0 = 0.38$, obtained from the first MCMC run, cannot provide a sufficient boost of the RG gravitational field to reproduce

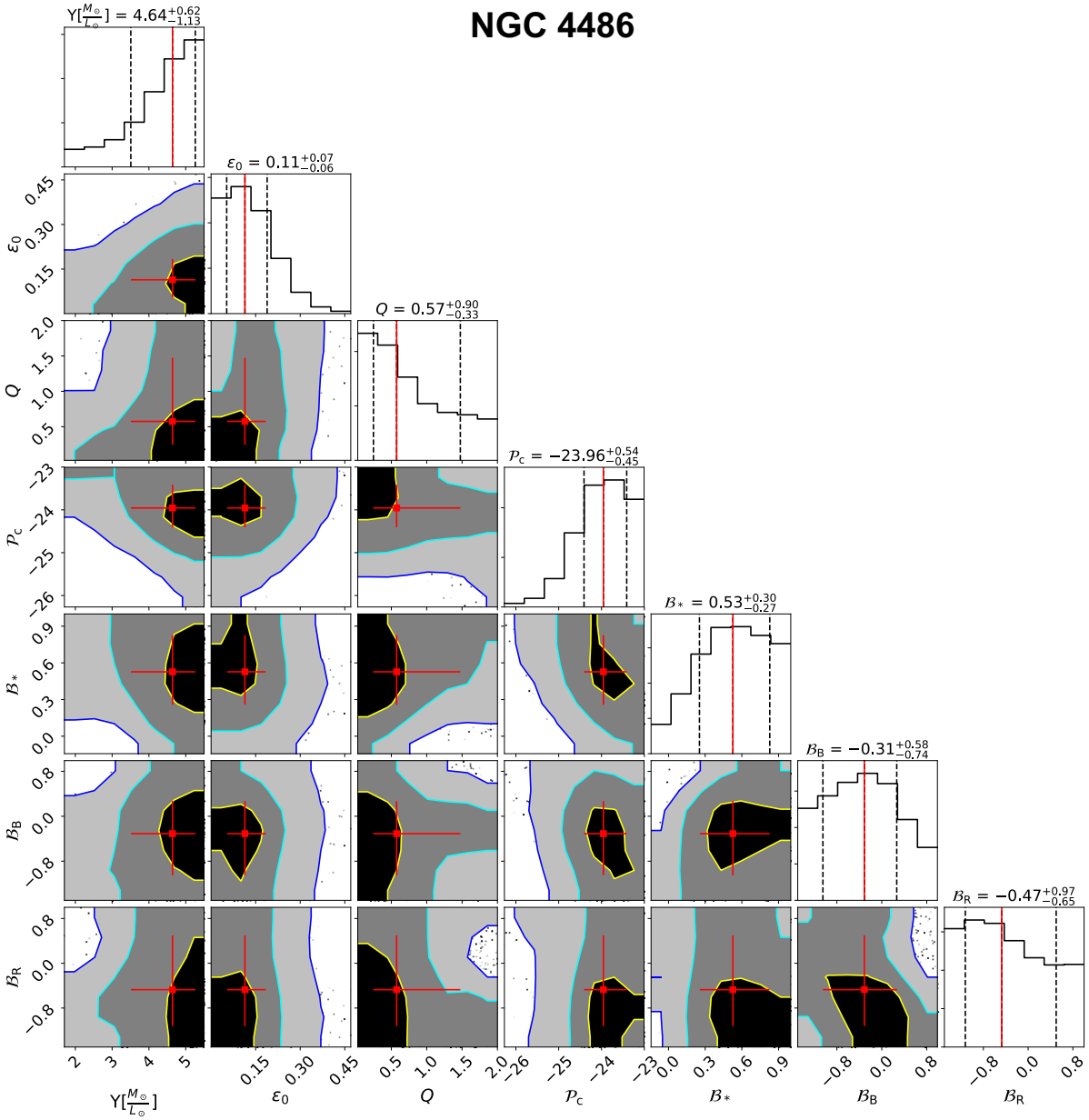

Figure 5.6: Same as Fig. 5.5 for NGC 4486.

the observed kinematic profile of the blue GCs, a $\epsilon_0 = 0.661$, obtained from the entire DMS sample, would provide an even more severe underestimation of the kinematic data, even for a larger value of Q. For this reason, it is thus preferable to force the ϵ_0 and Q parameters close to values that provide the adequate boost of the gravitational field to describe the data and to leave more freedom to the other parameters of the model.

For NGC 4486 and NGC 5846, the medians of the posterior distributions estimated from the first MCMC analysis reproduce the kinematic data well. We thus simply adopt Gaussian priors peaked on these values for these two galaxies. We set the standard deviations of the Gaussians for all the parameters, except Υ_* and $\mathcal{P}_c$, to the mean uncertainties estimated from the first analysis; for Υ and $\mathcal{P}_c$, we set the standard deviations to three times the mean uncertainties. We adopt larger dispersions for these two parameters because the relative widths of their posterior distributions derived in the first analysis are in the narrow range $[1.6, 22]\%$: setting the second moment to this range would thus limit the exploration of the parameter space in the second MCMC analysis. On the contrary, the relative widths of the other parameters are in the range $[43, 213]\%$ and setting the second moment of the Gaussians to this width provides sufficiently broad priors. The

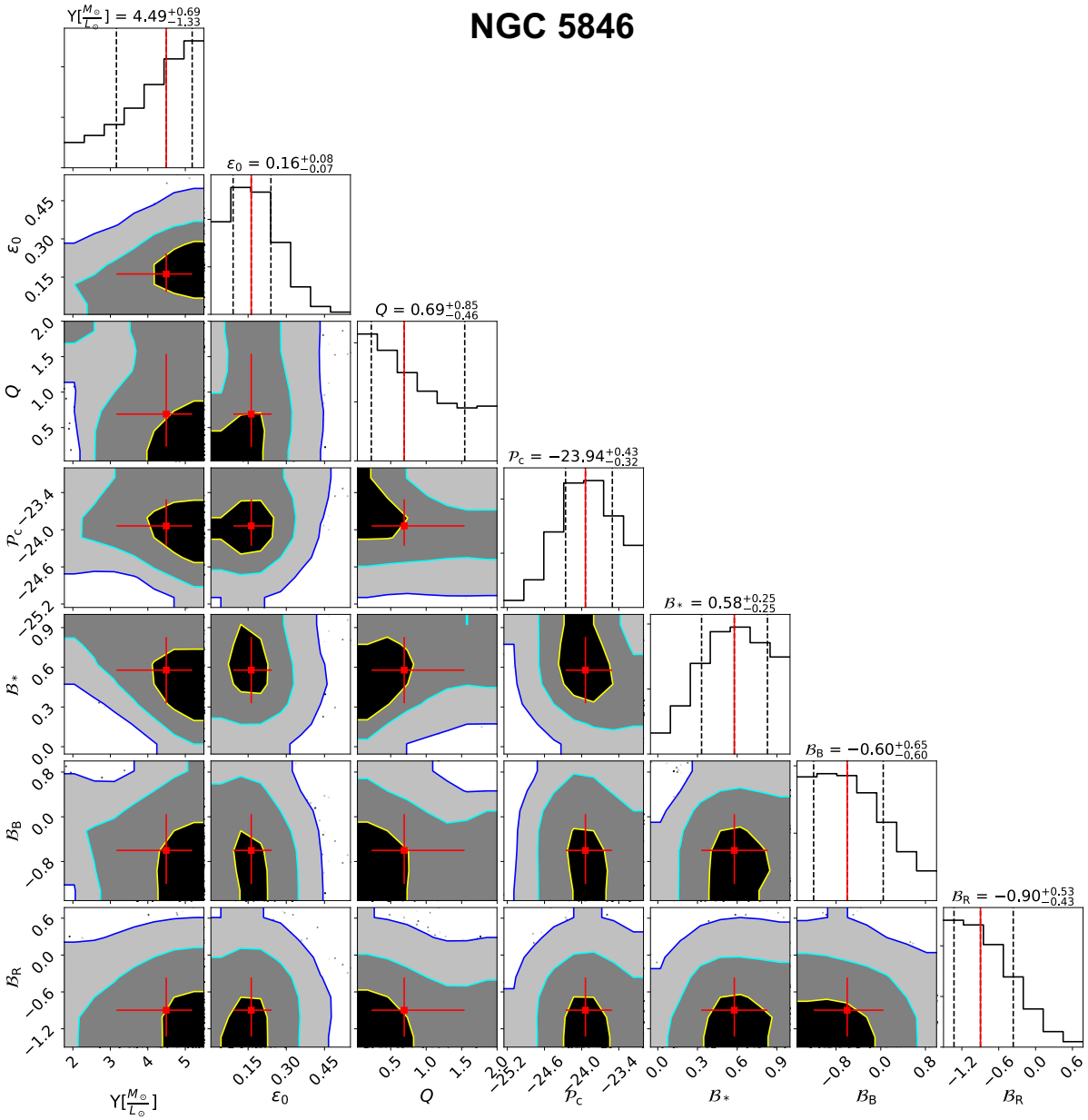

Figure 5.7: Same as Fig. 5.5 for NGC 5846.

Gaussian priors are set to zero outside the ranges listed in Table 5.7. This choice prevents the exploration of unphysical or unreasonable values.

5.4.3 Velocity dispersion profiles

The posterior distributions determined by our second MCMC analysis are shown in Figs. 5.9–5.11 and have well-identified peaks. We can thus adopt the medians of these distributions as the parameters of our model. As uncertainties on these parameters, we adopt the range between the 15.9 and the 84.1 percentiles of the posterior distributions. Table 5.8 lists the parameters that we find and that we use to plot the curves of the models shown in Fig. 5.12. Table 5.8 also lists the reduced χ^2's, Eq. (5.32), that quantify the agreement between these curves and the data.

The refinement of the priors improves the data description for all the three galaxies. For NGC 1407, the kinematics of the stars, red and blue GCs appears to be satisfactorily described by RG. The underestimation of the profile of the blue GCs disappears. For NGC 4486 and NGC 5846, the kinematic model of the stars and red GCs also appears

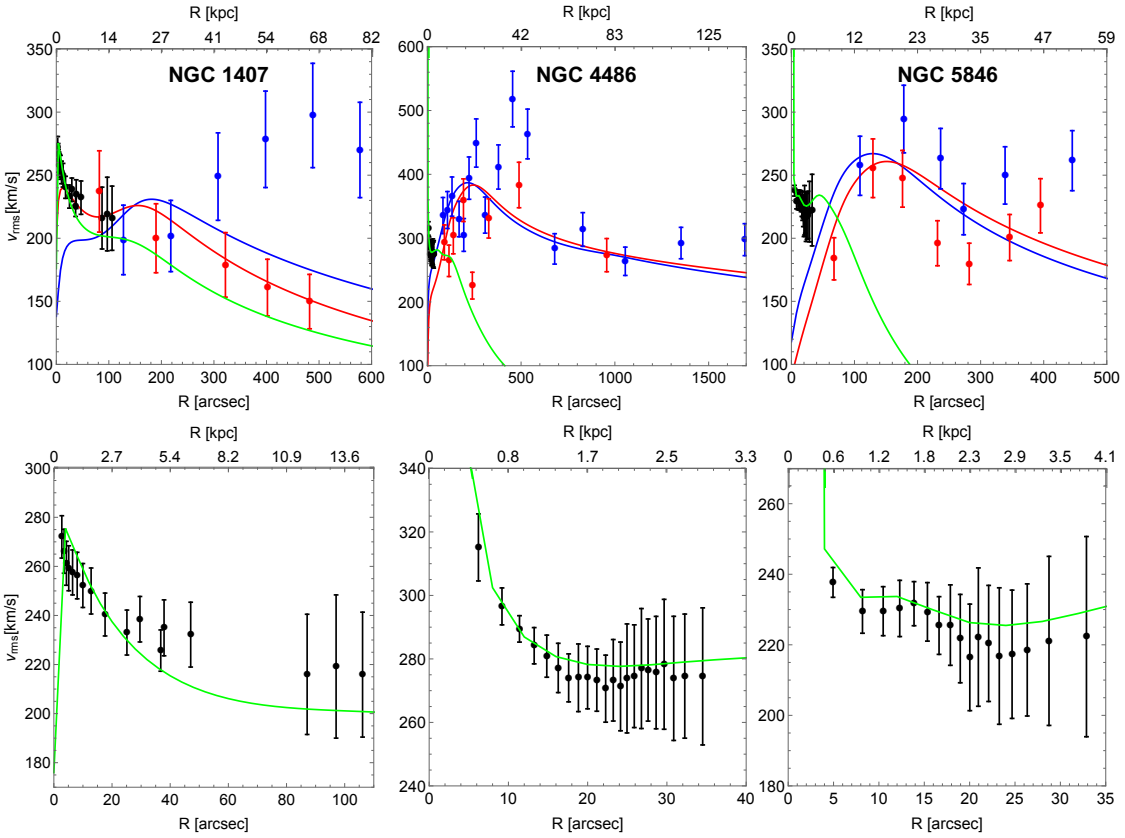

Figure 5.8: Models of the root-mean-square velocity dispersion profiles emerging from our first MCMC analysis. In the upper panels, the green, blue, and red solid lines show the model profiles for the stars, blue GCs, and red GCs, respectively. The lower panels show a zoom-in of the stellar profiles. The dots with error bars are the measured profiles from Fig. 5.3.

appropriate. This result is not shared, however, by the blue GCs. In NGC 5846, RG underestimates the outer points of the measured profile, whereas, in NGC 4486, RG cannot interpolate the peak of the velocity dispersion profile. These data are the main cause of the large values of the χ^2: if we remove these data points, the reduced χ^2's decrease from 1.71 to 0.99 and from 3.30 to 2.37, for NGC 5846 and NGC 4486, respectively. These poor fits might originate from the assumption that these two galaxies are isolated rather than embedded in a larger system, as we discuss below. The fits might also partly improve if we remove our assumption that the velocity anisotropy parameters β are independent of radius r or that the galaxies have null net rotation: albeit weak, the net galaxy rotation is not completely absent in the real galaxies.

Nevertheless, RG overall provides a global good description of the kinematic data of the three tracers for all the three galaxies with stellar mass-to-light ratios consistent with the SPS models. For NGC 1407, the values of Υ, $\mathcal{B}_*$, $\mathcal{B}_\mathrm{B}$, and $\mathcal{B}_\mathrm{R}$ that we obtain are at $+0.38\sigma$, $+0.67\sigma$, $+0.79\sigma$, and -0.17σ, respectively, from the parameters found by [81] in their analysis with Newtonian gravity and a DM halo.

The RG models require radial orbits for the stars and tangential orbits for the blue GCs in all the three galaxies. The red GCs have tangential orbits in NGC 4486 and NGC 5846, and radial orbits in NGC 1407, in agreement with the result found by [81] in Newtonian gravity for NGC 1407.

5.4.4 Parameters of the RG permittivity

The orange squares with error bars in Fig. 5.13 show the permittivity parameters estimated for the three E0 galaxies: the parameters are consistent with each other within $\sim 1\sigma$, suggesting their universality. Their mean values are $\{\epsilon_0, Q, \mathcal{P}_\mathrm{c}\} = \{0.15^{+0.05}_{-0.05}, 0.59^{+0.36}_{-0.25}, -24.51^{+0.58}_{-0.68}\}$. Figure 5.13 also shows the permittivity parameters derived from 30 disk

galaxies of the DMS sample [97]: the purple squares with error bars show the means of the parameters estimated for each individual DMS galaxy, whereas the green dots at the centre of the shaded areas show the global values derived with an approximate procedure from the entire 30 galaxy sample.

Our estimates of $\mathcal{P}_c$ and Q are within 1σ from the DMS mean values, whereas the DMS permittivity of the vacuum ϵ_0 is within 2.5σ from our values. This marginal discrepancy might originate from our simplistic modelling of the E0 galaxies. Indeed, here we assume that these galaxies have not net rotation and are relaxed and isolated, whereas, in fact, these galaxies are in clusters or groups and show sign of interactions with nearby galaxies: NGC 1407 is at the centre of the Eridanus A group [411] and certainly feels the gravitational influence of its neighbour galaxy NGC 1400. NGC 4486, namely M87, is the central giant elliptical galaxy of the Virgo cluster [365] and NGC 5846 is the central and brightest galaxy of a galaxy group [412]. Moreover, the GC sample of NGC 5846 might be contaminated by the GCs of its neighbour NGC 5846A [76]. The environment has a relevant effect on the intensity of the gravitational field in RG [300]; this effect clearly propagates into the actual values of the permittivity parameters. The environmental effects can also be responsible for the poor fitting of the velocity dispersion profiles of the blue GCs of NGC 4486 and NGC 5846 shown in Fig. 5.12. It would thus be necessary to refine our model by taking into account the effects of both rotation and the mass distribution surrounding the galaxies.

The tension between our permittivity parameters and those derived from the DMS sample might become more severe if we consider the DMS global values, namely the green dots in Fig. 5.13. Our $\mathcal{P}_c$ and Q are still within 3σ from the DMS parameters, whereas ϵ_0 shows a $\sim 10\sigma$ tension, clearly driven by the small width of the posterior distribution of the DMS global value. This discrepancy might be due to the approximate procedure adopted by [97] to estimate this DMS global value: with their MCMC analysis, Cesare and collaborators [97] only explore the space of the three permittivity parameters while keeping fixed the mass-to-light ratio Υ and the disk-scale height h_z of each of the 30 individual galaxies. This approach is a shortcut to the appropriate, but computationally overwhelming, procedure of exploring the 63-dimensional parameter space of the full sample, namely the properties, Υ and h_z, of all the galaxies and the three permittivity parameters. The set of the permittivity global parameters returned by this shortcut still describes the kinematic profiles of each galaxy, but the agreement is poorer than the agreement obtained by modelling each galaxy individually. Therefore these values of the permittivity parameters should be considered with caution.

We have to remember that the values of the permittivity parameters partially depend on the value of the Hubble constant, that we assume to be $H_0 = 73$ km s^{-1} Mpc^{-1} and it is subjected to large uncertainties. Indeed, the CMB power spectrum measured with the Planck satellite [413] suggests a Hubble parameter equal to 67 km s^{-1} Mpc^{-1}. Yet, a variation of the Hubble constant does not translate in a significant variation in the permittivity parameters such as to solve the tension with the vacuum permittivity derived from the DMS. We estimate that adopting $H_0 = 67$ km s^{-1} Mpc^{-1} might result in a change in the permittivity parameters of $\sim 0.5\%$ with respect to the case with $H_0 = 73$ km s^{-1} Mpc^{-1}.

Table 5.7: Priors of the parameters of the kinematic model, Eq. (5.26), adopted in our final analysis.

NGC	Υ_* $\left[\frac{M_\odot}{L_\odot}\right]$	ϵ_0	Q	$\mathcal{P}_\mathrm{c}$	$\mathcal{B}_*$	$\mathcal{B}_\mathrm{B}$	$\mathcal{B}_\mathrm{R}$
(1)	(2)	(3)	(4)	(5)	(6)	(7)	(8)
1407	$U[4.0, 11.2]$	$G(0.13, 0.05)$ $\in (0, 1]$	$G(0.38, 0.05)$ $\in [0.01, 2]$	$U[-27, -23]$	$U[-1.5, 1.0]$	$U[-1.5, 1.0]$	$U[-1.5, 1.0]$
4486	$G(4.64, 2.64)$ $\in (0, +\infty)$	$G(0.11, 0.07)$ $\in (0, 1]$	$G(0.57, 0.62)$ $\in [0.01, 2]$	$G(-23.96, 1.50)$ $\in [-27, -23]$	$G(0.53, 0.29)$	$G(-0.31, 0.66)$	$G(-0.47, 0.81)$
5846	$G(4.49, 3.03)$ $\in (0, +\infty)$	$G(0.16, 0.08)$ $\in (0, 1]$	$G(0.69, 0.66)$ $\in [0.01, 2]$	$G(-23.94, 1.14)$ $\in [-27, -23]$	$G(0.58, 0.25)$	$G(-0.60, 0.63)$	$G(-0.90, 0.48)$

Column 1: galaxy name; Cols. 2–8: free parameters of the kinematic model, Eq. (5.26). U and G stand for uniform and Gaussian distributions, respectively. For the uniform distributions, we list the entire range. For the Gaussian distributions, we list the mean, the standard deviation and, on the second line of each galaxy, the range explored by the MCMC.

Table 5.8: Parameters estimated from the three dynamical tracers.

NGC	Υ_* $\left[\frac{M_\odot}{L_\odot}\right]$	ϵ_0	Q	$\mathcal{P}_\mathrm{c}$	$\mathcal{B}_*$	$\mathcal{B}_\mathrm{B}$	$\mathcal{B}_\mathrm{R}$	$\chi^2_\mathrm{red,tot}$
(1)	(2)	(3)	(4)	(5)	(6)	(7)	(8)	(9)
1407	$8.4^{+1.6}_{-2.1}$	$0.14^{+0.05}_{-0.05}$	$0.37^{+0.06}_{-0.05}$	$-25.13^{+0.77}_{-0.81}$	$0.35^{+0.08}_{-0.10}$	$-0.58^{+0.80}_{-0.58}$	$0.17^{+0.56}_{-0.83}$	1.03
4486	$5.6^{+1.2}_{-1.6}$	$0.12^{+0.04}_{-0.04}$	$0.64^{+0.48}_{-0.30}$	$-24.33^{+0.56}_{-0.77}$	$0.45^{+0.25}_{-0.22}$	$-0.20^{+0.45}_{-0.52}$	$-0.42^{+0.87}_{-0.77}$	3.30
5846	$5.1^{+1.5}_{-1.5}$	$0.18^{+0.05}_{-0.05}$	$0.75^{+0.53}_{-0.39}$	$-24.08^{+0.42}_{-0.45}$	$0.51^{+0.21}_{-0.19}$	$-0.68^{+0.50}_{-0.58}$	$-0.92^{+0.37}_{-0.45}$	1.71

Column 1: galaxy name; Cols. 2–8: medians of the posterior distributions with their uncertanties; Col. 9: reduced chi-square, $\chi^2_\mathrm{red,tot}$, from Eq. (5.32).

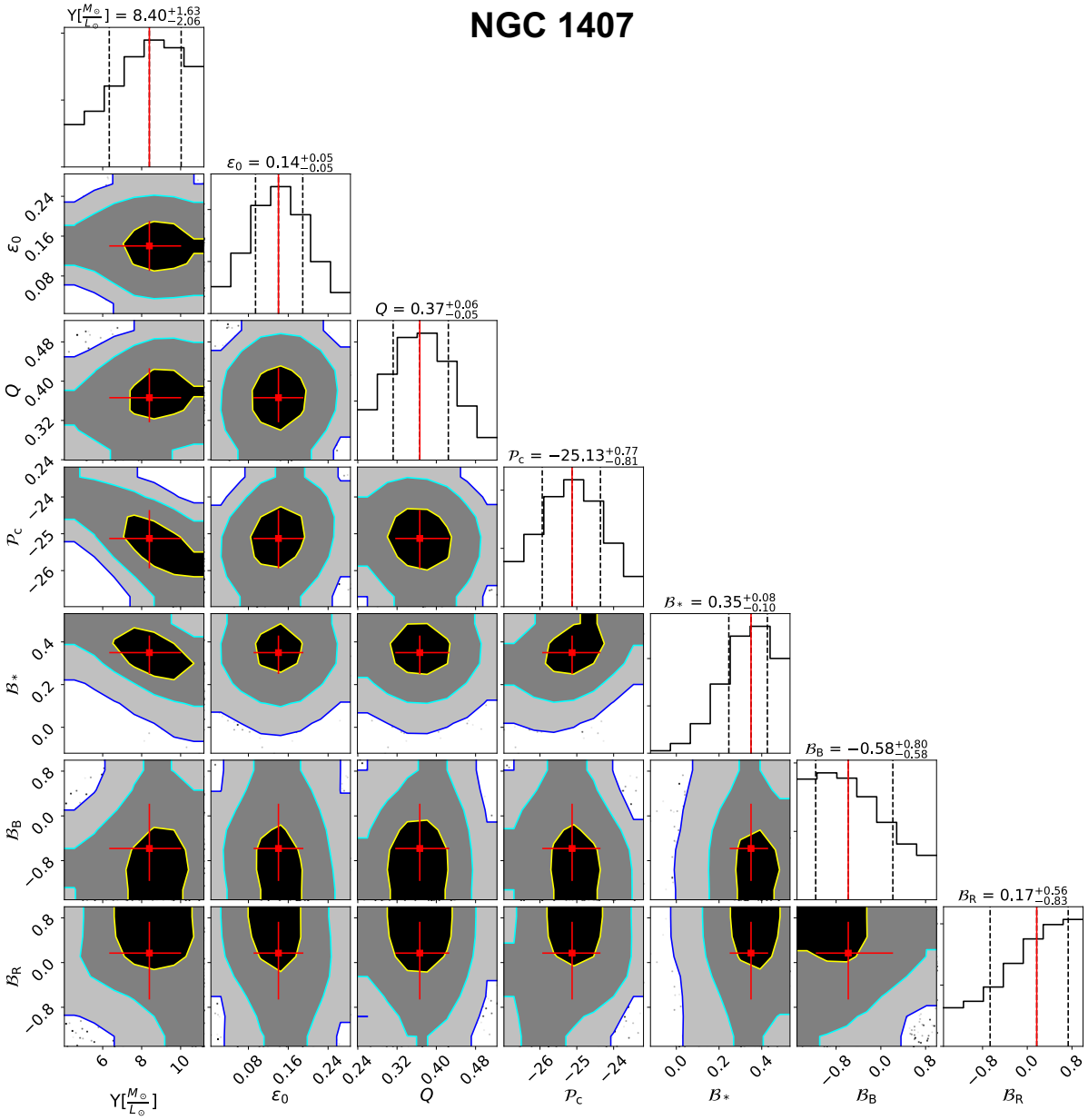

Figure 5.9: Same as Fig. 5.5 for our second MCMC analysis.

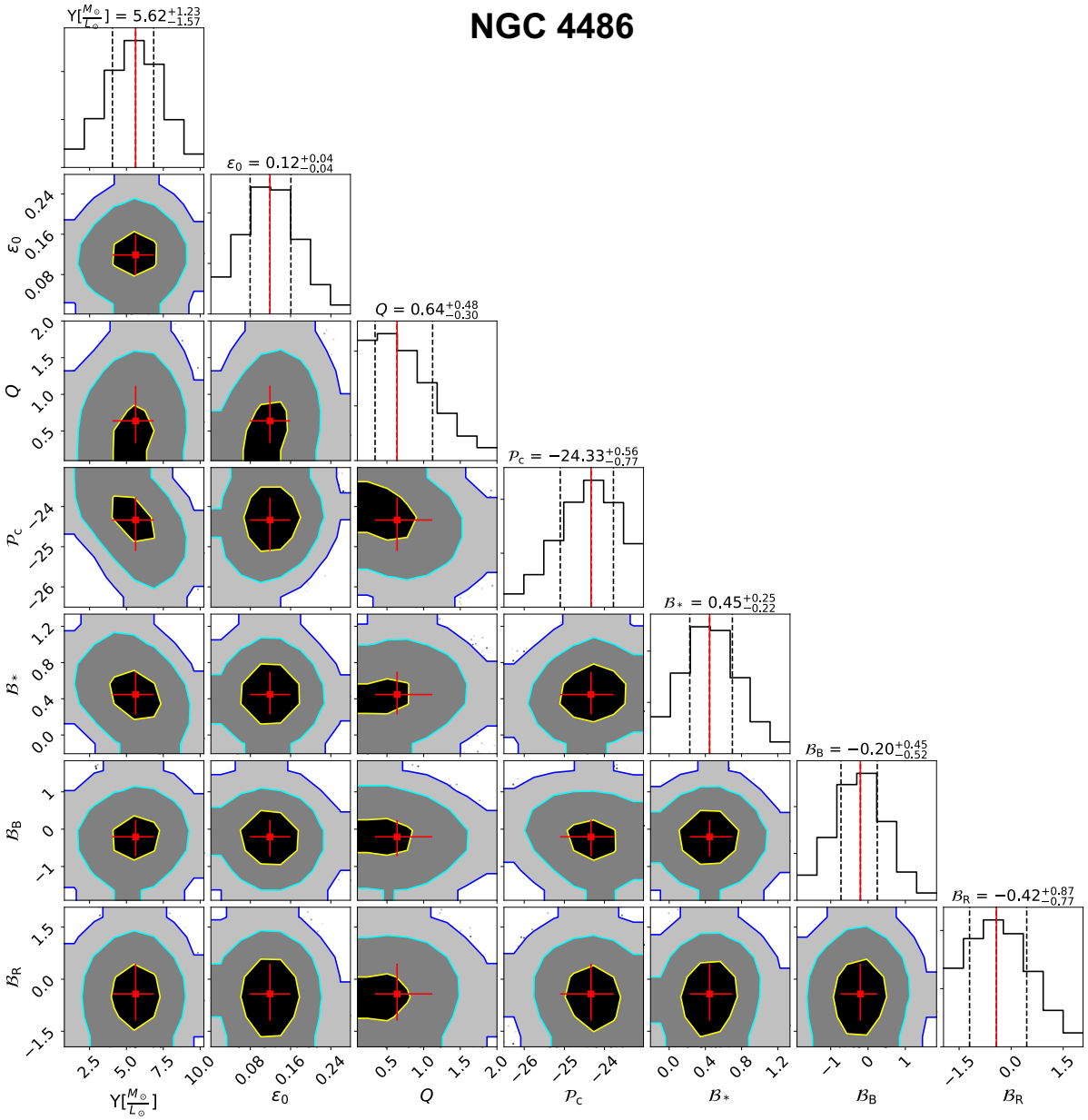

Figure 5.10: Same as Fig. 5.6 for our second MCMC analysis.

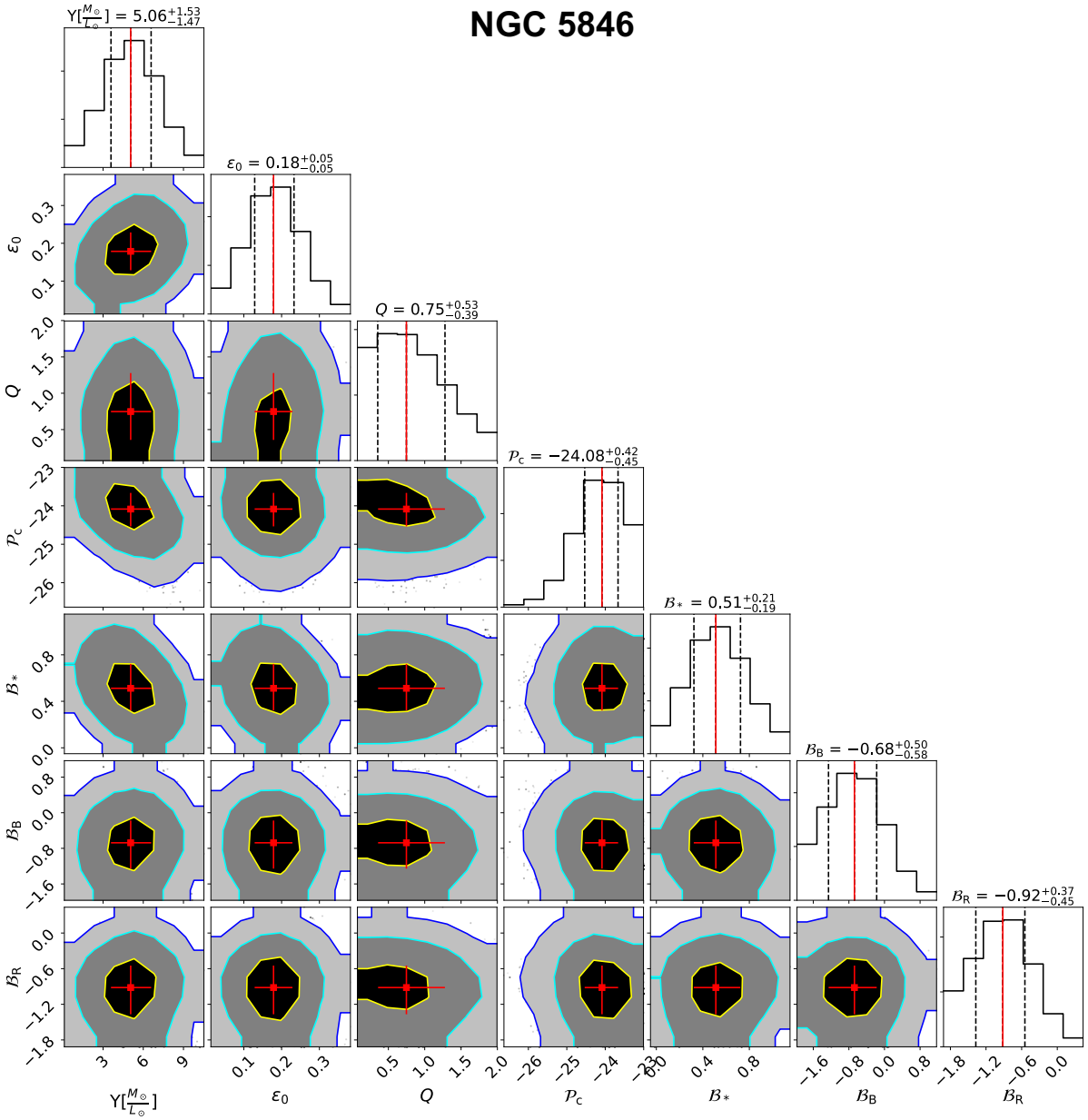

Figure 5.11: Same as Fig. 5.7 for our second MCMC analysis.

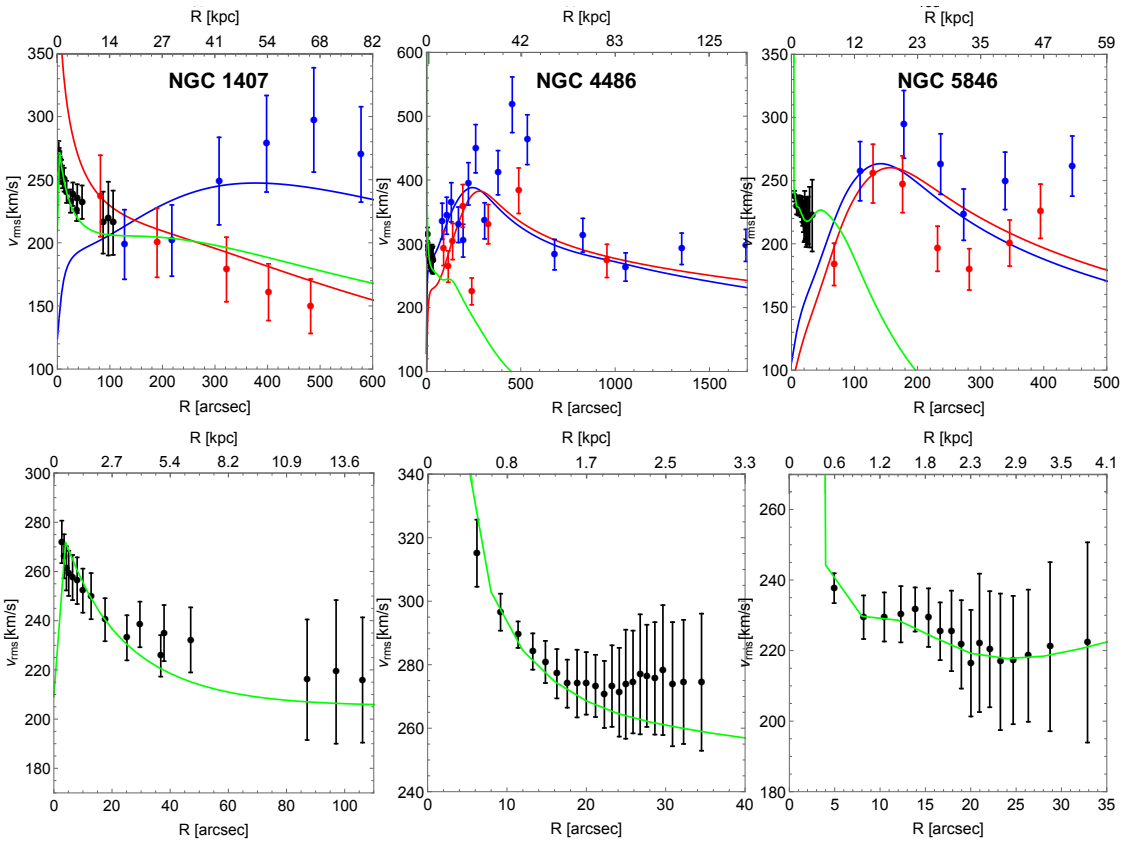

Figure 5.12: Same as Fig. 5.8 for our second MCMC analysis.

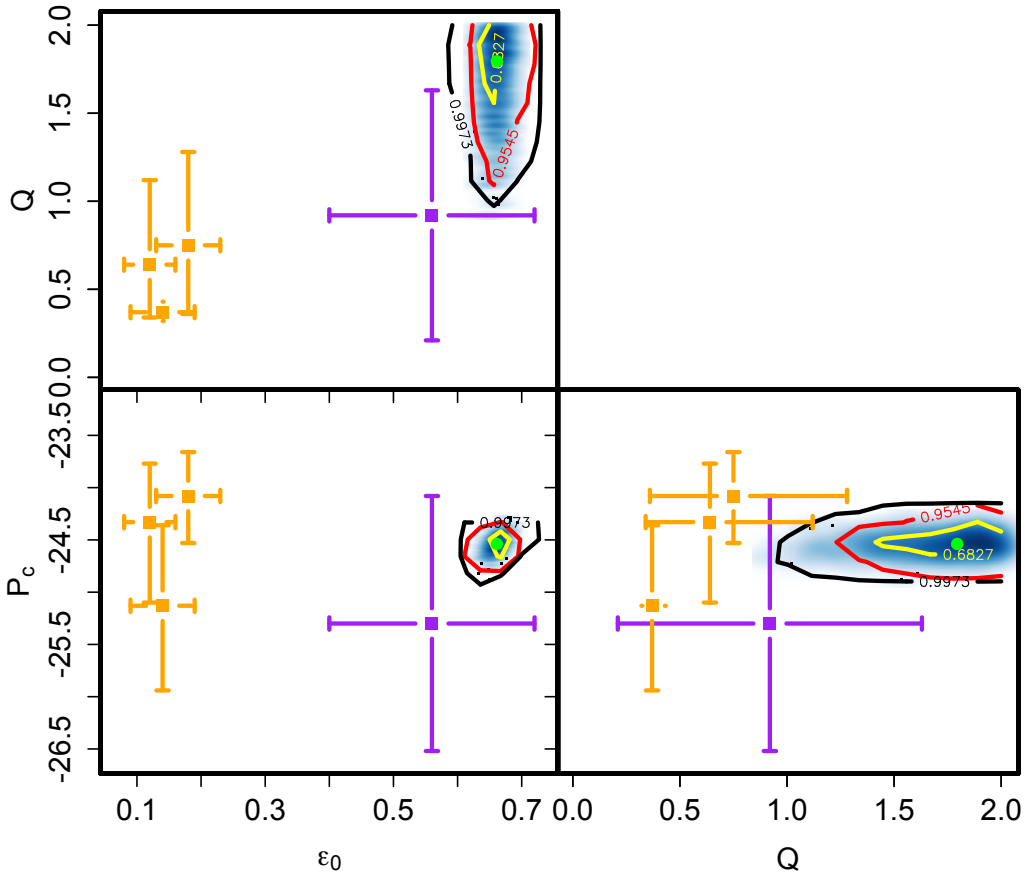

Figure 5.13: Permittivity parameters estimated from the three E0 galaxies in our sample (orange squares with error bars) compared with the permittivity paramaters estimated by [97] from the DMS disk galaxies: the purple squares with error bars show the means of the permittivity parameters found for the individual DMS galaxies, whereas the light blue shaded areas show the posterior distributions of the three permittivity parameters found with an approximate procedure from the entire DMS sample at the same time, with the green dots indicating their median values and the yellow, red, and black contours indicating the 1σ, 2σ, and 3σ levels, respectively.

Chapter 6

Discussion and conclusion

6.1 Summary of the main results

In this thesis, we test, on galaxy scale, the viability of RG, a theory of modified gravity that does not require the existence of DM to describe the dynamics of cosmic structures. RG is formulated in analogy to electrodynamics in matter and its modified Poisson equation contains the gravitational permittivity, a monotonic increasing function of the local mass density, which depends on three universal free parameters: the permittivity in vacuum, ϵ_0, the critical density, ρ_c, which sets where the transition between the Newtonian and the RG regimes occurs, and the parameter Q, which regulates the steepness of this transition. For our analyses, we adopt the smooth step function (3.5) for the gravitational permittivity.

We test RG with 30 disk galaxies from the DMS [317]. These galaxies appear almost face-on, having an inclination between 5 deg and 46 deg with respect to the line of sight. We can thus model, using a MCMC approach, both their rotation curves and their vertical velocity dispersion profiles. By modelling every galaxy with five free parameters, the mass-to-light ratio, Υ, the disk-scale height, h_z, and the three free parameters of the permittivity, our MCMC analysis demonstrates that RG can properly model the kinematic profiles of these galaxies with sensible values of Υ and h_z. In particular, the mass-to-light ratios agree with the predictions from the SPS models of [325] and this consistency improves when the vertical velocity dispersion profiles are included in the modelling. When we model the rotation curves alone, the disk-scale heights are in agreement with the disk thicknesses, $h_{z,\mathrm{SR}}$, observed from edge-on galaxies. When we model both the rotation curves and the vertical velocity dispersions, we obtain h_z $\sim$2 times smaller than $h_{z,\mathrm{SR}}$. Yet, this issue, already faced by Angus and collaborators by analysing the same galaxies in MOND [326], might not be due to a problem of RG but to an observational bias pointed out by [327] and quantified by [328]. Indeed, whereas the disk-scale heights observed in edge-on galaxies are inferred from near infrared photometry coming from old giant stars, with a larger vertical velocity dispersion and disk-scale height, the vertical velocity dispersions profiles are measured from integrated spectra near the V-band, whose signal is dominated by young giant stars, with a smaller vertical velocity dispersion and disk-scale height. For this reason, the disk-scale heights estimated from the measured vertical velocity dispersions result smaller than those inferred from the near infrared photometry. For the DMS sample, we estimate a mean ratio between these two velocity dispersions of 1.63, consistent within 1σ with the value suggested by [328]. Artificially increasing the measured vertical velocity dispersions by 1.63, the estimated disk-scale heights result consistent with those estimated from edge-on galaxies.

RG models the kinematic profiles of the DMS sample with permittivity parameters from individual galaxies consistent with each other, suggesting their universality. To better test the universality of these parameters, we explore, with a MCMC approach, the three-dimensional RG parameter space for the entire galaxy sample at the same time, setting the mass-to-light ratios and the disk-scale heights to the values found from our previous

analysis. This unique combination of permittivity parameters, $\{\epsilon_0, Q, \log_{10}[\rho_c\,(\mathrm{g/cm^3})]\} = \{0.661^{+0.007}_{-0.007}, 1.79^{+0.14}_{-0.26}, -24.54^{+0.08}_{-0.07}\}$, is consistent, within 1.2σ, with the means of the distributions of the permittivity parameters estimated from the individual galaxies, $\{\epsilon_0, Q, \log_{10}[\rho_c\,(\mathrm{g/cm^3})]\} = \{0.56 \pm 0.16, 0.92 \pm 0.71, -25.30 \pm 1.22\}$. Although, as expected, the models of the rotation curves and of the vertical velocity dispersion profiles worsen, and some χ^2 increase also of a factor of 5, they still appear to be reasonable for about half sample. This result suggests that a single combination of permittivity parameters that describes the kinematics of the DMS galaxies with sensible Υ and h_z might indeed exist.

RG can also describe the RAR built from the DMS data. The RAR modelled in RG interpolates these measurements rather well and reproduces the asymptotic limits of the observed RAR, given by Eq. (4.14). Yet, RG produces a RAR that slightly underestimates the data at low Newtonian accelerations and with an intrinsic scatter not consistent with zero, as galaxy samples different from DMS might suggest [44, 246]. Moreover, the residuals between the RAR modelled by RG and Eq. (4.14) show some correlations with some galaxy properties, apparently at odds with the uncorrelations claimed by [246] for the SPARC sample. In particular, for the three radially-dependent properties of the galaxies, radius, surface brightness and gas fraction, the correlations are statistically significant at largely more than 5σ. However, we also find significant correlations with radius and gas fraction, at more than 4σ, for the residuals of the DMS data.

Besides testing RG with the dynamics of flattened systems, we assess whether RG can also model the kinematic profiles of spherical systems. We, thus, model, at the same time, the root-mean-square velocity dispersions of the stars, the blue GCs, and the red GCs in three elliptical E0 galaxies belonging to the SLUGGS survey. The choice of these galaxies is due to the presence of two populations of GCs that probe their kinematics up to $\sim$10 effective radii from their centres, where the mass discrepancies, as interpreted in Newtonian gravity, are more important. Modelling the kinematic profiles of these systems up to their outermost regions provides a stringent test for modified theories of gravity.

Having a minor-to-major axis ratio in the range of $[0.86, 0.95]$, we approximate these galaxies as spherical systems and we model their kinematic profiles with the spherical Jeans equation derived from the RG gravitational potential. The theory properly models the kinematic profiles of the three populations with sets of permittivity parameters of the three E0 galaxies consistent with each other within $\sim 1\sigma$. Their values averaged over the three galaxies are $\{\epsilon_0, Q, \log_{10}[\rho_c\,(\mathrm{g/cm^3})]\} = \{0.15^{+0.05}_{-0.05}, 0.59^{+0.36}_{-0.25}, -24.51^{+0.58}_{-0.68}\}$. With this permittivity, RG requires mass-to-light ratios in agreement with SPS models and tangential or radial orbits for the GCs, depending on the galaxy and the colour of the GCs. In particular, for NGC 1407, the mass-to-light ratio and the orbital anisotropy parameters are within 1σ from the values found by [81], who model this galaxy with Newtonian gravity and a DM halo.

The values of $\log_{10}[\rho_c]$ and Q that we find here are within 1σ from the DMS average values and within 3σ from the DMS global values and support their universality. Similarly, our estimate of ϵ_0 is within 2.5σ if we consider the DMS average, 0.56 ± 0.16, of the individual galaxies. However, ϵ_0 is $\sim 10\sigma$ discrepant if we consider the DMS value $0.661^{+0.007}_{-0.007}$ estimated from the DMS sample as a whole.

This discrepancy is mostly driven by the width of the posterior distribution found by [97] which is small when compared to the uncertainties of the corresponding mean values (Fig. 5.13). If this width is not severely underestimated, this discrepancy might highlight at least three different possible problems: a simplistic model of the ellipticals, an incorrect form of the permittivity, or a fundamental fault of RG. The model of the ellipticals that we adopt here is oversimplified, because we treat them as isolated systems and completely neglect the galaxy net rotation. Indeed, NGC 1407 and NGC 5846 are within galaxy groups and NGC 4486 is the central galaxy of the Virgo cluster. Treating these galaxies as isolated systems, as we do here, can clearly overlook relevant interactions with neighbour galaxies that could actually affect the parameters of the permittivity.

Including these environmental effects requires modelling all the galaxies within the system at the same time, with each galaxy modelled according to its morphological type and shape. Properly modelling such a system is arduous and its nonlinear effects are difficult to assess at the present stage. We cannot thus exclude that they might be the origin of the possible discrepancy we find here. Alternatively, the explicit form of the permittivity $\epsilon(\rho)$ (Eq. (3.5)), that is chosen arbitrarily, might actually be inappropriate, especially in the low-density regime: hints from the weak-field limit of the covariant version of RG [301] might suggest a better motivated permittivity that might alleviate the tension. These possible explanations can also account for the poor fitting of some points of the blue GCs profiles in NGC 4486 and NGC 5846. In addition, we have to keep in mind that the global combination of permittivity parameters that we estimate from the DMS sample is derived through an approximate procedure, where we fix the mass-to-light ratios and disk-scale heights of the individual galaxies and we only explore the three dimentional space of the permittivity parameters. Properly exploring the 63-dimensional space of the individual Υ and h_z for each DMS galaxy and of the three permittivity parameters might reduce the discrepancy observed between the vacuum permittivities estimated from the three E0 galaxies and the DMS. Finally, all of the above might turn out to play a negligible role, and this possible tension on the permittivity of the vacuum might simply betray a fundamental fault of RG.

6.2 Future perspectives

6.2.1 Galaxy scale

Given the first successes on the scale of galaxies, we can conclude that RG is a theory of gravity that deserves further investigations. Before going to larger scales, additional tests of the dynamics of galaxies have to be accomplished to complete the study of RG of these systems.

First of all, we have to settle the two issues presented by RG on galaxy scale: the prediction of a RAR with a too large intrinsic scatter and correlations between its residuals and galaxy properties and the apparent nonuniversality of the vacuum permittivity. Specifically, we have to understand whether they are due to a failure of the theory or depend either on the chosen galaxy sample or to a too approximate modelling.

A re-analysis of the radial acceleration relation

The RAR produced by RG from the modelling of the DMS galaxies present strong correlations, at largely more than 5σ, between its residuals and the radially dependent properties of the galaxies. However, also the RAR built from the DMS data show some, although weaker, correlations between these two quantities which might partially drive the correlations observed for the RG models. The correlations observed in the DMS measurements are apparently at odds with the observed uncorrelations in SPARC [246], suggesting a difference between the two samples. At the moment we cannot state whether this difference really exists, since Lelli and collaborators [246] do not report the significance levels of these correlations. Moreover, the DMS is not the only galaxy sample where a correlation between the RAR residuals and the galaxy properties is observed. Di Paolo and coauthors [96] found a correlation between the RAR residuals and the galaxy radius from the accurate mass profiles of 36 dwarf disk spirals and 72 LSB galaxies, making the question of the RAR particularly puzzling. Yet, also this question requires further investigation, since also Di Paolo and coauthors [96] do not report the significance levels of this correlation.

To better assess whether the result obtained in RG from the DMS galaxies depends on the theory itself or on the DMS sample, we aim to repeat the study of the RAR with the SPARC galaxies. Differently from the DMS, whose galaxies are close to face-on, SPARC

sample contains edge-on galaxies. This provides more accurate rotation curves and, thus, allows a more robust study of the RAR. In particular, we will model the rotation curves of all the edge-on disk galaxies belonging to SPARC and we will derive the RAR from these models, as detailed in Sect. 4.4. Then, we will compute both the scatter and the residuals of the obtained RAR and we will compare these results with the ones from Lelli and collaborators [246] and from the DMS (Sect. 4.4). This study is already ongoing by Beordo and collaborators. Another interesting study that should be performed would consist in repeating the computations of the scatter and of the correlations for the separated groups of normal spirals and dwarf galaxies present in SPARC and for the sample considered by [96]. This analysis would better clarify the results obtained by [57] and [96], according to which the RAR behaves differently in normal spirals and in dwarf or LSB galaxies (see also Sects. 2.1.2 and 2.2 and Fig. 2.12), besides providing a further test for RG.

Elliptical galaxies

The study of the dynamics of elliptical galaxies in RG is certainly incomplete. Indeed, we have only considered three E0 galaxies in our sample. First of all, we aim to better investigate the possible nonuniversality of the vacuum permittivity and if the consistency between the other two RG parameters and the corresponding values found from the DMS still subsists for a larger sample of galaxies. To accomplish this task we will perform a less approximate description of the three galaxies we considered, including the interactions with their surrounding environment in our modelling, possibly by resorting to N-body simulations. We will improve the statistical significance of this study by including additional E0 galaxies with extended kinematic profiles in our sample. The galaxies in the ePN.S survey are suitable for this purpose, since their kinematics is probed up to their outer regions thanks to detection of Planetary Nebulae rather than GCs, as in the SLUGGS survey. Specifically, their kinematic profiles are measured until $\sim 13 R_{\mathrm{e}}$ from the galaxy centres (see also Sect. 2.1.2). Also the round elliptical galaxies considered in [302], [303], and [304] might be ideal to test the viability of RG. Their velocity dispersion profiles show a flattening beyond a certain radius, where both this radius and the amplitude of the velocity dispersion in its flat region are consistent with MOND expectations. Modelling these kinematic profiles with RG would show whether they can be reproduced by a field proportional to r^{-2} in the outermost regions of the galaxy of if they necessarily need a field proportional to r^{-1}, as in MOND. If this is the case, it would be an issue for the current formulation of RG.

Then, we will extend this study to elliptical galaxies with different ellipticities, both from the SLUGGS and the ePN.S surveys. This analysis would also allow to investigate the positive correlation found by Alexander Deur [82, 83] between the total mass-to-light ratios and the ellipticities of elliptical galaxies, which naturally arises within the framework of RG, as better discussed in Sect. 3.2. These galaxies, which have kinematic profiles more extended of a factor of ~ 10 with respect to the sample considered by [82, 83], will be determinant to validate or to reject this correlation. Considering elliptical galaxies with different degrees of flatness would allow the investigation of the possible dependence of the RG parameters on the morphological type of the galaxies, either ellipticals or disks, or on the geometry of the system, either spherical or flattened. Moreover, all these studies might shed light on the validity of the expression (3.5) for the gravitational permittivity.

Dwarf galaxies and globular clusters

Besides the dynamics of elliptical galaxies with different polar flattenings, the fact that the flatter a system the stronger the refraction of RG field lines toward its equatorial plane might also account for the different dynamical behaviours in dwarf galaxies and GCs (see Sect. 3.2). We aim to test this feature of RG, by modelling the rotation curves of a sample of dwarf galaxies belonging to the Milky Way halo (e.g. [414]) and to the

LITTLE THINGS survey [415], and the internal velocity dispersions of a sample of GCs settling in the most external regions of the Milky Way (e.g. [61, 62, 63, 64, 65, 66, 67]), where the background density drops below the RG critical value. The modelling of the rotation curves of the dwarf and the LSB galaxies from SPARC and from the sample considered in [96] that we would perform to better investigate the question of the RAR would also improve the statistical significance of this study.

This study would allow to test whether RG is indeed able to describe the larger mass discrepancies observed in dwarf galaxies with respect to spiral galaxies thanks to the dependence of the modification of the law of gravity on the local mass density, as better detailed in Sect. 3.2.

6.2.2 Larger scales

Galaxy clusters

If RG passes all the mentioned tests on galaxy scale, an investigation at larger scales should certainly be performed. In Sect. 3.3 we describe some studies that we aim to perform to investigate the validity of RG in galaxy clusters. They consists in extending the study of Matsakos & Diaferio [300] that modelled in RG the radial temperature profiles measured with the *Chandra* satellite of two galaxy clusters, A1991 and A1795. They are two low-redshift and relaxed galaxy clusters, where the assumption of dynamical equilibrium might be valid at every distance from the cluster centre, and they have a spectroscopic temperature of the gas, averaged between 70 kpc and r_{500}, of 2.83 keV (A1991) and 9.68 keV (A1795). r_{500} is the distance from the centre of the cluster where the average density is 500 times larger than the critical density of the Universe. These measurements are taken from [309], that provide the radial temperature profiles of other 11 nearby and relaxed galaxy clusters, besides the two mentioned ones, with redshifts in the range of $[0.0153, 0.2302]$ and average temperatures in the range of $[0.7, 9]$ keV. We aim to model the temperature profiles of the other 11 galaxy clusters by adopting the same methodology illustrated in [300]. In their modelling of the temperature profiles, Matsakos & Diaferio adopted the gravitational permittivity of Eq. (3.5) with RG parameters fixed a priori. We aim to repeat this study by leaving the three parameters free, as performed in our studies on galaxy scale, to see if the estimated values result consistent with each other. At a second stage, we want to adopt a less approximate modelling by including the mass profiles of the individual galaxies present in the clusters, exploiting the results from N-body simulations, as anticipated in Sect. 3.3.

Besides the temperature profiles, we also aim to test whether RG can model the galaxy velocity dispersion profiles of clusters of galaxies. To perform this task, we will consider the data in the CIRS and the HeCS samples [416, 417], that present the radial velocity dispersion profiles taken from the Sloan Digital Sky Survey and the *ROSAT* All-Sky Survey of 130 galaxy clusters in a redshift range of $[0.0, 0.3]$ and with different dynamical properties, from nonmerging and relaxed to merging and dynamically active. This study allows to investigate how the RG parameters are affected by the environment, either relaxed or interacting, extending on larger scales the study that we aim to perform with elliptical galaxies, illustrated in Sect. 6.2.1.

To complete the study of the dynamics of clusters of galaxies in RG, we aim to investigate the BTFR extended to galaxy groups and clusters given by Eq. (3.8) and illustrated in Sect. 3.3. As already anticipated in Sect. 3.3, we have to consider how the uncertainties on the equation of state and on the entropy profiles of the gas and the possible local deviations from hydrostatic equilibrium due to X-ray gas flows might affect the values of the RG parameters.

Cosmology

As detailed in Sect. 3.5, RG is extended in a covariant formulation [301]. Covariant RG presents some encouraging results, since it can reproduce the Hubble diagram of SNIa at high redshift measured in [418]. Differently from ΛCDM, the relativistic version of RG predicts a redshift-dependent equation of state of DE, which tends to -1 at the present epoch, in agreement with the observations. The equation of state of DE predicted by RG can be constrained from the measurements of the expansion rate of the Universe performed by the Dark Energy Survey (DES)[1] observing thousands of supernovae from August 31$^{\text{th}}$ 2013. Moreover, the upcoming Euclid mission[2] will measure the variation of the cosmic acceleration to an accuracy better than the 10% level, allowing further constraints for RG.

Other important cosmological observables that we aim to investigate with covariant RG are the formation, the evolution, and the distribution of large-scale structures. To accomplish this task, we aim to modify the publicly available code GADGET-2 [419] to perform N-body simulations in the relativistic RG framework. This project first requires the development of the linear theory of density perturbations in RG, so that initial conditions can be properly set in the N-body simulations. The original GADGET-2 code describes the evolution of two components: a collisionless one, made of DM and stars, and a collisional one, made of an ideal gas, both represented as a system of particles. The first components are modelled with the collisionless Boltzmann equation coupled to the Poisson equation in an expanding Universe with a Friedman-Lemaître geometry. The second component is modelled with smoothed particle hydrodynamics [420], a meshfree and Lagrangian method to describe the dynamics of fluids. We will compare the results of the simulations with the observations from DES survey, which probed the formation of structures with weak gravitational lensing and galaxy clusters, and the distribution of galaxies with the two-point correlation function. Further constraints will be given by the measurements taken with the Dark Energy Spectroscopic Instrument (DESI)[3], which started to observe in 2019, and with upcoming experiments like the Square Kilometer Array (SKA)[4] and Euclid, that are expected to start taking data in 2021 and 2022, respectively.

To complete the testing of RG on cosmological scales, we have to verify if it can reproduce the power spectrum of the CMB anisotropies, by comparing its predictions with the latest measurements from the Planck satellite [413]. Moreover, by estimating the cosmological parameters from different low-redshift galaxy surveys, like KIDS, CFHTLS, and DES, and from the CMB power spectrum we can assess whether RG can solve the tensions observed in the ΛCDM model.

[1] `https://www.darkenergysurvey.org`
[2] `https://sci.esa.int/web/euclid`
[3] `https://www.desi.lbl.gov`
[4] `https://www.skatelescope.org`

Chapter 7

Acknowledgements

I sincerely thank my Ph.D. advisor, Prof. Antonaldo Diaferio, who, besides supervising this work, accompanied me along a journey of professional growth started with my master thesis. I also thank all the other members of his group, the CAUSTIC group, with whom I collaborated and I spent pleasant moments during the weekly lunches. Specifically, I wish to thank my mates Michele Pizzardo, Arianna Gallo, Konstantinos Tanidis, and Stefano Ebagezio, for their special friendship, Ivan de Martino, Sankha Chakrabarty, Prof. Luisa Ostorero, and again Arianna, for their collaboration in writing the review about the problems of DM on small scale, Alistair Hodson and Stefano Camera, for inspiring discussions concerning my work about the DMS, and Mikołaj Grzędzielski, Heng Yu, Serafina Di Gioia, and Marta Campigotto.

I express a deserved thank to the revisors of my thesis, Dr. Xavier Hernández and Dr. Federico Lelli, for their precious pieces of advice and their detailed comments that improved the presentation of this work.

I want to thank in particular Dr. Titos Matsakos and Dr. Garry Angus, coauthors of my papers about RG, Andrea Sanna, who is working on the covariant extension of RG, and William Beordo, who is working on the re-analysis of the RAR in RG with the SPARC sample.

I express a sincere thank to Prof. Marco Aldinucci who did not just help me to parallelise with OpenMP the code for the modelling of the entire DMS sample at the same time, but transformed this test case in two papers describing a semi-automatic methodology to parallelise scientific codes and allowed me to present these results at the PDP 2020 conference. Moreover, thanks to his course of "Parallel and distributed computing systems", I improved my knowledge of several parallelisation techniques. Besides Prof. Aldinucci, I thank his team members, Iacopo Colonnelli, Gianluca Mittone, Alberto Riccardo Martinelli, Barbara Cantalupo, Maurizio Drocco, and Carlo Cavazzoni, coauthors of the papers about parallel computing.

I would like to thank Prof. Andrea Mignone, for his crucial help with the Poisson solver, the main part of the code for the modelling of the dynamics of galaxies, and for his course "Introduction to Parallel Programming with MPI", which provided me with essential basis to parallelise through MPI the Laplace solver, described in the second paper I wrote with Prof. Aldinucci and his group.

I wish to give a special thank to Alessandro Paggi and Valentina Missaglia, for the time that dedicated to help me with the analysis about the gas and the GCs of elliptical galaxies, to Prof. Michele Cappellari, for his help in the derivation of the stellar root-mean-square velocity dispersion profiles of NGC 4486 and NGC 5846, belonging to ATLAS^{3D} survey other than to the SLUGGS survey, to Dr. Ugo Becciani, Dr. Alberto Vecchiato, Dr. Fabio R. Vitello, and Dr. Ugo Varetto, for their constant encouragements, and to my parents, that supported me, both psicologically and professionally, during my Ph.D..

I additionally thank Dr. Michal Bílek, for his precious pieces of advice about the work on DMS galaxies, Dr. Emille Ishida, for her help with the MCMC analysis with the

software JAGS, and Compagnia di San Paolo (CSP), for funding my Ph.D. fellowship. I also acknowledge partial support from the INFN grant InDark and the Italian Ministry of Education, University and Research (MIUR) under the Departments of Excellence grant L.232/2016.

To conclude, I wish to thank all the people that have been to my side, helping me to grow both as a physicist and as a person. In particular, I give a special thank to all my relatives, to Prof. Mariangela Scanavino, for her teachings and her trust, to Najoua Mzaiche and her family, to Alessandra Cappati, Riccardo Finotello, Piero Rettegno, Elena Pinetti, Gloria Guilluy, Marco Giammaria, Chiara Signorile Signorile, Xiuhui Tan, Christoph Ternes, Raniere Menezes, Ana Maria Jimenez-Gallardo, Harold Peña, Vittoria Berta, Giovanna Speranza, Lorenzo Scotton, Ambra Ferrando, Laura Fadda, Michele Santone, Giordana Boga, Josephine Convertini, Jennifer Claudia Poma, Vanessa Pinnelli, Laura Bena, Cristina Salvini, Eleonora Cassina, Luca Olivero, Luca Rikler, Riccardo Caramellino, Andrea De Pascali, Luca Gambarana, Ruben De March, Ariful MD and his family, Nikolina Šarčević, and Oem Trivedi.

Appendix A

Modelling the mass distribution in the disk galaxies

Here, we describe how we model (1) the surface brightness of the bulge and the stellar disk (Appendix A.1); (2) the mass distribution of the gas (Appendix A.2); and (3) the total three-dimensional mass distribution (Appendix A.3) for the galaxies in the DiskMass Survey (DMS) (see Chapter 4).

A.1 Surface brightness of the bulge and the stellar disk

The surface brightness of disk galaxies is the sum of the contribution of the bulge, which dominates the inner regions, and the contribution of the disk, which dominates the external regions. The surface brightness profile usually shows a distinct change of slope at the radius that separates the central region dominated by the bulge and the outer region dominated by the disk (see sub-panels (a) of Figs. E.1-E.7).

To preserve the specific features of the distribution of the luminous matter, which in general correspond to features of the rotation curve, according to 'Renzo's rule' [335], we model the disk surface brightness with a linear interpolation of the surface brightness data points only beyond the central region. To estimate the disk contribution within the central region, we fit the surface brightness data point beyond the central region with an exponential profile [421, 422]:

$$I_{\rm d}(R) = I_{\rm d0} \exp\left(-\frac{R}{h_R}\right) \ , \tag{A.1}$$

where h_R is the disk-scale length.

Therefore, to describe the disk surface brightness on the full radial range of the galaxy, we adopt the exponential model for the disk contribution within the central region, dominated by the bulge, and the linear interpolation of the data points in the outer region. We also adopt the exponential model in the very outer region if the grid of the Poisson solver we use in Sects. 4.1, 4.2, 4.3, and 4.4 goes beyond the measured profile.

We model the bulge surface brightness with a Sérsic spherical profile:

$$I_{\rm b}(R) = I_{\rm e} \exp\left\{-7.67\left[\left(\frac{R}{R_{\rm e}}\right)^{\frac{1}{n_{\rm s}}} - 1\right]\right\} \ , \tag{A.2}$$

with $R_{\rm e}$ the effective radius, $I_{\rm e}$ the surface brightness at radius $R_{\rm e}$, and $n_{\rm s}$ the Sérsic index. The average bulge-to-total luminosity ratio in the K-band in the DMS galaxies is 0.09 (see Table 1 in [320]); therefore, ignoring the triaxiality of the bulge should introduce negligible systematic errors on the modelling of the galaxy luminosity.

For the bulge, we adopt the Sérsic model rather than interpolating the surface brightness data points as we do for the disk, for two reasons: (1) the seeing affects the central

region more than the outer region, as we detail below, and (2) unlike a two-dimensional disk, the bulge cannot be trivially deprojected without an analytical approximation. The deprojection is a required step to model the galaxy mass distribution we illustrate in Sect. A.3.

To model the surface brightness profile, we also consider the seeing that affects the measurements made with the 3.5 m diameter ground telescope at the Calar Alto Observatory. We model the seeing with a Gaussian point spread function,

$$p_{\rm PSF}(R) = \frac{1}{2\pi\sigma^2} \exp\left[-\frac{(R-R_{\rm peak})^2}{2\sigma^2}\right] , \tag{A.3}$$

where σ is the average effective seeing, as listed in Tables 3 and 4 of [320], and $R_{\rm peak}$ is the location of the surface brightness peak.

According to [320], we only convolve the bulge profile (Eq. A.2) with Eq. (A.3):

$$I_{\rm obs}(R) = \int_{-\infty}^{+\infty} I_{\rm true}(R') p_{\rm PSF}(R'-R)\, dR' . \tag{A.4}$$

Ignoring the effect of the seeing on the disk should introduce negligible systematic errors because the disk is a factor of ten more luminous than the bulge, on average, and spatially more extended.

The galaxy disks in the DMS sample appear almost face-on, with small inclination angles i. If we neglect the dust extinction within the galaxy, the observed surface brightness of the disk is brighter than the intrinsic surface brightness because the observed flux appears to come from an area $\cos i$ times smaller than the actual disk area. Therefore, to derive the light distribution of the disk from the measured surface brightness, μ_K, we need to correct for the inclination of the disk with respect to the line of sight.

By assuming the Tully-Fisher relation [423],

$$\log_{10} v_{\rm TF} = -0.30103 + (5.12 - M_K)/11.3 , \tag{A.5}$$

Martinsson et al. [320] estimate the inclination angle,

$$\sin i_{\rm TF} = \frac{v_{\rm obs}}{v_{\rm TF}} , \tag{A.6}$$

from the observed luminosity, M_K, and the observed rotation velocity, $v_{\rm obs}$. The face-on surface brightness of the disk is thus:

$$\mu_K^i = \mu_K - 2.5 C_k \log(\cos i_{\rm TF}) , \tag{A.7}$$

where $C_k = 1$, for a transparent disk, as assumed by [320].

For the conversion of the surface brightness from the astronomical units mag arcsec^{-2} to units $\mathrm{L}_\odot$ pc^{-2}, we use the equation [424]:

$$\mu\left(\frac{\rm mag}{\rm arcsec^2}\right) = M_{\odot,K} + 21.572 - 2.5 \log_{10} I\left(\frac{\mathrm{L}_\odot}{\rm pc^2}\right) , \tag{A.8}$$

where $M_{\odot,K} = 3.28$ is the absolute magnitude of the Sun in the K-band. This equation neglects the expansion of the Universe because all the DMS galaxies are nearby, with the farthest galaxy (UGC 4622) at $z = 0.043$, namely at the distance 178.2 Mpc (see Table 1 of [320]).

We now illustrate the steps we adopt to model the entire surface brightness profile. We apply this procedure to the surface brightness profiles that were already corrected for inclination with Eq. (A.7) by [320].

As anticipated, most observed surface brightness profiles in the DMS sample show a distinct change of slope that suggests how extended the bulge is. We remove the central

data points at radii smaller than the location of the slope change. The removed data points for each galaxy are shown in sub-panels (a) of Figs. E.1-E.7 as green dots. We assume that the remaining profile, given by the red dots in sub-panels (a) of Figs. E.1-E.7, is only due to the surface brightness of the disk. We linearly interpolate this remaining profile. The disk contribution in the most inner region, where the bulge contribution is dominant, is estimated with the exponential model of Eq. (A.1), with the parameters of the model set by the least-square best fit to the data points of the outer region alone.

We now subtract the extrapolated surface brightness profile of the disk from the observed total surface brightness profile of the central region, namely the green data points in sub-panels (a) of Figs. E.1-E.7. The remaining profile is the surface brightness profile of the bulge that we now model with Eq. (A.4). Because of the presence of the convolution integral, to estimate the three parameters $I_{\rm e}$, $R_{\rm e}$ and $n_{\rm s}$ of the bulge, it is more convenient to apply a MCMC approach. We run the MCMC algorithm with JAGS[1], a free software that adopts the Gibbs sampling algorithm to generate the Markov chains.

We adopt Gaussian priors on the three free parameters; we set the Gaussian tails to zero for the unphysical negative values of the parameters. The Gaussian dispersions are set to $1/\sqrt{200}$ $\mathrm{L}_\odot$ pc^{-2}, $1/\sqrt{200}$ arcsec, and $1/\sqrt{200}$ for $I_{\rm e}$, $R_{\rm e}$ and $n_{\rm s}$, respectively. Assuming a Gaussian prior avoids the choice of an upper limit required in a uniform prior. To determine the means of the Gaussian priors, we compare the surface brightness profiles with the model profiles with a number of different choices of the parameters set by hand. We pick up the set of parameters that qualitatively best reproduce the data. This simple approach is sufficient to set the means of the Gaussian priors to reasonable values. The burn-in chain has $10,000$ steps and we then run the chain for $100,000$ steps.

For the best parameter estimates and their uncertainties, we adopt the medians and the standard deviations of the posterior distributions obtained from the MCMC runs. This choice is justified by the fact that the posterior distributions show a single peak and are basically symmetric.

By adopting this procedure, we find that two galaxies, UGC 1862 and UGC 9965, have no surface brightness in excess to the disk in the central region and we thus consider them bulgeless, a finding that is in agreement with [320]. Martinsson et al. [320] find two additional bulgeless galaxies: UGC 3091 and UGC 7244; however, for these galaxies, we do find a non-negligible light excess in the central region.

Table A.1 lists the parameters estimated from the MCMC analysis for the bulge profiles and the best-fit parameters of the exponential profile used to estimate the disk surface brightness in the central region. The uncertainties on the parameters $I_{\rm d0}$ and h_R are derived from the covariance matrix obtained from the least-square fit. Sub-panels (a) of Figs. E.1-E.7 show the 30 measured profiles, corrected for inclination, in green the region where the bulge contribution is dominant, and in red the region where the disk contribution is dominant; the models are in blue and are the sum of Eq. (A.4) and the surface brightness of the disk.

To convert the fit parameters from angular (arcsec) to physical (kpc) radial units we use the relation:

$$R(\mathrm{kpc}) = 4.84814 \times 10^{-6} D(\mathrm{kpc}) R(\mathrm{arcsec}) \,, \tag{A.9}$$

where 4.84814×10^{-6} is the conversion factor from arcsec to radians and D(kpc) is the galaxy distance reported in Table 1 of [320]. This relation is strictly valid in a nonexpanding Euclidean geometry, but it can be applied to our DMS galaxies because they all are at redshift smaller than 0.043.

[1] https://sourceforge.net/projects/mcmc-jags/

Table A.1: Parameters of the model of the surface brightness.

UGC	$I_{\rm d0}$ $\left[\frac{\rm L_\odot}{\rm pc^2}\right]$	h_R [arcsec]	h_R [kpc]	$I_{\rm e}$ $\left[\frac{\rm L_\odot}{\rm pc^2}\right]$	$R_{\rm e}$ [arcsec]	$R_{\rm e}$ [kpc]	$n_{\rm s}$
(1)	(2)	(3)	(4)	(5)	(6)	(7)	(8)
448	603 ± 44	12.29 ± 0.47	3.89 ± 0.19	2500.00 ± 0.07	1.08 ± 0.05	0.34 ± 0.02	6.47 ± 0.07
463	1357 ± 23	13.17 ± 0.16	3.81 ± 0.14	83.00 ± 0.07	4.50 ± 0.07	1.30 ± 0.05	2.03 ± 0.01
1081	573 ± 12	14.79 ± 0.20	3.00 ± 0.16	4.69 ± 0.07	2.02 ± 0.07	0.41 ± 0.02	0.47 ± 0.02
1087	598 ± 25	10.41 ± 0.33	3.01 ± 0.14	0.44 ± 0.02	4.72 ± 0.07	1.36 ± 0.05	0.46 ± 0.03
1529	872 ± 29	12.19 ± 0.27	3.64 ± 0.15	4.70 ± 0.07	3.01 ± 0.07	0.90 ± 0.04	0.61 ± 0.02
1635	477 ± 17	14.11 ± 0.37	3.19 ± 0.17	3.16 ± 0.07	2.97 ± 0.07	0.67 ± 0.03	0.46 ± 0.02
1862	329.7 ± 8.5	17.29 ± 0.39	1.54 ± 0.18	-	-	-	-
1908	1406 ± 42	9.21 ± 0.19	4.91 ± 0.14	35.00 ± 0.07	1.09 ± 0.06	0.58 ± 0.03	0.48 ± 0.03
3091	467 ± 36	9.30 ± 0.53	3.33 ± 0.21	1.06 ± 0.06	3.97 ± 0.07	1.42 ± 0.05	0.60 ± 0.03
3140	1426 ± 68	11.23 ± 0.31	3.38 ± 0.15	3749.96 ± 0.07	0.82 ± 0.04	0.25 ± 0.01	4.64 ± 0.07
3701	151 ± 16	16.7 ± 1.3	3.51 ± 0.32	0.24 ± 0.01	7.02 ± 0.07	1.47 ± 0.07	0.37 ± 0.02
3997	165 ± 25	13.7 ± 1.2	5.52 ± 0.50	0.82 ± 0.05	7.00 ± 0.07	2.82 ± 0.08	0.98 ± 0.04
4036	985 ± 12	12.87 ± 0.08	3.18 ± 0.13	1.24 ± 0.06	3.70 ± 0.07	0.91 ± 0.04	0.44 ± 0.03
4107	669 ± 16	13.26 ± 0.23	3.29 ± 0.15	2.50 ± 0.06	2.99 ± 0.07	0.74 ± 0.04	0.49 ± 0.02
4256	1327 ± 29	11.78 ± 0.14	4.27 ± 0.13	305.00 ± 0.07	5.03 ± 0.06	1.82 ± 0.06	3.55 ± 0.02
4368	726 ± 18	9.49 ± 0.07	2.59 ± 0.10	0.42 ± 0.03	4.50 ± 0.07	1.23 ± 0.05	0.34 ± 0.04
4380	473 ± 36	9.78 ± 0.45	4.98 ± 0.25	0.50 ± 0.04	7.03 ± 0.07	3.58 ± 0.08	0.66 ± 0.04
4458	254 ± 22	28.0 ± 1.3	9.27 ± 0.52	180.00 ± 0.07	24.99 ± 0.07	8.29 ± 0.26	3.26 ± 0.01
4555	799 ± 13	10.99 ± 0.10	3.29 ± 0.12	1.71 ± 0.07	1.99 ± 0.07	0.60 ± 0.03	0.37 ± 0.03
4622	520 ± 27	8.59 ± 0.26	7.42 ± 0.24	14.20 ± 0.07	1.07 ± 0.06	0.92 ± 0.05	0.55 ± 0.03
6903	137 ± 11	34.5 ± 2.4	5.23 ± 0.52	0.84 ± 0.05	13.50 ± 0.07	2.05 ± 0.14	0.79 ± 0.04
6918	3372 ± 40	10.96 ± 0.08	1.16 ± 0.12	3.79 ± 0.07	4.02 ± 0.07	0.42 ± 0.05	0.43 ± 0.02
7244	202 ± 18	10.81 ± 0.32	3.43 ± 0.15	0.61 ± 0.04	6.51 ± 0.07	2.06 ± 0.07	0.70 ± 0.04
7917	686.0 ± 9.8	14.53 ± 0.10	7.25 ± 0.17	12.00 ± 0.07	7.01 ± 0.07	3.50 ± 0.09	1.13 ± 0.01
8196	1085 ± 54	9.63 ± 0.25	5.59 ± 0.18	144.00 ± 0.07	7.00 ± 0.07	4.06 ± 0.09	2.57 ± 0.02
9177	362 ± 23	11.06 ± 0.44	7.10 ± 0.31	3.12 ± 0.07	2.99 ± 0.07	1.92 ± 0.06	0.60 ± 0.02
9837	97 ± 11	28.2 ± 2.3	5.91 ± 0.58	4.98 ± 0.07	30.00 ± 0.07	6.28 ± 0.33	2.69 ± 0.02
9965	739 ± 15	10.25 ± 0.19	3.51 ± 0.14	-	-	-	-
11318	1090 ± 27	11.04 ± 0.19	4.56 ± 0.14	90.00 ± 0.07	9.99 ± 0.07	4.13 ± 0.11	3.46 ± 0.02
12391	622 ± 22	11.31 ± 0.30	3.66 ± 0.15	2.04 ± 0.06	5.95 ± 0.07	1.93 ± 0.06	0.97 ± 0.02

Column 1: UGC number; Cols. 2, 3: best-fit parameters of the exponential profile (A.1), which are used to model the disk surface brightness in the central regions of the galaxies; Cols. 5, 6, 8: MCMC parameters for the bulge surface brightness profile; Cols. 4, 7: disk-scale length, h_R, and bulge effective radius, $R_{\rm e}$, in physical units (kpc).

A.2 Gas surface mass density

The gas component of each galaxy is distributed in a disk-like structure that is thinner and more extended than the stellar disk. In addition, both the atomic and the molecular gas contribute to the gas component.

The observed atomic profile is set to $\Sigma_{\rm atom} = 1.4\Sigma_{\rm HI}$ [324], where $\Sigma_{\rm HI}$ is the measured HI gas surface mass density estimated from 21-cm radio synthesis observations (see Sect. 2.5 of [425]). Similarly to the surface brightness of the disk, we linearly interpolate the data points of the surface mass density of the atomic gas.

Martinsson [425] measured $\Sigma_{\rm HI}$ only for 24 galaxies out of the original sample of 30 galaxies. For the remaining six (UGC 1081, UGC 1529, UGC 1862, UGC 1908, UGC 3091, UGC 12391), Martinsson [425] modelled the $\Sigma_{\rm HI}$ profiles with a Gaussian with mean and dispersion taken from the average of the other galaxies with measured $\Sigma_{\rm HI}$ (see Sect. 3.1 of [324] for details), obtaining synthetic data. For these six galaxies, we clearly adopt their synthetic Gaussian profiles.

The molecular gas surface mass density, $\Sigma_{\rm mol}$, is indirectly derived from 24-μm *Spitzer* observations, based on the CO line detection (see Sect. 3.2 of [324]). Again, we linearly interpolate the measures of the surface mass density of the molecular gas.

In sub-panels (b) and (c) of Figs. E.1-E.7, the red dots with error bars are the measures of the surface mass density of the atomic and molecular gas; the blue lines show the linearly interpolated profiles.

A.3 Three-dimensional mass density model

We model the total baryonic mass density as the sum of the disk mass density, $\Upsilon_{\rm d} j_{\rm d}(R,z)$, the bulge mass density, $\Upsilon_{\rm b} j_{\rm b}(r)$, with $r=(R^2+z^2)^{1/2}$, and the atomic and molecular gas mass densities, $\rho_{\rm atom}(R,z)$ and $\rho_{\rm mol}(R,z)$:

$$\rho(R,z) = \Upsilon_{\rm d} j_{\rm d}(R,z) + \Upsilon_{\rm b} j_{\rm b}(r) + \rho_{\rm atom}(R,z) + \rho_{\rm mol}(R,z) \ , \tag{A.10}$$

where $\Upsilon_{\rm d}$ and $\Upsilon_{\rm b}$ are the mass-to-light ratios of the stellar populations of the disk and the bulge, respectively. We assume that the mass-to-light ratios are independent of R and z. In addition, we set $\Upsilon_{\rm b}=\Upsilon_{\rm d}=\Upsilon$ because the bulge is, on average, an order of magnitude less luminous than the disk, as mentioned in Sect. A.1. Equation (A.10) is the total mass distribution of the galaxy in modified gravity models where the dark matter component is assumed to be absent.

We model the three-dimensional luminosity density of the disk by multiplying the disk surface brightness profile, $I_{\rm d}(R)$, which is the sum of the exponential model and the interpolated profile, by an exponentially decreasing density profile along the vertical axis z,

$$j_{\rm d}(R,z) = \frac{I_{\rm d}(R)}{2h_z} \exp\left(-\frac{|z|}{h_z}\right) \ , \tag{A.11}$$

where the disk-scale height h_z is a free parameter. The factor $1/(2h_z)$ provides the correct normalisation. In Chapter 4 we compare our estimate of h_z with the scale height $h_{z,\rm SR}$ obtained from the relation derived in [321] from a combined sample of 60 edge-on late-type galaxies,

$$\log_{10}\left(\frac{h_R}{h_{z,\rm SR}}\right) = 0.367 \log_{10}\left(\frac{h_R}{\rm kpc}\right) + 0.708 \pm 0.095 \ , \tag{A.12}$$

where the term ± 0.095 quantifies the $\sim$25% intrinsic scatter. We estimate the uncertainty on $h_{z,\rm SR}$ as the sum in quadrature of the intrisic scatter of the relation (A.12) and the uncertainty on h_R. The latter contribution is negligible with respect to the former, so the error on $h_{z,\rm SR}$ nearly coincides with its intrinsic scatter.

We model the three-dimensional luminosity density of the bulge with the Abel integral:

$$j_{\rm b}(r) = -\frac{1}{\pi} \int_r^\infty \frac{dI_{\rm b}}{dR} \frac{dR}{\sqrt{R^2-r^2}} \ , \tag{A.13}$$

where $I_{\rm b}(R)$ is the surface brightness profile modelled as described in Sect. A.1, R is the radius projected on the sky and r is the three-dimensional radius. The equation above assumes a spherically symmetric bulge. As mentioned in Sect. A.1, neglecting the triaxial structure of the bulge should introduce negligible systematic errors in the mass estimates because the galaxy luminosity is dominated by the disk [326]. As anticipated, adopting an analytical model for the two-dimensional surface brightness of the bulge, rather than interpolating the data points as we do for the disk, facilitates its deprojection into three dimensions.

We consider both the atomic and molecular gas distributions as razor-thin disks [324],

$$\rho_{\rm atom,mol}(R,z) = \Sigma_{\rm atom,mol}(R)\delta(z) \ , \tag{A.14}$$

where $\Sigma(R)$ is the linearly interpolated mass surface density of the gas disk and $\delta(z)$ is the Dirac δ function.

Appendix B

Successive Over Relaxation Poisson solver

B.1 Numerical solution of the Poisson equation

For the theories of gravity we consider here, deriving the gravitational potential ϕ that originates from the mass density distribution ρ requires solving the Poisson equation,

$$\nabla^2\phi(R,z) + S(\rho;R,z) = 0\ , \tag{B.1}$$

where the source term S is a generic function of the density ρ. For axisymmetric disk galaxies, we limit the equation to cylindrical coordinates R and z. We only consider static models and Eq. (B.1) is thus an elliptic partial differential equation independent of time.

We solve the Poisson equation with a successive over relaxation (SOR) algorithm, an iterative procedure based on the Jacobi and the Gauss-Seidel algorithms [426]. We find the solution on a rectangular grid of size $L_R \times L_z$, with $(N_R+1)\times(N_z+1)$ grid points and steps $\Delta_R = L_R/N_R$ and $\Delta_z = L_z/N_z$ in the two dimensions (Table B.1).

Given the solution of the gravitational potential $\phi^n_{i,k}$ at the n-th iteration on the grid point of indexes (i,k), the solution at the following $(n+1)$-th iteration is:

$$\begin{aligned}\phi^{n+1}_{i,k} = {}& \phi^n_{i,k}(1-\omega_{\rm SOR})+ \\ & + \frac{\omega_{\rm SOR}}{2R_i(\Delta_R^2+\Delta_z^2)}\left[\phi^{n+1}_{i+1,k}\left(R_i+\frac{1}{2}\Delta_R\right)\Delta_z^2+\right. \\ & + \phi^{n+1}_{i-1,k}\left(R_i-\frac{1}{2}\Delta_R\right)\Delta_z^2 + (\phi^{n+1}_{i,k+1}+\phi^{n+1}_{i,k-1})R_i\Delta_R^2+ \\ & \left.+R_iS_{i,k}\Delta_R^2\Delta_z^2\right]\ ,\end{aligned} \tag{B.2}$$

where $S_{i,k}$ is the source term on the grid and $\omega_{\rm SOR}$ is a parameter in the range of $(0,2)$ to guarantee the convergence. The value of $\omega_{\rm SOR}$ which guarantees the fastest convergence is $\omega_{\rm SOR} = 2/(1+\pi/N)$ for a square grid and $\omega_{\rm SOR} = 2/(1+\pi/N_{\rm min})$ for a rectangular grid, where $N_{\rm min}$ is the smallest number between N_R and N_z. In general, it is computationally convenient to choose the number of grid points N such that $\omega_{\rm SOR}$ is in the range of $(1,2)$; with this choice, the number of iterations necessary to reach convergence is linearly proportional to N, whereas for $\omega_{\rm SOR}$ in the range of $(0,1)$ the number of iterations is proportional to N^2 [426].

We adopt $L_R = 2\times 12h_R$ for almost all galaxies and $L_z = 2\times 100h_{z,\rm SR}$ for all galaxies, where $h_{z,\rm SR}$ is derived from Eq. (A.12). With this choice, the grid domain is substantially larger than the galaxy size, and we can adopt the asymptotic behaviour of the gravitational potential to set the proper boundary conditions (BCs), as we describe in Sect. B.3 below. For UGC 4368 and UGC 6918, we adopt $L_R = 2\times 20h_R$ and $L_R = 2\times 18h_R$, respectively, because $L_R = 2\times 12h_R$ is smaller than the extension of the measured rotation curve. UGC

4458 has $h_R = 9.27$ kpc and, with this large scale length, we adopt $L_R = 2 \times 10 h_R$, which is already sufficient to reach the asymptotic behaviour of the gravitational potential.

The radial resolution of the rotation curves and of the vertical velocity dispersion profiles measured for each galaxy in the DMS sample differs from galaxy to galaxy. For each galaxy, we thus choose N_R and N_z that yield both $\omega_{\rm SOR}$ in the range of $(1, 2)$ and the numerical resolution $\Delta_R = L_R/N_R$ and $\Delta_z = L_z/N_z$ comparable to the observed resolution.

For most galaxies, the grid where we compute the mass distribution and the galactic potential is more extended than the measured surface brightness of the disk and the measured gas surface mass density. To estimate the mass distribution in these regions, we extrapolate the disk surface brightness with Eq. (A.1) with the parameters listed in Table A.1; we instead set to zero the gas mass density because its contribution to the galaxy mass is negligible in these outer regions.

Table B.1: Parameters of the computational grid for the Poisson solver.

UGC (1)	L_R [kpc] (2)	L_z [kpc] (3)	N_R (4)	N_z (5)	Δ_R [kpc] (6)	Δ_z [kpc] (7)	$h_{z,\rm SR}$ [kpc] (8)
448	93.36	92.00	331	326	0.28	0.28	0.46 ± 0.10
463	91.44	92.00	355	358	0.26	0.26	0.46 ± 0.10
1081	72.00	78.00	399	390	0.18	0.20	0.39 ± 0.09
1087	72.24	78.00	281	304	0.26	0.26	0.39 ± 0.09
1529	87.36	88.00	329	330	0.27	0.27	0.44 ± 0.10
1635	76.56	82.00	367	394	0.21	0.21	0.41 ± 0.09
1862	36.96	52.00	341	306	0.11	0.17	0.26 ± 0.06
1908	117.84	108.00	301	276	0.39	0.39	0.54 ± 0.12
3091	79.92	84.00	287	302	0.28	0.28	0.42 ± 0.09
3140	94.08	94.00	303	314	0.27	0.27	0.42 ± 0.10
3701	84.24	86.00	387	394	0.22	0.22	0.43 ± 0.10
3997	132.48	116.00	369	324	0.36	0.36	0.58 ± 0.13
4036	76.32	82.00	347	374	0.22	0.22	0.41 ± 0.09
4107	78.96	84.00	357	380	0.22	0.22	0.42 ± 0.09
4256	102.48	98.00	317	304	0.32	0.32	0.49 ± 0.11
4368	103.60	72.00	395	274	0.26	0.26	0.36 ± 0.08
4380	119.52	108.00	321	290	0.37	0.37	0.54 ± 0.12
4458	185.40	160.00	475	360	0.39	0.44	0.80 ± 0.18
4555	78.96	84.00	295	314	0.27	0.27	0.42 ± 0.09
4622	178.08	140.00	401	316	0.44	0.44	0.70 ± 0.15
6903	125.52	112.00	371	330	0.30	0.30	0.56 ± 0.13
6918	41.76	42.00	397	398	0.11	0.11	0.21 ± 0.05
7244	82.32	86.00	293	306	0.28	0.28	0.43 ± 0.09
7917	174.00	138.00	395	314	0.44	0.44	0.69 ± 0.15
8196	134.16	116.00	377	326	0.36	0.36	0.58 ± 0.13
9177	170.40	136.00	383	306	0.44	0.44	0.68 ± 0.15
9837	141.84	120.00	365	310	0.33	0.33	0.60 ± 0.14
9965	84.24	86.00	237	242	0.36	0.36	0.43 ± 0.10
11318	109.44	102.00	297	278	0.37	0.37	0.51 ± 0.11
12391	87.84	90.00	349	356	0.25	0.25	0.45 ± 0.10

Column 1: UGC number; Col. 2: size of the computational grid in the R-direction; Col. 3: size of the computational grid in the z-direction; Col. 4: grid points in the R-direction; Col. 5: grid points in the z-direction; Col. 6: grid step in the R-direction; Col. 7: grid step in the z-direction; Col. 8: disk-scale height derived with Eq. (A.12).

We centre the computational domain on the origin $R = z = 0$. The coordinate R appears at the denominator in Eq. (B.2). Therefore, to avoid divergences, we choose the grid so that the $R = 0$ axis is not a grid strand, unlike the $z = 0$ axis. We can thus compute both the rotation curve in the plane $z = 0$ and the vertical velocity dispersion at $z = 0$ for any $R \neq 0$.

We set the initial values of the potential to $\phi^0_{i,k} = 0$ over the entire domain except the boundaries (see Sect. B.3) and stop the iteration when:

$$\varepsilon^{n+1} = \frac{1}{(N_R - 1)(N_z - 1)} \sum_{i,k} |\phi^{n+1}_{i,k} - \phi^n_{i,k}| < 10^{-9} \, . \tag{B.3}$$

We test our algorithm with mass density distributions where the Poisson equation in Newtonian gravity can be solved analytically: the Miyamoto-Nagai disk (see Eqs. (B.12) and (B.13)), Satoh disk, logarithmic potential, Plummer sphere, isochrone potential, Hernquist sphere, and Navarro-Frenk-White potential [427]. We compare the numerical and the analytical potentials as a function of R and z.

Within the half-scale length from the centre, the numerical solution is within 1% of the analytic solution for the Miyamoto-Nagai and the Satoh disks, 0.05% for the logarithmic potential, 0.25% for the Plummer sphere, 0.13% for the isochrone potential, 4% for the Hernquist sphere, and 2% for the Navarro-Frenk-White potential. The agreement improves outwards: beyond two scale lengths, it is smaller than 0.5% for the Miyamoto-Nagai and Satoh disks, Hernquist and Navarro-Frenk-White spheres, 0.1% for the Plummer sphere, 0.05% for the isochrone potential, and 0.015% for the logarithmic potential.

B.2 The source term $S(R, z)$

In this work, we consider two gravity theories: MOND and RG.

In the QUMOND formulation of MOND [243], we have:

$$S_{\rm MOND}(R,z) = -\nabla\cdot\left[\nu\left(\frac{|\nabla\phi_{\rm N}|}{a_0}\right)\nabla\phi_{\rm N}\right] \ , \tag{B.4}$$

where $\phi_{\rm N}$ is the Newtonian gravitational potential due to the mass density distribution of the baryonic matter, and $\nu(y)$ is the MOND interpolating function, with $y = |\nabla\phi_{\rm N}|/a_0$. Here, we adopt the simple ν-function, given by Eq. (4.11) (see Eq. (50) with $n = 1$ of [54]).

In cylindrical coordinates, Eq. (B.4) becomes:

$$\begin{aligned} S_{\rm MOND}(R,z) = \ -\Bigg(&\frac{\nu}{R}\frac{\partial\phi_{\rm N}}{\partial R} + \frac{\partial\nu}{\partial R}\frac{\partial\phi_{\rm N}}{\partial R} + \nu\frac{\partial^2\phi_{\rm N}}{\partial R^2} + \\ &+\frac{\partial\nu}{\partial z}\frac{\partial\phi_{\rm N}}{\partial z} + \nu\frac{\partial^2\phi_{\rm N}}{\partial z^2}\Bigg) \ . \end{aligned} \tag{B.5}$$

Deriving the QUMOND gravitational potential clearly requires to solve the Poisson equation twice: first, to estimate the Newtonian potential $\phi_{\rm N}$, where, in Eq. (B.2), we use the standard source term:

$$S_{\rm N}(R,z) = -4\pi G\rho(R,z) \ , \tag{B.6}$$

and, subsequently, to compute $\phi_{\rm MOND}$ with the source term $S_{\rm MOND}(R, z)$ of Eq. (B.5).

To derive the source term in the RG case, we need to recast the RG Poisson equation (3.3),

$$\nabla\cdot[\epsilon(\rho)\nabla\phi_{\rm RG}] = 4\pi G\rho \ , \tag{B.7}$$

as:

$$\nabla\epsilon(\rho)\cdot\nabla\phi_{\rm RG} + \epsilon(\rho)\nabla^2\phi_{\rm RG} = 4\pi G\rho \ , \tag{B.8}$$

so that the source term is:

$$S_{\rm RG}(R,z) = -\frac{4\pi G\rho(R,z) - \nabla\epsilon(\rho)\cdot\nabla\phi_{\rm RG}(R,z)}{\epsilon(\rho)} \ . \tag{B.9}$$

Here, the source term contains the unknown $\phi_{\rm RG}$. At each iteration step, in the source term, we insert the potential $\phi_{\rm RG}$ estimated at the previous step.

The form of Eq. (B.9) requires some additional care in the numerical algorithm: the source term increases when the vacuum permittivity ϵ_0 decreases, and the Poisson solver does not necessarily converge with the optimal value $\omega_{\rm SOR} = 2/(1+\pi/N) \sim 1.97 - 1.98$, for our typical N_R and N_z. To make the Poisson solver converge for ϵ_0 in the flat prior

range of $[0.10-1]$, we need to set $\omega_{\rm SOR}$ to values smaller than $\sim 1.97-1.98$. For example $\omega_{\rm SOR}=2/(1+\pi/25)$ guarantees convergence for every ϵ_0 in our flat prior range. Yet, setting $\omega_{\rm SOR}$ to this unique value would increase the total computational time by at least a factor of 4. We thus vary $\omega_{\rm SOR}$ from $2/(1+\pi/25)$, for ϵ_0 close to 0.10, to $2/(1+\pi/200)$, for ϵ_0 close to 1, according to the explored value of ϵ_0 within the flat prior range.

In MOND, this issue is not present and we can use the same value of $\omega_{\rm SOR}$ for all the parameter combinations, namely $2/(1+\pi/N)$ for a square grid or $2/(1+\pi/N_{\rm min})$ for a rectangular grid.

Numerically, we compute all the derivatives present in all the above equations with the leap-frog method. The first and second derivatives of a function f at a point x are

$$\frac{\partial f}{\partial x}=\frac{f(x+\Delta x)-f(x-\Delta x)}{2\Delta x} \tag{B.10}$$

and

$$\frac{\partial^2 f}{\partial x^2}=\frac{f(x+\Delta x)+f(x-\Delta x)-2f(x)}{\Delta x^2}\,, \tag{B.11}$$

where Δx is the grid step. With the grid steps we adopt, the leap-frog method guarantees relative errors smaller than 5% on the estimated derivatives.

B.3 Boundary conditions

Elliptic equations, like our Poisson equations, require BCs to be set. To facilitate the choice of the BCs we put the disk galaxy at the centre of the grid domain and choose the size of the domain substantially larger than the galaxy size. We could use the axial symmetry of the problem and only consider a fourth of that domain, with two BCs along the R and z axes. This choice would clearly reduce the computation time by a factor of four, but it would pose the nontrivial problem of setting the BCs on the two axes cutting through the galaxy centre. We thus prefer to compute the potential in all the four quadrants and to set the BCs far from the galaxy centre.

Since the bulge and gas components are not dynamically dominant in the DMS galaxies [317], we use only the disk component to set the BCs. In the external regions of the domain we model this component with a double exponential disk (Eq. A.11), since we use the exponential profile (A.1) to extrapolate the disk surface brightness in these regions. In Newtonian gravity, this mass distribution generates a gravitational potential that does not have a close analytic expression, but it is well approximated by the sum of the gravitational potentials of three Miyamoto-Nagai disks [428]. The Miyamoto-Nagai disk has mass density distribution [429]:

$$\rho_{\rm MN}(R,z)=\left(\frac{b^2M_{\rm MN}}{4\pi}\right)\frac{aR^2+(a+3\sqrt{z^2+b^2})(a+\sqrt{z^2+b^2})^2}{[R^2+(a+\sqrt{z^2+b^2})^2]^{5/2}(z^2+b^2)^{3/2}}\,, \tag{B.12}$$

and generates the Newtonian gravitational potential (e.g. [427],

$$\phi_{\rm MN}(R,z)=-\frac{GM_{\rm MN}}{\sqrt{R^2+(a+\sqrt{z^2+b^2})^2}}\,, \tag{B.13}$$

where $M_{\rm MN}$ is the disk mass and a and b are its scale length and scale height.

The gravitational potential of a double exponential disk can thus be approximated by

the equation:

$$\begin{aligned}\phi_{\rm exp}(R,z) = &- \frac{GM_1}{\sqrt{R^2+(a_1+\sqrt{z^2+b^2})^2}} + \\ &- \frac{GM_2}{\sqrt{R^2+(a_2+\sqrt{z^2+b^2})^2}} + \\ &- \frac{GM_3}{\sqrt{R^2+(a_3+\sqrt{z^2+b^2})^2}} \ ,\end{aligned} \tag{B.14}$$

where M_1, M_2 and M_3 are the three Miyamoto-Nagai disk masses, a_1, a_2, a_3 are their scale lengths, and b is the scale height which is equal in all the three disks. The three disks are only mathematical artefacts to generate the physical gravitational potential, but they do not correspond to three physical disks. Indeed, the mass M_2 of the second disk is always negative.

The parameters of the Miyamoto-Nagai disks are related to the parameters of the double exponential disk (Eq. A.11) and its total mass $M_{\rm d}$ according to the equations [428]

$$\frac{b}{h_R} = -0.269\left(\frac{h_z}{h_R}\right)^3 + 1.080\left(\frac{h_z}{h_R}\right)^2 + 1.092\frac{h_z}{h_R} \ , \tag{B.15}$$

$$\begin{aligned}\frac{M_1}{M_{\rm d}} = &-0.0090\left(\frac{b}{h_R}\right)^4 + 0.0640\left(\frac{b}{h_R}\right)^3 + \\ &- 0.1653\left(\frac{b}{h_R}\right)^2 + 0.1164\frac{b}{h_R} + 1.9487 \ ,\end{aligned} \tag{B.16}$$

$$\begin{aligned}\frac{M_2}{M_{\rm d}} = &\ 0.0173\left(\frac{b}{h_R}\right)^4 - 0.0903\left(\frac{b}{h_R}\right)^3 + \\ &+ 0.0877\left(\frac{b}{h_R}\right)^2 + 0.2029\frac{b}{h_R} - 1.3077 \ ,\end{aligned} \tag{B.17}$$

$$\begin{aligned}\frac{M_3}{M_{\rm d}} = &-0.0051\left(\frac{b}{h_R}\right)^4 + 0.0287\left(\frac{b}{h_R}\right)^3 + \\ &- 0.0361\left(\frac{b}{h_R}\right)^2 - 0.0544\frac{b}{h_R} + 0.2242 \ ,\end{aligned} \tag{B.18}$$

$$\begin{aligned}\frac{a_1}{h_R} = &-0.0358\left(\frac{b}{h_R}\right)^4 + 0.2610\left(\frac{b}{h_R}\right)^3 + \\ &- 0.6987\left(\frac{b}{h_R}\right)^2 - 0.1193\frac{b}{h_R} + 2.0074 \ ,\end{aligned} \tag{B.19}$$

$$\begin{aligned}\frac{a_2}{h_R} = &-0.0830\left(\frac{b}{h_R}\right)^4 + 0.4992\left(\frac{b}{h_R}\right)^3 + \\ &- 0.7967\left(\frac{b}{h_R}\right)^2 - 1.2966\frac{b}{h_R} + 4.4441 \ ,\end{aligned} \tag{B.20}$$

$$\begin{aligned}\frac{a_3}{h_R} = &-0.0247\left(\frac{b}{h_R}\right)^4 + 0.1718\left(\frac{b}{h_R}\right)^3 + \\ &- 0.4124\left(\frac{b}{h_R}\right)^2 - 0.5944\frac{b}{h_R} + 0.7333 \ .\end{aligned} \tag{B.21}$$

In Newtonian gravity, we impose that the gravitational potential equals Eq. (B.14) on the borders of the rectangular domain. In MOND, when the acceleration drops below the critical acceleration, $a_0 = 3600\ \mathrm{kpc}^{-1}\ (\mathrm{km\ s}^{-1})^2$, the gravitational field has the asymptotic behaviour [241]:

$$g = \sqrt{a_0 |g_{\mathrm{N}}|}\ , \tag{B.22}$$

which, in cylindrical components, becomes (see also Sect. 3.1):

$$\frac{\partial \phi}{\partial R} = \sqrt{a_0 \left| \frac{\partial \phi_{\mathrm{N}}}{\partial R} \right|}\ , \tag{B.23}$$

and

$$\frac{\partial \phi}{\partial z} = \sqrt{a_0 \left| \frac{\partial \phi_{\mathrm{N}}}{\partial z} \right|}\ . \tag{B.24}$$

To solve the MOND Poisson equation, we thus impose the Neumann BCs (B.23) and (B.24), with $\partial \phi_{\mathrm{N}}/\partial R$ and $\partial \phi_{\mathrm{N}}/\partial z$ derived analytically from Eq. (B.14).

As illustrated in [300], at sufficiently large distances from the galaxy centre, RG recovers the MOND asymptotic behaviour of the radial gravitational field. We thus impose the Neumann condition (B.23) on the four borders of the domain for the radial component of the gravitational field. For the vertical component, we resort to the fact that the field lines are refracted and, at large distances from the source, they are almost parallel to the disk plane. We thus set:

$$\frac{\partial \phi}{\partial z} = 0 \tag{B.25}$$

on the domain borders (see also Sect. 3.1).

In the analysis of the DMS galaxies, both the disk-scale height b and the disk mass M_{d}, which appear in Eqs. (B.14)-(B.21), are initially unknown. These parameters depend on h_z and Υ, which are two free parameters of the fit. Therefore, we update the BCs derived from Eqs. (B.23) and (B.24) at each step of the MCMC chain.

Appendix C

Parallel computing: the astroMP code and the 2D Laplace solver[1]

As mentioned in Sect. 4.3, we parallelise the C++ code to model the entire DMS sample at the same time with OpenMP. Indeed, since this code involves 30 galaxies, whose quantities are discretised, for each of them, on a grid of 100-150k points, its sequential execution can become very slow when several MCMC iterations are required to reach a good convergence. In particular, the most computationally expensive region of the code is the Poisson solver, which we have to run 2×30 times per MCMC iteration. By parallelising the code, we pass from a total computing time of 6.1 Ms ($\sim$71 days) to a total computing time of 0.52 Ms ($\sim$6 days), considering 20000 MCMC iterations. This code is publicly available at `https://github.com/alpha-unito/astroMP` under the name of astroMP.

To achieve the best gain in performance with respect to its sequential version, we apply to this code a semi-automatic methodology aimed to parallelise, with a limited re-designing effort, scientific applications designed with a purely sequential programming mindset, thus possibly using global variables, aliasing, random number generators, and stateful functions. This methodology works for the parallelisation in the shared-memory model (via OpenMP), message-passing model (via MPI), and General Purpose Computing on GPU model (via OpenACC) and it can be applied to any code whose control flow statements are made of loops, which can be defined either in sequence or nested [342, 343].

In [342] and in [343] we apply this methodology to four real-world sequential (community) codes in the domain of physics and material science: the astroMP code (parallelised with OpenMP), the SprayWeb code (parallelised with CUDA and OpenACC), the SimpleMD code (parallelised with MPI) and the 2D Laplace solver (parallelised with MPI). In the following sections we detail the mentioned methodology and the structure, the parallelisation procedure and the scaling properties of two of these programs on which we directly worked on: the astroMP code and the 2D Laplace solver.

C.1 The semi-automatic methodology

The most prominent control flow statement in scientific codes is the *loop*, which denotes iterative computations. Pragmatically, the *for-loop* iterates over arrays of data, whereas the *while loop* iterates up to a given convergence criterion [430]. They can appear juxtaposed in a sequence or nested in any order. Code in the loop body might exhibit a network of dependencies among different loops and iterations of the same loop. Examples are in:

- *Particle simulations*, in which an internal loop computes quantities related to each particle and an external loop advances the simulation time step.

[1] The results in this chapter are published in [342] and in [343].

- *Optimization algorithms*, in which one or more internal loops iterate over a subset of the solution space and an external loop updates the best solution and the heuristic parameters.
- *ODE solvers*, in which internal loops iterate over different functions or subsystems and an external loop advances the time step.

To parallelise a nested loop program, we advocate the following methodology:

1. Identify all parallelisable loops in the code, according to a depth-first search strategy.
2. Evaluate the potential performance gain obtainable by modifying each parallelisable loop, filtering out those that are not worth the parallelisation effort.
3. Make each of the remaining candidate loops self-contained, to remove true data dependencies among different iterations.
4. Use nonparallelisable loops as a reference to implement a checkpointing logic, to support stop-resume behaviour.

We detail these steps in the sections below.

C.1.1 Identify parallelisable loops

We say that A and B are nested loops when the statements of loop B are a proper subset of the statements of loop A. In the most general case, due to procedure/function calls, the described loop inclusion relationship generates a (cyclic) graph of loops and is too weak to identify parallelisable loops. For this, given a code containing multi-level nested loops, it is useful to induce a partial order relation in the inclusion graph using some additional relations to turn the graph into a tree. A good example is the domination relationship [431], which induces the *loop-nest tree*, in which each node refers to a distinct loop and a node B is a child of node A if they are nested loops, and no other loop appears between them. To put all loops in the same tree, we can consider the entire program body as a pseudo-loop with only one iteration, and we can use it as the root of the tree.

A generic and formal treatment of this concept requires some technicalities from graph theory. However, in many common cases, it is quite simple to construct such a tree just by carefully analysing the code. Such representation of multi-level nested loops suggests a parallelising strategy consisting in considering one loop at a time with a *depth-first search* technique, starting from the most external level. In this setting, we consider the single iteration of the loop as an *atomic work unit*, and a synchronisation barrier is (implicitly or explicitly) placed at the end of each loop, ensuring to preserve potential inter-loop dependencies.

Bernstein's seminal paper clearly states that the problem of determining if two arbitrary program sections are parallelisable is undecidable and offers sufficient conditions to assert that two sections can be executed in parallel by way of three kinds of data dependencies: *true dependencies*, *anti-dependencies* and *output dependencies* [432].

We can categorized loops as:

- *Loop-independent*, when iteration i does not depend on any iteration $j < i, \forall i < N$.
- *Loop-carried* when $\exists n \geq 1$ such that iteration i depends on iteration $i - n$.

Loops with independent iterations can be trivially parallelised, whereas in the presence of loop-carried dependencies things get more involved. Unfortunately, loops that are not written with a parallel mindset can sometimes contain unnecessary dependencies. They are generally due to certain sequential coding habits, such as "reusing" variable names for other purposes (inducing anti- and output dependencies). They can be automatically

removed using techniques such as *variable privatisation*, i.e., using multiple copies of the same variable. Loop induction variables are a typical example of variables that can be privatised. True dependencies are much harder to address and have been the object of intense research [433]. The parallelisation of loops that have loop-carried dependencies in their original form is often possible by transforming the loop into some new form in which the dependencies are removed or arranged to occur at a sufficient distance so that concurrent iterations do not conflict. A paradigmatic example is the substitution of an accumulator variable with a *reduce* (higher-order) function (over an array of privatised variables). However, not all true dependencies can be eliminated via a *reduce* function. A typical case is when the accumulation operation is not associative, as it happens for updating a variable with the next random number in a sequence.

A practical way to parallelise a program is to descend the loop hierarchy until a parallelisable loop is found. Unfortunately, things can get a bit more complicated in the presence of conditional branches, which can make the parallelisability of a loop a data-dependent property. In this case, it is useful to identify the most computationally demanding paths in the control flow graph and separate them from the rest of the code in dedicated procedure calls to reduce complexity. Another potential source of complication arises in those cases when a function containing a loop in its body is called multiple times in the code. In such a scenario, the same loop can appear multiple times in different positions of the hierarchy, with different parallelisability properties each time. In this case, a good strategy would be to maintain a serial version of the function for the nonparallelisable cases, together with one or more parallel versions for the others.

C.1.2 Evaluate potential performance gain

Every time the previously described depth-first search encounters a parallelisable loop, it is necessary to evaluate the potential benefit introduced by a parallel implementation, which always comes with a certain amount of overhead introduced by synchronisations among different workers. When the effective computation time of a parallel section (called *grain*) becomes too small, parallelisation can result in even worse performances than the original serial version. On a modern multi-core platform, the mainstream frameworks such as OpenMP or Intel TBB exhibit a lower limit for the grain which can be considered on the order of tens of thousands of clock cycles. Finer grains can be addressed only with lock-free programming frameworks, such as Fastflow, that can support grains down to hundreds of clock cycles [434].

Some useful quantities that should be taken into account when estimating the potential performance gain introduced by the parallelisation of a specific loop are the *number of iterations*, which affect the maximum obtainable degree of parallelism, and the *total time* spent by the program inside the loop, which determines the maximum achievable speedup. In some cases, when these estimations are complicated due to the presence of a high number of branching constructs or external procedure calls, a call-graph tool like Callgrind [435] can be considerably helpful.

In general, it would be better to parallelise an outer loop instead of one of its nested counterparts, because this strategy minimises the introduced overheads, e.g., for thread creation and synchronisation, even if we cannot define a better strategy. For example, if a loop has very few iterations, the parallelisation of one or more of its inner loops can lead to better results and, if the code runs on many processors, the parallelisation of both inner and outer loops can be more convenient [436]. Nevertheless, an effective greedy technique would be to start parallelising the suitable outermost loop, where suitable means both feasible and convenient, and then descend the loop hierarchy parallelising suitable nested loops until either performance requirements are met, or no noticeable speedup is brought by further optimisations.

Once all candidates for parallelisation have been identified, it is worth to evaluate the

maximum performance gain that can be expected after the effective transformation of the program. To predict the performance of a parallel code, we have to investigate its potential strong and weak scalability. *Strong scaling* represents the ability of a software to solve a problem of fixed size faster with a higher amount of computing resources and it is strictly related to the notion of *speedup* of a program. The speedup S is defined as the ratio between the time t_s taken by the sequential code and the time $t_\mathrm{p}(n)$ taken by the parallel code with an increasing number of processing elements n.

The ideal speedup is linear. Nevertheless, in a real scenario, it is limited by those portions of the code that cannot be parallelised. More precisely, as Amdahl stated in 1967 [437], an upper bound for a program speedup can be expressed as the inverse of $s + p/n$, where s is the fraction of the total execution time of the code spent by the serial portion of the code, and p is the fraction of the total execution time of the code spent by the parallelised part. Unfortunately, Amdahl's law does not take into account all the overheads introduced by a parallel implementation, e.g., communications and synchronisations among different workers or initialisation of processes/threads. Indeed, actual performances of a program are usually worse than those derived from such law.

Whereas strong scaling is investigated for a problem of fixed size, *weak scaling* is investigated for a problem of variable size, keeping constant the amount of work assigned to each computing resource. Gustafson's law, formulated in 1988 [438], describes the *scaled speedup* as $s + p \times n$. This law states that the size of a problem scales with the available number of processors: the time spent in the parallel part of the code linearly grows with processors, whereas the time spent in the serial part of the code remains constant with the size of the problem. This means that, if a code is fully parallelisable, the time spent by a problem of size n to run on n processors will remain constant. The scaled speedup does not have an upper limit.

C.1.3 Make loops self-contained

Once we have identified a loop that is worth to parallelise, it is necessary to transform the iterative construct into a self-contained procedure call, which takes in input all the externally declared variables used inside an iteration. If the code is parallelised on a many-core accelerator with a local address space, all the external variables have to be passed by value as arguments of the newly created procedure. Otherwise, this is necessary only for the variables that have to be written inside the body of the procedure. Nevertheless, some modern programming models for hardware accelerators (such as latest versions of CUDA) provide an abstract unified address space between host and device memory and manage data transfers under the hood, considerably reducing the programming effort.

Frequently a loop is used to iterate over an array of inputs to produce an array of outputs, but it is not uncommon that such loop is immediately followed by another loop that combines all the produced elements in a single value, by means of an associative binary operator (e.g., the sum or the product). When thinking about parallel implementations, this particular pattern can be transformed into a *reduce* operation. With an input array of n elements and n workers, a reduce pattern is able to produce the final output in $\log n$ time steps.

Both the transformation of iterative constructs into self-contained procedure calls and the implementation of the reduce function can either be performed manually or left to an external library like OpenMP or OpenACC. It is always recommended to start with the second approach since it is much easier and faster to implement and can guarantee better performance portability among different hardware architectures. Instead, we can resort to a manual implementation only when appropriate.

C.1.4 Deal with random number generators

The complexity in dealing with random number generators in parallel codes is due to their stateful nature, which is primarily aimed at approximating genuinely random numbers with actually deterministic numbers generated with pseudo-random number generators (PRNG). These numbers can be reproduced if the state of the PRNG is known. PRNGs appearing in sections of code that are sequentially executed do not need special care but rather the moment of generation can be used as a checkpoint (see Sect. C.1.5). On the contrary, their parallelisation requires special care. Firstly, the PRNG implementation should be *thread-safe*, i.e., performed from multiple threads safely and *reentrant*, i.e., performed from multiple actors of the same thread safely (called multiple times within the same thread). Secondly, to enforce reproducibility, the random sequence generated in each parallel section should be deterministic, thus independent of the relative execution order of the parallel sections. This is achieved by privatising the random induction variable. In object-oriented languages, this can be easily achieved by using an array of PRNG objects. Thirdly, to enforce correctness and reproducibility, the array of PRNG objects should be initialised with a seed generated with a master PRNG implemented with another algorithm, since using the same algorithm is going to reduce the period and induce loss of uniformity of distribution in generated numbers. Once the seed of the master PRNG is fixed, the sequence of random numbers generated in each parallel section should be deterministic. Fourthly, scientists should know that parallelising a section of code with PRNG breaks *sequential equivalence*, i.e., the results computed by the sequential and the parallel codes are different. It is a scientist's duty to prove that the sequential and the parallel codes compute the same stochastic process.

C.1.5 Implement checkpointing logic

The sequential regions of a parallel code do not provide a gain in performance, but they can provide another advantage. Indeed, since they define a global order in the execution of the program, they can be defined as checkpoints. A *checkpoint* is a snapshot of the entire state of the process at the moment it was taken, which represents all the information needed to restart the process from that point [439]. Usually, checkpoints are recorded on *stable storage* that is persistent storage with some reliability requirements.

Two essential concepts related to checkpoints are the *checkpointing overhead*, i.e., the increase in the total execution time caused by the introduction of the checkpointing procedure, and the *checkpointing latency*, i.e., the time needed to save the checkpoint. The aim of an appropriate checkpointing strategy is to minimise the first quantity. In order to do that, two different approaches are possible. The first is to try to minimise latency, either using more advanced storage and communication technologies or reducing the amount of data that must be stored. The other is to store checkpointing data *asynchronously*, reducing overhead regardless of latency. Often, a combination of the two gives the best results.

As an example, a checkpoint can be defined in a random sequence of numbers initialised with a given seed. If the application fail-stops in a given point in the sequence, it is possible to restart it from the same point, provided that the state of the random number generator is saved at every iteration in permanent storage. In this work, we can see that this procedure is particularly useful in Monte Carlo Markov Chains (MCMCs), that can be quite computationally expensive.

We show now how this methodology applies to the astroMP and the 2D Laplace solver codes.

C.2 The astroMP code

In a nutshell, the astroMP code [342, 343] (Algorithm 1) models, at the same time, the rotation curves and the vertical velocity dispersions from the mass distributions of 30 disk galaxies belonging to the DMS, exploring the agreement between the models and the measured data with a Bayesian approach. We run a MCMC for 19000 iterations after 1000 burn-in steps, a number suitable to reach a good convergence (see Sect. 4.3).

We adopt flat priors for the free parameters of the model and a Metropolis-Hastings acceptance criterion for the MCMC, obtaining the random variate $\vec{x}$ at the step $i+1$ from the multi-variate Gaussian probability density $G(\vec{x}|\vec{x}_i)$ peaked at $\vec{x}_i$, the random variate at the previous MCMC step. We define a Metropolis-Hasting ratio

$$R_{\rm MH} = \frac{p(\vec{x}) \times \mathcal{L}(\vec{x})}{p(\vec{x}_i) \times \mathcal{L}(\vec{x}_i)} \frac{G(\vec{x}|\vec{x}_i)}{G(\vec{x}_i|\vec{x})}, \tag{C.1}$$

where $\vec{x}$ is the free parameters vector, $p(\vec{x})$ is the product of the priors of the parameters and $\mathcal{L}(\vec{x}) = \sqrt{\exp\left[-\chi^2_{\rm tot}(\vec{x})\right]}$ is the likelihood. If $R_{\rm MH} \geq 1$ $\vec{x}$ is accepted, else it is accepted with probability $R_{\rm MH}$ or rejected with probability $1 - R_{\rm MH}$ (see also Sect. 4.1 for the description of the MCMC and the Metropolis-Hastings algorithms).

C.2.1 Serial version

The overall structure of the code is reported in black in Algorithm 28. A first preparatory step imports some input data from external files (line 1). Among them we find, for each galaxy, the mass density, the kinematic data, that have to be compared with the models, and the features of the grid where the gravitational potential, the gravitational field and the kinematic profiles of the galaxy are computed. Right after the data import, we set the priors, initialise the MCMC (line 2), and we define two PRNG with the same seed (line 3) in order to sample: a real uniform distribution, $U(0, 1)$, for the Metropolis-Hastings criterion (line 26) and a multi-variate Gaussian distribution, $G(\mathbf{0}, \mathbf{1})$, used to generate the free parameters (line 17) in the second step of the MCMC.

The main body of the program consists of two nested for-loops. The most external loop iterates on the number of MCMC iterations we decide to perform (lines 6–28), while the internal one iterates on the number of galaxies present in the sample. Within the second level for-loop (lines 13–16) we have to execute the same sequence of operations for every galaxy (lines 14–15):

1. Computation of the galaxy's gravitational potential ϕ from its mass density ρ, solving the Poisson equation (B.1) with a SOR Poisson solver [426] (see Appendix B).
2. Computation of the radial and vertical derivatives of ϕ (gravitational field).
3. Computation of the rotation curve and the vertical velocity dispersion profile (Eqs. (2.2) and (4.7)) and their respective χ^2 (Eqs. (4.2) and (4.9)).

After that, the χ^2 of the rotation curve and of the vertical velocity dispersion computed for each galaxy are reduced (with sum operation) to obtain the global likelihood (line 16). Then, both the inner for-loop (lines 22–25) and the reduce operation (line 25) are repeated for the second part of the MCMC, starting from a new combination of free parameters randomly generated from the previous one (line 17). Finally, a Metropolis-Hastings acceptance criterion is applied to accept or reject the last combination of parameters for the next iteration of the MCMC (line 26).

C.2.2 Semi-automatic parallelisation

First of all, we identify the code regions with true data dependencies, that is that are not parallelisable. The first important region is the MCMC, which is a sequential process

by definition as the new combination of free parameters is drawn from the previous one at every step. This region cannot, therefore, be parallelised, but it can be used for checkpointing purposes (more details are in Sect. C.2.3). The second region is made of the innermost loops, which compute the field of every galaxy from the potential and the kinematic profiles from the field.

Then, we identify the points without true data dependencies, which can be parallelised. This region is made of the second level for-loops that iterate on the number of galaxies in the sample (lines 13–16 and 22–25). Since we independently perform the same operations for every galaxy, these loops result embarrassingly parallelisable. Also, the reduce operations (lines 16 and 25) can be parallelised, implying an eliminable dependence since they are based on an associative binary operator (the sum in this case) on the χ^2 derived from the kinematic profiles of each galaxy. For this reason, we put the reduce operations within the for-loops that iterate on the number of galaxies. We parallelise these for-loops using the OpenMP library, with the `#pragma omp parallel for shared(`χ^2`) reduction(+:` $\chi^2_{\rm tot}$`)` directive before each loop (lines 12 and 21).

Algorithm 28 shows in red the modifications with respect to the serial code that provide its parallelisation.

C.2.3 Checkpoints

The MCMC can be very computationally demanding, requiring an execution time of one week on a modern platform even after an adequate optimisation process. During such a long period, the code can be interrupted for many reasons and restarting it from the beginning after every stop would result in a severe loss of time.

In our MCMC, we implement two random sequences initialised with the same seed (line 3). The first is the sequence for a random number U, that follows a real uniform distribution between 0 and 1. Its definition is necessary for the Metropolis-Hastings criterion: if $R_{\rm MH} \geq U$ $\vec{x}_{i+1} = \vec{x}$, else $\vec{x}_{i+1} = \vec{x}_i$. The second is the sequence for a multi-variate random variable that follows a normal distribution peaked on the previous combination of free parameters with a given standard deviation, used to generate the new combination of free parameters from the previous one.

To implement these two random sequences, we define two pseudo uniform random number generators, $\rm PRNG_1$ and $\rm PRNG_2$, from the C++ library Boost. Every 1000 iterations we print in text files, using the `ofstream` operator, the following information: 1) the values of the generators $\rm PRNG_1$ and $\rm PRNG_2$ at the beginning of the MCMC iteration (lines 7–8)); 2) the parameters chains at the end of the MCMC iteration (lines 27–28). If, for any reason, the execution is interrupted between the $n \times 1000$ and the $(n+1) \times 1000$ MCMC iterations, before restarting the main loop, we can just import from disk the chains made of the first $n \times 1000$ parameters and the two generators saved at step $n \times 1000$ and resuming the MCMC loop from iteration $n \times 1000$, instead of restarting it from scratch.

C.2.4 Performance evaluation

We investigate the strong and the weak scaling of this code to test its performance. To perform these tests, we only take 5 MCMC iterations to operate in reasonable timescales. We perform the tests on a Linux OS running on a 48-core platform (quad-socket Intel Xeon E7, 12 physical cores per socket) with 768 GB of memory. The following performance analysis also includes the impact of the *numa control* on the results. On UNIX systems, a process can be launched with the `numactl` command, which spreads the computation on different sockets and affects how data are stored in different cache levels. In particular, the *interleave all* mode keeps all the cores available in all the sockets, whatever the number of threads, allocating memory on all sockets using a round-robin strategy. Conversely, the *block* mode uses one socket per time, until the number of threads saturates its cores.

Algorithm 1: Parallel DiskMass Survey

```
1  data_import(density, kinematic data, grid features)
2  x⃗_t ← init_MCMC()
3  PRNG_1(seed), PRNG_2(seed)
4  U ← U(0, 1)
5  G ← G(0, 1)
6  for t ← 1 to T do
7      if t mod 1000 == 0 then
8          save(PRNG_1, PRNG_2)                                   // checkpoint
9      χ²_tot(x⃗_t) ← 0
10     omp_set_dynamic(0)
11     omp_set_num_threads(Nthreads)
12     #pragma omp parallel for shared(χ²_j(x⃗_t)) reduction(+: χ²_tot(x⃗_t))
13     for j ← 0 to N_gal do
14         potentials[j] ← compute_potential(x⃗_t)
15         χ²[j]← compute_chi2(potentials[j])
16         χ²_tot(x⃗_t) += χ²[j]                                   // reduce
17     y⃗ ← x⃗_t + jump × G(PRNG_2)
18     χ²_tot(y⃗) ← 0
19     omp_set_dynamic(0)
20     omp_set_num_threads(Nthreads)
21     #pragma omp parallel for shared(χ²_j(y⃗)) reduction(+: χ²_tot(y⃗))
22     for j ← 0 to N_gal do
23         potentials[j] ← compute_potential(y⃗)
24         χ²[j]← compute_chi2(potentials[j])
25         χ²_tot(y⃗) += χ²[j]                                     // reduce
26     x⃗_t ← MH_acceptance_criterion(χ²_tot(x⃗_t), χ²_tot(y⃗), U(PRNG_1))
27     if t mod 1000 == 0 then
28         save(x⃗_t)                                              // checkpoint
```

For comparison, we also investigate the strong and the weak scaling of the code on a Linux OS running on a 24-core platform (two-socket Intel Xeon E5, 12 physical cores per socket) with 128 GB of memory, using the default policy of the machine (without the *numa control*).

Strong scaling

To investigate the strong scaling of this code, we consider the entire galaxy sample. To measure the actual speedup of our code we take the CPU time of each MCMC iteration with the function `gettimeofday` (μs) setting in the latter an increasing number of threads from 1 to 48 with the `omp_set_num_threads(Nthreads)` function (lines 11 and 20), where the number of threads `Nthreads` is taken in input from an external file.

The left panel of Fig. C.1 shows the strong scaling (speedup) with the *numa control* in the *block* mode (red line) and in the *interleave all* mode (blue line) and with the default policy of the machine (green line) on the 48-core platform, where t_s and t_p are the execution times for the sequential and the parallel code, respectively. Each point of the plot is the average over 5 MCMC runs. The errors on the ratio t_s/t_p, shown in the figure as shaded areas, are calculated by propagating the uncertainties on t_s and t_p, which in turn are the standard deviations of the times of the five respective iterations.

This figure shows that the ideal law $S = N_{\rm threads}$ (black dashed line) holds more or less from 1 to 4 threads, but there is still a quite good linear trend until 9-10 threads. Then, the measures start to increase more slowly, converging to an asymptotic value around 12. According to the Amdahl's law, this means that the time of the serial fraction of the code is about 1/12 of the total computational time. However, this asymptotic value is reached in different ways in the three modes.

The speedup of the code is comparable among the three modes only for a number of threads between 1 and 9 and between 35 and 48. For an intermediate number of threads, the speedup in the *block* mode increases more slowly than in the other two cases. This means that, if we operate in the *block* mode, we need a number of threads equal to the resources of the entire machine, or of a large part of it, to obtain the maximum gain in performance. Instead, with the default policy of the machine and in the *interleave all*

mode, whose strong scaling curves are very similar, we only need a number of threads equal to half of the resources of the machine. Between 10 and 34 threads, the default and the *interleave all* modes provide a better gain in performance than the *block* mode.

From the left panel of Fig. C.1 we can notice the big jump in performance between 24 and 25 threads in the default and in the *interleave all* modes. In the *block* mode, we can observe an abrupt slowdown of the parallel code in correspondence of 13 threads, which is where the number of threads has saturated the first socket and has just started to use the second one.

The left panel of Fig. C.2 shows the strong scaling with the default policy of the machine on the 24-core platform. Qualitatively the trend of this strong scaling curve is quite similar to the corresponding one on the 48-core platform. Nevertheless, the most striking difference is the asymptotic value reached by the speedup that on the 24-core platform is around 8 and on the 48-core platform is around 12.

Weak scaling

In order to investigate weak scaling, we have to define a unit of work. Since the parallelised for-loop iterates on the number of galaxies in the considered sample, so that the larger the number of galaxies, the more computational demanding the code, we define *one galaxy* as our unit of work. At this point, we measure the time spent by the program with n galaxies run on n threads, where n goes from 1 to 48. The galaxies in our original sample are all different from each other. Nevertheless, to consider homogeneous units of work, we choose a single galaxy and we run the related computation once on a single-core, twice on two cores and so forth.

In the right panel of Fig. C.1 we plot the mean time in seconds of each MCMC iteration in function of the number of used threads, which coincides with the number of used galaxies, for the default (green line), the *interleave all* (blue line) and the *block* modes (red line). As in the left panel of the same figure, the shaded areas show the error bars of the measures, taken as the standard deviations of the times of the five respective iterations. If the code were fully parallelisable the time would remain constant, for whichever number of threads equal to the number of galaxies but there is often a section of code which remains sequential which makes the trend not perfectly constant.

We can observe different trends in the three modes. As for the strong scaling, the weak scaling curves corresponding to the default and the *interleave all* modes are quite similar. With these two modes, there is a very gradual slowdown of the code from 1 to 37 threads, where the time passes from 4.9 to 5.9 seconds in the *interleave all* mode and from 4.9 to 6.2 seconds in the default mode. We can thus state that weak scalability is mostly satisfied in this range of threads. Then the code shows a steeper slowdown from 37 to 48 threads, where we lose almost two seconds in performance, passing from ~ 6 to 7.7 or 7.9 seconds, in the *interleave all* and in the default modes, respectively. We can see regular bumps of the time from 4 to 37 threads.

In the *block* mode, we observe almost the same global trend as in the default and in the *interleave all* modes, but passing from 1 to 14 threads, which means that the slowdown of the code occurs faster. After 14 threads, the mean time of each MCMC iteration remains almost constant, around 7.5 seconds, and the standard deviation of the measures increases. Also this test shows that the default and the *interleave all* modes provide the highest efficiency, which means that to obtain the best performance gain we have to use the entire machine. In this test, the *interleave all* mode appears slightly more efficient than the default mode. Conversely, using only a part of the machine sufficient to host the number of used threads, as in the *block* mode, leads to a loss in performance.

The right panel of Fig. C.2 shows the weak scaling in the default policy of the machine on the 24-core platform. The time remains mostly constant from 1 to 10 threads, and it shows a gradual slowdown until 24 threads, passing along the entire considered range of

threads from 4.7 to 5.8 seconds. So, the default mode on the 24-core platform from 1 to 24 threads almost behaves like the corresponding curve on the 48-core platform between 1 and 37 threads. The default curve on the 48-core platform appears flatter than the corresponding curve on the 24-core platform between 1 and 24 threads.

We can state that our code satisfies weak scalability since the mean time of one MCMC iteration remains mostly constant for quite long intervals of threads equal to the number of galaxies.

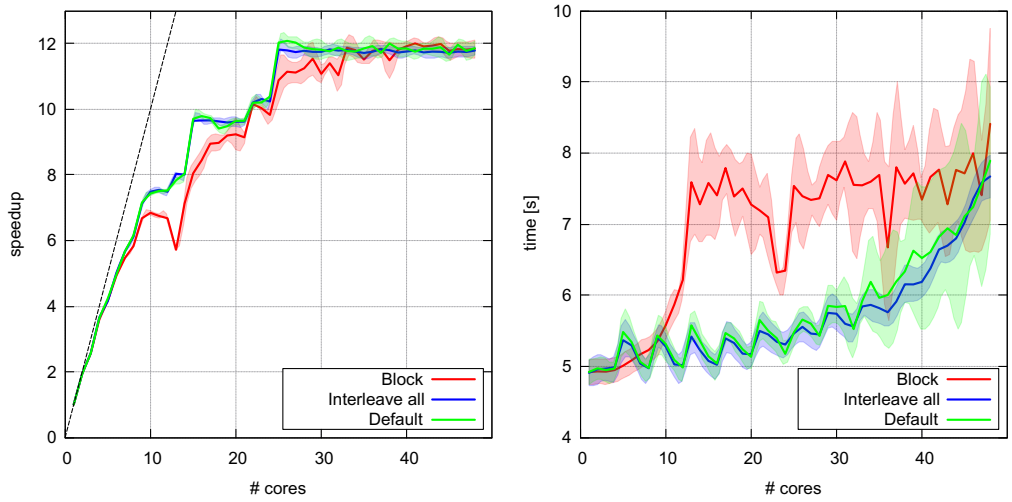

Figure C.1: Left panel: strong scaling (Amdahl's law). Right panel: weak scaling (Gustafson's law). Both plots are referred to an Intel 48-core platform. The three solid lines (red, blue, green) refer to application run using different *NUMA control* policies for scheduling threads onto cores. The black dashed line shows the ideal Amdahl's law.

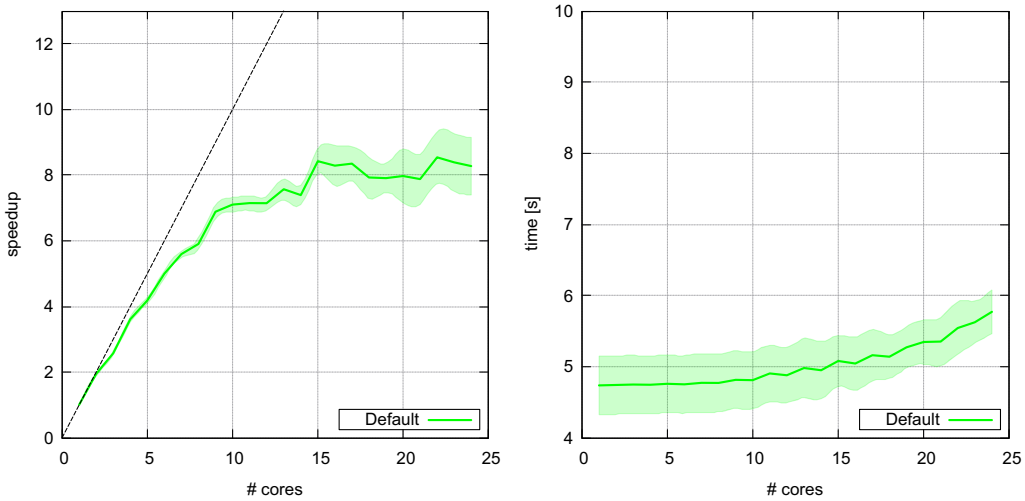

Figure C.2: Left panel: strong scaling (Amdahl's law). Right panel: weak scaling (Gustafson's law). Both plots are referred to an Intel 24-core platform. The black dashed line shows the ideal Amdahl's law.

C.3 The 2D Laplace solver

A 2D Laplace solver [343] (Algorithm 2) iteratively searches for an approximate solution of the Laplace equation, i.e. a Poisson equation (Eq. (B.1)) with a source term S equal to 0, on a $N_x \times N_y$ evenly spaced cartesian grid (black dots in Fig. C.3).

First of all, the value of the potential ϕ at the boundaries of the domain has to be fixed a priori (line 13), while other points are simply initialised to 0 (line 12). We extend the

grid on each side by one point where the BCs are set (red points in Figs. C.3 and C.4, left panel). Then, for each point in the grid, the new value of ϕ is computed upon the values assumed by all its neighbours in the previous iteration (line 22). The algorithm iterates until ε, the sum of all the differences between the computed potentials in the last two iterations (line 23), goes below a given tolerance *tol* (line 14).

This Laplace solver presents the same structure of the Poisson solver illustrated in Appendix B and adopted in the astroMP code. The only differences are due to the fact that this Laplace solver is based on a Jacobi instead of a SOR iterative algorithm, adopts Dirichlet instead of Neumann BCs and, of course, the source term is now equal to 0.

C.3.1 Semi-automatic parallelisation

Wanting to parallelise the Laplace solver by applying the proposed methodology, the first thing to do is to reorganise the serial code by dividing the global domain in $T_x \times T_y$ equally-sized sub-domains (or tiles). In order to compute the solution of the equation, it is now necessary to firstly iterate over the tiles along each dimension (line 17) and then to iterate over the cells in each tile (lines 18–19), resulting in 4 nested for loops.

Algorithm 3 shows in red how it is possible to parallelise with MPI the two external for loops and to combine each sub-solution with the `MPI_Allreduce` function (line 24) to derive the global solution. The decomposition of the domain is performed in parallel through the `MPI_Cart_create` function, which assigns each sub-domain to an individual process according to the topology illustrated in Fig. C.4. This function returns a communicator that encodes the new MPI topology. In an execution with `size` processes, the number of processes along each dimension of the grid is determined through a manual *maximally squared decomposition*, where $\texttt{np}_\texttt{x} = \sqrt{\texttt{size}}$ and $\texttt{np}_\texttt{y} = \texttt{size}/\texttt{np}_\texttt{x}$. If $\texttt{np}_\texttt{x} \times \texttt{np}_\texttt{y} \neq \texttt{size}$, the domain cannot be decomposed and the execution does not start.

Since we compute Laplace equation in parallel on different portions of the grid, the number of BCs increases: besides physical BCs set at the borders of the global domain, also inter-processes BCs are now present. The definition of inter-processes BCs requires communication among the different neighbour processes in the new MPI topology, since each process has to send to and to receive from its neighbours the arrays containing the potential computed in the most external interior points of the sub-grid. These arrays are then saved at the boundaries of each local domain such that Laplace equation can be solved on every process. This halo-swap communication is performed through the `MPI_Neighbor_alltoall` function (line 16), as shown in the right panel of Fig. C.4.

Algorithm 2: Seq. Laplace with tiling

```
1  T_x ← nTiles_x, T_y ← nTiles_y;
2  ;
3  ;
4  mallocs: φ_0[N_x + 2, N_y + 2],
     φ_1[N_x + 2, N_y + 2];
   // φ_0 and φ_1 globally describe the
      problem, boundary conditions need a
      halo of 2
5  φ_A ← φ_0; φ_B ← φ_1 ;     // duplication of
     pointers
   // φ_B is step i + 1 (write), φ_A step i
      (read)
6  for sx ← 0 to T_x − 1 do              // init
7      for sy ← 0 to T_y − 1 do
8          for ii ← 1 to N_x/T_x do
9              for jj ← 1 to N_y/T_y do
10                 i ← sx × (N_x/T_x) + ii;
11                 j ← sy × (N_y/T_y) + jj;
12                 φ_A[i, j] ← 0;
13 init_boundary_conditions(φ_A, N_x, N_y);
14 while (ε < tol) do
15     ε ← 0;
16     for sx ← 0 to T_x − 1 do        // global
         solver
17         for sy ← 0 to T_y − 1 do
18             for ii ← 1 to N_x/T_x do
19                 for jj ← 1 to N_y/T_y do
20                     i ← sx × (N_x/T_x) + ii;
21                     j ← sy × (N_y/T_y) + jj;
22                     φ_B[i, j] ← F(φ_A[i −
                         1, j], φ_A[i + 1, j], φ_A[i, j −
                         1], φ_A[i, j + 1]);
23                     ε ← ε+F(φ_B[i, j]−φ_A[i, j])
24     ;
25     swap_pointers(φ_A, φ_B);
```

Algorithm 3: Parallel MPI Laplace

```
1  T_x ← nTiles_x = np_x, T_y ← nTiles_y = np_y;
2  Cartesian_create_comm(COMM_WORLD,
     2, np[], periods, 0, COMM_CART);
3  Cartesian_get_comm(COMM_CART, 2,
     np[], periods, coords);
4  mallocs: φ_0[N_x + 2, N_y + 2],
     φ_1[N_x + 2, N_y + 2];
   // φ_0 and φ_1 are partitions of the
      problem, boundary conditions need a
      halo of 2
5  φ_A ← φ_0; φ_B ← φ_1 ;     // duplication of
     pointers
   // φ_B is step i + 1 (write), φ_A step i
      (read)
6  // parallel init
7  ;
8  for ii ← 1 to N_x/T_x do
9      for jj ← 1 to N_y/T_y do
10         i ← ii;
11         j ← jj;
12         φ_A[i, j] ← 0;
13 init_boundary_conditions(φ_A, N_x, N_y);
14 while (ε < tol) do
15     ε_loc ← 0;
16     Neighbor_alltoall(bounds(φ_A),
         max(N_x/T_x, N_y/T_y) + 2, bounds(φ_A),
         max(N_x/T_x, N_y/T_y) + 2,
         COMM_CART);
17     for ii ← 1 to N_x/T_x do        // local
         solver
18         for jj ← 1 to N_y/T_y do
19             i ← ii;
20             j ← jj;
21             φ_B[i, j] ← ;
22             F(φ_A[i − 1, j], φ_A[i + 1, j], φ_A[i, j −
                 1], φ_A[i, j + 1]);
23             ε_loc ← ε_loc + F(φ_B[i, j] − φ_A[i, j])
24     Allreduce (ε_loc, ε, sum);
25     swap_pointers(φ_A, φ_B);
```

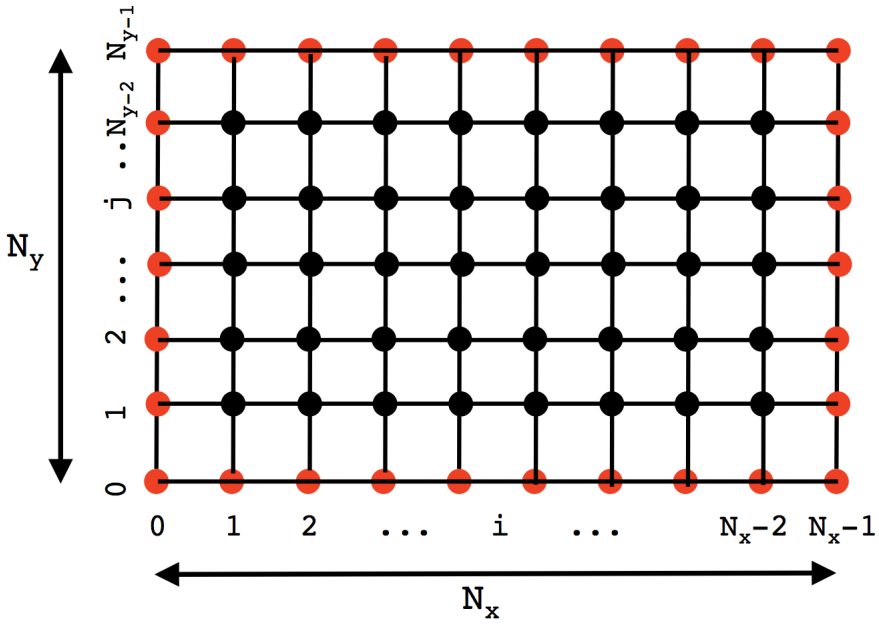

Figure C.3: Two-dimensional evenly spaced cartesian grid where Laplace equation is computed (black dots). Red dots represent the points where BCs are fixed.

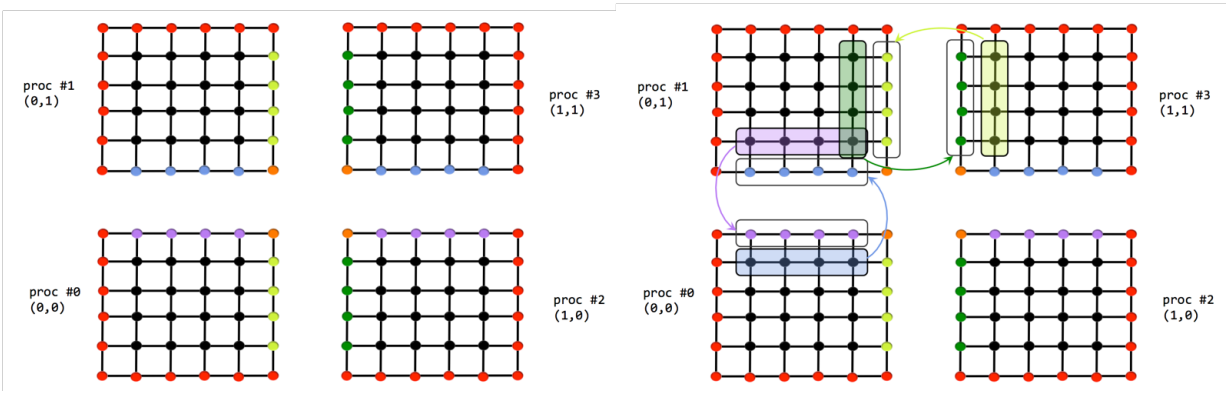

Figure C.4: Left panel: Example of a Cartesian decomposition between 4 processes of the domain performed with the `MPI_Cart_create` function. Each portion of the global domain is mapped to a single process and to a pair of coordinates. Black dots show the points of the local grids where Laplace equation is computed iteratively. Red dots show the points where physical BCs are set whereas the dots coloured in different ways show the points where inter-processes BCs are defined. Right panel: Halo-swap operation between inter-processes BCs.

C.3.2 Performance evaluation

Strong scaling

The strong scaling performance of the parallelised Laplace solver has been tested on the CRESCO6 cluster, using an OpenMPI version compiled specifically for Intel processors. We evaluate the solver using a grid of size 32768×32768, which is sufficiently large to guarantee computational times significantly larger than the communication ones, and we set a sufficiently challenging tolerance of 4×10^{-7}. Moreover, we decide to allocate only half of the cores available on each node (i.e. 24 cores out of 48), since we empirically observe that a greater occupation of the node resources led to a rapid deterioration in performance of the node itself. The left panel of Fig. C.5 shows the average speedups on 10 executions: Amdahl's law holds until 16 cores but, albeit more slowly, the speedup continues growing along the entire range of considered cores, achieving a maximum value of $\sim$778 with 2808 cores.

Weak scaling

To investigate the parallelized Laplace solver's weak scalability, we kept constant the number of grid points per core, meaning that we added 32768×32768 points to the grid for every core used in the run. This implies an increase in the global grid's resolution since its dimensions are fixed; consequently, runs with a different number of processors will converge at different speeds, thus making the results not comparable among each other. For this reason we did not use a fixed tolerance as the ending condition of the program, but we run all the computations for a fixed number of iterations, making the runs comparable. As for the strong scaling, we allocate only half of the cores available on each node. The right panel of Fig. C.5 illustrates the weak scaling result, with the times being averaged on 10 executions. The time slowly increases from ∼2200 to ∼2800 s, up to 624 processes, and then it remains constant around this value, showing a rather good weak scalability.

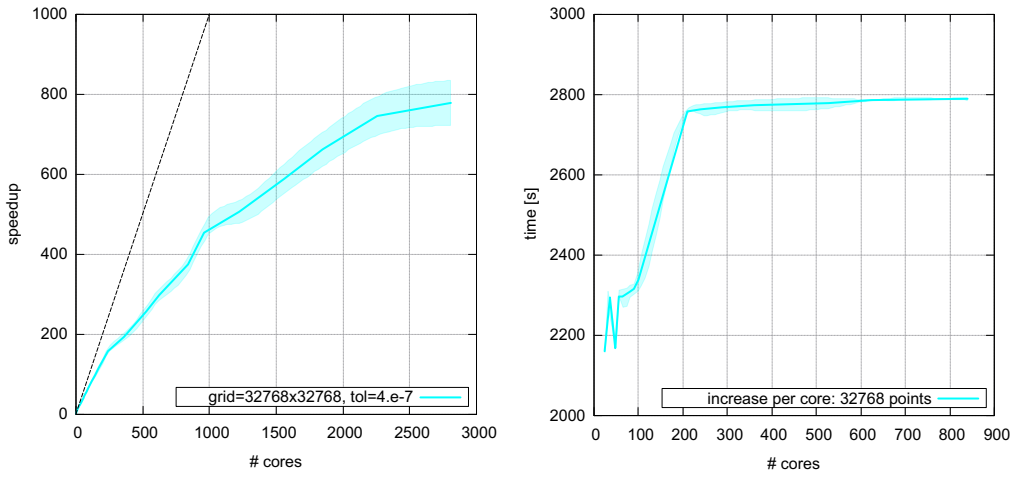

Figure C.5: **Left:** strong scaling (Amdahl's law) and **right** weak scaling (Gustafson's law) for the Laplace solver code, averaged on ten executions on the CRESCO6 platform. The shaded areas represent the errors on the measurements and the black dashed line is the ideal Amdahl's law.

Appendix D

Convergence tests of the MCMC chains

D.1 The variance ratio method

The variance ratio method of [344] is a convergence diagnostic test for monitoring the convergence of MCMC chains: in other words, it estimates how close to convergence a chain is and if the convergence can be improved with additional steps of the chain [440].

The test compares the output of $m \geq 2$ independent chains that have different starting points. Each chain has $n_0 + n$ elements, where the first n_0 are the discarded burn-in chain. Each chain i, at each step t, returns an estimate of a given parameter of interest $\theta_i(\mathbf{x}^t) \equiv \theta_i^t$, where $\mathbf{x}$ are the variables of the problem updated at each chain step t. For each chain, we compute the mean of the parameter estimates,

$$\bar{\theta}_i = \frac{1}{n} \sum_{t=n_0+1}^{n_0+n} \theta_i^t \ , \tag{D.1}$$

the mean of the means of the m chains,

$$\bar{\theta} = \frac{1}{m} \sum_{i=1}^{m} \bar{\theta}_i \ , \tag{D.2}$$

and their variance,

$$\frac{B}{n} = \frac{1}{m-1} \sum_{i=1}^{m} (\bar{\theta}_i - \bar{\theta})^2 \ . \tag{D.3}$$

In addition, we compute the variance of θ_i^t within each chain,

$$s_i^2 = \frac{1}{n-1} \sum_{t=n_0+1}^{n_0+n} (\theta_i^t - \bar{\theta}_i)^2 \ , \tag{D.4}$$

and their mean,

$$W = \frac{1}{m} \sum_{i=1}^{m} s_i^2 \ . \tag{D.5}$$

Gelman and Rubin [344] assume that the mean of the posterior distribution of the parameter θ is $\hat{\mu} = \bar{\theta}$ and that its variance is:

$$\hat{\sigma}^2 = \frac{n-1}{n} W + \frac{B}{n}. \tag{D.6}$$

Gelman and Rubin [344] model the variability of $\hat{\mu}$ and $\hat{\sigma}^2$ due to sampling with an approximate Student's t distribution with mean $\hat{\mu} = \bar{\theta}$, variance

$$\hat{V} = \hat{\sigma}^2 + \frac{1}{m} \frac{B}{n}, \tag{D.7}$$

and number of degrees of freedom $\nu = 2\hat{V}^2/\hat{\text{var}}(\hat{V})$, where

$$\begin{aligned}\hat{\text{var}}(\hat{V}) = &\left(\frac{n-1}{n}\right)^2 \frac{1}{m}\hat{\text{var}}(s_i^2) + \left(\frac{m+1}{mn}\right)^2 \frac{2}{m-1}B^2 + \\ &+ 2\frac{(m+1)(n-1)}{mn^2}\frac{n}{m}\left[\hat{\text{cov}}(s_i^2, \bar{\theta}_i^2) - 2\bar{\theta}\hat{\text{cov}}(s_i^2, \bar{\theta}_i)\right],\end{aligned} \tag{D.8}$$

and where the variance $\hat{\text{var}}(s_i^2)$ and the covariances $\hat{\text{cov}}(s_i^2, \bar{\theta}_i^2)$ and $\hat{\text{cov}}(s_i^2, \bar{\theta}_i)$ are estimated with the m values $\bar{\theta}_i$ and s_i^2.

To monitor the convergence of the chains, [344] compute the *potential scale reduction factor*

$$\hat{R} = \frac{\hat{V}}{W}\frac{\nu}{\nu - 2}\,. \tag{D.9}$$

If $\hat{R} \to 1$ as $n \to \infty$, the estimated variance $\hat{V}$ of the expected posterior distribution of θ is increasingly closer to the variance W estimated from the chains for an increasingly large number of steps. In other words, values of $\hat{R} \gg 1$ suggest that the estimate of the target distribution can be improved with additional steps, whereas values of $\hat{R} \sim 1$ suggest that the chains are close to the target distribution.

D.2 The MCMC convergence for the universal combination of the RG parameters

In our MCMC analysis we adopt a burn-in chain with $n_0 = 1000$ and a chain with $n = 19000$ iterations. To assess the convergence of the chains, in Sect. 4.3 we adopt the variance ratio method.

We run the test for the first $n = 13000$ iterations. If the test is positive for this n, we are confident that running the chains for $n = 19000$ iterations will provide a posterior distribution close to the target distribution. We consider $m = 3$ chains.

The values we obtain for the potential scale reduction factor, $\hat{R}$, for each RG parameter, ϵ_0, Q and ρ_c, are 1.01, 1.04 and 1.004, respectively. According to the interpretation of [344], these values suggest that our distributions estimated with $n = 13000$ iterations already are reasonably close to the target distributions. The results we show in the text are for $n = 19000$ iterations and we are thus confident that our values for ϵ_0, Q and ρ_c are robust estimates of the target values.

Appendix E

Figures of the individual DiskMass Survey galaxies

In this Appendix, we collect all the figures showing the relevant quantities of each DMS galaxy. Figures E.1–E.7 show the profiles of the surface brightness, the surface mass density of the atomic and molecular gas and the kinematic profiles. Each galaxy appears in an individual panel. Figures E.6 and E.7 show the five galaxies that we analysed both in RG and in QUMOND. Each panel contains 8 sub-panels in Figs. E.1–E.5 and 12 sub-panels in Figs. E.6–E.7.

The sub-panels (a) show the surface brightness. The filled circles with error bars are the data in the K-band, corrected for inclination [320] and the blue solid curves are our models (Sect. A.1). The green data points are removed before performing the fit with the exponential profile (A.1). We only use this exponential model to estimate the disk surface brightness both in the central region, to separate the disk and the bulge contributions, and in the outer regions not covered by the data but still within the numerical domain of our Poisson solver. The grey vertical lines show the radius for our bulge-disk decomposition.

The sub-panels (b) show the surface mass density profile of the atomic gas. The filled circles with error bars are the estimates according to [324] and the blue solid curves are our linear interpolations (Sect. A.2). The sub-panels (c) show the surface mass density profile of the molecular gas (Sect. A.2). Symbols and lines are as in the sub-panels (b).

The sub-panels (d) show the rotation curves. The filled circles with error bars are the data; the blue solid lines show the RG models whose parameters are the medians of their posterior distributions estimated from the rotation curve alone (Sect. 4.1). The dashed magenta vertical lines show the bulge effective radius, whereas the dashed green vertical lines show the bulge radius we adopt in our disk-bulge decomposition for the surface brightness fit (Sect. A.1). For the galaxy UGC 1087, these two radii coincide. The dashed green vertical lines coincide with the grey lines of sub-panels (a). These two vertical lines are repeated in all sub-panels (d)-(h).

The sub-panels (e) again show the rotation curves and the sub-panels (f) show the vertical velocity dispersion profiles. In the sub-panels (e), the data are the same as in the sub-panels (d). In the sub-panels (f), the data are the filled circles with error bars. In the sub-panels (e) and (f), the blue solid lines show the RG models whose parameters are the medians of their posterior distributions estimated from the rotation curve and the vertical velocity dispersion profile at the same time (Sect. 4.2). In the sub-panels (f), the cyan solid lines show the vertical velocity dispersion profile when we adopt the same parameters as for the blue lines except for the disk-scale height h_z; for the cyan solid lines, h_z is the value derived from Eq. (A.12). For the galaxy UGC 6918 (Fig. E.4), the cyan line overlaps the blue line because the estimated h_z coincides with the value derived from Eq. (A.12).

The sub-panels (g) and (h) again show the rotation curves and the vertical velocity dispersion profiles. In these sub-panels, the blue solid lines show the RG models where

the mass-to-light ratios and the disk-scale heights are set to the values derived in Sect. 4.2 and listed in Table 4.2, whereas the values of the three RG parameters ϵ_0, Q , and ρ_c are set to those of the unique combination found in Sect. 4.3.

Figures E.6 and E.7 show four additional sub-panels. The sub-panels (i) and (k) show the rotation curves and the sub-panels (j) and (l) show the velocity dispersion profiles. The measured velocity dispersion profiles in these sub-panels are artificially increased by the factor 1.63, which is our estimate of the observational bias suggested by [328] (Sect. 4.2.1). The blue curves are the models whose parameters are the medians of their posterior distributions estimated from the rotation curve and the vertical velocity dispersion profile at the same time (Sect. 4.2.1). The sub-panels (i) and (j) show the RG models and the sub-panels (k) and (l) show the QUMOND models. The cyan lines in the sub-panels (j) and (l) show the models where the scale height h_z is set by Eq. (A.12). For the galaxy UGC 4107 (Fig. E.6), the cyan lines in sub-panels (j) and (l) overlap the blue lines because the estimated h_z in both RG and QUMOND are almost identical to the values obtained with Eq. (A.12). The vertical magenta and green lines are the same as in the sub-panels (d)-(h).

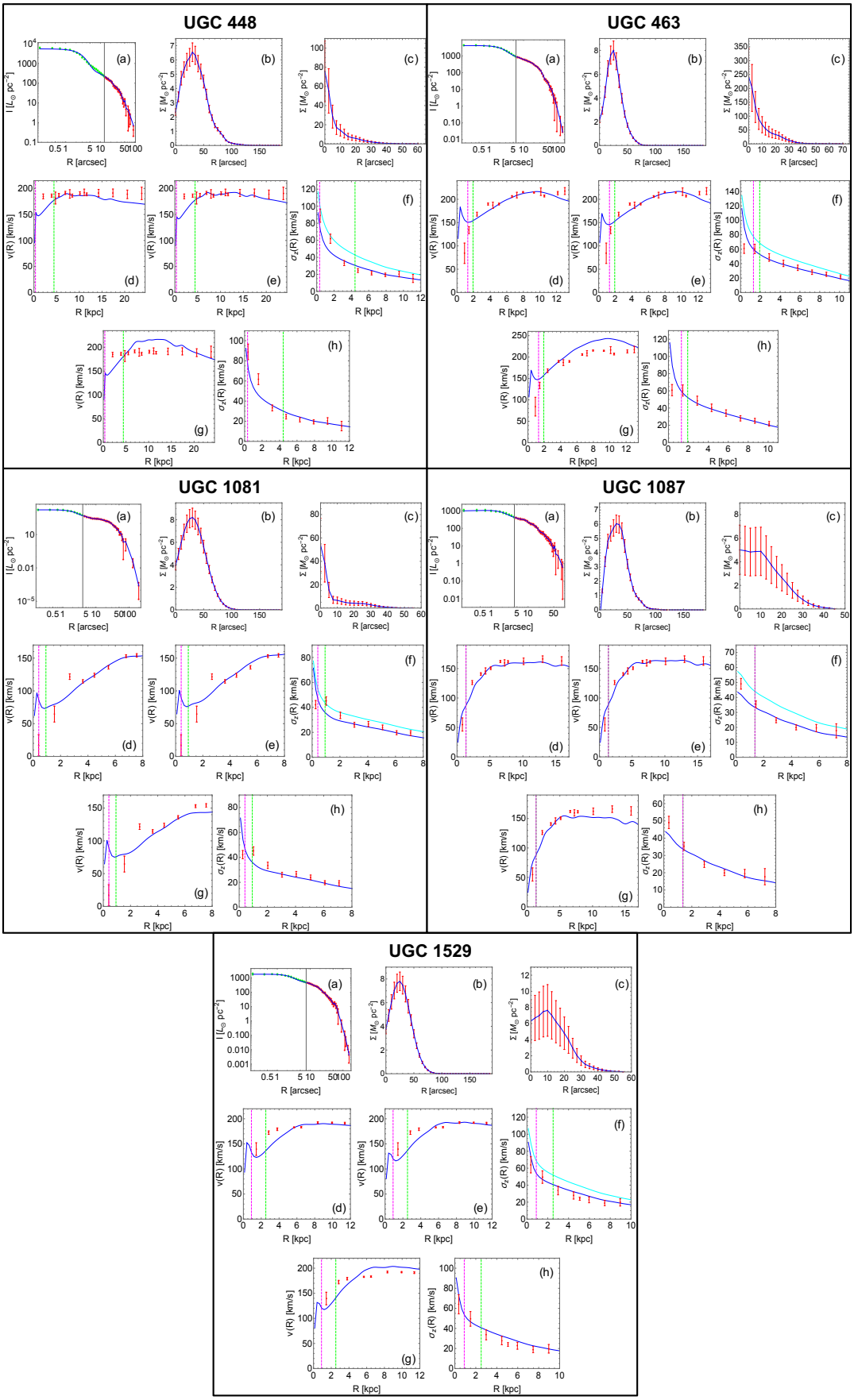

Figure E.1: Surface brightness, surface mass densities of the atomic and molecular gas profiles and kinematic profiles of the DMS galaxies and their modelling according to our different analyses (see text of Appendix E).

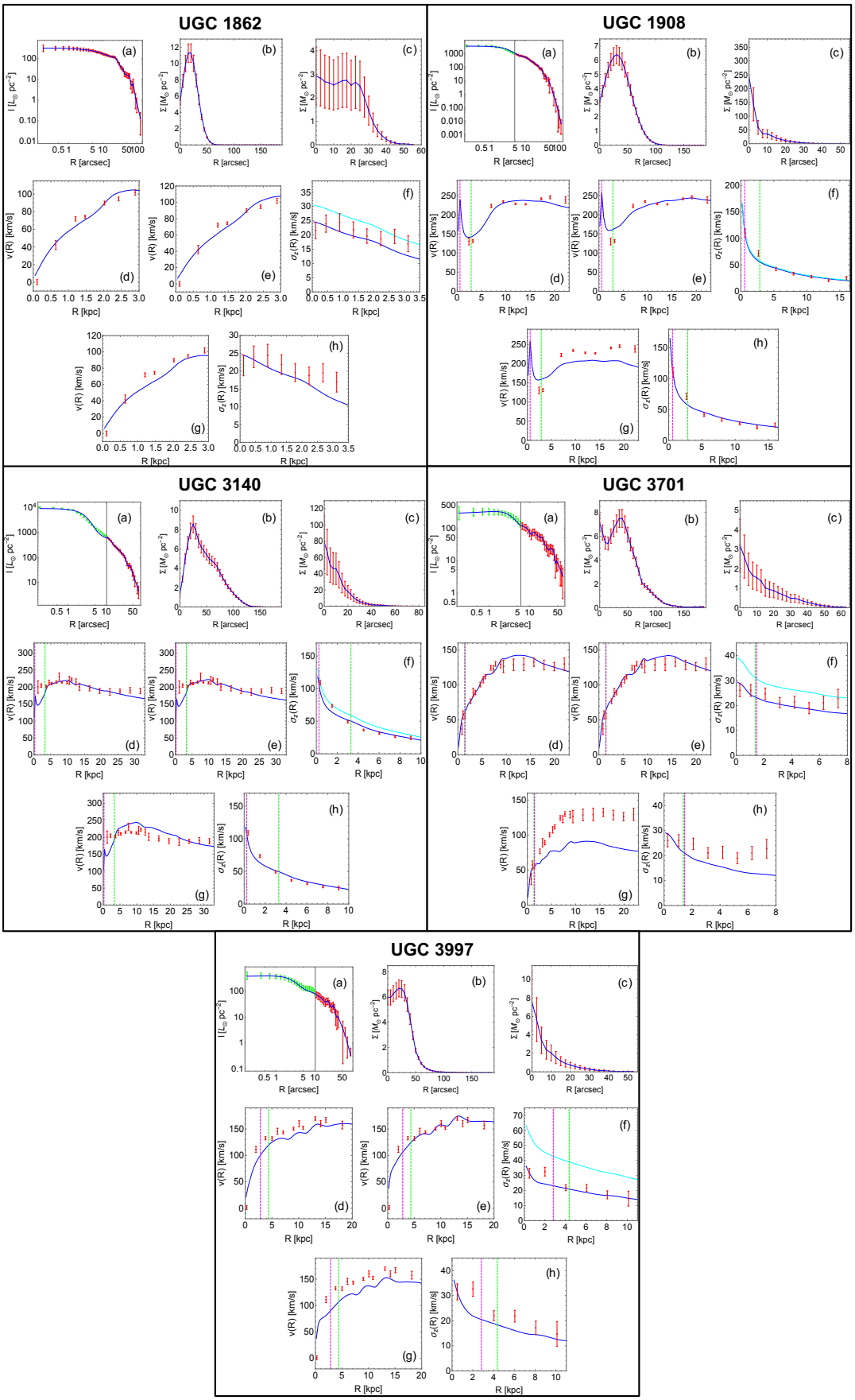

Figure E.2: Same as in Fig. E.1.

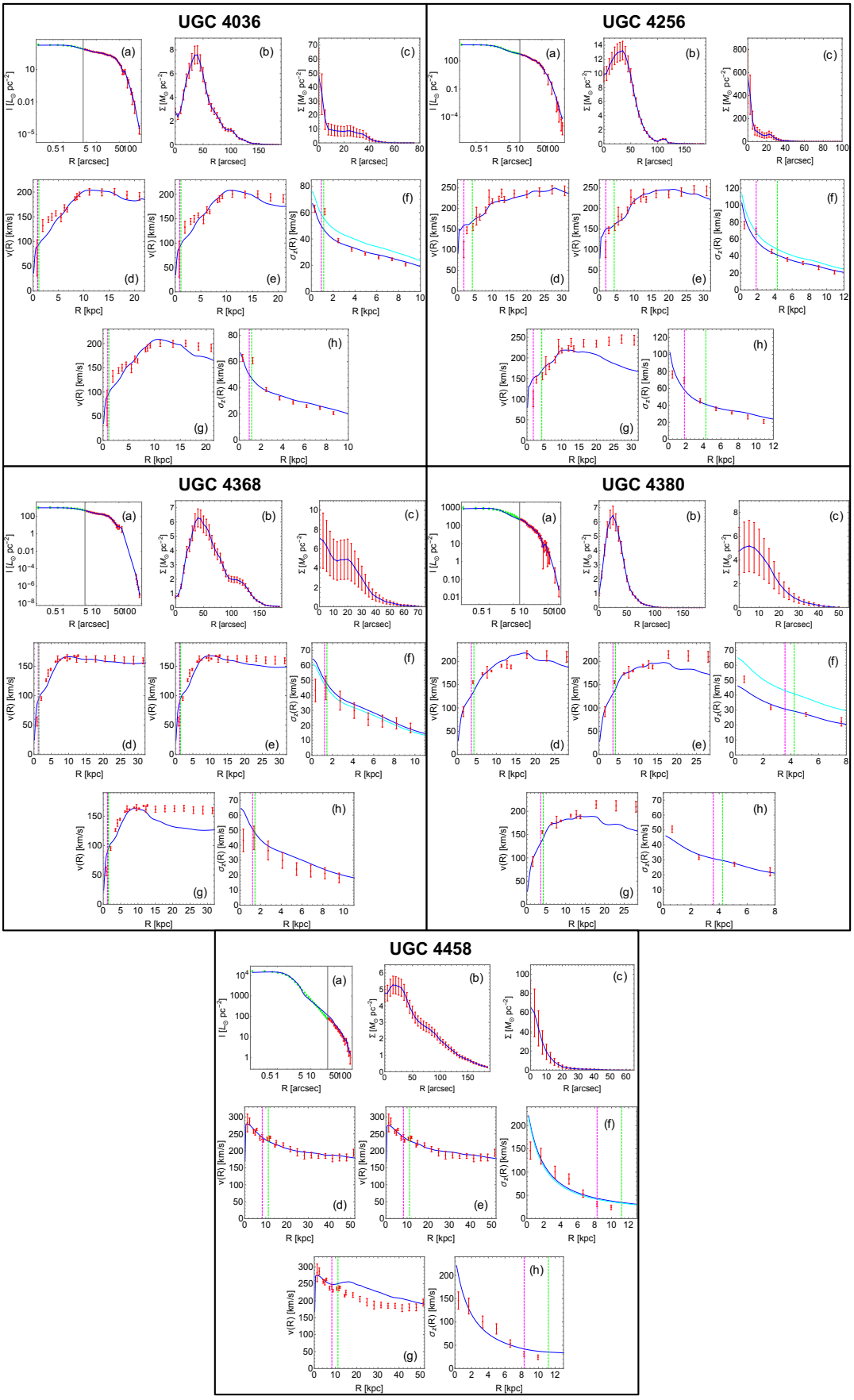

Figure E.3: Same as in Fig. E.1.

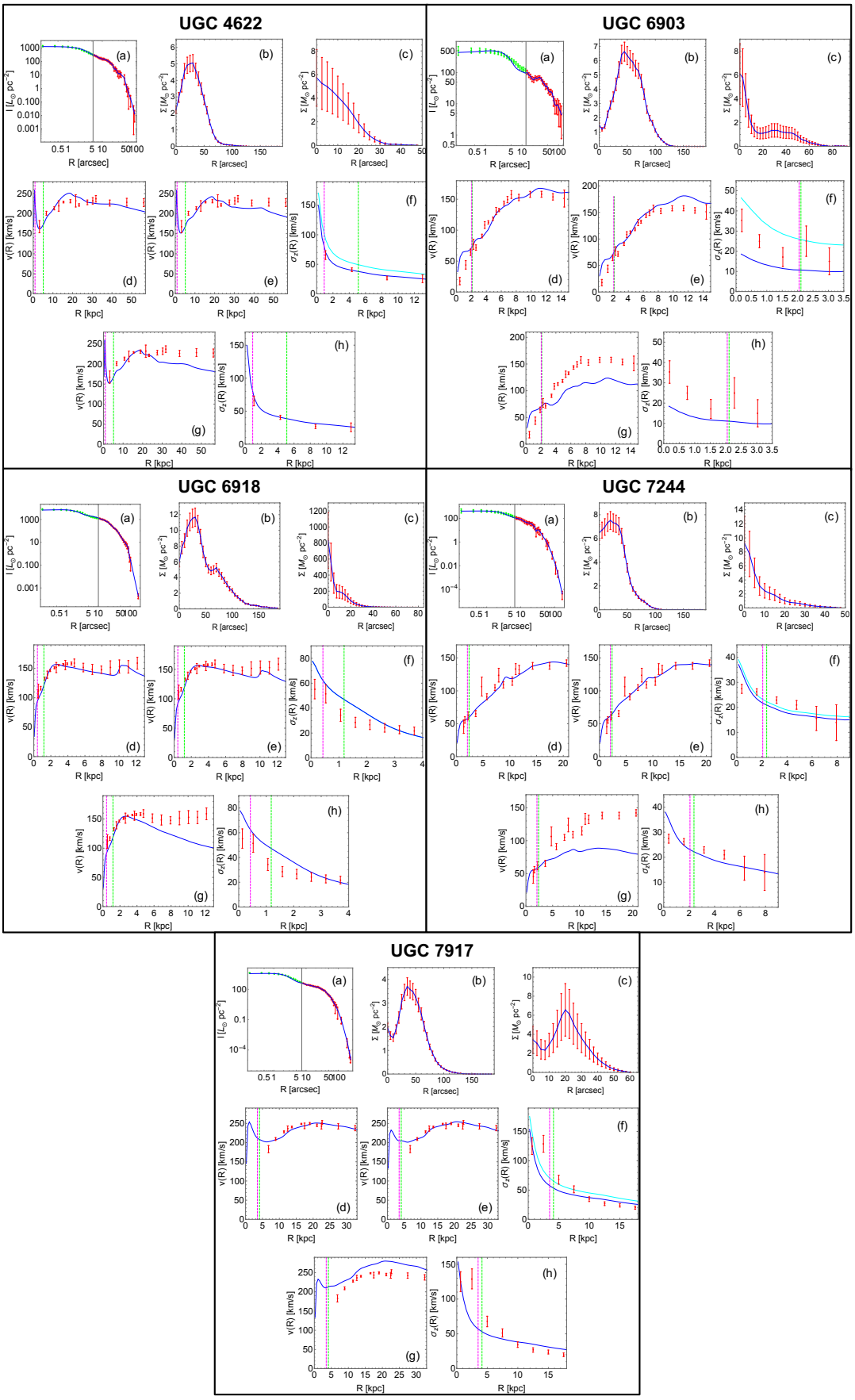

Figure E.4: Same as in Fig. E.1.

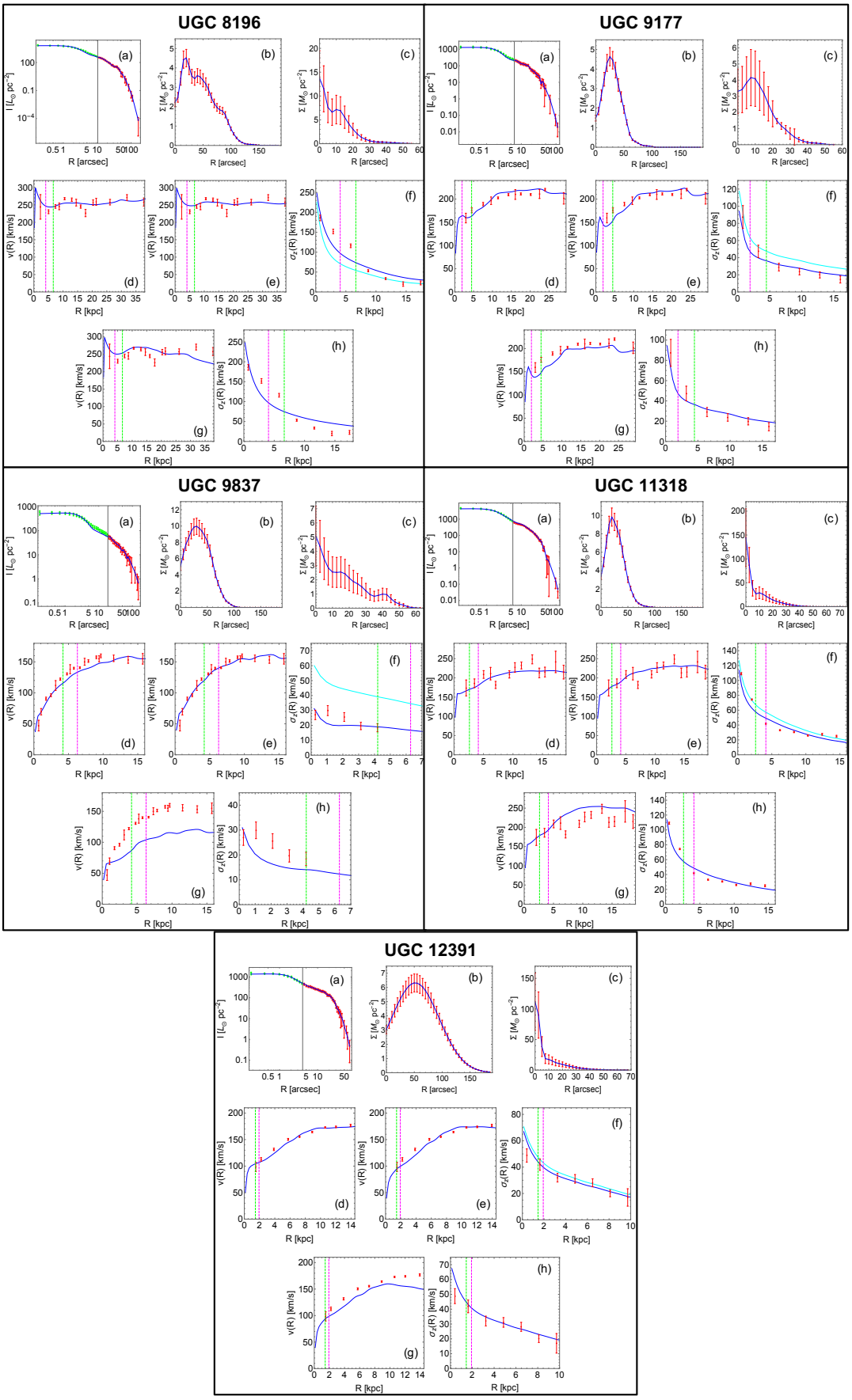

Figure E.5: Same as in Fig. E.1.

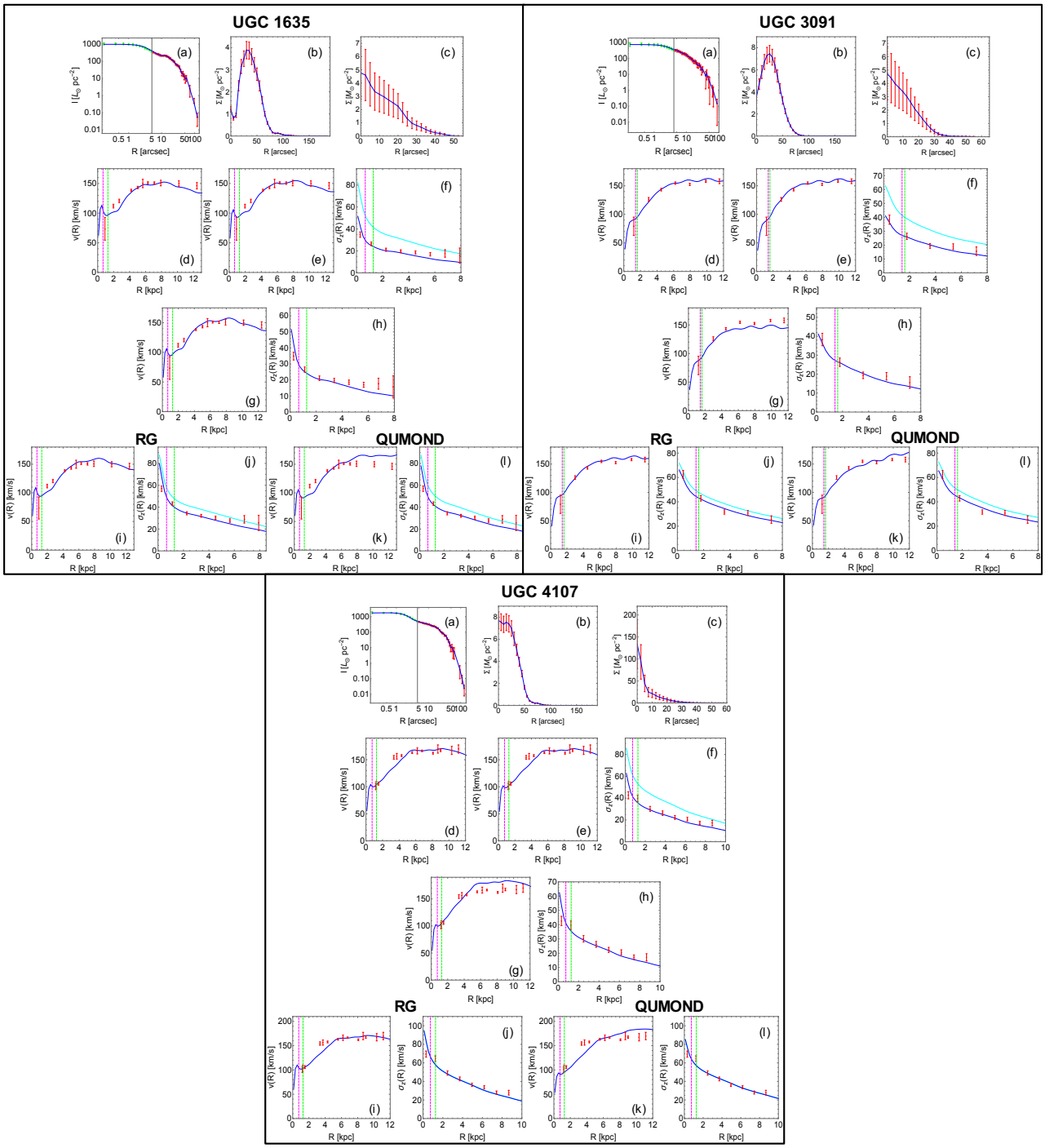

Figure E.6: Same as in Fig. E.1 with the additional analyses with the vertical velocity dispersion profiles artificially increased by the factor 1.63 in RG and QUMOND.

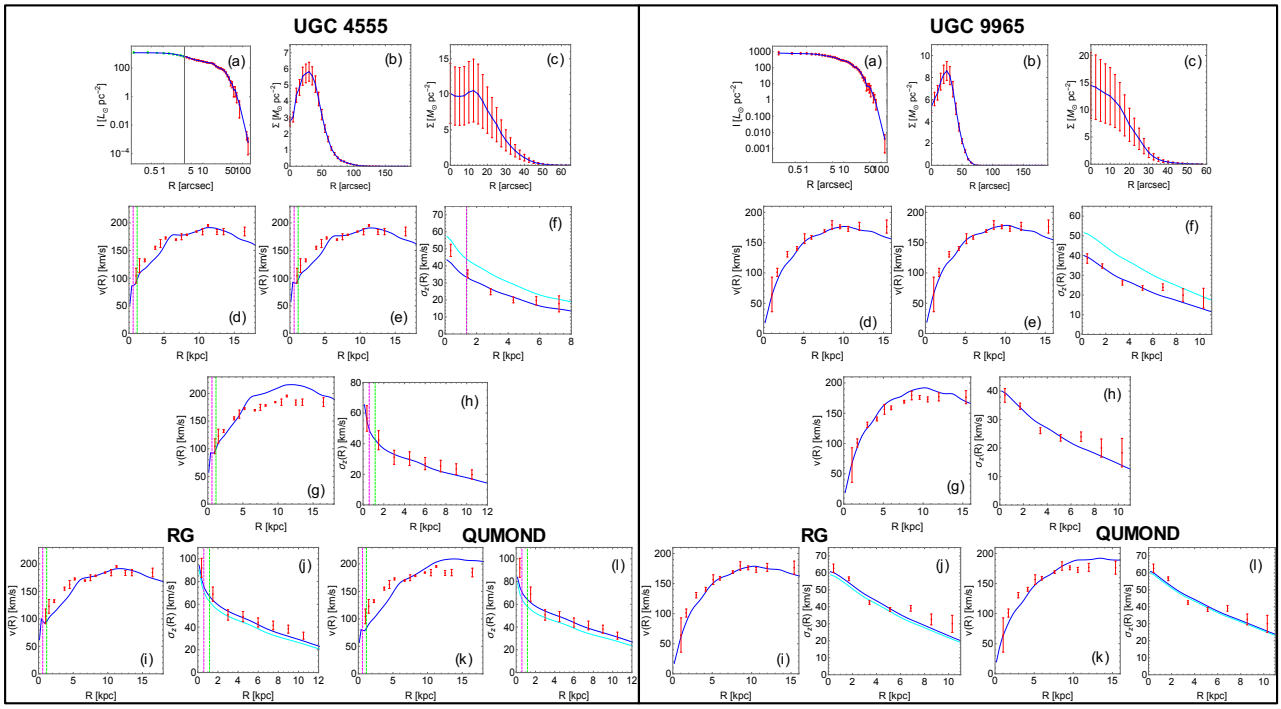

Figure E.7: Same as in Fig. E.6.

Appendix F

Derivation of the uncertainties on the root-mean-square velocity dispersions of GCs in the three nearby E0 galaxies

We adopt the procedure of [398] to estimate the uncertainties $\Delta V_{\rm rms}(R)$ on the values of the root-mean-square velocity dispersion profile $V_{\rm rms}(R)$ that we compute with Eq. (5.23). In the reference frame of the centre of mass of the galaxy, the line-of-sight velocity of the i-th GC is

$$v_{||,i} = \frac{V_{{\rm rad},i} - V_{\rm sys}}{1 + V_{\rm sys}/c}, \tag{F.1}$$

where $V_{{\rm rad},i}$ is the observed radial velocity of the GC, $V_{\rm sys}$ is the systemic velocity of the galaxy, and $c = 3 \times 10^5$ km s^{-1} is the speed of light. The three E0 galaxies of our analysis have redshift $z < 0.007$ and we set to 1 the denominator of Eq. (F.1). The variance of the radial velocities of GCs in each radial bin of radius R is

$$\sigma^2_{||}(R) = \frac{1}{N-1} \sum_{i=1}^{N} v^2_{||,i}\,, \tag{F.2}$$

where N is the number of GCs in the bin. This equation neglects the errors on $V_{\rm rad}$ and $V_{\rm sys}$.

The quantity

$$S^2(R) = (N-1)\frac{\sigma^2_{||}(R)}{V^2_{\rm rms}(R)}, \tag{F.3}$$

is a χ^2_ν random variate with $\nu = N-1$ degrees of freedom. We define S^2_- and S^2_+ with the probability α of having S^2 in the range (S^2_-, S^2_+). The value $\alpha = 0.68$ defines the upper, indicated with the + sign, and lower, indicated with the − sign, 1σ uncertainty on the dispersion of the radial velocities derived with Eq. (F.2):

$$\Delta\sigma^2_{||,\pm}(R) = \left[\left(\frac{\nu}{S^2_\mp(R)}\right)^{1/2} - 1\right]^2 \sigma^2_{||}(R) + \frac{\bar{\delta^2_*}}{N}\left(1 + \frac{\bar{\delta^2_*}}{2\sigma^2_{||}(R)}\right), \tag{F.4}$$

where $\bar{\delta^2_*}$ is

$$\bar{\delta^2_*} = \frac{\Delta V_{\rm sys}}{1 + V_{\rm sys}/c} \tag{F.5}$$

and $\Delta V_{\rm sys}$ is the uncertainty on $V_{\rm sys}$; $\bar{\delta^2_*} = \Delta V_{\rm sys}$ in our analysis.

Finally, the upper and lower 1σ uncertainties on $V_{\rm rms}(R)$ are

$$\Delta V_{{\rm rms},\pm}(R) = V_{\rm rms}(R)\left[\frac{1}{5N} + \left(\frac{\Delta\sigma_{||,\pm}(R)}{\sigma_{||}(R)}\right)^2\right]^{1/2}. \tag{F.6}$$

In our analysis, we use the symmetrised uncertainty

$$\Delta V_{\rm rms}(R) = \frac{\Delta V_{\rm rms,-}(R) + \Delta V_{\rm rms,+}(R)}{2} \,. \tag{F.7}$$

Bibliography

[1] Ivan de Martino, Sankha S. Chakrabarty, Valentina Cesare, Arianna Gallo, Luisa Ostorero, and Antonaldo Diaferio. Dark Matters on the Scale of Galaxies. *Universe*, 6(8):107, August 2020.

[2] Planck Collaboration, N. Aghanim, Y. Akrami, M. Ashdown, J. Aumont, C. Baccigalupi, M. Ballardini, A. J. Banday, R. B. Barreiro, N. Bartolo, S. Basak, R. Battye, K. Benabed, J. P. Bernard, M. Bersanelli, P. Bielewicz, J. J. Bock, J. R. Bond, J. Borrill, F. R. Bouchet, F. Boulanger, M. Bucher, C. Burigana, R. C. Butler, E. Calabrese, J. F. Cardoso, J. Carron, A. Challinor, H. C. Chiang, J. Chluba, L. P. L. Colombo, C. Combet, D. Contreras, B. P. Crill, F. Cuttaia, P. de Bernardis, G. de Zotti, J. Delabrouille, J. M. Delouis, E. Di Valentino, J. M. Diego, O. Doré, M. Douspis, A. Ducout, X. Dupac, S. Dusini, G. Efstathiou, F. Elsner, T. A. Enßlin, H. K. Eriksen, Y. Fantaye, M. Farhang, J. Fergusson, R. Fernandez-Cobos, F. Finelli, F. Forastieri, M. Frailis, A. A. Fraisse, E. Franceschi, A. Frolov, S. Galeotta, S. Galli, K. Ganga, R. T. Génova-Santos, M. Gerbino, T. Ghosh, J. González-Nuevo, K. M. Górski, S. Gratton, A. Gruppuso, J. E. Gudmundsson, J. Hamann, W. Handley, F. K. Hansen, D. Herranz, S. R. Hildebrandt, E. Hivon, Z. Huang, A. H. Jaffe, W. C. Jones, A. Karakci, E. Keihänen, R. Keskitalo, K. Kiiveri, J. Kim, T. S. Kisner, L. Knox, N. Krachmalnicoff, M. Kunz, H. Kurki-Suonio, G. Lagache, J. M. Lamarre, A. Lasenby, M. Lattanzi, C. R. Lawrence, M. Le Jeune, P. Lemos, J. Lesgourgues, F. Levrier, A. Lewis, M. Liguori, P. B. Lilje, M. Lilley, V. Lindholm, M. López-Caniego, P. M. Lubin, Y. Z. Ma, J. F. Macías-Pérez, G. Maggio, D. Maino, N. Mandolesi, A. Mangilli, A. Marcos-Caballero, M. Maris, P. G. Martin, M. Martinelli, E. Martínez-González, S. Matarrese, N. Mauri, J. D. McEwen, P. R. Meinhold, A. Melchiorri, A. Mennella, M. Migliaccio, M. Millea, S. Mitra, M. A. Miville-Deschênes, D. Molinari, L. Montier, G. Morgante, A. Moss, P. Natoli, H. U. Nørgaard-Nielsen, L. Pagano, D. Paoletti, B. Partridge, G. Patanchon, H. V. Peiris, F. Perrotta, V. Pettorino, F. Piacentini, L. Polastri, G. Polenta, J. L. Puget, J. P. Rachen, M. Reinecke, M. Remazeilles, A. Renzi, G. Rocha, C. Rosset, G. Roudier, J. A. Rubiño-Martín, B. Ruiz-Granados, L. Salvati, M. Sandri, M. Savelainen, D. Scott, E. P. S. Shellard, C. Sirignano, G. Sirri, L. D. Spencer, R. Sunyaev, A. S. Suur-Uski, J. A. Tauber, D. Tavagnacco, M. Tenti, L. Toffolatti, M. Tomasi, T. Trombetti, L. Valenziano, J. Valiviita, B. Van Tent, L. Vibert, P. Vielva, F. Villa, N. Vittorio, B. D. Wand elt, I. K. Wehus, M. White, S. D. M. White, A. Zacchei, and A. Zonca. Planck 2018 results. VI. Cosmological parameters. *A&A*, 641:A6, September 2020.

[3] P. J. Peebles and Bharat Ratra. The cosmological constant and dark energy. *Reviews of Modern Physics*, 75(2):559–606, April 2003.

[4] G. R. Blumenthal, S. M. Faber, J. R. Primack, and M. J. Rees. Formation of galaxies and large-scale structure with cold dark matter. *Nature*, 311:517–525, October 1984.

[5] J. P. Ostriker and P. J. E. Peebles. A Numerical Study of the Stability of Flattened Galaxies: or, can Cold Galaxies Survive? *ApJ*, 186:467–480, December 1973.

[6] J. P. Ostriker, P. J. E. Peebles, and A. Yahil. The Size and Mass of Galaxies, and the Mass of the Universe. *ApJL*, 193:L1, October 1974.

[7] Robert H. Sanders. *The Dark Matter Problem: A Historical Perspective*. Cambridge University Press, 2010.

[8] V. C. Rubin and W. K. Ford Jr. Rotation of the Andromeda Nebula from a Spectroscopic Survey of Emission Regions. *ApJ*, 159:379, February 1970.

[9] R. H. Sanders. Mass discrepancies in galaxies: dark matter and alternatives. *A&ARv*, 2(1):1–28, January 1990.

[10] F. Zwicky. Die Rotverschiebung von extragalaktischen Nebeln. *Helvetica Physica Acta*, 6:110–127, January 1933.

[11] M. Markevitch. Chandra Observation of the Most Interesting Cluster in the Universe. In A. Wilson, editor, *The X-ray Universe 2005*, volume 604 of *ESA Special Publication*, page 723, January 2006.

[12] Douglas Clowe, Maruša Bradač, Anthony H. Gonzalez, Maxim Markevitch, Scott W. Randall, Christine Jones, and Dennis Zaritsky. A Direct Empirical Proof of the Existence of Dark Matter. *ApJL*, 648(2):L109–L113, September 2006.

[13] D. Paraficz, J. P. Kneib, J. Richard, A. Morandi, M. Limousin, E. Jullo, and J. Martinez. The Bullet cluster at its best: weighing stars, gas, and dark matter. *A&A*, 594:A121, October 2016.

[14] M. Davis, G. Efstathiou, C. S. Frenk, and S. D. M. White. The evolution of large-scale structure in a universe dominated by cold dark matter. *ApJ*, 292:371–394, May 1985.

[15] Volker Springel, Carlos S. Frenk, and Simon D. M. White. The large-scale structure of the Universe. *Nature*, 440(7088):1137–1144, April 2006.

[16] Neil Turok. *Critical Dialogues in Cosmology: Princeton, New Jersey, USA, 24-27 June 1996, in Celebration of the 250th Anniversary of Princeton University*. World Scientific, 1997.

[17] Malcolm S. Longair. *The Determination of Cosmological Parameters*, pages 186–216. Springer Berlin Heidelberg, Berlin, Heidelberg, 1998.

[18] A. Friedmann. On the Curvature of Space. *General Relativity and Gravitation*, 31:1991, December 1999.

[19] C. Jones and W. Forman. The structure of clusters of galaxies observed with Einstein. *ApJ*, 276:38–55, January 1984.

[20] L. P. David, K. A. Arnaud, W. Forman, and C. Jones. Einstein Observations of the Hydra A Cluster and the Efficiency of Galaxy Formation in Groups and Clusters. *ApJ*, 356:32, June 1990.

[21] H. Bohringer, R. A. Schwarz, and U. G. Briel. Cosmological Implications of ROSAT Observations of Galaxy Clusters. In Guido L. Chincarini, Angela Iovino, Tommaso Maccacaro, and Dario Maccagni, editors, *Observational Cosmology*, volume 51 of *Astronomical Society of the Pacific Conference Series*, page 368, January 1993.

[22] Xiang-Ping Wu, Tzihong Chiueh, Li-Zhi Fang, and Yan-Jie Xue. A comparison of different cluster mass estimates: consistency or discrepancy? *MNRAS*, 301(3):861–871, December 1998.

[23] Andisheh Mahdavi, Henk Hoekstra, Arif Babul, David D. Balam, and Peter L. Capak. A Dark Core in Abell 520. *ApJ*, 668(2):806–814, October 2007.

[24] M. Girardi, R. Barrena, W. Boschin, and E. Ellingson. Cluster Abell 520: a perspective based on member galaxies. A cluster forming at the crossing of three filaments? *A&A*, 491(2):379–395, November 2008.

[25] T. Lasserre, C. Afonso, J. N. Albert, J. Andersen, R. Ansari, É. Aubourg, P. Bareyre, F. Bauer, J. P. Beaulieu, G. Blanc, A. Bouquet, S. Char, X. Charlot, F. Couchot, C. Coutures, F. Derue, R. Ferlet, J. F. Glicenstein, B. Goldman, A. Gould, D. Graff, M. Gros, J. Haissinski, J. C. Hamilton, D. Hardin, J. de Kat, A. Kim, É. Lesquoy, C. Loup, C. Magneville, B. Mansoux, J. B. Marquette, É. Maurice, A. Milsztajn, M. Moniez, N. Palanque-Delabrouille, O. Perdereau, L. Prévot, N. Regnault, J. Rich, M. Spiro, A. Vidal-Madjar, L. Vigroux, S. Zylberajch, and EROS Collaboration. Not enough stellar mass Machos in the Galactic halo. *A&A*, 355:L39–L42, March 2000.

[26] P. Tisserand, L. Le Guillou, C. Afonso, J. N. Albert, J. Andersen, R. Ansari, É. Aubourg, P. Bareyre, J. P. Beaulieu, X. Charlot, C. Coutures, R. Ferlet, P. Fouqué, J. F. Glicenstein, B. Goldman, A. Gould, D. Graff, M. Gros, J. Haissinski, C. Hamadache, J. de Kat, T. Lasserre, É. Lesquoy, C. Loup, C. Magneville, J. B. Marquette, É. Maurice, A. Maury, A. Milsztajn, M. Moniez, N. Palanque-Delabrouille, O. Perdereau, Y. R. Rahal, J. Rich, M. Spiro, A. Vidal-Madjar, L. Vigroux, S. Zylberajch, and EROS-2 Collaboration. Limits on the Macho content of the Galactic Halo from the EROS-2 Survey of the Magellanic Clouds. *A&A*, 469(2):387–404, July 2007.

[27] Alinka Lépine-Szily and Pierre Descouvemont. Nuclear astrophysics: nucleosynthesis in the Universe. *International Journal of Astrobiology*, 11:243–250, October 2012.

[28] G. Efstathiou and J. R. Bond. Microwave Background Fluctuations and Dark Matter. *Philosophical Transactions of the Royal Society of London Series A*, 320(1556):585–594, December 1986.

[29] A. Einstein and W. de Sitter. On the Relation between the Expansion and the Mean Density of the Universe. *Proceedings of the National Academy of Science*, 18(3):213–214, March 1932.

[30] C. S. Frenk and S. D. M. White. Dark matter and cosmic structure. *Annalen der Physik*, 524(9-10):507–534, October 2012.

[31] V. A. Lyubimov, E. G. Novikov, V. Z. Nozik, E. F. Tretyakov, and V. S. Kosik. An Estimate of the electron-Neutrino Mass from the beta Spectrum of Tritium in the Valine Molecule. *Phys. Lett. B*, 94:266–268, 1980.

[32] Matthew R. Buckley and Annika H. G. Peter. Gravitational probes of dark matter physics. *Physics Reports*, 761:1–60, October 2018.

[33] S. D. M. White, C. S. Frenk, and M. Davis. Clustering in a neutrino-dominated universe. *ApJL*, 274:L1–L5, November 1983.

[34] J. Silk. Dark matter and galaxy formation. *Annalen der Physik*, 15(1):75–83, January 2006.

[35] N. A. Bahcall, J. P. Ostriker, S. Perlmutter, and P. J. Steinhardt. The Cosmic Triangle: Revealing the State of the Universe. *Science*, 284:1481, May 1999.

[36] Ho Seong Hwang, Margaret J. Geller, Changbom Park, Daniel G. Fabricant, Michael J. Kurtz, Kenneth J. Rines, Juhan Kim, Antonaldo Diaferio, H. Jabran Zahid, Perry Berlind, Michael Calkins, Susan Tokarz, and Sean Moran. HectoMAP and Horizon Run 4: Dense Structures and Voids in the Real and Simulated Universe. *ApJ*, 818(2):173, February 2016.

[37] A. Bosma. *The distribution and kinematics of neutral hydrogen in spiral galaxies of various morphological types*. PhD thesis, -, January 1978.

[38] T. S. van Albada, J. N. Bahcall, K. Begeman, and R. Sancisi. Distribution of dark matter in the spiral galaxy NGC 3198. *ApJ*, 295:305–313, August 1985.

[39] T. S. van Albada and R. Sancisi. Dark Matter in Spiral Galaxies. *Philosophical Transactions of the Royal Society of London Series A*, 320(1556):447–464, December 1986.

[40] J. F. Navarro, C. S. Frenk, and S. D. M. White. The Structure of Cold Dark Matter Halos. *ApJ*, 462:563, May 1996.

[41] J. F. Navarro, C. S. Frenk, and S. D. M. White. A Universal Density Profile from Hierarchical Clustering. *ApJ*, 490(2):493–508, December 1997.

[42] S. S. McGaugh, J. M. Schombert, G. D. Bothun, and W. J. G. de Blok. The Baryonic Tully-Fisher Relation. *ApJL*, 533(2):L99–L102, April 2000.

[43] S. S. McGaugh. The Mass Discrepancy-Acceleration Relation: Disk Mass and the Dark Matter Distribution. *ApJ*, 609(2):652–666, July 2004.

[44] S. S. McGaugh, F. Lelli, and J M. Schombert. Radial Acceleration Relation in Rotationally Supported Galaxies. *Phys. Rev. Lett.*, 117(20):201101, November 2016.

[45] S. S. McGaugh. The Baryonic Tully-Fisher Relation of Gas-rich Galaxies as a Test of ΛCDM and MOND. *AJ*, 143(2):40, February 2012.

[46] Federico Lelli, Stacy S. McGaugh, and James M. Schombert. The Small Scatter of the Baryonic Tully-Fisher Relation. *ApJL*, 816(1):L14, January 2016.

[47] H. Desmond and R. H. Wechsler. The Tully-Fisher and mass-size relations from halo abundance matching. *MNRAS*, 454(1):322–343, November 2015.

[48] G. D. Bothun, M. Aaronson, B. Schommer, J. Mould, J. Huchra, and III Sullivan, W. T. A catalog of radio, optical, and infrared observations of spiral galaxies in clusters. *ApJS*, 57:423–472, March 1985.

[49] M. A. W. Verheijen. *The Ursa Major Cluster of Galaxies: TF-relations and dark matter*. PhD thesis, -, January 1997.

[50] Rachel A. Pildis, James M. Schombert, and Ann Eder. Gas-rich Dwarf Galaxies from the Second Palomar Sky Survey. II. Optical Properties. *ApJ*, 481(1):157–168, May 1997.

[51] Jo Ann Eder and James M. Schombert. Gas-rich Dwarfs from the PSS-II. III. H I Profiles and Dynamical Masses. *ApJS*, 131(1):47–70, November 2000.

[52] Stacy S. McGaugh and W. J. G. de Blok. Testing the Dark Matter Hypothesis with Low Surface Brightness Galaxies and Other Evidence. *ApJ*, 499(1):41–65, May 1998.

[53] L. D. Matthews, W. van Driel, and III Gallagher, J. S. High-Resolution, High Signal-to-Noise, Global H i Spectra of Southern, Extreme Late-Type Spiral Galaxies. *AJ*, 116(3):1169–1185, September 1998.

[54] Benoît Famaey and Stacy S. McGaugh. Modified Newtonian Dynamics (MOND): Observational Phenomenology and Relativistic Extensions. *Living Reviews in Relativity*, 15(1):10, September 2012.

[55] F. Lelli, S. S. McGaugh, and J. M. Schombert. SPARC: Mass Models for 175 Disk Galaxies with Spitzer Photometry and Accurate Rotation Curves. *AJ*, 152(6):157, December 2016.

[56] P. Li, F. Lelli, S. S. McGaugh, and J. M. Schombert. Fitting the radial acceleration relation to individual SPARC galaxies. *A&A*, 615:A3, July 2018.

[57] I. M. E. Santos-Santos, J. F. Navarro, A. Robertson, A. Benítez-Llambay, K. A. Oman, M. R. Lovell, C. S. Frenk, A. D. Ludlow, A. Fattahi, and A. Ritz. Baryonic clues to the puzzling diversity of dwarf galaxy rotation curves. *MNRAS*, 495(1):58–77, April 2020.

[58] M. L. Mateo. Dwarf Galaxies of the Local Group. *Ann. Rev. Astron. Astrophys.*, 36:435–506, January 1998.

[59] L. E. Strigari, J. S. Bullock, M. Kaplinghat, J. D. Simon, M. Geha, B. Willman, and M. G. Walker. A common mass scale for satellite galaxies of the Milky Way. *Nature*, 454(7208):1096–1097, August 2008.

[60] C. Di Paolo, P. Salucci, and A. Erkurt. The universal rotation curve of low surface brightness galaxies - IV. The interrelation between dark and luminous matter. *MNRAS*, 490(4):5451–5477, December 2019.

[61] H. Baumgardt, E. K. Grebel, and P. Kroupa. Using distant globular clusters as a test for gravitational theories. *MNRAS*, 359(1):L1–L4, May 2005.

[62] K. Jordi, E. K. Grebel, M. Hilker, H. Baumgardt, M. Frank, P. Kroupa, H. Haghi, P. Côté, and S. G. Djorgovski. Testing Fundamental Physics with Distant Star Clusters: Analysis of Observational Data on Palomar 14. *AJ*, 137(6):4586–4596, June 2009.

[63] H. Baumgardt, P. Côté, M. Hilker, M. Rejkuba, S. Mieske, S. G. Djorgovski, and P. Stetson. The velocity dispersion and mass-to-light ratio of the remote halo globular cluster NGC2419. *MNRAS*, 396(4):2051–2060, July 2009.

[64] A. Sollima and C. Nipoti. Globular clusters in modified Newtonian dynamics: velocity dispersion profiles from self-consistent models. *MNRAS*, 401(1):131–142, January 2010.

[65] R. Ibata, A. Sollima, C. Nipoti, M. Bellazzini, S. C. Chapman, and E. Dalessandro. The Globular Cluster NGC 2419: A Crucible for Theories of Gravity. *ApJ*, 738(2):186, September 2011.

[66] R. Ibata, A. Sollima, C. Nipoti, M. Bellazzini, S. C. Chapman, and E. Dalessandro. Polytropic Model Fits to the Globular Cluster NGC 2419 in Modified Newtonian Dynamics. *ApJ*, 743(1):43, December 2011.

[67] M. J. Frank, M. Hilker, H. Baumgardt, P. Côté, E. K. Grebel, H. Haghi, A. H. W. Küpper, and S. G. Djorgovski. The velocity dispersion and mass function of the outer halo globular cluster Palomar 4. *MNRAS*, 423(3):2917–2932, July 2012.

[68] Sergey Mashchenko and Alison Sills. Globular Clusters with Dark Matter Halos. I. Initial Relaxation. *ApJ*, 619(1):243–257, January 2005.

[69] Ben Moore. Constraints on the global mass-to-light ratios and on the extent of dark matter halos in globular clusters and dwarf spheroidals. *The Astrophysical Journal*, 461(1), apr 1996.

[70] Duncan A. Forbes, Paul Lasky, Alister W. Graham, and Lee Spitler. Uniting old stellar systems: from globular clusters to giant ellipticals. *MNRAS*, 389(4):1924–1936, October 2008.

[71] M. Cappellari, E. Emsellem, D. Krajnović, R. M. McDermid, N. Scott, G. A. Verdoes Kleijn, L. M. Young, K. Alatalo, R. Bacon, L. Blitz, M. Bois, F. Bournaud, M. Bureau, R. L. Davies, T. A. Davis, P. T. de Zeeuw, Pierre-Alain Duc, S. Khochfar, H. Kuntschner, Pierre-Yves Lablanche, R. Morganti, T. Naab, T. Oosterloo, M. Sarzi, P. Serra, and Anne-Marie Weijmans. The ATLAS^{3D} project - I. A volume-limited sample of 260 nearby early-type galaxies: science goals and selection criteria. *MNRAS*, 413(2):813–836, May 2011.

[72] S. M. Croom, J. S. Lawrence, J. Bland-Hawthorn, J. J. Bryant, L. Fogarty, S. Richards, M. Goodwin, T. Farrell, S. Miziarski, R. Heald, D. H. Jones, S. Lee, M. Colless, S. Brough, A. M. Hopkins, A. E. Bauer, M. N. Birchall, S. Ellis, A. Horton, S. Leon-Saval, G. Lewis, Á. R. López-Sánchez, Seong-Sik Min, C. Trinh, and H. Trowland. The Sydney-AAO Multi-object Integral field spectrograph. *MNRAS*, 421(1):872–893, March 2012.

[73] S. F. Sánchez, R. C. Kennicutt, A. Gil de Paz, G. van de Ven, J. M. Vílchez, L. Wisotzki, C. J. Walcher, D. Mast, J. A. L. Aguerri, S. Albiol-Pérez, A. Alonso-Herrero, J. Alves, J. Bakos, T. Bartáková, J. Bland-Hawthorn, A. Boselli, D. J. Bomans, A. Castillo-Morales, C. Cortijo-Ferrero, A. de Lorenzo-Cáceres, A. Del Olmo, R. J. Dettmar, A. Díaz, S. Ellis, J. Falcón-Barroso, H. Flores, A. Gallazzi, B. García-Lorenzo, R. González Delgado, N. Gruel, T. Haines, C. Hao, B. Husemann, J. Iglésias-Páramo, K. Jahnke, B. Johnson, B. Jungwiert, V. Kalinova, C. Kehrig, D. Kupko, Á. R. López-Sánchez, M. Lyubenova, R. A. Marino, E. Mármol-Queraltó, I. Márquez, J. Masegosa, S. Meidt, J. Mendez-Abreu, A. Monreal-Ibero, C. Montijo, A. M. Mourão, G. Palacios-Navarro, P. Papaderos, A. Pasquali, R. Peletier, E. Pérez, I. Pérez, A. Quirrenbach, M. Relaño, F. F. Rosales-Ortega, M. M. Roth, T. Ruiz-Lara, P. Sánchez-Blázquez, C. Sengupta, R. Singh, V. Stanishev, S. C. Trager, A. Vazdekis, K. Viironen, V. Wild, S. Zibetti, and B. Ziegler. CALIFA, the Calar Alto Legacy Integral Field Area survey. I. Survey presentation. *A&A*, 538:A8, February 2012.

[74] Kevin Bundy, Matthew A. Bershady, David R. Law, Renbin Yan, Niv Drory, Nicholas MacDonald, David A. Wake, Brian Cherinka, José R. Sánchez-Gallego, Anne-Marie Weijmans, Daniel Thomas, Christy Tremonti, Karen Masters, Lodovico Coccato, Aleksandar M. Diamond-Stanic, Alfonso Aragón-Salamanca, Vladimir Avila-Reese, Carles Badenes, Jésus Falcón-Barroso, Francesco Belfiore, Dmitry Bizyaev, Guillermo A. Blanc, Joss Bland-Hawthorn, Michael R. Blanton, Joel R. Brownstein, Nell Byler, Michele Cappellari, Charlie Conroy, Aaron A. Dutton, Eric Emsellem, James Etherington, Peter M. Frinchaboy, Hai Fu, James E. Gunn, Paul Harding, Evelyn J. Johnston, Guinevere Kauffmann, Karen Kinemuchi, Mark A. Klaene, Johan H. Knapen, Alexie Leauthaud, Cheng Li, Lihwai Lin, Roberto Maiolino, Viktor Malanushenko, Elena Malanushenko, Shude Mao, Claudia Maraston, Richard M. McDermid, Michael R. Merrifield, Robert C. Nichol, Daniel Oravetz, Kaike Pan, John K. Parejko, Sebastian F. Sanchez, David Schlegel, Audrey Simmons, Oliver Steele, Matthias Steinmetz, Karun Thanjavur, Benjamin A. Thompson, Jeremy L. Tinker, Remco C. E. van den Bosch, Kyle B. Westfall, David Wilkinson, Shelley Wright, Ting Xiao, and Kai Zhang. Overview of the SDSS-IV

MaNGA Survey: Mapping nearby Galaxies at Apache Point Observatory. *ApJ*, 798(1):7, January 2015.

[75] R. N. Proctor, D. A. Forbes, A. J. Romanowsky, J. P. Brodie, J. Strader, M. Spolaor, J. T. Mendel, and L. Spitler. Probing the 2D kinematic structure of early-type galaxies out to three effective radii. *MNRAS*, 398(1):91–108, September 2009.

[76] Vincenzo Pota, Duncan A. Forbes, Aaron J. Romanowsky, Jean P. Brodie, Lee R. Spitler, Jay Strader, Caroline Foster, Jacob A. Arnold, Andrew Benson, Christina Blom, Jonathan R. Hargis, Katherine L. Rhode, and Christopher Usher. The SLUGGS Survey: kinematics for over 2500 globular clusters in 12 early-type galaxies. *MNRAS*, 428(1):389–420, January 2013.

[77] M. Cappellari, N. Scott, K. Alatalo, L. Blitz, M. Bois, F. Bournaud, M. Bureau, A. F. Crocker, R. L. Davies, T. A. Davis, P. T. de Zeeuw, Pierre-Alain Duc, E. Emsellem, S. Khochfar, D. Krajnović, H. Kuntschner, R. M. McDermid, R. Morganti, T. Naab, T. Oosterloo, M. Sarzi, P. Serra, Anne-Marie Weijmans, and L. M. Young. The ATLAS^{3D} project - XV. Benchmark for early-type galaxies scaling relations from 260 dynamical models: mass-to-light ratio, dark matter, Fundamental Plane and Mass Plane. *MNRAS*, 432(3):1709–1741, July 2013.

[78] Lodovico Coccato, Ortwin Gerhard, and Magda Arnaboldi. Distinct core and halo stellar populations and the formation history of the bright Coma cluster early-type galaxy NGC 4889. *MNRAS*, 407(1):L26–L30, September 2010.

[79] Mark A. Norris, Ray M. Sharples, Terry Bridges, Karl Gebhardt, Duncan A. Forbes, Robert Proctor, Favio Raúl Faifer, Juan Carlos Forte, Michael A. Beasley, Stephen E. Zepf, and David A. Hanes. Gemini/GMOS spectroscopy of the spheroid and globular cluster system of NGC 3923. *MNRAS*, 385(1):40–52, March 2008.

[80] C. Pulsoni, O. Gerhard, M. Arnaboldi, L. Coccato, A. Longobardi, N. R. Napolitano, E. Moylan, C. Narayan, V. Gupta, A. Burkert, M. Capaccioli, A. L. Chies-Santos, A. Cortesi, K. C. Freeman, K. Kuijken, M. R. Merrifield, A. J. Romanowsky, and C. Tortora. The extended Planetary Nebula Spectrograph (ePN.S) early-type galaxy survey: The kinematic diversity of stellar halos and the relation between halo transition scale and stellar mass. *A&A*, 618:A94, October 2018.

[81] Vincenzo Pota, Aaron J. Romanowsky, Jean P. Brodie, Jorge Peñarrubia, Duncan A. Forbes, Nicola R. Napolitano, Caroline Foster, Matthew G. Walker, Jay Strader, and Joel C. Roediger. The SLUGGS survey: multipopulation dynamical modelling of the elliptical galaxy NGC 1407 from stars and globular clusters. *MNRAS*, 450(3):3345–3358, July 2015.

[82] A. Deur. A relation between the dark mass of elliptical galaxies and their shape. *MNRAS*, 438(2):1535–1551, February 2014.

[83] A. Deur. A correlation between the dark content of elliptical galaxies and their ellipticity. *arXiv e-prints*, page arXiv:2010.06692, October 2020.

[84] Antonino Del Popolo and Morgan Le Delliou. Small Scale Problems of the ΛCDM Model: A Short Review. *Galaxies*, 5(1):17, February 2017.

[85] Steven Weinberg. The cosmological constant problem. *Reviews of Modern Physics*, 61(1):1–23, January 1989.

[86] M. J. Luo. The cosmological constant problem and re-interpretation of time. *Nuclear Physics B*, 884:344–356, July 2014.

[87] H. E. S. Velten, R. F. vom Marttens, and W. Zimdahl. Aspects of the cosmological "coincidence problem". *European Physical Journal C*, 74:3160, November 2014.

[88] Pierre Fleury, Hélène Dupuy, and Jean-Philippe Uzan. Can All Cosmological Observations Be Accurately Interpreted with a Unique Geometry? *Phys. Rev. Lett.*, 111(9):091302, August 2013.

[89] Marian Douspis, Laura Salvati, and Nabila Aghanim. On the tension between Large Scale Structures and Cosmic Microwave Background. *arXiv e-prints*, page arXiv:1901.05289, January 2019.

[90] Laura Salvati, Marian Douspis, and Nabila Aghanim. Constraints from thermal Sunyaev-Zel'dovich cluster counts and power spectrum combined with CMB. *A&A*, 614:A13, June 2018.

[91] Planck Collaboration, R. Adam, N. Aghanim, M. Ashdown, J. Aumont, C. Baccigalupi, M. Ballardini, A. J. Banday, R. B. Barreiro, N. Bartolo, S. Basak, R. Battye, K. Benabed, J. P. Bernard, M. Bersanelli, P. Bielewicz, J. J. Bock, A. Bonaldi, L. Bonavera, J. R. Bond, J. Borrill, F. R. Bouchet, F. Boulanger, M. Bucher, C. Burigana, E. Calabrese, J. F. Cardoso, J. Carron, H. C. Chiang, L. P. L. Colombo, C. Combet, B. Comis, F. Couchot, A. Coulais, B. P. Crill, A. Curto, F. Cuttaia, R. J. Davis, P. de Bernardis, A. de Rosa, G. de Zotti, J. Delabrouille, E. Di Valentino, C. Dickinson, J. M. Diego, O. Doré, M. Douspis, A. Ducout, X. Dupac, F. Elsner, T. A. Enßlin, H. K. Eriksen, E. Falgarone, Y. Fantaye, F. Finelli, F. Forastieri, M. Frailis, A. A. Fraisse, E. Franceschi, A. Frolov, S. Galeotta, S. Galli, K. Ganga, R. T. Génova-Santos, M. Gerbino, T. Ghosh, J. González-Nuevo, K. M. Górski, A. Gruppuso, J. E. Gudmundsson, F. K. Hansen, G. Helou, S. Henrot-Versillé, D. Herranz, E. Hivon, Z. Huang, S. Ilić, A. H. Jaffe, W. C. Jones, E. Keihänen, R. Keskitalo, T. S. Kisner, L. Knox, N. Krachmalnicoff, M. Kunz, H. Kurki-Suonio, G. Lagache, A. Lähteenmäki, J. M. Lamarre, M. Langer, A. Lasenby, M. Lattanzi, C. R. Lawrence, M. Le Jeune, F. Levrier, A. Lewis, M. Liguori, P. B. Lilje, M. López-Caniego, Y. Z. Ma, J. F. Macías-Pérez, G. Maggio, A. Mangilli, M. Maris, P. G. Martin, E. Martínez-González, S. Matarrese, N. Mauri, J. D. McEwen, P. R. Meinhold, A. Melchiorri, A. Mennella, M. Migliaccio, M. A. Miville-Deschênes, D. Molinari, A. Moneti, L. Montier, G. Morgante, A. Moss, P. Naselsky, P. Natoli, C. A. Oxborrow, L. Pagano, D. Paoletti, B. Partridge, G. Patanchon, L. Patrizii, O. Perdereau, L. Perotto, V. Pettorino, F. Piacentini, S. Plaszczynski, L. Polastri, G. Polenta, J. L. Puget, J. P. Rachen, B. Racine, M. Reinecke, M. Remazeilles, A. Renzi, G. Rocha, M. Rossetti, G. Roudier, J. A. Rubiño-Martín, B. Ruiz-Granados, L. Salvati, M. Sandri, M. Savelainen, D. Scott, G. Sirri, R. Sunyaev, A. S. Suur-Uski, J. A. Tauber, M. Tenti, L. Toffolatti, M. Tomasi, M. Tristram, T. Trombetti, J. Valiviita, F. Van Tent, P. Vielva, F. Villa, N. Vittorio, B. D. Wandelt, I. K. Wehus, M. White, A. Zacchei, and A. Zonca. Planck intermediate results. XLVII. Planck constraints on reionization history. *A&A*, 596:A108, December 2016.

[92] Stacy S. McGaugh. Balance of Dark and Luminous Mass in Rotating Galaxies. *Phys. Rev. Lett.*, 95(17):171302, October 2005.

[93] Benoit Famaey, Justin Khoury, and Riccardo Penco. Emergence of the mass discrepancy-acceleration relation from dark matter-baryon interactions. *JCAP*, 2018(3):038, March 2018.

[94] Aaron A. Dutton. The baryonic Tully-Fisher relation and galactic outflows. *MNRAS*, 424(4):3123–3128, August 2012.

[95] Arianna Di Cintio and Federico Lelli. The mass discrepancy acceleration relation in a ΛCDM context. *MNRAS*, 456(1):L127–L131, February 2016.

[96] C. Di Paolo, P. Salucci, and J. P. Fontaine. The Radial Acceleration Relation (RAR): Crucial Cases of Dwarf Disks and Low-surface-brightness Galaxies. *ApJ*, 873(2):106, March 2019.

[97] V. Cesare, A. Diaferio, T. Matsakos, and G. Angus. Dynamics of DiskMass Survey galaxies in refracted gravity. *A&A*, 637:A70, May 2020.

[98] James S. Bullock and Michael Boylan-Kolchin. Small-Scale Challenges to the ΛCDM Paradigm. *Ann. Rev. Astron. Astrophys.*, 55(1):343–387, August 2017.

[99] Joe Wolf, Gregory D. Martinez, James S. Bullock, Manoj Kaplinghat, Marla Geha, Ricardo R. Muñoz, Joshua D. Simon, and Frank F. Avedo. Accurate masses for dispersion-supported galaxies. *MNRAS*, 406(2):1220–1237, August 2010.

[100] Da-Ming Chen and Stacy McGaugh. Contradiction between strong lensing statistics and a feedback solution to the cusp/core problem. *Research in Astronomy and Astrophysics*, 10(12):1215–1222, December 2010.

[101] David H. Weinberg, James S. Bullock, Fabio Governato, Rachel Kuzio de Naray, and Annika H. G. Peter. Cold dark matter: Controversies on small scales. *Proceedings of the National Academy of Science*, 112(40):12249–12255, October 2015.

[102] Shea Garrison-Kimmel, Michael Boylan-Kolchin, James S. Bullock, and Evan N. Kirby. Too big to fail in the Local Group. *MNRAS*, 444(1):222–236, October 2014.

[103] Marcel S. Pawlowski. The planes of satellite galaxies problem, suggested solutions, and open questions. *Modern Physics Letters A*, 33(6):1830004, February 2018.

[104] Austin Joyce, Bhuvnesh Jain, Justin Khoury, and Mark Trodden. Beyond the cosmological standard model. *Physics Reports*, 568:1–98, March 2015.

[105] Steven Weinberg. Anthropic bound on the cosmological constant. *Phys. Rev. Lett.*, 59(22):2607–2610, November 1987.

[106] Lenny Susskind. The Anthropic Landscape of String Theory. In *The Davis Meeting On Cosmic Inflation*, page 26, March 2003.

[107] Raphael Bousso and Joseph Polchinski. Quantization of four-form fluxes and dynamical neutralization of the cosmological constant. *Journal of High Energy Physics*, 2000(6):006, June 2000.

[108] Shamit Kachru, Renata Kallosh, Andrei Linde, and Sandip P. Trivedi. de Sitter vacua in string theory. *Phys. Rev. D*, 68(4):046005, August 2003.

[109] Michael R. Douglas. The statistics of string/M theory vacua. *Journal of High Energy Physics*, 2003(5):046, May 2003.

[110] Michael R. Douglas and Shamit Kachru. Flux compactification. *Reviews of Modern Physics*, 79(2):733–796, April 2007.

[111] Rampei Kimura, Tsutomu Kobayashi, and Kazuhiro Yamamoto. Vainshtein screening in a cosmological background in the most general second-order scalar-tensor theory. *Phys. Rev. D*, 85(2):024023, January 2012.

[112] Justin Khoury and Amanda Weltman. Chameleon Fields: Awaiting Surprises for Tests of Gravity in Space. *Phys. Rev. Lett.*, 93(17):171104, October 2004.

[113] Limin Wang, R. R. Caldwell, J. P. Ostriker, and Paul J. Steinhardt. Cosmic Concordance and Quintessence. *ApJ*, 530(1):17–35, February 2000.

[114] Eric V. Linder. The dynamics of quintessence, the quintessence of dynamics. *General Relativity and Gravitation*, 40(2-3):329–356, February 2008.

[115] J. A. Frieman, M. S. Turner, and D. Huterer. Dark energy and the accelerating universe. *Ann. Rev. Astron. Astrophys.*, 46:385–432, September 2008.

[116] Shinji Tsujikawa. Quintessence: a review. *Classical and Quantum Gravity*, 30(21):214003, November 2013.

[117] R. R. Caldwell and Eric V. Linder. Limits of Quintessence. *Phys. Rev. Lett.*, 95(14):141301, September 2005.

[118] Takeshi Chiba. w and w$'$ of scalar field models of dark energy. *Phys. Rev. D*, 73(6):063501, March 2006.

[119] Robert J. Scherrer. Dark energy models in the w-w$'$ plane. *Phys. Rev. D*, 73(4):043502, February 2006.

[120] V. Barger, E. Guarnaccia, and D. Marfatia. Classification of dark energy models in the (w$_{</SUB>,w<SUB>}$) plane. *Physics Letters B*, 635(2-3):61–65, April 2006.

[121] Eric V. Linder. Paths of quintessence. *Phys. Rev. D*, 73(6):063010, March 2006.

[122] Robert J. Scherrer and A. A. Sen. Thawing quintessence with a nearly flat potential. *Phys. Rev. D*, 77(8):083515, April 2008.

[123] Takeshi Chiba, Antonio De Felice, and Shinji Tsujikawa. Observational constraints on quintessence: Thawing, tracker, and scaling models. *Phys. Rev. D*, 87(8):083505, April 2013.

[124] R. R. Caldwell. A phantom menace? Cosmological consequences of a dark energy component with super-negative equation of state. *Physics Letters B*, 545(1-2):23–29, October 2002.

[125] Valerio Faraoni and A. Dolgov. Superquintessence. *International Journal of Modern Physics D*, 11(4):471–481, January 2002.

[126] Robert R. Caldwell, Marc Kamionkowski, and Nevin N. Weinberg. Phantom Energy: Dark Energy with w<-1 Causes a Cosmic Doomsday. *Phys. Rev. Lett.*, 91(7):071301, August 2003.

[127] Yi-Fu Cai, Emmanuel N. Saridakis, Mohammad R. Setare, and Jun-Qing Xia. Quintom cosmology: Theoretical implications and observations. *Physics Reports*, 493(1):1–60, August 2010.

[128] Takeshi Chiba, Takahiro Okabe, and Masahide Yamaguchi. Kinetically driven quintessence. *Phys. Rev. D*, 62(2):023511, July 2000.

[129] C. Armendariz-Picon, V. Mukhanov, and Paul J. Steinhardt. Dynamical Solution to the Problem of a Small Cosmological Constant and Late-Time Cosmic Acceleration. *Phys. Rev. Lett.*, 85(21):4438–4441, November 2000.

[130] Roland de Putter and Eric V. Linder. Kinetic k-essence and quintessence. *Astroparticle Physics*, 28(3):263–272, November 2007.

[131] Ratbay Myrzakulov. F(T) gravity and k-essence. *General Relativity and Gravitation*, 44(12):3059–3080, December 2012.

[132] P. H. Brax and J. Martin. Quintessence and supergravity. *Physics Letters B*, 468:40–45, November 1999.

[133] Philippe Brax and Jérôme Martin. Robustness of quintessence. *Phys. Rev. D*, 61(10):103502, May 2000.

[134] A. Masiero, M. Pietroni, and F. Rosati. SUSY QCD and quintessence. *Phys. Rev. D*, 61(2):023504, January 2000.

[135] E. J. Copeland, N. J. Nunes, and F. Rosati. Quintessence models in supergravity. *Phys. Rev. D*, 62(12):123503, December 2000.

[136] Renata Kallosh, Andrei Linde, Sergey Prokushkin, and Marina Shmakova. Supergravity, dark energy, and the fate of the universe. *Phys. Rev. D*, 66(12):123503, December 2002.

[137] Kiwoon Choi. String or M theory axion as a quintessence. *Phys. Rev. D*, 62(4):043509, August 2000.

[138] Paul K. Townsend. Quintessence from M-theory. *Journal of High Energy Physics*, 2001(11):042, November 2001.

[139] M. Gasperini, F. Piazza, and G. Veneziano. Quintessence as a runaway dilaton. *Phys. Rev. D*, 65(2):023508, January 2002.

[140] T. Damour, F. Piazza, and G. Veneziano. Violations of the equivalence principle in a dilaton-runaway scenario. *Phys. Rev. D*, 66(4):046007, August 2002.

[141] Thibault Damour, Federico Piazza, and Gabriele Veneziano. Runaway Dilaton and Equivalence Principle Violations. *Phys. Rev. Lett.*, 89(8):081601, August 2002.

[142] Tsutomu Kobayashi. Horndeski theory and beyond: a review. *Reports on Progress in Physics*, 82(8):086901, August 2019.

[143] M. Ostrogradsky. Mémoires sur les équations différentielles, relatives au problème des isopérimètres. *Mem. Acad. St. Petersbourg*, 6(4):385–517, 1850.

[144] R. P. Woodard. The Theorem of Ostrogradsky. *arXiv e-prints*, page arXiv:1506.02210, June 2015.

[145] Gregory Walter Horndeski. Second-Order Scalar-Tensor Field Equations in a Four-Dimensional Space. *International Journal of Theoretical Physics*, 10(6):363–384, September 1974.

[146] T. Kobayashi, M. Yamaguchi, and J. Yokoyama. Generalized G-Inflation — Inflation with the Most General Second-Order Field Equations —. *Progress of Theoretical Physics*, 126(3):511–529, September 2011.

[147] B. P. Abbott, R. Abbott, T. D. Abbott, F. Acernese, K. Ackley, C. Adams, T. Adams, P. Addesso, R. X. Adhikari, V. B. Adya, and et al. Gravitational Waves and Gamma-Rays from a Binary Neutron Star Merger: GW170817 and GRB 170817A. *ApJL*, 848(2):L13, October 2017.

[148] Paolo Creminelli and Filippo Vernizzi. Dark Energy after GW170817 and GRB170817A. *Phys. Rev. Lett.*, 119(25):251302, December 2017.

[149] Jeremy Sakstein and Bhuvnesh Jain. Implications of the Neutron Star Merger GW170817 for Cosmological Scalar-Tensor Theories. *Phys. Rev. Lett.*, 119(25):251303, December 2017.

[150] Johannes Noller and Andrina Nicola. Cosmological parameter constraints for Horndeski scalar-tensor gravity. *Phys. Rev. D*, 99(10):103502, May 2019.

[151] C. Brans and R. H. Dicke. Mach's Principle and a Relativistic Theory of Gravitation. *Physical Review*, 124(3):925–935, November 1961.

[152] Wayne Hu and Ignacy Sawicki. Models of f(R) cosmic acceleration that evade solar system tests. *Phys. Rev. D*, 76(6):064004, September 2007.

[153] A. A. Starobinsky. Disappearing cosmological constant in f(R) gravity. *Soviet Journal of Experimental and Theoretical Physics Letters*, 86(3):157–163, October 2007.

[154] S. Appleby and R. Battye. Do consistent F(R)F(R) models mimic general relativity plus Λ? *Physics Letters B*, 654(1-2):7–12, October 2007.

[155] Shin'Ichi Nojiri and Sergei D. Odintsov. Modified f(R) gravity unifying R^m inflation with the ΛCDM epoch. *Phys. Rev. D*, 77(2):026007, January 2008.

[156] Thomas P. Sotiriou and Valerio Faraoni. f(R) theories of gravity. *Reviews of Modern Physics*, 82(1):451–497, January 2010.

[157] Ignazio Ciufolini and Erricos C Pavlis. A confirmation of the general relativistic prediction of the lense–thirring effect. *Nature*, 431(7011):958–960, 2004.

[158] B. Bertotti, L. Iess, and P. Tortora. A test of general relativity using radio links with the Cassini spacecraft. *Nature*, 425:374–376, 2003.

[159] David Hobbs, Berry Holl, Lennart Lindegren, Frédéric Raison, Sergei Klioner, and Alexey Butkevich. Determining PPN γ with Gaia's astrometric core solution. In Sergei A. Klioner, P. Kenneth Seidelmann, and Michael H. Soffel, editors, *Relativity in Fundamental Astronomy: Dynamics, Reference Frames, and Data Analysis*, volume 261, pages 315–319, January 2010.

[160] Antonio Genova, Erwan Mazarico, Sander Goossens, Frank G. Lemoine, Gregory A. Neumann, David E. Smith, and Maria T. Zuber. Solar system expansion and strong equivalence principle as seen by the NASA MESSENGER mission. *Nature Communications*, 9:289, January 2018.

[161] Pierre Touboul, Gilles Métris, Manuel Rodrigues, Yves André, Quentin Baghi, Joël Bergé, Damien Boulanger, Stefanie Bremer, Patrice Carle, Ratana Chhun, Bruno Christophe, Valerio Cipolla, Thibault Damour, Pascale Danto, Hansjoerg Dittus, Pierre Fayet, Bernard Foulon, Claude Gageant, Pierre-Yves Guidotti, Daniel Hagedorn, Emilie Hardy, Phuong-Anh Huynh, Henri Inchauspe, Patrick Kayser, Stéphanie Lala, Claus Lämmerzahl, Vincent Lebat, Pierre Leseur, Françoise Liorzou, Meike List, Frank Löffler, Isabelle Panet, Benjamin Pouilloux, Pascal Prieur, Alexandre Rebray, Serge Reynaud, Benny Rievers, Alain Robert, Hanns Selig, Laura Serron, Timothy Sumner, Nicolas Tanguy, and Pieter Visser. MICROSCOPE Mission: First Results of a Space Test of the Equivalence Principle. *Phys. Rev. Lett.*, 119(23):231101, December 2017.

[162] Justin Khoury and Amanda Weltman. Chameleon cosmology. *Phys. Rev. D*, 69(4):044026, February 2004.

[163] Ph. Brax, C. van de Bruck, A. C. Davis, J. Khoury, and A. Weltman. Chameleon Dark Energy. In C. J. A. P. Martins, P. P. Avelino, M. S. Costa, K. Mack, M. F. Mota, and M. Parry, editors, *Phi in the Sky: The Quest for Cosmological Scalar Fields*, volume 736 of *American Institute of Physics Conference Series*, pages 105–110, November 2004.

[164] Philippe Brax, Carsten van de Bruck, Anne-Christine Davis, Justin Khoury, and Amanda Weltman. Detecting dark energy in orbit: The cosmological chameleon. *Phys. Rev. D*, 70(12):123518, December 2004.

[165] Kurt Hinterbichler and Justin Khoury. Screening Long-Range Forces through Local Symmetry Restoration. *Phys. Rev. Lett.*, 104(23):231301, June 2010.

[166] Kurt Hinterbichler, Justin Khoury, Aaron Levy, and Andrew Matas. Symmetron cosmology. *Phys. Rev. D*, 84(10):103521, November 2011.

[167] Massimo Pietroni. Dark energy condensation. *Phys. Rev. D*, 72(4):043535, August 2005.

[168] Keith A. Olive and Maxim Pospelov. Environmental dependence of masses and coupling constants. *Phys. Rev. D*, 77(4):043524, February 2008.

[169] A.I. Vainshtein. To the problem of nonvanishing gravitation mass. *Physics Letters B*, 39(3):393 – 394, 1972.

[170] Ruifeng Dong, William H. Kinney, and Dejan Stojkovic. Symmetron inflation. *JCAP*, 2014(1):021, January 2014.

[171] C. Armendáriz-Picón, T. Damour, and V. Mukhanov. k-Inflation. *Physics Letters B*, 458(2-3):209–218, July 1999.

[172] Jaume Garriga and V. F. Mukhanov. Perturbations in k-inflation. *Physics Letters B*, 458(2-3):219–225, July 1999.

[173] Alberto Nicolis, Riccardo Rattazzi, and Enrico Trincherini. Galileon as a local modification of gravity. *Phys. Rev. D*, 79(6):064036, March 2009.

[174] E. Babichev, C. Deffayet, and R. Ziour. Recovering General Relativity from Massive Gravity. *Phys. Rev. Lett.*, 103(20):201102, November 2009.

[175] E. Babichev, C. Deffayet, and R. Ziour. Recovery of general relativity in massive gravity via the Vainshtein mechanism. *Phys. Rev. D*, 82(10):104008, November 2010.

[176] Kazuya Koyama, Gustavo Niz, and Gianmassimo Tasinato. Analytic Solutions in Nonlinear Massive Gravity. *Phys. Rev. Lett.*, 107(13):131101, September 2011.

[177] Ismael Ferrero, Julio F. Navarro, Mario G. Abadi, Laura V. Sales, Richard G. Bower, Robert A. Crain, Carlos S. Frenk, Matthieu Schaller, Joop Schaye, and Tom Theuns. Size matters: abundance matching, galaxy sizes, and the Tully-Fisher relation in EAGLE. *MNRAS*, 464(4):4736–4746, February 2017.

[178] Ismael Ferrero and Mario G. Abadi. Redshift evolution of Tully-Fisher relation. In Armando Gil de Paz, Johan H. Knapen, and Janice C. Lee, editors, *Formation and Evolution of Galaxy Outskirts*, volume 321, pages 126–126, March 2017.

[179] Julio F. Navarro, Vincent R. Eke, and Carlos S. Frenk. The cores of dwarf galaxy haloes. *MNRAS*, 283(3):L72–L78, December 1996.

[180] Sergey Mashchenko, H. M. P. Couchman, and James Wadsley. The removal of cusps from galaxy centres by stellar feedback in the early Universe. *Nature*, 442(7102):539–542, August 2006.

[181] O. Y. Gnedin and H. Zhao. Maximum Feedback and Dark Matter Profiles of Dwarf Galaxies. In *American Astronomical Society Meeting Abstracts*, volume 199 of *American Astronomical Society Meeting Abstracts*, page 21.05, December 2001.

[182] Sergey Mashchenko, James Wadsley, and H. M. P. Couchman. Stellar Feedback in Dwarf Galaxy Formation. *Science*, 319(5860):174, January 2008.

[183] Amr El-Zant, Isaac Shlosman, and Yehuda Hoffman. Dark Halos: The Flattening of the Density Cusp by Dynamical Friction. *ApJ*, 560(2):636–643, October 2001.

[184] Emilio Romano-Díaz, Isaac Shlosman, Yehuda Hoffman, and Clayton Heller. Erasing Dark Matter Cusps in Cosmological Galactic Halos with Baryons. *ApJL*, 685(2):L105, October 2008.

[185] J. R. Jardel and J. A. Sellwood. Halo Density Reduction by Baryonic Settling? *ApJ*, 691(2):1300–1306, February 2009.

[186] J. I. Read and D. Erkal. Abundance matching with the mean star formation rate: there is no missing satellites problem in the Milky Way above $M_{200} \sim 10^9$ $M_\odot$. *MNRAS*, 487(4):5799–5812, August 2019.

[187] Michael Boylan-Kolchin, James S. Bullock, and Manoj Kaplinghat. The Milky Way's bright satellites as an apparent failure of ΛCDM. *MNRAS*, 422(2):1203–1218, May 2012.

[188] Alyson M. Brooks and Adi Zolotov. Why Baryons Matter: The Kinematics of Dwarf Spheroidal Satellites. *ApJ*, 786(2):87, May 2014.

[189] Aaron A. Dutton, Andrea V. Macciò, Jonas Frings, Liang Wang, Gregory S. Stinson, Camilla Penzo, and Xi Kang. NIHAO V: too big does not fail - reconciling the conflict between ΛCDM predictions and the circular velocities of nearby field galaxies. *MNRAS*, 457(1):L74–L78, March 2016.

[190] Tobias Buck, Andrea V. Macciò, Aaron A. Dutton, Aura Obreja, and Jonas Frings. NIHAO XV: the environmental impact of the host galaxy on galactic satellite and field dwarf galaxies. *MNRAS*, 483(1):1314–1341, February 2019.

[191] Noam I. Libeskind, Yehuda Hoffman, R. Brent Tully, Helene M. Courtois, Daniel Pomarède, Stefan Gottlöber, and Matthias Steinmetz. Planes of satellite galaxies and the cosmic web. *MNRAS*, 452(1):1052–1059, September 2015.

[192] Noam I. Libeskind, Alexander Knebe, Yehuda Hoffman, and Stefan Gottlöber. The universal nature of subhalo accretion. *MNRAS*, 443(2):1274–1280, September 2014.

[193] Robert E. Smith and Katarina Markovic. Testing the warm dark matter paradigm with large-scale structures. *Phys. Rev. D*, 84(6):063507, September 2011.

[194] Christophe Yèche, Nathalie Palanque-Delabrouille, Julien Baur, and Hélion du Mas des Bourboux. Constraints on neutrino masses from Lyman-alpha forest power spectrum with BOSS and XQ-100. *JCAP*, 2017(6):047, June 2017.

[195] J. Zavala, Y. P. Jing, A. Faltenbacher, G. Yepes, Y. Hoffman, S. Gottlöber, and B. Catinella. The Velocity Function in the Local Environment from ΛCDM and ΛWDM Constrained Simulations. *ApJ*, 700(2):1779–1793, August 2009.

[196] Emmanouil Papastergis, Ann M. Martin, Riccardo Giovanelli, and Martha P. Haynes. The Velocity Width Function of Galaxies from the 40% ALFALFA Survey: Shedding Light on the Cold Dark Matter Overabundance Problem. *ApJ*, 739(1):38, September 2011.

[197] Scott Tremaine and James E. Gunn. Dynamical role of light neutral leptons in cosmology. *Phys. Rev. Lett.*, 42(6):407–410, February 1979.

[198] Mark R. Lovell, Vincent Eke, Carlos S. Frenk, Liang Gao, Adrian Jenkins, Tom Theuns, Jie Wang, Simon D. M. White, Alexey Boyarsky, and Oleg Ruchayskiy. The haloes of bright satellite galaxies in a warm dark matter universe. *MNRAS*, 420(3):2318–2324, March 2012.

[199] A. Schneider, D. Anderhalden, A. V. Maccio, and J. Diemand . Warm dark matter does not do better than cold dark matter in solving small-scale inconsistencies. *MNRAS*, 441:L6–L10, June 2014.

[200] Matteo Viel, Julien Lesgourgues, Martin G. Haehnelt, Sabino Matarrese, and Antonio Riotto. Constraining warm dark matter candidates including sterile neutrinos and light gravitinos with WMAP and the Lyman-α forest. *Phys. Rev. D*, 71(6):063534, March 2005.

[201] Francisco Villaescusa-Navarro and Neal Dalal. Cores and cusps in warm dark matter halos. *JCAP*, 2011(3):024, March 2011.

[202] Andrea V. Macciò, Sinziana Paduroiu, Donnino Anderhalden, Aurel Schneider, and Ben Moore. Cores in warm dark matter haloes: a Catch 22 problem. *MNRAS*, 424(2):1105–1112, August 2012.

[203] Sean Tulin and Hai-Bo Yu. Dark matter self-interactions and small scale structure. *Physics Reports*, 730:1–57, February 2018.

[204] C. Firmani, E. D'Onghia, V. Avila-Reese, G. Chincarini, and X. Hernández. Evidence of self-interacting cold dark matter from galactic to galaxy cluster scales. *MNRAS*, 315(3):L29–L32, July 2000.

[205] Oliver D. Elbert, James S. Bullock, Shea Garrison-Kimmel, Miguel Rocha, Jose Oñorbe, and Annika H. G. Peter. Core formation in dwarf haloes with self-interacting dark matter: no fine-tuning necessary. *MNRAS*, 453(1):29–37, October 2015.

[206] C. Firmani, E. D'Onghia, G. Chincarini, X. Hernández, and V. Avila-Reese. Constraints on dark matter physics from dwarf galaxies through galaxy cluster haloes. *MNRAS*, 321(4):713–722, March 2001.

[207] Massimo Meneghetti, Naoki Yoshida, Matthias Bartelmann, Lauro Moscardini, Volker Springel, Giuseppe Tormen, and Simon D. M. White. Giant cluster arcs as a constraint on the scattering cross-section of dark matter. *MNRAS*, 325(1):435–442, July 2001.

[208] J. Zavala, M. Vogelsberger, and M. G. Walker. Constraining self-interacting dark matter with the Milky way's dwarf spheroidals. *MNRAS*, 431:L20–L24, April 2013.

[209] Gregory A. Dooley, Annika H. G. Peter, Mark Vogelsberger, Jesús Zavala, and Anna Frebel. Enhanced tidal stripping of satellites in the galactic halo from dark matter self-interactions. *MNRAS*, 461(1):710–727, September 2016.

[210] Mark Vogelsberger, Jesus Zavala, and Abraham Loeb. Subhaloes in self-interacting galactic dark matter haloes. *MNRAS*, 423(4):3740–3752, July 2012.

[211] Abraham Loeb and Neal Weiner. Cores in Dwarf Galaxies from Dark Matter with a Yukawa Potential. *Phys. Rev. Lett.*, 106(17):171302, April 2011.

[212] R. Foot and Z. K. Silagadze. Thin disk of co-rotating dwarfs: A fingerprint of dissipative (mirror) dark matter? *Physics of the Dark Universe*, 2(3):163–165, September 2013.

[213] Lisa Randall and Jakub Scholtz. Dissipative dark matter and the Andromeda plane of satellites. *JCAP*, 2015(9):057, September 2015.

[214] Miguel Rocha, Annika H. G. Peter, James S. Bullock, Manoj Kaplinghat, Shea Garrison-Kimmel, Jose Oñorbe, and Leonidas A. Moustakas. Cosmological simulations with self-interacting dark matter - I. Constant-density cores and substructure. *MNRAS*, 430(1):81–104, March 2013.

[215] Pedro Colín, Vladimir Avila-Reese, Octavio Valenzuela, and Claudio Firmani. Structure and Subhalo Population of Halos in a Self-interacting Dark Matter Cosmology. *ApJ*, 581(2):777–793, December 2002.

[216] Steven Weinberg. A new light boson? *Phys. Rev. Lett.*, 40(4):223–226, January 1978.

[217] F. Wilczek. Problem of strong P and T invariance in the presence of instantons. *Phys. Rev. Lett.*, 40(5):279–282, January 1978.

[218] R.D. Peccei and Helen R. Quinn. CP Conservation in the Presence of Instantons. *Phys. Rev. Lett.*, 38:1440–1443, 1977.

[219] R.D. Peccei and Helen R. Quinn. Constraints Imposed by CP Conservation in the Presence of Instantons. *Phys. Rev. D*, 16:1791–1797, 1977.

[220] L. F. Abbott and P. Sikivie. A cosmological bound on the invisible axion. *Physics Letters B*, 120(1-3):133–136, January 1983.

[221] John Preskill, Mark B. Wise, and Frank Wilczek. Cosmology of the invisible axion. *Physics Letters B*, 120(1-3):127–132, January 1983.

[222] Michael Dine and Willy Fischler. The not-so-harmless axion. *Physics Letters B*, 120(1-3):137–141, January 1983.

[223] David J. E. Marsh and Ana-Roxana Pop. Axion dark matter, solitons and the cusp-core problem. *MNRAS*, 451(3):2479–2492, August 2015.

[224] Wayne Hu, Rennan Barkana, and Andrei Gruzinov. Fuzzy Cold Dark Matter: The Wave Properties of Ultralight Particles. *Phys. Rev. Lett.*, 85(6):1158–1161, August 2000.

[225] Luca Amendola and Riccardo Barbieri. Dark matter from an ultra-light pseudo-Goldsone-boson. *Physics Letters B*, 642(3):192–196, November 2006.

[226] Lam Hui, Jeremiah P. Ostriker, Scott Tremaine, and Edward Witten. Ultralight scalars as cosmological dark matter. *Phys. Rev. D*, 95(4):043541, February 2017.

[227] Hoang Nhan Luu, S. H. Henry Tye, and Tom Broadhurst. Multiple ultralight axionic wave dark matter and astronomical structures. *Physics of the Dark Universe*, 30:100636, December 2020.

[228] Hsi-Yu Schive, Tzihong Chiueh, and Tom Broadhurst. Cosmic structure as the quantum interference of a coherent dark wave. *Nature Physics*, 10(7):496–499, July 2014.

[229] Lawrence M. Widrow and Nick Kaiser. Using the Schroedinger Equation to Simulate Collisionless Matter. *ApJL*, 416:L71, October 1993.

[230] Erminia Calabrese and David N. Spergel. Ultra-light dark matter in ultra-faint dwarf galaxies. *MNRAS*, 460(4):4397–4402, August 2016.

[231] Alma X. González-Morales, David J. E. Marsh, Jorge Peñarrubia, and Luis A. Ureña-López. Unbiased constraints on ultralight axion mass from dwarf spheroidal galaxies. *MNRAS*, 472(2):1346–1360, December 2017.

[232] Shu-Rong Chen, Hsi-Yu Schive, and Tzihong Chiueh. Jeans analysis for dwarf spheroidal galaxies in wave dark matter. *MNRAS*, 468(2):1338–1348, June 2017.

[233] Tom Broadhurst, Ivan De Martino, Hoang Nhan Luu, George F. Smoot, and S. H. Henry Tye. Ghostly galaxies as solitons of Bose-Einstein dark matter. *Phys. Rev. D*, 101(8):083012, April 2020.

[234] Alvaro Pozo, Tom Broadhurst, Ivan De Martino, Hoang Nhan Luu, George F. Smoot, Jeremy Lim, and Mark Neyrinck. Wave Dark Matter and Ultra Diffuse Galaxies. *arXiv e-prints*, page arXiv:2003.08313, March 2020.

[235] Ivan De Martino, Tom Broadhurst, S. H. Henry Tye, Tzihong Chiueh, and Hsi-Yu Schive. Dynamical evidence of a dark solitonic core of $10^9 M_\odot$ in the milky way. *Physics of the Dark Universe*, 28:100503, May 2020.

[236] Xiaolong Du, Christoph Behrens, and Jens C. Niemeyer. Substructure of fuzzy dark matter haloes. *MNRAS*, 465(1):941–951, February 2017.

[237] J. Bekenstein and M. Milgrom. Does the missing mass problem signal the breakdown of Newtonian gravity? *ApJ*, 286:7–14, November 1984.

[238] R. H. Sanders. Alternatives to dark matter. *MNRAS*, 223:539–555, December 1986.

[239] Robert H. Sanders and Stacy S. McGaugh. Modified Newtonian Dynamics as an Alternative to Dark Matter. *Ann. Rev. Astron. Astrophys.*, 40:263–317, January 2002.

[240] A. Finzi. On the validity of Newton's law at a long distance. *MNRAS*, 127:21, January 1963.

[241] M. Milgrom. A modification of the Newtonian dynamics as a possible alternative to the hidden mass hypothesis. *ApJ*, 270:365–370, July 1983.

[242] Mordehai Milgrom. The Mond Limit from Spacetime Scale Invariance. *ApJ*, 698(2):1630–1638, June 2009.

[243] Mordehai Milgrom. Quasi-linear formulation of MOND. *MNRAS*, 403(2):886–895, April 2010.

[244] M. Milgrom. Dynamics with a Nonstandard Inertia-Acceleration Relation: An Alternative to Dark Matter in Galactic Systems. *Annals of Physics*, 229(2):384–415, February 1994.

[245] M. Milgrom. A modification of the Newtonian dynamics - Implications for galaxies. *ApJ*, 270:371–383, July 1983.

[246] Federico Lelli, Stacy S. McGaugh, James M. Schombert, and Marcel S. Pawlowski. One Law to Rule Them All: The Radial Acceleration Relation of Galaxies. *ApJ*, 836(2):152, February 2017.

[247] Rafael Brada and Mordehai Milgrom. Exact solutions and approximations of MOND fields of disc galaxies. *MNRAS*, 276(2):453–459, September 1995.

[248] R. H. Sanders. The Virial Discrepancy in Clusters of Galaxies in the Context of Modified Newtonian Dynamics. *ApJL*, 512(1):L23–L26, February 1999.

[249] R. H. Sanders. Clusters of galaxies with modified Newtonian dynamics. *MNRAS*, 342(3):901–908, July 2003.

[250] Alistair O. Hodson and Hongsheng Zhao. Generalizing MOND to explain the missing mass in galaxy clusters. *A&A*, 598:A127, February 2017.

[251] Jacob D. Bekenstein. Phase coupling gravitation: Symmetries and gauge fields. *Physics Letters B*, 202(4):497–500, March 1988.

[252] R. H. Sanders. Phase coupling gravity and astronomical mass discrepancies. *MNRAS*, 235:105–121, November 1988.

[253] Jacob D. Bekenstein. Relativistic gravitation theory for the modified Newtonian dynamics paradigm. *Phys. Rev. D*, 70(8):083509, October 2004.

[254] X. Hernandez, R. A. Sussman, and L. Nasser. Approaching the Dark Sector through a bounding curvature criterion. *MNRAS*, 483(1):147–151, February 2019.

[255] Constantinos Skordis and Tom Złosnik. A new relativistic theory for Modified Newtonian Dynamics. *arXiv e-prints*, page arXiv:2007.00082, June 2020.

[256] Mirek Giersz. Monte Carlo simulations of star clusters - III. A million-body star cluster. *MNRAS*, 371(1):484–494, September 2006.

[257] J. W. Moffat. Scalar tensor vector gravity theory. *JCAP*, 2006(3):004, March 2006.

[258] J. W. Moffat and S. Rahvar. The MOG weak field approximation and observational test of galaxy rotation curves. *MNRAS*, 436(2):1439–1451, December 2013.

[259] J. W. Moffat and V. T. Toth. The bending of light and lensing in modified gravity. *MNRAS*, 397(4):1885–1892, August 2009.

[260] S. Rahvar and J. W. Moffat. Propagation of electromagnetic waves in MOG: gravitational lensing. *MNRAS*, 482(4):4514–4518, February 2019.

[261] J. R. Brownstein and J. W. Moffat. The Bullet Cluster 1E0657-558 evidence shows modified gravity in the absence of dark matter. *MNRAS*, 382(1):29–47, November 2007.

[262] J. W. Moffat and S. Rahvar. The MOG weak field approximation - II. Observational test of Chandra X-ray clusters. *MNRAS*, 441(4):3724–3732, July 2014.

[263] Ivan De Martino and Mariafelicia De Laurentis. On the universality of MOG weak field approximation at galaxy cluster scale. *Physics Letters B*, 770:440–444, July 2017.

[264] R. N. Izmailov, R. Kh Karimov, E. R. Zhdanov, and K. K. Nand i. Modified gravity black hole lensing observables in weak and strong field of gravity. *MNRAS*, 483(3):3754–3761, March 2019.

[265] Mahmood Roshan. Exact cosmological solutions for MOG. *European Physical Journal C*, 75:405, September 2015.

[266] Suhail Dhawan, Ariel Goobar, and Edvard Mörtsell. The effect of inhomogeneities on dark energy constraints. *JCAP*, 2018(7):024, July 2018.

[267] M. H. Zhoolideh Haghighi and S. Rahvar. Testing MOG, non-local gravity and MOND with rotation curves of dwarf galaxies. *MNRAS*, 468(4):4048–4055, July 2017.

[268] M. A. Green and J. W. Moffat. Modified Gravity (MOG) fits to observed radial acceleration of SPARC galaxies. *Physics of the Dark Universe*, 25:100323, September 2019.

[269] Pieter van Dokkum, Shany Danieli, Yotam Cohen, Allison Merritt, Aaron J. Romanowsky, Roberto Abraham, Jean Brodie, Charlie Conroy, Deborah Lokhorst, Lamiya Mowla, Ewan O'Sullivan, and Jielai Zhang. A galaxy lacking dark matter. *Nature*, 555(7698):629–632, March 2018.

[270] J. W. Moffat and V. T. Toth. NGC 1052-DF2 and modified gravity (MOG) without dark matter. *MNRAS*, 482(1):L1–L3, January 2019.

[271] J. W. Moffat and V. T. Toth. Rotational velocity curves in the Milky Way as a test of modified gravity. *Phys. Rev. D*, 91(4):043004, February 2015.

[272] Carolina Negrelli, Maria Benito, Susana Landau, Fabio Iocco, and Lucila Kraiselburd. Testing modified gravity theory in the Milky Way. *Phys. Rev. D*, 98(10):104061, November 2018.

[273] Hosein Haghi and Vahid Amiri. Testing modified gravity with dwarf spheroidal galaxies. *MNRAS*, 463(2):1944–1951, December 2016.

[274] G. Torrealba, V. Belokurov, S. E. Koposov, T. S. Li, M. G. Walker, J. L. Sanders, A. Geringer-Sameth, D. B. Zucker, K. Kuehn, N. W. Evans, and W. Dehnen. The hidden giant: discovery of an enormous Galactic dwarf satellite in Gaia DR2. *MNRAS*, 488(2):2743–2766, September 2019.

[275] Ivan de Martino. Giant low-surface-brightness dwarf galaxy as a test bench for MOdified Gravity. *MNRAS*, 493(2):2373–2376, April 2020.

[276] Martin Kunz. Degeneracy between the dark components resulting from the fact that gravity only measures the total energy-momentum tensor. *Phys. Rev. D*, 80(12):123001, December 2009.

[277] Martin Kunz, Andrew R. Liddle, David Parkinson, and Changjun Gao. Constraining the dark fluid. *Phys. Rev. D*, 80(8):083533, October 2009.

[278] Elisa G. M. Ferreira, Guilherme Franzmann, Justin Khoury, and Robert Brandenberger. Unified superfluid dark sector. *JCAP*, 2019(8):027, August 2019.

[279] Martín Makler, Sérgio Quinet de Oliveira, and Ioav Waga. Constraints on the generalized Chaplygin gas from supernovae observations. *Physics Letters B*, 555(1-2):1–6, February 2003.

[280] Robert Brandenberger, Rodrigo R. Cuzinatto, Jürg Fröhlich, and Ryo Namba. New scalar field quartessence. *JCAP*, 2019(2):043, February 2019.

[281] M. C. Bento, O. Bertolami, and A. A. Sen. Generalized Chaplygin gas, accelerated expansion, and dark-energy-matter unification. *Phys. Rev. D*, 66(4):043507, August 2002.

[282] Daniela Carturan and Fabio Finelli. Cosmological effects of a class of fluid dark energy models. *Phys. Rev. D*, 68(10):103501, November 2003.

[283] Håvard B. Sandvik, Max Tegmark, Matias Zaldarriaga, and Ioav Waga. The end of unified dark matter? *Phys. Rev. D*, 69(12):123524, June 2004.

[284] Robert J. Scherrer. Purely Kinetic k Essence as Unified Dark Matter. *Phys. Rev. Lett.*, 93(1):011301, June 2004.

[285] Dimitrios Giannakis and Wayne Hu. Challenges for the kinetic unified dark matter model. *Phys. Rev. D*, 72(6):063502, September 2005.

[286] Marco Bruni, Ruth Lazkoz, and Alberto Rozas-Fernández. Phenomenological models for unified dark matter with fast transition. *MNRAS*, 431(3):2907–2916, May 2013.

[287] Iker Leanizbarrutia, Alberto Rozas-Fernández, and Ismael Tereno. Cosmological constraints on a unified dark matter-energy scalar field model with fast transition. *Phys. Rev. D*, 96(2):023503, July 2017.

[288] M. Cadoni, R. Casadio, A. Giusti, W. Mück, and M. Tuveri. Effective fluid description of the dark universe. *Physics Letters B*, 776:242–248, January 2018.

[289] M. Cadoni, R. Casadio, A. Giusti, and M. Tuveri. Emergence of a dark force in corpuscular gravity. *Phys. Rev. D*, 97(4):044047, February 2018.

[290] Stephon Alexander, Tirthabir Biswas, and Gianluca Calcagni. Cosmological Bardeen-Cooper-Schrieffer condensate as dark energy. *Phys. Rev. D*, 81(4):043511, February 2010.

[291] L. Sebastiani, S. Vagnozzi, and R. Myrzakulov. Mimetic gravity: a review of recent developments and applications to cosmology and astrophysics. *arXiv e-prints*, page arXiv:1612.08661, December 2016.

[292] Lasha Berezhiani, Justin Khoury, and Junpu Wang. Universe without dark energy: Cosmic acceleration from dark matter-baryon interactions. *Phys. Rev. D*, 95(12):123530, June 2017.

[293] Philip D. Mannheim and Demosthenes Kazanas. Exact Vacuum Solution to Conformal Weyl Gravity and Galactic Rotation Curves. *ApJ*, 342:635, July 1989.

[294] Robert Nesbet. Conformal Gravity: Dark Matter and Dark Energy. *Entropy*, 15(1):162–176, January 2013.

[295] M. C. Campigotto, A. Diaferio, and L. Fatibene. Conformal gravity: light deflection revisited and the galactic rotation curve failure. *Classical and Quantum Gravity*, 36(24):245014, December 2019.

[296] M. Campigotto and L. Fatibene. Gauge natural formulation of conformal gravity. *Annals of Physics*, 354:328–337, March 2015.

[297] M. Campigotto and L. Fatibene. Generally covariant vs. gauge structure for conformal field theories. *Annals of Physics*, 362:521–528, November 2015.

[298] Marta Campigotto and Lorenzo Fatibene. Conformal gravity as a Gauge natural theory. *International Journal of Geometric Methods in Modern Physics*, 13(8):1650052–528, March 2016.

[299] A. Arbey and J. F. Coupechoux. Unifying dark matter, dark energy and inflation with a fuzzy dark fluid. *arXiv e-prints*, page arXiv:2007.05376, July 2020.

[300] Titos Matsakos and Antonaldo Diaferio. Dynamics of galaxies and clusters in *refracted gravity*. *arXiv e-prints*, page arXiv:1603.04943, March 2016.

[301] Andrea P. Sanna, Titos Matsakos, and Antonaldo Diaferio. Relativistic Formulation of *Refracted Gravity*, *in preparation*.

[302] M. A. Jiménez, G. Garcia, X. Hernandez, and L. Nasser. The Massive Elliptical Galaxy NGC 4649 from the Perspective of Extended Gravity. *ApJ*, 768(2):142, May 2013.

[303] R. Durazo, X. Hernandez, B. Cervantes Sodi, and S. F. Sánchez. A Universal Velocity Dispersion Profile for Pressure Supported Systems: Evidence for MONDian Gravity across Seven Orders of Magnitude in Mass. *ApJ*, 837(2):179, March 2017.

[304] R. Durazo, X. Hernandez, B. Cervantes Sodi, and S. F. Sanchez. A Test of MONDian Gravity in ∼300 Pressure-supported Elliptical Galaxies from the MaNGA Survey. *ApJ*, 863(1):107, August 2018.

[305] X. Hernandez and M. A. Jiménez. The Outskirts of Globular Clusters as Modified Gravity Probes. *ApJ*, 750(1):9, May 2012.

[306] X. Hernandez, M. A. Jiménez, and C. Allen. Flattened velocity dispersion profiles in globular clusters: Newtonian tides or modified gravity? *MNRAS*, 428(4):3196–3205, February 2013.

[307] X. Hernandez and A. J. Lara-D I. Asymptotic kinematics of globular clusters: The emergence of a Tully-Fisher relation. *MNRAS*, 491(1):272–280, January 2020.

[308] X. Hernandez, M. A. Jiménez, and C. Allen. Isothermal Distributions in MONDian Gravity as a Simple Unifying Explanation for the Ubiquitousρvpropr $^{-3}$ Density Profiles in Tenuous Stellar Halos. *ApJ*, 770(2):83, June 2013.

[309] A. Vikhlinin, A. Kravtsov, W. Forman, C. Jones, M. Markevitch, S. S. Murray, and L. Van Speybroeck. Chandra Sample of Nearby Relaxed Galaxy Clusters: Mass, Gas Fraction, and Mass-Temperature Relation. *ApJ*, 640(2):691–709, April 2006.

[310] V. Biffi, S. Borgani, G. Murante, E. Rasia, S. Planelles, G. L. Granato, C. Ragone-Figueroa, A. M. Beck, M. Gaspari, and K. Dolag. On the Nature of Hydrostatic Equilibrium in Galaxy Clusters. *ApJ*, 827(2):112, August 2016.

[311] Luc Blanchet. Gravitational polarization and the phenomenology of MOND. *Classical and Quantum Gravity*, 24(14):3529–3539, July 2007.

[312] Luc Blanchet and Alexandre Le Tiec. Model of dark matter and dark energy based on gravitational polarization. *Phys. Rev. D*, 78(2):024031, July 2008.

[313] Luc Blanchet and Alexandre Le Tiec. Phenomenology of the Modified Newtonian Dynamics and the Concordance Cosmological Scenario. *arXiv e-prints*, page arXiv:0807.1200, July 2008.

[314] Luc Blanchet and Alexandre Le Tiec. Dipolar dark matter and dark energy. *Phys. Rev. D*, 80(2):023524, July 2009.

[315] Luc Blanchet and Lavinia Heisenberg. Dipolar dark matter as an effective field theory. *Phys. Rev. D*, 96(8):083512, October 2017.

[316] Lasma Alberte. Equivalence principle on cosmological backgrounds in scalar-tensor theories. *Classical and Quantum Gravity*, 36(22):225001, November 2019.

[317] Matthew A. Bershady, Marc A. W. Verheijen, Rob A. Swaters, David R. Andersen, Kyle B. Westfall, and Thomas Martinsson. The DiskMass Survey. I. Overview. *ApJ*, 716(1):198–233, June 2010.

[318] Valentina Cesare, Antonaldo Diaferio, and Titos Matsakos. The dynamics of three nearby E0 galaxies in refracted gravity. *arXiv e-prints*, page arXiv:2102.12499, February 2021.

[319] Adam G. Riess, Lucas M. Macri, Samantha L. Hoffmann, Dan Scolnic, Stefano Casertano, Alexei V. Filippenko, Brad E. Tucker, Mark J. Reid, David O. Jones, Jeffrey M. Silverman, Ryan Chornock, Peter Challis, Wenlong Yuan, Peter J. Brown,

and Ryan J. Foley. A 2.4% Determination of the Local Value of the Hubble Constant. *ApJ*, 826(1):56, July 2016.

[320] T. P. K. Martinsson, M. A. W. Verheijen, K. B. Westfall, M. A. Bershady, A. Schechtman-Rook, D. R. Andersen, and R. A. Swaters. The DiskMass Survey. VI. Gas and stellar kinematics in spiral galaxies from PPak integral-field spectroscopy. *A&A*, 557:A130, September 2013.

[321] M. A. Bershady, M. A. W. Verheijen, K. B. Westfall, D. R. Andersen, R. A. Swaters, and T. Martinsson. The DiskMass Survey. II. Error Budget. *ApJ*, 716:234–268, June 2010.

[322] K. B. Westfall, M. A. Bershady, and M. A. W. Verheijen. The DiskMass Survey. III. Stellar Kinematics Via Cross-Correlation. *ApJS*, 193:21, March 2011.

[323] K. B. Westfall, M. A. Bershady, M. A. W. Verheijen, D. R. Andersen, T. P. K. Martinsson, R. A. Swaters, and A. Schechtman-Rook. The DiskMass Survey. IV. The Dark-matter-dominated Galaxy UGC 463. *ApJ*, 742:18, November 2011.

[324] T. P. K. Martinsson, M. A. W. Verheijen, K. B. Westfall, M. A. Bershady, D. R. Andersen, and R. A. Swaters. The DiskMass Survey. VII. The distribution of luminous and dark matter in spiral galaxies. *A&A*, 557:A131, September 2013.

[325] Eric F. Bell and Roelof S. de Jong. Stellar Mass-to-Light Ratios and the Tully-Fisher Relation. *ApJ*, 550(1):212–229, March 2001.

[326] G. W. Angus, G. Gentile, R. Swaters, B. Famaey, A. Diaferio, S. S. McGaugh, and K. J. van der Heyden. Mass models of disc galaxies from the DiskMass Survey in modified Newtonian dynamics. *MNRAS*, 451(4):3551–3580, August 2015.

[327] Mordehai Milgrom. Critical take on "Mass models of disk galaxies from the DiskMass Survey in MOND". *arXiv e-prints*, page arXiv:1511.08087, November 2015.

[328] S. Aniyan, K. C. Freeman, O. E. Gerhard, M. Arnaboldi, and C. Flynn. The influence of a kinematically cold young component on disc-halo decompositions in spiral galaxies: insights from solar neighbourhood K-giants. *MNRAS*, 456(2):1484–1494, February 2016.

[329] Michiel Kregel, Pieter C. van der Kruit, and Richard de Grijs. Flattening and truncation of stellar discs in edge-on spiral galaxies. *MNRAS*, 334(3):646–668, August 2002.

[330] M. Pohlen, R.-J. Dettmar, R. Lütticke, and U. Schwarzkopf. Three-dimensional modelling of edge-on disk galaxies. *A&AS*, 144:405–428, June 2000.

[331] U. Schwarzkopf and R.-J. Dettmar. The influence of interactions and minor mergers on the structure of galactic disks I. Observations and disk models. *A&AS*, 144:85–121, May 2000.

[332] E. M. Xilouris, N. D. Kylafis, J. Papamastorakis, E. V. Paleologou, and G. Haerendel. The distribution of stars and dust in spiral galaxies: the edge-on spiral UGC 2048. *A&A*, 325:135–143, September 1997.

[333] E. M. Xilouris, Y. I. Byun, N. D. Kylafis, E. V. Paleologou, and J. Papamastorakis. Are spiral galaxies optically thin or thick? *A&A*, 344:868–878, April 1999.

[334] John Geweke. Evaluating the accuracy of sampling-based approaches to the calculation of posterior moments. In *IN BAYESIAN STATISTICS*, pages 169–193. University Press, 1992.

[335] R. Sancisi. The visible matter – dark matter coupling. In S. Ryder, D. Pisano, M. Walker, and K. Freeman, editors, *Dark Matter in Galaxies*, volume 220, page 233, July 2004.

[336] Stacy S. McGaugh and James M. Schombert. Color-Mass-to-light-ratio Relations for Disk Galaxies. *AJ*, 148(5):77, November 2014.

[337] James Schombert, Stacy McGaugh, and Federico Lelli. The mass-to-light ratios and the star formation histories of disc galaxies. *MNRAS*, 483(2):1496–1512, February 2019.

[338] Eric F. Bell and Richard G. Bower. Exploring the evolution of spiral galaxies. *MNRAS*, 319(1):235–254, November 2000.

[339] R. Nagai and M. Miyamoto. A family of self-gravitating stellar systems with axial symmetry. *PASJ*, 28(1):1–17, January 1976.

[340] Carlo Nipoti, Pasquale Londrillo, HongSheng Zhao, and Luca Ciotti. Vertical dynamics of disc galaxies in modified Newtonian dynamics. *MNRAS*, 379(2):597–604, August 2007.

[341] A. C. Robin, C. Reylé, S. Derrière, and S. Picaud. A synthetic view on structure and evolution of the Milky Way. *A&A*, 409:523–540, October 2003.

[342] V. Cesare, I. Colonnelli, and M. Aldinucci. Practical parallelization of scientific applications. In *2020 28th Euromicro International Conference on Parallel, Distributed and Network-Based Processing (PDP)*, pages 376–384, 2020.

[343] Marco Aldinucci, Valentina Cesare, Iacopo Colonnelli, Alberto R. Martinelli, Gianluca Mittone, Carlo Cavazzoni, and Maurizio Drocco. Practical Parallelization of Scientific Applications with OpenMP, OpenACC and MPI, *submitted*. *JPDC*.

[344] Andrew Gelman and Donald B. Rubin. Inference from Iterative Simulation Using Multiple Sequences. *Statistical Science*, 7:457–472, Jan 1992.

[345] Federico Lelli, Stacy S. McGaugh, and James M. Schombert. SPARC: Mass Models for 175 Disk Galaxies with Spitzer Photometry and Accurate Rotation Curves. *AJ*, 152(6):157, December 2016.

[346] Stacy S. McGaugh and James M. Schombert. Weighing Galaxy Disks With the Baryonic Tully-Fisher Relation. *ApJ*, 802(1):18, March 2015.

[347] Sharon E. Meidt, Eva Schinnerer, Glenn van de Ven, Dennis Zaritsky, Reynier Peletier, Johan H. Knapen, Kartik Sheth, Michael Regan, Miguel Querejeta, Juan-Carlos Muñoz-Mateos, Taehyun Kim, Joannah L. Hinz, Armando Gil de Paz, E. Athanassoula, Albert Bosma, Ronald J. Buta, Mauricio Cisternas, Luis C. Ho, Benne Holwerda, Ramin Skibba, E. Laurikainen, H. Salo, D. A. Gadotti, Jarkko Laine, S. Erroz-Ferrer, Sébastien Comerón, K. Menéndez-Delmestre, M. Seibert, and T. Mizusawa. Reconstructing the Stellar Mass Distributions of Galaxies Using S^4G IRAC 3.6 and 4.5 μm Images. II. The Conversion from Light to Mass. *ApJ*, 788(2):144, June 2014.

[348] James Schombert and Stacy McGaugh. Stellar Populations and the Star Formation Histories of LSB Galaxies: III. Stellar Population Models. *PASA*, 31:e036, September 2014.

[349] M. G. Kendall. A new measure of rank correlation. *Biometrika*, 30(1/2):81–93, 1938.

[350] C. Spearman. The proof and measurement of association between two things. *The American Journal of Psychology*, 15(1):72–101, 1904.

[351] D. J. Best. Extended tables for kendall's tau. *Biometrika*, 60(2):429–430, 1973.

[352] Maurice George Kendall. *Rank correlation methods.* Charles Griffin & Co. Ltd., London, 202 p., 1975.

[353] Jean P. Brodie, Aaron J. Romanowsky, Jay Strader, Duncan A. Forbes, Caroline Foster, Zachary G. Jennings, Nicola Pastorello, Vincenzo Pota, Christopher Usher, Christina Blom, Justin Kader, Joel C. Roediger, Lee R. Spitler, Alexa Villaume, Jacob A. Arnold, Sreeja S. Kartha, and Kristin A. Woodley. The SAGES Legacy Unifying Globulars and GalaxieS Survey (SLUGGS): Sample Definition, Methods, and Initial Results. *ApJ*, 796(1):52, November 2014.

[354] Duncan A. Forbes, Adebusola Alabi, Jean P. Brodie, Aaron J. Romanowsky, Jay Strader, Caroline Foster, Christopher Usher, Lee Spitler, Sabine Bellstedt, Nicola Pastorello, Alexa Villaume, Asher Wasserman, and Vincenzo Pota. The SLUGGS Survey: A Catalog of Over 4000 Globular Cluster Radial Velocities in 27 Nearby Early-type Galaxies. *AJ*, 153(3):114, March 2017.

[355] A. Dekel, F. Stoehr, G. A. Mamon, T. J. Cox, G. S. Novak, and J. R. Primack. Lost and found dark matter in elliptical galaxies. *Nature*, 437(7059):707–710, September 2005.

[356] Gary A. Mamon and Ewa L. Łokas. Dark matter in elliptical galaxies - II. Estimating the mass within the virial radius. *MNRAS*, 363(3):705–722, November 2005.

[357] I. J. Danziger. Dark Matter in Early-Type Galaxies. In Massimo Persic and Paolo Salucci, editors, *Dark and Visible Matter in Galaxies and Cosmological Implications*, volume 117 of *Astronomical Society of the Pacific Conference Series*, page 28, January 1997.

[358] William G. Mathews and Fabrizio Brighenti. Hot Gas in and around Elliptical Galaxies. *Ann. Rev. Astron. Astrophys.*, 41:191–239, January 2003.

[359] N. Werner, B. R. McNamara, E. Churazov, and E. Scannapieco. Hot Atmospheres, Cold Gas, AGN Feedback and the Evolution of Early Type Galaxies: A Topical Perspective. *Space Sci. Rev.*, 215(1):5, January 2019.

[360] Doug Geisler, Myung Gyoon Lee, and Eunhyeuk Kim. Washington Photometry of the Globular Cluster System of NGC 4472.I.Analysis of the Metallicities. *AJ*, 111:1529, April 1996.

[361] K. M. Ashman and S. E. Zepf. Globular cluster systems. *Cambridge Astrophysics Series*, 30, January 1998.

[362] Lilia P. Bassino, Tom Richtler, and Boris Dirsch. Globular cluster systems in low-luminosity early-type galaxies near the Fornax cluster centre. *MNRAS*, 367(1):156–168, March 2006.

[363] Jean P. Brodie and Jay Strader. Extragalactic Globular Clusters and Galaxy Formation. *Ann. Rev. Astron. Astrophys.*, 44(1):193–267, September 2006.

[364] Favio R. Faifer, Juan C. Forte, Mark A. Norris, Terry Bridges, Duncan A. Forbes, Stephen E. Zepf, Mike Beasley, Karl Gebhardt, David A. Hanes, and Ray M. Sharples. Gemini/GMOS imaging of globular cluster systems in five early-type galaxies*. *MNRAS*, 416(1):155–177, September 2011.

[365] Jay Strader, Aaron J. Romanowsky, Jean P. Brodie, Lee R. Spitler, Michael A. Beasley, Jacob A. Arnold, Naoyuki Tamura, Ray M. Sharples, and Nobuo Arimoto. Wide-field Precision Kinematics of the M87 Globular Cluster System. *ApJS*, 197(2):33, December 2011.

[366] Duncan A. Forbes, Trevor Ponman, and Ewan O'Sullivan. The baryonic haloes of elliptical galaxies: radial distribution of globular clusters and diffuse hot gas. *MNRAS*, 425(1):66–73, September 2012.

[367] Myung Gyoon Lee, Hong Soo Park, Eunhyeuk Kim, Ho Seong Hwang, Sang Chul Kim, and Doug Geisler. Washington CCD Photometry of the Globular Cluster System of the Giant Elliptical Galaxy M60 in Virgo. *ApJ*, 682(1):135–154, July 2008.

[368] Y. Schuberth, T. Richtler, M. Hilker, B. Dirsch, L. P. Bassino, A. J. Romanowsky, and L. Infante. The globular cluster system of NGC 1399. V. dynamics of the cluster system out to 80 kpc. *A&A*, 513:A52, April 2010.

[369] Kristen L. Shapiro, Reinhard Genzel, and Natascha M. Förster Schreiber. Star-forming galaxies at z ~2 and the formation of the metal-rich globular cluster population. *MNRAS*, 403(1):L36–L40, March 2010.

[370] M. Cappellari. Measuring the inclination and mass-to-light ratio of axisymmetric galaxies via anisotropic Jeans models of stellar kinematics. *MNRAS*, 390(1):71–86, October 2008.

[371] N. R. Napolitano, A. J. Romanowsky, L. Coccato, M. Capaccioli, N. G. Douglas, E. Noordermeer, O. Gerhard, M. Arnaboldi, F. de Lorenzi, K. Kuijken, M. R. Merrifield, E. O'Sullivan, A. Cortesi, P. Das, and K. C. Freeman. The Planetary Nebula Spectrograph elliptical galaxy survey: the dark matter in NGC 4494. *MNRAS*, 393(2):329–353, February 2009.

[372] John L. Tonry, Alan Dressler, John P. Blakeslee, Edward A. Ajhar, André B. Fletcher, Gerard A. Luppino, Mark R. Metzger, and Christopher B. Moore. The SBF Survey of Galaxy Distances. IV. SBF Magnitudes, Colors, and Distances. *ApJ*, 546(2):681–693, January 2001.

[373] Simona Mei, John P. Blakeslee, Patrick Côté, John L. Tonry, Michael J. West, Laura Ferrarese, Andrés Jordán, Eric W. Peng, André Anthony, and David Merritt. The ACS Virgo Cluster Survey. XIII. SBF Distance Catalog and the Three-dimensional Structure of the Virgo Cluster. *ApJ*, 655(1):144–162, January 2007.

[374] Nicholas Scott, Michele Cappellari, Roger L. Davies, Gijs Verdoes Kleijn, Maxime Bois, Katherine Alatalo, Leo Blitz, Frédéric Bournaud, Martin Bureau, Alison Crocker, Timothy A. Davis, P. T. de Zeeuw, Pierre-Alain Duc, Eric Emsellem, Sadegh Khochfar, Davor Krajnović, Harald Kuntschner, Richard M. McDermid, Raffaella Morganti, Thorsten Naab, Tom Oosterloo, Marc Sarzi, Paolo Serra, Anne-Marie Weijmans, and Lisa M. Young. The ATLAS^{3D} project - XXI. Correlations between gradients of local escape velocity and stellar populations in early-type galaxies. *MNRAS*, 432(3):1894–1913, July 2013.

[375] Max Spolaor, Duncan A. Forbes, George K. T. Hau, Robert N. Proctor, and Sarah Brough. The early-type galaxies NGC 1407 and NGC 1400 - I. Spatially resolved radial kinematics and surface photometry. *MNRAS*, 385(2):667–674, April 2008.

[376] S. P. Rusli, P. Erwin, R. P. Saglia, J. Thomas, M. Fabricius, R. Bender, and N. Nowak. Depleted Galaxy Cores and Dynamical Black Hole Masses. *AJ*, 146(6):160, December 2013.

[377] L. Ciotti and G. Bertin. Analytical properties of the $R^{1/m}$ law. *A&A*, 352:447–451, December 1999.

[378] Kevork N. Abazajian, Jennifer K. Adelman-McCarthy, Marcel A. Agüeros, Sahar S. Allam, Carlos Allende Prieto, Deokkeun An, Kurt S. J. Anderson, Scott F. Anderson, James Annis, Neta A. Bahcall, C. A. L. Bailer-Jones, J. C. Barentine, Bruce A. Bassett, Andrew C. Becker, Timothy C. Beers, Eric F. Bell, Vasily Belokurov, Andreas A. Berlind, Eileen F. Berman, Mariangela Bernardi, Steven J. Bickerton, Dmitry Bizyaev, John P. Blakeslee, Michael R. Blanton, John J. Bochanski, William N. Boroski, Howard J. Brewington, Jarle Brinchmann, J. Brinkmann, Robert J. Brunner, Tamás Budavári, Larry N. Carey, Samuel Carliles, Michael A. Carr, Francisco J. Castander, David Cinabro, A. J. Connolly, István Csabai, Carlos E. Cunha, Paul C. Czarapata, James R. A. Davenport, Ernst de Haas, Ben Dilday, Mamoru Doi, Daniel J. Eisenstein, Michael L. Evans, N. W. Evans, Xiaohui Fan, Scott D. Friedman, Joshua A. Frieman, Masataka Fukugita, Boris T. Gänsicke, Evalyn Gates, Bruce Gillespie, G. Gilmore, Belinda Gonzalez, Carlos F. Gonzalez, Eva K. Grebel, James E. Gunn, Zsuzsanna Györy, Patrick B. Hall, Paul Harding, Frederick H. Harris, Michael Harvanek, Suzanne L. Hawley, Jeffrey J. E. Hayes, Timothy M. Heckman, John S. Hendry, Gregory S. Hennessy, Robert B. Hindsley, J. Hoblitt, Craig J. Hogan, David W. Hogg, Jon A. Holtzman, Joseph B. Hyde, Shin-ichi Ichikawa, Takashi Ichikawa, Myungshin Im, Željko Ivezić, Sebastian Jester, Linhua Jiang, Jennifer A. Johnson, Anders M. Jorgensen, Mario Jurić, Stephen M. Kent, R. Kessler, S. J. Kleinman, G. R. Knapp, Kohki Konishi, Richard G. Kron, Jurek Krzesinski, Nikolay Kuropatkin, Hubert Lampeitl, Svetlana Lebedeva, Myung Gyoon Lee, Young Sun Lee, R. French Leger, Sébastien Lépine, Nolan Li, Marcos Lima, Huan Lin, Daniel C. Long, Craig P. Loomis, Jon Loveday, Robert H. Lupton, Eugene Magnier, Olena Malanushenko, Viktor Malanushenko, Rachel Mand elbaum, Bruce Margon, John P. Marriner, David Martínez-Delgado, Takahiko Matsubara, Peregrine M. McGehee, Timothy A. McKay, Avery Meiksin, Heather L. Morrison, Fergal Mullally, Jeffrey A. Munn, Tara Murphy, Thomas Nash, Ada Nebot, Jr. Neilsen, Eric H., Heidi Jo Newberg, Peter R. Newman, Robert C. Nichol, Tom Nicinski, Maria Nieto-Santisteban, Atsuko Nitta, Sadanori Okamura, Daniel J. Oravetz, Jeremiah P. Ostriker, Russell Owen, Nikhil Padmanabhan, Kaike Pan, Changbom Park, George Pauls, Jr. Peoples, John, Will J. Percival, Jeffrey R. Pier, Adrian C. Pope, Dimitri Pourbaix, Paul A. Price, Norbert Purger, Thomas Quinn, M. Jordan Raddick, Paola Re Fiorentin, Gordon T. Richards, Michael W. Richmond, Adam G. Riess, Hans-Walter Rix, Constance M. Rockosi, Masao Sako, David J. Schlegel, Donald P. Schneider, Ralf-Dieter Scholz, Matthias R. Schreiber, Axel D. Schwope, Uroš Seljak, Branimir Sesar, Erin Sheldon, Kazu Shimasaku, Valena C. Sibley, A. E. Simmons, Thirupathi Sivarani, J. Allyn Smith, Martin C. Smith, Vernesa Smolčić, Stephanie A. Snedden, Albert Stebbins, Matthias Steinmetz, Chris Stoughton, Michael A. Strauss, Mark SubbaRao, Yasushi Suto, Alexander S. Szalay, István Szapudi, Paula Szkody, Masayuki Tanaka, Max Tegmark, Luis F. A. Teodoro, Aniruddha R. Thakar, Christy A. Tremonti, Douglas L. Tucker, Alan Uomoto, Daniel E. Vanden Berk, Jan Vandenberg, S. Vidrih, Michael S. Vogeley, Wolfgang Voges, Nicole P. Vogt, Yogesh Wadadekar, Shannon Watters, David H. Weinberg, Andrew A. West, Simon D. M. White, Brian C. Wilhite, Alainna C. Wonders, Brian Yanny, D. R. Yocum, Donald G. York, Idit Zehavi, Stefano Zibetti, and Daniel B. Zucker. The Seventh Data Release of the Sloan Digital Sky Survey. *ApJS*, 182(2):543–558, June 2009.

[379] E. Emsellem, G. Monnet, and R. Bacon. The multi-gaussian expansion method: a tool for building realistic photometric and kinematical models of stellar systems I. The formalism. *A&A*, 285:723–738, May 1994.

[380] William E. Harris, J. W. B. Allwright, Christopher J. Pritchet, and Sidney van den Bergh. The Luminosity Distribution of Globular Clusters in Three Giant Virgo Ellipticals. *ApJS*, 76:115, May 1991.

[381] Bradley C. Whitmore, William B. Sparks, Ray A. Lucas, F. Duccio Macchetto, and John A. Biretta. Hubble Space Telescope Observations of Globular Clusters in M87 and an Estimate of H 0. *ApJL*, 454:L73, December 1995.

[382] Arunav Kundu and Bradley C. Whitmore. Wide Field Planetary Camera 2 Imaging of the Globular Cluster System of the S0 Galaxy NGC 3115. *AJ*, 116(6):2841–2853, December 1998.

[383] H. R. Merrett, K. Kuijken, M. R. Merrifield, A. J. Romanowsky, N. G. Douglas, N. R. Napolitano, M. Arnaboldi, M. Capaccioli, K. C. Freeman, O. Gerhard, N. W. Evans, M. I. Wilkinson, C. Halliday, T. J. Bridges, and D. Carter. Tracing the star stream through M31 using planetary nebula kinematics. *MNRAS*, 346(4):L62–L66, December 2003.

[384] Zhongli Zhang, Haiguang Xu, Yu Wang, Tao An, Yueheng Xu, and Xiang-Ping Wu. Probing the Mass Distributions in NGC 1407 and Its Associated Group with the X-Ray Imaging Spectroscopic and Optical Photometric and Line-Strength Indices Data. *ApJ*, 656(2):805–817, February 2007.

[385] N. Grevesse and A. J. Sauval. Standard Solar Composition. *Space Sci. Rev.*, 85:161–174, May 1998.

[386] Alessandro Paggi, Dong-Woo Kim, Craig Anderson, Doug Burke, Raffaele D'Abrusco, Giuseppina Fabbiano, Antonella Fruscione, Tara Gokas, Jen Lauer, Michael McCollough, Doug Morgan, Amy Mossman, Ewan O'Sullivan, Ginevra Trinchieri, Saeqa Vrtilek, Silvia Pellegrini, Aaron J. Romanowsky, and Jean Brodie. Constraining the Physical State of the Hot Gas Halos in NGC 4649 and NGC 5846. *ApJ*, 844(1):5, July 2017.

[387] Randall K. Smith, Nancy S. Brickhouse, Duane A. Liedahl, and John C. Raymond. Collisional Plasma Models with APEC/APED: Emission-Line Diagnostics of Hydrogen-like and Helium-like Ions. *ApJL*, 556(2):L91–L95, August 2001.

[388] D. Fabricant, M. Lecar, and P. Gorenstein. X-ray measurements of the mass of M 87. *ApJ*, 241:552–560, October 1980.

[389] Caroline Foster, Nicola Pastorello, Joel Roediger, Jean P. Brodie, Duncan A. Forbes, Sreeja S. Kartha, Vincenzo Pota, Aaron J. Romanowsky, Lee R. Spitler, Jay Strader, Christopher Usher, and Jacob A. Arnold. The SLUGGS Survey: stellar kinematics, kinemetry and trends at large radii in 25 early-type galaxies. *MNRAS*, 457(1):147–171, March 2016.

[390] Michele Cappellari, R. Bacon, M. Bureau, M. C. Damen, Roger L. Davies, P. T. de Zeeuw, Eric Emsellem, Jesús Falcón-Barroso, Davor Krajnović, Harald Kuntschner, Richard M. McDermid, Reynier F. Peletier, Marc Sarzi, Remco C. E. van den Bosch, and Glenn van de Ven. The SAURON project - IV. The mass-to-light ratio, the virial mass estimator and the Fundamental Plane of elliptical and lenticular galaxies. *MNRAS*, 366(4):1126–1150, March 2006.

[391] Michele Cappellari, Eric Emsellem, R. Bacon, M. Bureau, Roger L. Davies, P. T. de Zeeuw, Jesús Falcón-Barroso, Davor Krajnović, Harald Kuntschner, Richard M. McDermid, Reynier F. Peletier, Marc Sarzi, Remco C. E. van den Bosch, and Glenn van de Ven. The SAURON project - X. The orbital anisotropy of elliptical and lenticular galaxies: revisiting the $(V/\sigma, \in)$ diagram with integral-field stellar kinematics. *MNRAS*, 379(2):418–444, August 2007.

[392] Roeland P. van der Marel and Marijn Franx. A New Method for the Identification of Non-Gaussian Line Profiles in Elliptical Galaxies. *ApJ*, 407:525, April 1993.

[393] O. E. Gerhard. Line-of-sight velocity profiles in spherical galaxies: breaking the degeneracy between anisotropy and mass. *MNRAS*, 265:213, November 1993.

[394] J. Thomas, R. P. Saglia, R. Bender, P. Erwin, and M. Fabricius. The Dynamical Fingerprint of Core Scouring in Massive Elliptical Galaxies. *ApJ*, 782(1):39, February 2014.

[395] Davor Krajnović, Eric Emsellem, Michele Cappellari, Katherine Alatalo, Leo Blitz, Maxime Bois, Frédéric Bournaud, Martin Bureau, Roger L. Davies, Timothy A. Davis, P. T. de Zeeuw, Sadegh Khochfar, Harald Kuntschner, Pierre-Yves Lablanche, Richard M. McDermid, Raffaella Morganti, Thorsten Naab, Tom Oosterloo, Marc Sarzi, Nicholas Scott, Paolo Serra, Anne-Marie Weijmans, and Lisa M. Young. The ATLAS^{3D} project - II. Morphologies, kinemetric features and alignment between photometric and kinematic axes of early-type galaxies. *MNRAS*, 414(4):2923–2949, Jul 2011.

[396] Antti Rantala, Peter H. Johansson, Thorsten Naab, Jens Thomas, and Matteo Frigo. The Simultaneous Formation of Cored, Tangentially Biased, and Kinematically Decoupled Centers in Massive Early-type Galaxies. *ApJL*, 872(2):L17, February 2019.

[397] J. C. Jackson. On the reality of the velocity dispersions in groups of galaxies. *The Observatory*, 93:19–23, February 1973.

[398] L. Danese, G. de Zotti, and G. di Tullio. On velocity dispersions of galaxies in rich clusters. *A&A*, 82:322–327, February 1980.

[399] Margaret J. Geller, Ho Seong Hwang, Antonaldo Diaferio, Michael J. Kurtz, Dan Coe, and Kenneth J. Rines. A Redshift Survey of the Strong-lensing Cluster Abell 383. *ApJ*, 783(1):52, March 2014.

[400] J. H. Jeans. On the theory of star-streaming and the structure of the universe. *MNRAS*, 76:70–84, December 1915.

[401] Philip J. Humphrey, David A. Buote, Fabio Gastaldello, Luca Zappacosta, James S. Bullock, Fabrizio Brighenti, and William G. Mathews. A Chandra View of Dark Matter in Early-Type Galaxies. *ApJ*, 646(2):899–918, August 2006.

[402] Eric F. Bell, Daniel H. McIntosh, Neal Katz, and Martin D. Weinberg. The Optical and Near-Infrared Properties of Galaxies. I. Luminosity and Stellar Mass Functions. *ApJS*, 149(2):289–312, December 2003.

[403] Stefano Zibetti, Stéphane Charlot, and Hans-Walter Rix. Resolved stellar mass maps of galaxies - I. Method and implications for global mass estimates. *MNRAS*, 400(3):1181–1198, December 2009.

[404] Pavel Kroupa. On the variation of the initial mass function. *MNRAS*, 322(2):231–246, April 2001.

[405] Edwin E. Salpeter. The Luminosity Function and Stellar Evolution. *ApJ*, 121:161, January 1955.

[406] R. Bottema. The stellar kinematics of galactic disks. *A&A*, 275:16–36, August 1993.

[407] Brian Kimmig, Anil Seth, Inese I. Ivans, Jay Strader, Nelson Caldwell, Tim Anderton, and Dylan Gregersen. Measuring Consistent Masses for 25 Milky Way Globular Clusters. *AJ*, 149(2):53, February 2015.

[408] H. Baumgardt. N -body modelling of globular clusters: masses, mass-to-light ratios and intermediate-mass black holes. *MNRAS*, 464(2):2174–2202, January 2017.

[409] Lars Hernquist. An Analytical Model for Spherical Galaxies and Bulges. *ApJ*, 356:359, June 1990.

[410] Hongsheng Zhao. Analytical models for galactic nuclei. *MNRAS*, 278(2):488–496, January 1996.

[411] Sarah Brough, Duncan A. Forbes, Virginia A. Kilborn, Warrick Couch, and Matthew Colless. Eridanus - a supergroup in the local Universe? *MNRAS*, 369(3):1351–1374, July 2006.

[412] Andisheh Mahdavi, Neil Trentham, and R. Brent Tully. The NGC 5846 Group: Dynamics and the Luminosity Function to M_R=-12. *AJ*, 130(4):1502–1515, October 2005.

[413] Planck Collaboration, N. Aghanim, Y. Akrami, F. Arroja, M. Ashdown, J. Aumont, C. Baccigalupi, M. Ballardini, A. J. Banday, R. B. Barreiro, N. Bartolo, S. Basak, R. Battye, K. Benabed, J. P. Bernard, M. Bersanelli, P. Bielewicz, J. J. Bock, J. R. Bond, J. Borrill, F. R. Bouchet, F. Boulanger, M. Bucher, C. Burigana, R. C. Butler, E. Calabrese, J. F. Cardoso, J. Carron, B. Casaponsa, A. Challinor, H. C. Chiang, L. P. L. Colombo, C. Combet, D. Contreras, B. P. Crill, F. Cuttaia, P. de Bernardis, G. de Zotti, J. Delabrouille, J. M. Delouis, F. X. Désert, E. Di Valentino, C. Dickinson, J. M. Diego, S. Donzelli, O. Doré, M. Douspis, A. Ducout, X. Dupac, G. Efstathiou, F. Elsner, T. A. Enßlin, H. K. Eriksen, E. Falgarone, Y. Fantaye, J. Fergusson, R. Fernandez-Cobos, F. Finelli, F. Forastieri, M. Frailis, E. Franceschi, A. Frolov, S. Galeotta, S. Galli, K. Ganga, R. T. Génova-Santos, M. Gerbino, T. Ghosh, J. González-Nuevo, K. M. Górski, S. Gratton, A. Gruppuso, J. E. Gudmundsson, J. Hamann, W. Handley, F. K. Hansen, G. Helou, D. Herranz, S. R. Hildebrandt, E. Hivon, Z. Huang, A. H. Jaffe, W. C. Jones, A. Karakci, E. Keihänen, R. Keskitalo, K. Kiiveri, J. Kim, T. S. Kisner, L. Knox, N. Krachmalnicoff, M. Kunz, H. Kurki-Suonio, G. Lagache, J. M. Lamarre, M. Langer, A. Lasenby, M. Lattanzi, C. R. Lawrence, M. Le Jeune, J. P. Leahy, J. Lesgourgues, F. Levrier, A. Lewis, M. Liguori, P. B. Lilje, M. Lilley, V. Lindholm, M. López-Caniego, P. M. Lubin, Y. Z. Ma, J. F. Macías-Pérez, G. Maggio, D. Maino, N. Mandolesi, A. Mangilli, A. Marcos-Caballero, M. Maris, P. G. Martin, M. Martinelli, E. Martínez-González, S. Matarrese, N. Mauri, J. D. McEwen, P. D. Meerburg, P. R. Meinhold, A. Melchiorri, A. Mennella, M. Migliaccio, M. Millea, S. Mitra, M. A. Miville-Deschênes, D. Molinari, A. Moneti, L. Montier, G. Morgante, A. Moss, S. Mottet, M. Münchmeyer, P. Natoli, H. U. Nørgaard-Nielsen, C. A. Oxborrow, L. Pagano, D. Paoletti, B. Partridge, G. Patanchon, T. J. Pearson, M. Peel, H. V. Peiris, F. Perrotta, V. Pettorino, F. Piacentini, L. Polastri, G. Polenta, J. L. Puget, J. P. Rachen, M. Reinecke, M. Remazeilles, C. Renault, A. Renzi, G. Rocha, C. Rosset, G. Roudier, J. A. Rubiño-Martín, B. Ruiz-Granados, L. Salvati, M. Sandri, M. Savelainen, D. Scott, E. P. S. Shellard, M. Shiraishi, C. Sirignano, G. Sirri, L. D. Spencer, R. Sunyaev, A. S. Suur-Uski, J. A. Tauber, D. Tavagnacco, M. Tenti, L. Terenzi, L. Toffolatti, M. Tomasi, T. Trombetti, J. Valiviita, B. Van Tent, L. Vibert, P. Vielva, F. Villa, N. Vittorio, B. D. Wandelt, I. K. Wehus, M. White, S. D. M. White, A. Zacchei, and A. Zonca. Planck 2018 results. I. Overview and the cosmological legacy of Planck. *A&A*, 641:A1, September 2020.

[414] Paolo Salucci, Mark I. Wilkinson, Matthew G. Walker, Gerard F. Gilmore, Eva K. Grebel, Andreas Koch, Christiane Frigerio Martins, and Rosemary F. G. Wyse. Dwarf spheroidal galaxy kinematics and spiral galaxy scaling laws. *MNRAS*, 420(3):2034–2041, March 2012.

[415] Se-Heon Oh, Deidre A. Hunter, Elias Brinks, Bruce G. Elmegreen, Andreas Schruba, Fabian Walter, Michael P. Rupen, Lisa M. Young, Caroline E. Simpson, Megan C. Johnson, Kimberly A. Herrmann, Dana Ficut-Vicas, Phil Cigan, Volker Heesen, Trisha Ashley, and Hong-Xin Zhang. High-resolution Mass Models of Dwarf Galaxies from LITTLE THINGS. *AJ*, 149(6):180, June 2015.

[416] Kenneth Rines and Antonaldo Diaferio. CIRS: Cluster Infall Regions in the Sloan Digital Sky Survey. I. Infall Patterns and Mass Profiles. *AJ*, 132(3):1275–1297, September 2006.

[417] Kenneth Rines, Margaret J. Geller, Antonaldo Diaferio, and Michael J. Kurtz. Measuring the Ultimate Halo Mass of Galaxy Clusters: Redshifts and Mass Profiles from the Hectospec Cluster Survey (HeCS). *ApJ*, 767(1):15, April 2013.

[418] R. Amanullah, C. Lidman, D. Rubin, G. Aldering, P. Astier, K. Barbary, M. S. Burns, A. Conley, K. S. Dawson, S. E. Deustua, M. Doi, S. Fabbro, L. Faccioli, H. K. Fakhouri, G. Folatelli, A. S. Fruchter, H. Furusawa, G. Garavini, G. Goldhaber, A. Goobar, D. E. Groom, I. Hook, D. A. Howell, N. Kashikawa, A. G. Kim, R. A. Knop, M. Kowalski, E. Linder, J. Meyers, T. Morokuma, S. Nobili, J. Nordin, P. E. Nugent, L. Östman, R. Pain, N. Panagia, S. Perlmutter, J. Raux, P. Ruiz-Lapuente, A. L. Spadafora, M. Strovink, N. Suzuki, L. Wang, W. M. Wood-Vasey, N. Yasuda, and The Supernova Cosmology Project. Spectra and Hubble Space Telescope Light Curves of Six Type Ia Supernovae at $0.511 < z < 1.12$ and the Union2 Compilation. *ApJ*, 716(1):712–738, June 2010.

[419] Volker Springel. The cosmological simulation code GADGET-2. *MNRAS*, 364(4):1105–1134, December 2005.

[420] Zhi-Bin Wang, Rong Chen, Hong Wang, Qiang Liao, Xun Zhu, and Shu-Zhe Li. An overview of smoothed particle hydrodynamics for simulating multiphase flow. *Applied Mathematical Modelling*, 40(23):9625 – 9655, 2016.

[421] G. de Vaucouleurs. General Physical Properties of External Galaxies. *Handbuch der Physik*, 53:311, 1959.

[422] K. C. Freeman. On the Disks of Spiral and S0 Galaxies. *ApJ*, 160:811, June 1970.

[423] Marc A. W. Verheijen. The Ursa Major Cluster of Galaxies. V. H I Rotation Curve Shapes and the Tully-Fisher Relations. *ApJ*, 563(2):694–715, December 2001.

[424] James Binney and Michael Merrifield. *Galactic Astronomy*. 1998.

[425] T. P. K. Martinsson. *The distribution of mass within spiral galaxies: unique solution*. PhD thesis, University of Groningen, 2011.

[426] David Young. Iterative methods for solving partial difference equations of elliptic type. *Transactions of the American Mathematical Society*, 76(1):92–111, 1954.

[427] J. Binney and S. Tremaine. *Galactic Dynamics: Second Edition*. Princeton University Press, 2008.

[428] R. Smith, C. Flynn, G. N. Candlish, M. Fellhauer, and B. K. Gibson. Simple and accurate modelling of the gravitational potential produced by thick and thin exponential discs. *MNRAS*, 448:2934–2940, April 2015.

[429] M. Miyamoto and R. Nagai. Three-dimensional models for the distribution of mass in galaxies. *PASJ*, 27:533–543, 1975.

[430] Niklaus Wirth. *Algorithms Data Structures*. Prentice-Hall, Inc., USA, 1985.

[431] Andrew W. Appel and Maia Ginsburg. *Modern Compiler Implementation in C.* Cambridge University Press, USA, 2004.

[432] A. J. Bernstein. Analysis of programs for parallel processing. *IEEE Transactions on Electronic Computers*, EC-15(5):757–763, 1966.

[433] Christian Lengauer. Loop parallelization in the polytope model. In *Proceedings of the 4th International Conference on Concurrency Theory*, CONCUR '93, page 398â416, Berlin, Heidelberg, 1993. Springer-Verlag.

[434] Marco Aldinucci, Marco Danelutto, Peter Kilpatrick, and Massimo Torquati. *Fastflow: High-Level and Efficient Streaming on Multicore*, chapter 13, pages 261–280. John Wiley Sons, Ltd, 2017.

[435] Josef Weidendorfer, Markus Kowarschik, and Carsten Trinitis. A tool suite for simulation based analysis of memory access behavior. In Marian Bubak, Geert Dick van Albada, Peter M. A. Sloot, and Jack Dongarra, editors, *Computational Science - ICCS 2004*, pages 440–447, Berlin, Heidelberg, 2004. Springer Berlin Heidelberg.

[436] Yoshizumi Tanaka, Kenjiro Taura, Mitsuhisa Sato, and Akinori Yonezawa. Performance evaluation of openmp applications with nested parallelism. In Sandhya Dwarkadas, editor, *Languages, Compilers, and Run-Time Systems for Scalable Computers*, pages 100–112, Berlin, Heidelberg, 2000. Springer Berlin Heidelberg.

[437] Gene M. Amdahl. Validity of the single processor approach to achieving large scale computing capabilities. In *Proceedings of the April 18-20, 1967, Spring Joint Computer Conference*, AFIPS '67 (Spring), page 483â485, New York, NY, USA, 1967. Association for Computing Machinery.

[438] John L. Gustafson. Reevaluating amdahl's law. *Commun. ACM*, 31(5):532â533, May 1988.

[439] Israel Koren and C. Mani Krishna. *Fault-Tolerant Systems.* Morgan Kaufmann Publishers Inc., San Francisco, CA, USA, 1st edition, 2007.

[440] Stephen P Brooks and Gareth O Roberts. Assessing convergence of markov chain monte carlo algorithms. *Statistics and Computing*, 8(4):319–335, 1998.